DOE-ER-0313/39
Distribution
Categories
UC-423, -424

FUSION MATERIALS
SEMIANNUAL PROGRESS REPORT
FOR THE PERIOD ENDING
December 31, 2005

Prepared for
DOE Office of Fusion Energy Sciences
(AT 60 20 10 0)

DATE PUBLISHED: MARCH 2006

Prepared for
OAK RIDGE NATIONAL LABORATORY
Oak Ridge, Tennessee 37831
Managed by
UT-Battelle, LLC
For the
U.S. DEPARTMENT OF ENERGY

FOREWORD

This is the thirty-ninth in a series of semiannual technical progress reports on fusion materials science activities supported by the Fusion Energy Sciences Program of the U.S. Department of Energy. This report focuses on research addressing the effects on materials properties and performance from exposure to the neutronic, thermal, and chemical environments anticipated in the chambers of fusion experiments and energy systems. This research is a major element of the national effort to establish the materials knowledge base of an economically and environmentally attractive fusion energy source. Research activities on issues related to the interaction of materials with plasmas are reported separately.

The results reported are the product of a national effort involving a number of national laboratories and universities. A large fraction of this work, particularly in relation to fission reactor irradiations, is carried out collaboratively with partners in Japan, Russia, and the European Union. The purpose of this series of reports is to provide a working technical record for the use of program participants, and to provide a means of communicating the efforts of fusion materials scientists to the broader fusion community, both nationally and worldwide.

This report has been compiled and edited under the guidance of R. L. Klueh and Teresa Roe, Oak Ridge National Laboratory. Their efforts, and the efforts of the many persons who made technical contributions, are gratefully acknowledged.

G. R. Nardella
Research Division
Office of Fusion Energy Sciences

TABLE OF CONTENTS

1.0 VANADIUM ALLOYS

FURTHER OBSERVATIONS ON V-4Cr-4Ti PRESSURIZED CREEP TUBES—D. S. Gelles, R. J. Kurtz, M. B. Toloczko, and L. E. Thomas (Pacific Northwest National Laboratory)*

OBJECTIVE

The objective of this effort is to continue microstructural examinations of creep tubes to determine the deformation processes controlling thermal creep in vanadium alloys for comparison with creep response under irradiation.

SUMMARY

Further observations are provided for pressurized thermal creep tubes of V-4Cr-4Ti examined following testing in the range 650 to 800°C for tests lasting up to ~ 10^4 h. Precipitate particles have been analyzed by EELS to define interstitial contents, and are shown to be either C or O rich with only minor N contents. Grain shape aspect ratios as a function of strain have been measured and these data shows shape change as a result of effective mid-wall strains as high as 12.7%. Deformation mechanisms are considered to explain Newtonian viscous flow response at 800°C below effective midwall stresses of 70 MPa, and it is concluded that grain boundary sliding probably is the predominant mechanism based on the microstructural information presented here, but there is evidence that Harper-Dorn creep may also be a contributing creep mechanism under these conditions.

PROGRESS AND STATUS

Introduction

In our previous report on V-4Cr-4Ti pressurized creep tube examinations, [1] calculations suggested that nitrogen contamination may be responsible for increased precipitation of (Ti,V) oxy-carbo-nitride precipitates during testing. Increased precipitation near the outer surface extending inwards a distance of 30 and 70 μm, respectively, was found at 650 and 700°C after ~ 10^4 h and across the entire tube wall thickness at 800°C, and may have affected creep response. Also, the mechanism controlling creep behavior at higher stresses and lower temperatures was shown to most likely be viscous glide controlled creep arising from the presence of Ti and Cr solid solution hardening. The mechanism controlling behavior at lower stresses and higher temperatures could be grain boundary sliding or Coble creep, but given evidence for extensive dislocation production and rearrangement, an alternate explanation of Harper-Dorn creep was possible. The purpose of the present effort is to give further consideration to these issues. Electron energy loss spectroscopy (EELS) is applied to precipitates in specimen AR13 tested at 700°C and 119 MPa effective midwall stress for 9663 h and grain shape aspect ratios and precipitate particle distributions were examined to investigate applicability of Nabarro-Herring, Coble, Harper-Dorn creep or grain boundary sliding deformation mechanisms.

Experimental Procedure

Specimens selected for further examination are listed in Table 1. Detailed information on specimen preparation and creep testing procedures were reported previously [2,3]. One of the tubes failed during testing, and therefore, the applied stress was removed while at temperature. The vacuum furnace was shut down immediately upon detecting a tube failure so the time at temperature in the unstressed condition was minimal. The other two tubes did not fail and were allowed to cool while still under pressure. A section of as-received tubing was heated treated at 1000°C for 1 h (designated AR) to provide comparison with deformed microstructures.

*Pacific Northwest National Laboratory (PNNL) is operated for the U.S. Department of Energy by Battelle Memorial Institute under contract DE-AC06-76RLO-1830.

Table 1. Test conditions for specimens examined in this report

Specimen ID	Test Temperature (°C)	Midwall Effective Stress (MPa)	Time to failure (h)	Effective mid-wall strain (%)	Comments on failure
AR	Not tested				
AR02	650	200	10601	8.9	Burst
AR13	700	119	9663*	2.3	Did not fail
AR20	800	48	6052*	12.7	Did not fail

*Specimen did not fail. The time listed is the total time at temperature.

Optical metallography was repeated using a hydrofluoric-nitric acid etch (15 ml lactic acid, 15 ml HNO_3, and ~ 1 ml HF for ~ 1.5 min.) in order to better define grain boundary structure and (25 ml H_2O, 12.5 ml HNO_3, 12.5 ml HF for ~ 1 min [4]) to show precipitate stringers.

Specimen preparation for EELS analysis used a cross-section procedure, requiring dimple grinding and ion milling on a Gatan precision ion polishing system operating with 5 KeV argon ions. EELS was performed on a JEOL 2010F transmission electron microscope (TEM) operating at 200 KeV and equipped with a Gatan parallel EEL spectrometer.

Results

Metallography

In an effort to differentiate between different creep mechanisms, grain aspect ratio change was investigated. Figure 1 provides examples of the grain shapes in specimens AR, AR02, AR13, and AR20. All of the grain structures in these specimens appear equiaxed, with only a few examples of acicular grains elongated in the radial direction. It can be noted from Table 1, that effective midwall strains were 8.9, 2.3, and 12.7% respectively; however corresponding differences in grain elongation in the tube tangential direction are not apparent from these images.

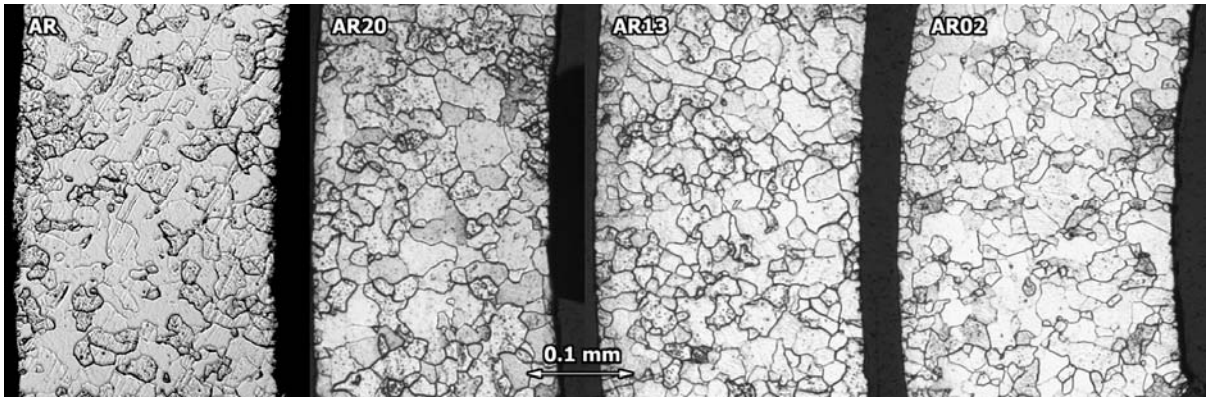

Fig. 1. Grain structure in V-4Cr-4Ti pressurized creep tubes.

A longitudinal section of specimen AR20 was examined following etching both to show grain structure and precipitate stringers [5] in order to determine if stringers could be used as markers to differentiate between operating creep mechanisms [6,7]. It should be noted that the longitudinal section is the only one that shows stringers but it is not ideal for differentiating between creep mechanisms because creep tubes show negligible change in length. Few well defined stringers were found and only one extended over several grains. It is shown in Fig. 2. The stringer does not appear to show any off-set due to grain boundary sliding or diffusional creep processes, suggesting that Harper-Dorn creep is more likely [7].

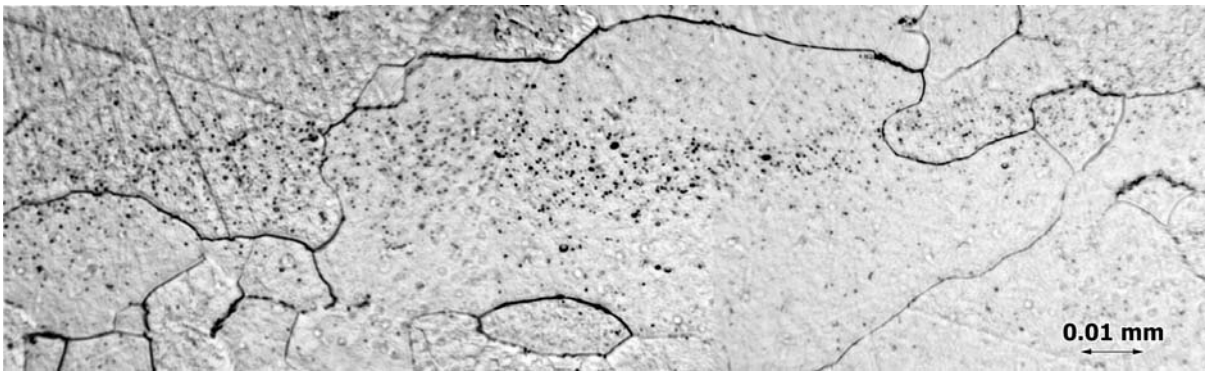

Fig. 2. Longitudinal stringer in specimen AR20.

It the course of examining for stringers in the longitudinal section of specimen AR20, several examples were found where precipitate particles appeared to collect on grain boundaries oriented in the longitudinal direction, whereas few boundaries oriented in the radial direction showed precipitate decoration. As hoop strain results in wall thinning, those boundaries oriented longitudinally would collect particles by diffusion processes involving grain boundaries. Four examples are provided in Fig. 3. Therefore, during creep at 800°C in specimen AR20, a diffusional process involving either bulk or grain boundary diffusion would need to operate for particles to collect as observed.

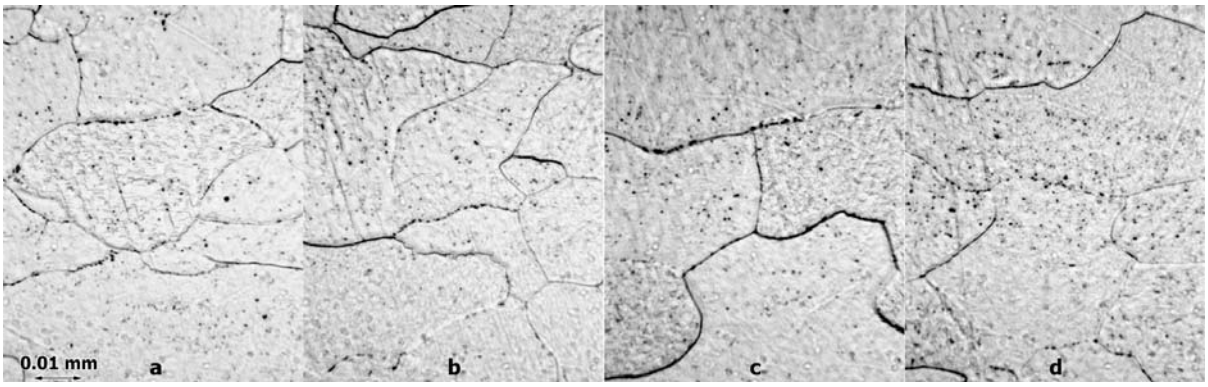

Fig. 3. Precipitation at grain boundaries in specimen AR20. The orientation is the same as in Fig. 2.

Analysis of grain aspect ratios

Grain aspect ratio measurements in tube radial and circumferential directions were made based on images similar to Fig. 1. Evidence for grain aspect ratio change was found as shown in Fig. 4. Note the bars bracketing the average values (open squares) for each specimen represent the range of measured aspect ratios and do not represent measurement error. It is noteworthy that the grain aspect ratio decreases approximately linearly with increasing midwall strain. In diffusion creep, the elongation of the grains will match the overall strain in the sample; whereas if deformation occurs predominantly by grain boundary sliding, there will be no significant grain elongation [7], so the grain aspect ratio will not change. The expected radial-to-circumferential aspect ratio can be estimated assuming none of the deformation is due to grain boundary sliding. As an example consider specimen AR20, which reached an effective mid-wall strain of 0.127. This is equivalent to a mid-wall hoop strain of 0.11. Since the longitudinal strain is zero for a pressurized creep tube and the radial strain is equal, but opposite in sign to the hoop strain the following equations give the predicted grain aspect ratio for AR20 after 12.7% deformation:

$$\varepsilon_c = 0.11 = \ln\left(\frac{c}{c_o}\right)$$
$$\varepsilon_r = -0.11 = \ln\left(\frac{r}{r_o}\right) \qquad (1)$$
$$\frac{r}{c} = \frac{r_o}{c_o} e^{-0.22} = 0.803 \frac{r_o}{c_o} = 0.803 * 1.10 = 0.88$$

where r_o/c_o is the grain aspect ratio for the undeformed specimen. This calculation suggests that grain boundary sliding contributes significantly to the deformation of the specimen since the measured aspect ratio for AR20 is 1.02. As shown in Fig. 4, similar results were obtained for AR02 and AR13 suggesting grain boundary sliding may also contribute some fraction of the overall deformation for these specimens as well.

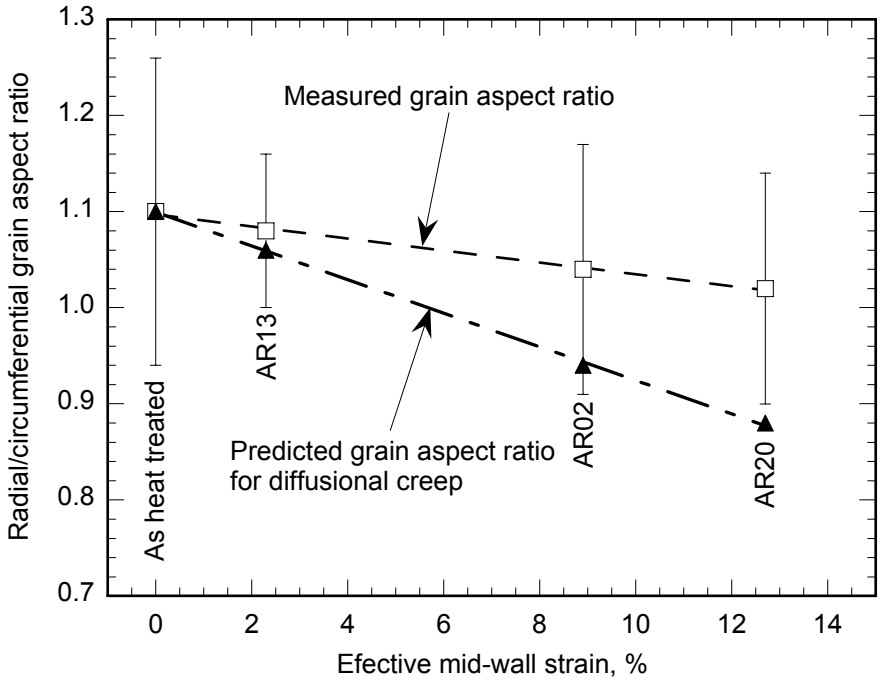

Fig. 4. Measured and predicted grain aspect ratio in pressurized creep tubes as a function of effective mid-wall strain.

Precipitate Interstitial contents from EELS

Precipitate particles in thinned regions of specimen AR13 near the outer diameter were analyzed using electron energy loss spectroscopy (EELS). Results for the first 15 particles analyzed are shown in Fig. 5. Typical energy loss spectra are only shown for the matrix, particle 2 and particle 3, and all spectra are provided using second difference analysis so that edges appear as ringing signals, with the relative size of the peak proportional to the height of the edge. The peak locations for V, Ti, C, N, and O are indicated.

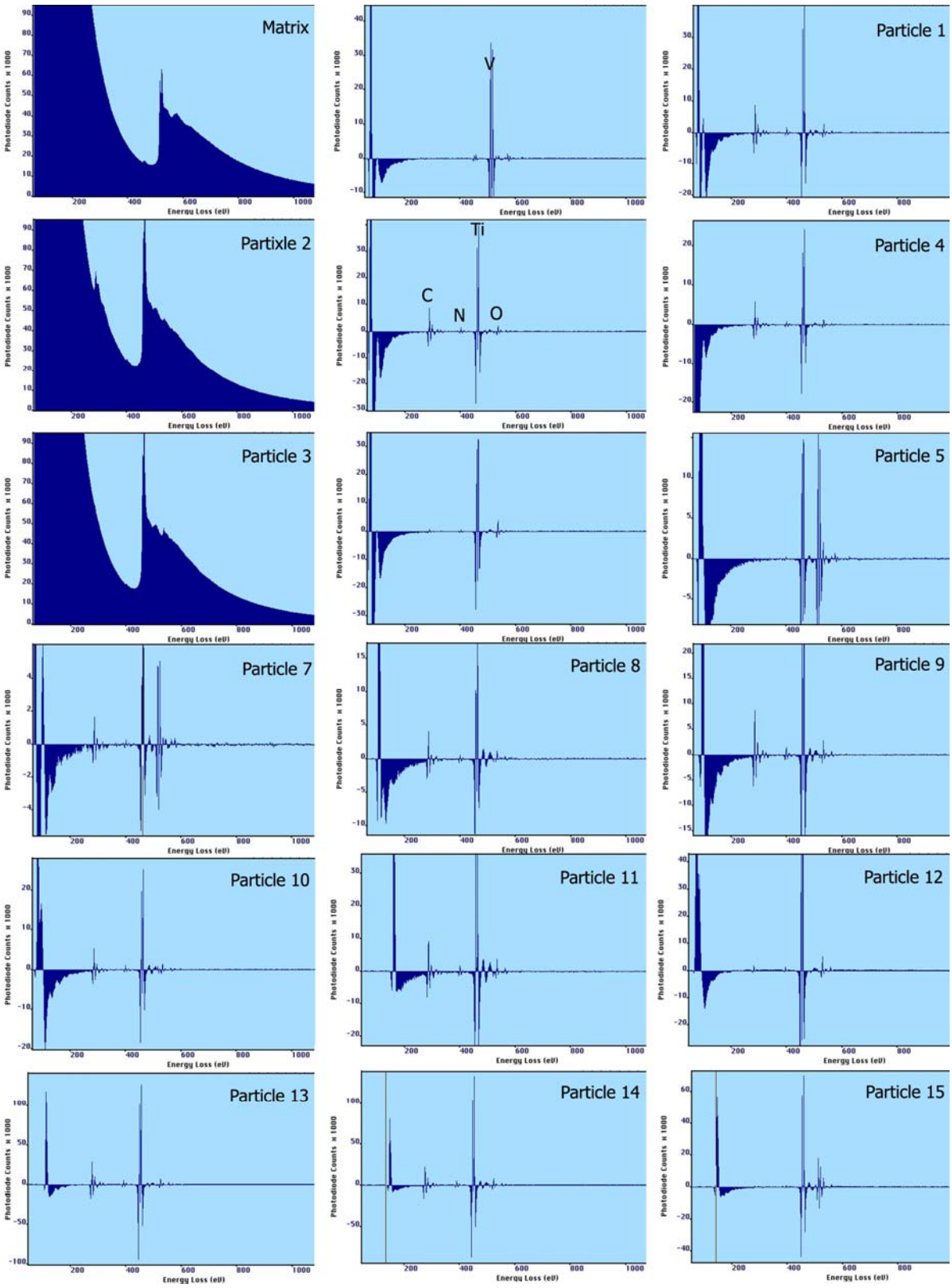

Fig. 5. EELS results for particles near the outer diameter of V-4Cr-4Ti creep tube AR13.

For the matrix spectrum, the large edge denotes V, and smaller edges correspond to Ti and Cr, showing up on either side of the V edge in the second difference analysis. In comparison, second difference spectra of particles 1, 2, and 4 shows that all particles are carbon rich, with less O and even less N. Particle 3 is different, rich in O and showing only slight traces of C and N. Particle 5 appears to be high in Ti and V, with moderate O showing. Spectra for the remaining particles show similar response and similar results were obtained for another 10 particles. Therefore, there was no evidence found for nitrogen rich particles near the outer surface of specimen AR13. All particles examined appeared to be similar to those expected in the as-heat treated alloy [5]. These results conflict with predictions that V-4Cr-4Ti thermal creep tests may have been affected by the environment [1].

Discussion

Our previous work has shown that V-4Cr-4Ti pressurized tubes tested at 800°C and low stress can deform at creep rates with a stress exponent near 1 (0.84) or Newtonian creep, and that the corresponding microstructure showed subgrain dislocation evolution indicative of significant dislocation motion and rearrangement during creep [1]. It was therefore suggested that grain boundary sliding or Coble creep might not be the operating creep mechanism. Figure 6 is provided to show creep response as a function of stress in order to emphasize the dependence on stress, and it is apparent that for stress conditions below 2 x 10^{-3} σ/G, behavior can be interpreted as linear or Newtonian. It can be noted that such behavior had previously been assumed to be due to Coble creep [8] and more recently, it was concluded that this linear response does not exist [9]. It is considered to be important to resolve these differences, because if Newtonian creep is misinterpreted, creep predictions will contain large errors at low stresses.

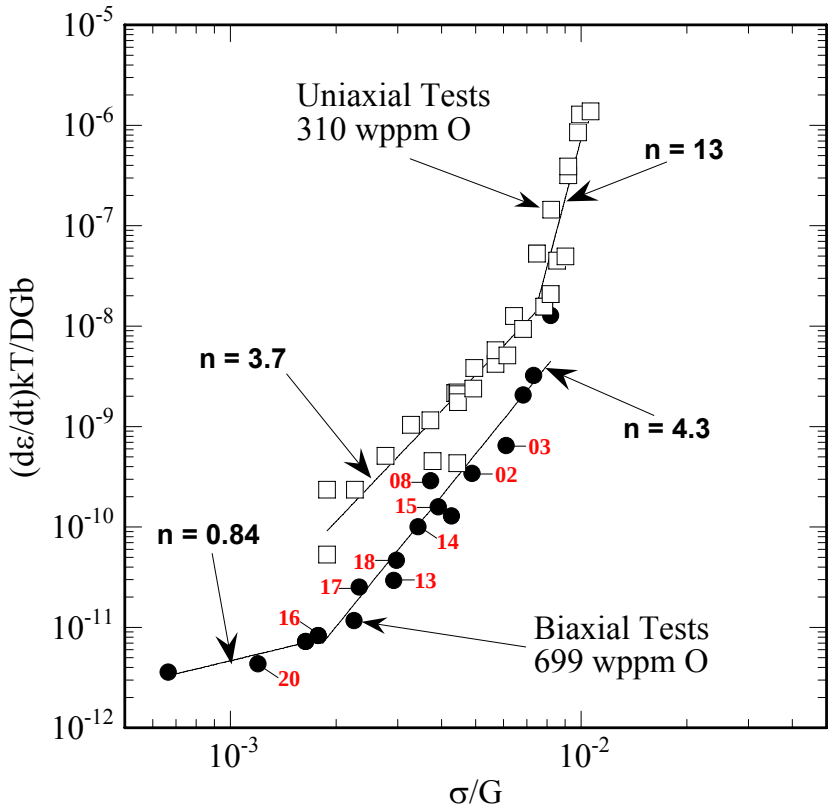

Fig. 6. Stress dependence of the normalized effective mid-wall creep strain for unirradiated vanadium alloys, with pressurized tube specimens chosen for microstructural examination identified by number.

All V-4Cr-4Ti pressurized tube specimen conditions examined by electron microscopy were found to show dislocation rearrangements due to applied stress. Table 2 summarizes the microstructural observations made on pressurized tubes and is organized with increasing test temperature and applied stress. It can be noted that higher stress conditions showed dislocation tangles and lower stress conditions developed examples of subgrain structure, understood to have developed by relaxation of deforming dislocations into lower energy configurations. From this information, it is apparent that specimen AR20 is behaving similarly to specimens tested at higher stress, and therefore it is reasonable to conclude that a dislocation mechanism such as Harper-Dorn creep is at least in part responsible for deformation during Newtonian response in this condition.

Table 2. Summary of microstructural observations on V-4Cr-4Ti pressurized tubes

ID	T_{test} (°C)	$(\sigma/G) \times 10^{-3}$	Strain (%)	Time (h)	Microstructural Features
AR02	650	4.876	9	1060	Complex dislocation tangles between fine precipitates.[1]
AR03	650	6.095	4.4	10,601	Complex dislocation tangles between fine precipitates.[1]
AR13	700	2.919	2.3	9963*	Moderate dislocation density with some subgrain structure.[1]
AR14	700	3.421	15	6667	Subgrain structure with low dislocation density in cells.[9]
AR15	700	3.912	13	2804	Complex dislocation tangles.[8]
AR08	725	3.714	> 5	1506	Moderate dislocation tangles with some fine precipitates.[1]
AR20	800	1.197	13	6052*	Subgrain structure with low dislocation density in cells.[1]
AR16	800	1.776	52	4029	Subgrain structure with low dislocation density in cells.[11]
AR17	800	2.329	14	864	Moderate dislocation tangles between fine precipitates.[10]
AR19	800	3.446	15	242	Moderate dislocation tangles between fine precipitates.[10]

*Did not fail

The purpose of the grain aspect ratio and stringer study given in Figs. 1–4 was to differentiate between diffusion, grain boundary sliding and Harper-Dorn creep mechanisms as proposed by Langdon [6,7], but markers were not ideally oriented and were difficult to find. Based on stringer position across grain boundaries, Harper-Dorn Creep was indicated, but collection of particles on suitably oriented grain boundaries contradicted that conclusion and indicated either Nabarro-Herring or Coble creep was operating to some extent. Wang [12] has noted that Harper-Dorn creep should maintain a constant dislocation density irrespective of the operating stress, but the dislocation structures found in V-4Cr-4Ti pressurized tubes tested at 800°C and low stress developed a recovered dislocation structure containing subgrains. However, Cadek [13] has concluded that subgrain development should be possible only if the grain size exceeds the subgrain size applicable for the applied stress. In the case of the present experiments, the grain size (~ 20 μm) is larger than the predicted subgrain size, $\lambda = 20b(G/\sigma) \approx 3$ μm. It can be argued that grain boundary sliding must allow accommodation that may take the form of dislocation evolution, which may account for the subgrain structure observed. Alternately, it may be argued that subgrains can behave as internal grain boundaries producing Nabarro-Herring or Coble creep.

Consider instead prediction from theory. The normalized steady state creep rate can be written for Harper-Dorn, Nabarro-Herring, Coble creep and grain boundary sliding as follows:

$$\frac{\dot{\varepsilon} kT}{DGb} = A\left(\frac{b}{d}\right)^{p}\left(\frac{\sigma}{G}\right)^{n} \tag{2}$$

where A is an appropriate dimensionless constant, D is the lattice diffusion coefficient, G is the shear modulus, b is the Burgers vector (0.262 nm for vanadium), k is Boltzmann's constant, d is the grain size (~ 20 μm), p is the appropriate grain size exponent, n is the stress exponent, and σ is the applied stress. The respective parameters are given in Table 3.

Table 3. Parameters for theoretical creep predictions

Parameter	Harper-Dorn	Nabarro-Herring	Coble	Grain Boundary Sliding
A	$1.4(\tau_p/G)^2$	27	54	106
p	0	2	3	2
n	1	1	1	1

Experimentally, the linear stress dependence is found to begin at a normalized stress level ~ 2 x 10^{-3} for tests at 800°C, yielding a normalized strain of ~ 8 x 10^{-12}. For Harper-Dorn the value of A depends upon the normalized Peierls stress, τ_p/G, which can be estimated from the procedure given by Wang [12] as 7.6 x 10^{-5} at 800°C. Thus, the computed normalized creep strain at a stress of 2 x 10^{-3} for Harper-Dorn is 1.6 x 10^{-11}, for Nabarro-Herring it is 9.3 x 10^{-12}, for Coble creep it is 2 x 10^{-9}, and for grain boundary sliding creep it is 3.6 x 10^{-11}. The computed value for Nabarro-Herring creep is very close to the observed value in the biaxial creep tests, the computed creep rate for Coble creep is approximately 250 times larger than was observed, and the computed values for Harper-Dorn and grain boundary sliding creep are about 2–4 times higher than was observed. These calculations suggest that grain boundary sliding and Harper-Dorn creep mechanisms are more likely to describe pressurized tube creep behavior than Nabarro-Herring or Coble mechanisms since the Nabarro-Herring mechanism is considered to be operable only at very high homologous temperatures and the Coble model significantly over predicts the observed steady-state creep rate. On the other hand, the pressurized tube creep data may be significantly influenced by interstitial impurities remaining in solution such that comparisons with models that do not include such effects may be difficult to interpret.

In summary, evidence can be found for all three Newtonian creep mechanisms and grain boundary sliding contributing to creep in V-4Cr-4Ti at 800°C and low stress. Creep rate calculations predict Nabarro-Herring creep to be more favorable than Coble creep, but this seems unlikely at 800°C. Metallographic evidence shows precipitate pile-ups on favorably oriented grain boundaries in agreement with both diffusional creep mechanisms. Microstructural evidence indicates that grain boundary sliding and Harper-Dorn creep should operate, supported by the grain aspect ratio measurements and the observed dislocation production and rearrangement. Most likely, each of these mechanisms plays a role in the deformation process, as a function of distance from active grain boundaries.

Conclusions

The mechanism controlling creep behavior at higher stresses/lower temperatures in V-4Cr-4Ti was shown to most likely be viscous glide controlled creep arising from the presence of Ti and Cr solid solution hardening. The predominant mechanism controlling creep behavior at lower stresses/higher temperatures should be grain boundary sliding or Coble creep, but given evidence for extensive dislocation production and rearrangement, Harper-Dorn creep may also contribute to the deformation process.

References

[1] D. S. Gelles and R. J. Kurtz, DOE/ER-0313/36 (2004) 2.
[2] R. J. Kurtz and M. L. Hamilton, DOE/ER-0313/25 (1999) 7.
[3] R. J. Kurtz, A. M. Ermi, and H. Matsui in DOE/ER-0313/31 (2002) 7.
[4] D. T. Hoelzer, ORNL, private communication.
[5] D. T. Hoelzer and J. Bentley, 6th IEA and JUPITER Joint Workshop on Vanadium Alloys for Fusion Energy Applications, Tucson, Arizona, June 21–22, 2002.
[6] T. G. Langdon, Met. Trans. 33A (2002) 249.
[7] T. G. Langdon, Mater. Sci. Eng. A283 (2000) 266.
[8] M. Li and S. J. Zinkle, J. ASTM Int. 2(10) (2005), paper ID JAI12462.
[9] M. Li, T. Hagasaka, D. T. Hoelzer, M. L. Grossbeck, S. J. Zinkle, T. Muroga, K. Fukumoto, H. Matsui, and M. Narui, presented at the 12th International Conference on Fusion Reactor Materials.
[10] D. S. Gelles, M. L. Hamilton, and R. J. Kurtz, DOE/ER-0313/26 (1999) 11.
[11] D. S. Gelles, DOE/ER-0313/31 (2001) 17.
[12] J. N. Wang, Acta Mater. 44 (1996) 855.
[13] J. Cadek, Creep in Metallic Materials, Mater. Sci. Monographs, Elsevier (1988) 151.

COMPRESSION TESTING OF UNIRRADIATED V-4Cr-4Ti—M. M. Fryd (Lawrence University),[1] M. B. Toloczko, and R. J. Kurtz (Pacific Northwest National Laboratory)[2]

OBJECTIVE

The objective of this effort is to better understand the deformation behavior of vanadium alloys after irradiation.

SUMMARY

The NIFS-1 heat and heat 832665 of unirradiated V-4Cr-4Ti were tested in compression at temperatures of 25°C, ~ 250°C, and ~ 420°C. Test traces at all temperatures show an upper and lower yield point. Yield strength in compression and a strain hardening exponent were extracted from the test traces. The yield strength in compression mirrors yield strength values in tension from the literature. The strain hardening exponent at room temperature matches uniform elongation values in tension, but at elevated temperatures, the strain hardening exponent from the compression tests was much greater than uniform elongation values in the literature. Values for the yield strength in compression of the NIFS-1 heat were about 10% lower than heat 832665 which is probably due to the lower oxygen content in the NIFS-1 heat.

PROGRESS AND STATUS

Introduction

Vanadium alloys are of interest to the Fusion program as potential first wall structural materials because of their good thermal conductivity, good elevated temperature tensile strength, good high temperature creep resistance, and relative resilience to becoming radioactive [1–12]. The expected irradiation conditions for the first wall structural material include a range of temperatures where very high hardening caused by a high density of small, but shearable defect clusters results in a type of deformation called "localized deformation" [3,4,9,12–15]. At the onset of yield in a tensile test, a dislocation may move through a grain shearing the obstacles and clearing out a channel. Subsequent dislocations may easily pass through this channel. As the test progresses, more channels form. Up to the point of tensile instability plastic deformation is confined to these channels. One important macroscopic result of this deformation behavior is rapid onset of necking in a tensile test and very low uniform elongation. As a means to help understand the range of stress states where localized deformation may adversely affect macroscopic ductility in vanadium alloys, compression test specimens fabricated from two heats of V-4Cr-4Ti are currently under irradiation in the High Flux Isotope Reactor (HFIR). The results of 25°C, ~ 250°C, and ~ 420°C compression tests on the unirradiated control materials are presented here and compared with uniaxial tensile values from the literature.

Experimental Procedure

Cylindrical compression specimens were fabricated from V-4Cr-4Ti heats 832665 and NIFS-1. Heat 832665 is reported to have an oxygen content of 330 wppm, and the NIFS-1 heat is reported to have an oxygen content of 181 wppm [2]. The cylindrical specimens are 3mm in diameter and 3.5 mm tall. Heat 832665 was received in a 40% cold-worked condition, while the NIFS-1 heat was received in a 98% cold-worked condition. Before testing, individual specimens from both heats were wrapped in tantalum and titanium foil and annealed in a vacuum furnace for two hours at 1000^{o}C at 1×10^{-6} torr or better. Identification codes were laser engraved onto one end of each specimen.

---

[1]Undergraduate student, Lawrence University, Appleton, Wisconsin.

[2]Pacific Northwest National Laboratory (PNNL) is operated for the U.S. Department of Energy by Battelle Memorial Institute under contract DE-AC06-76RLO-1830.

Compression tests were performed in a 10,000 lb screw-driven Instron test frame with a 1000 lb load cell. A special compression test fixture, as shown in Fig. 1, was constructed for the testing. The upper and lower loading surfaces of the fixture were made from a high modulus tungsten carbide composite with a polished surface. The upper loading surface is in the form of a piston that is guided by a cylinder made from machineable carbide composite. A tight tolerance was maintained between the piston and cylinder to limit axial misalignment between the upper and lower loading surfaces. Silicon powder was used as a lubricant on upper and lower loading surfaces. Specimen displacement was monitored with a capacitance-type displacement transducer with a resolution better than 0.0002 mm (better than 0.006% strain).

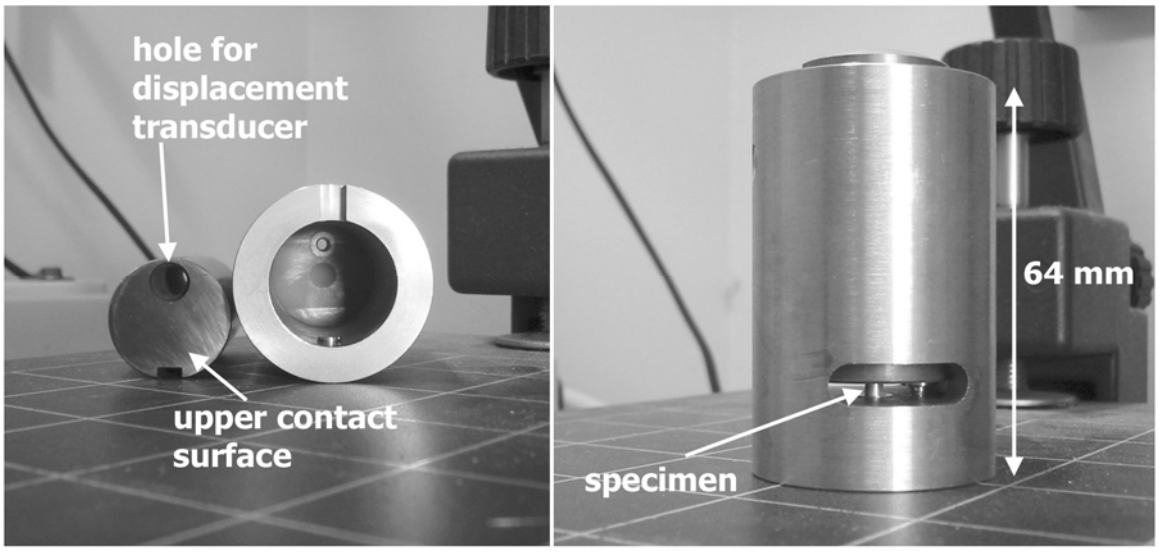

Fig. 1. Pictures of the compression test fixture.

Compression tests were performed at constant crosshead speed and with an initial strain rate of $5x10^{-4}$ s^{-1}. The target test temperatures were 250°C and 425°C. Heating was performed in a vacuum furnace capable of operation in an inert atmosphere or in a vacuum. Tests at 250°C were performed in 99.99% purity argon flowing at a rate of 2 L/min, and tests at 425°C were performed in a vacuum at 0.150 torr in an attempt to lower the partial pressure of oxygen during testing. The vacuum furnace was heated at a rate of 5.1°C/min for tests at 250°C and 9°C/min for tests at 425°C. All data were monitored and recorded electronically. The 0.2% offset yield stress and, when present, the upper yield point was measured from engineering stress versus engineering strain plots. The power law strain hardening (PLSH) exponent was measured from true stress versus true plastic strain plots in the range of 1–2% true plastic strain.

Results

The actual test temperatures were 25°C, 250–255°C, and 405–435°C. Engineering stress versus engineering strain curves for heat 832665 and the NIFS-1 heat are shown in Fig. 2. In most all of the tests, an upper and lower yield point was observed. The yield stress at 250°C was approximately 30% lower than at room temperature. The yield stress at ~ 415°C is essentially the same as at 250°C. Heat 832665 is consistently stronger than Heat NIFS-1 at all temperatures. All samples showed a continuous load increase during plastic deformation up to the load limit of the load cell. Serrations from dynamic strain aging occurred only in CA06. As is common in a compression test, some barreling of the samples occurred.

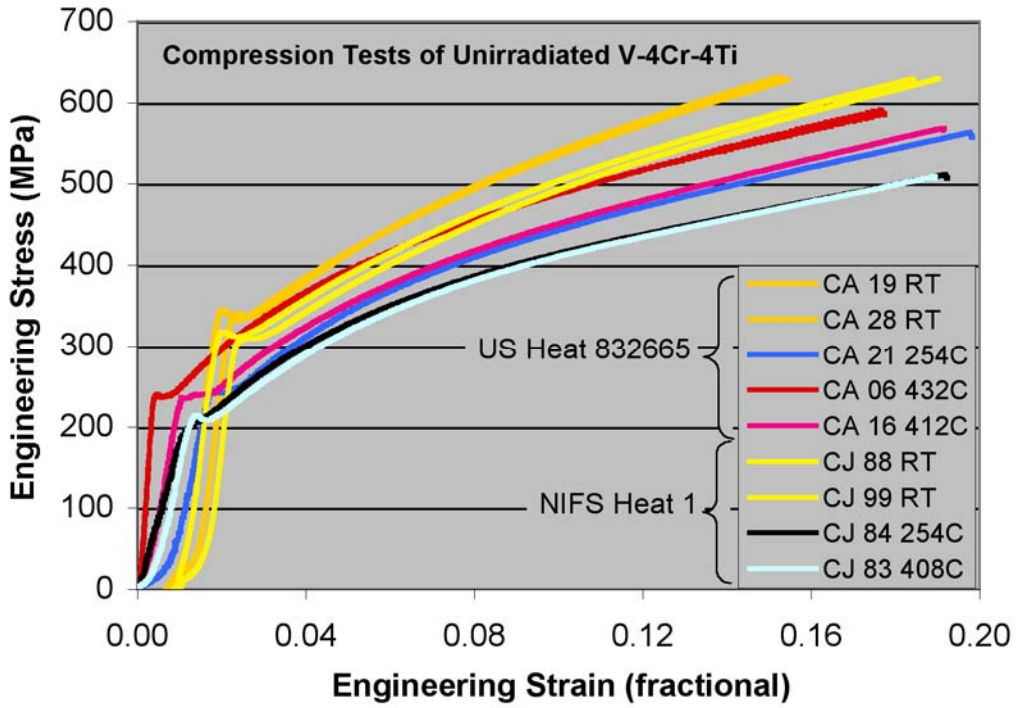

Fig. 2. Engineering stress vs. engineering strain curves for unirradiated V-4Cr-4Ti at 25°C, 250°C, and ~ 420°C.

Table 1 shows the average test temperature, 0.2% offset yield stress, upper yield points, elastic moduli, and PLSH exponents. All values except temperature were calculated by hand. The upper yield point and 0.2% offset yield point were within 4 MPa for all heats. The 0.2% offset yield stress for heat 832665 samples remained approximately 22 MPa higher than the NIFS-1 samples at all test temperatures as

Table 1. Compression test properties of unirradiated V-4Cr-4Ti at 25°C, 250°C, and ~420°C. CA** = 832665 Heat and CJ** = NIFS-1 Heat.

Specimen ID	Average Test Temp (˚C)	0.2% Offset Yield Stress (MPa)	Upper yield point (MPa)	PLSH exponent from .01≤ ε_{pl} ≤ .02
CA 19	RT	340	340	0.17
CA 28	RT	344	344	0.16
CA 21	254	244	245	0.3
CA 06	432	236	240	0.25
CA 16	412	235	235	0.28
CJ 88	RT	310	310	0.16
CJ 99	RT	315	315	0.17
CJ 84	254	222	none	0.28
CJ 83	408	213	214	0.34

shown in Fig. 3. Strain hardening exponents were calculated from 0.01 to 0.02 true plastic strain following the reasoning from [16] and assuming V-4Cr-4Ti follows the power law strain hardening equation ($\sigma = k\varepsilon^n$). Fig. 4 shows the strain hardening exponent versus temperature.

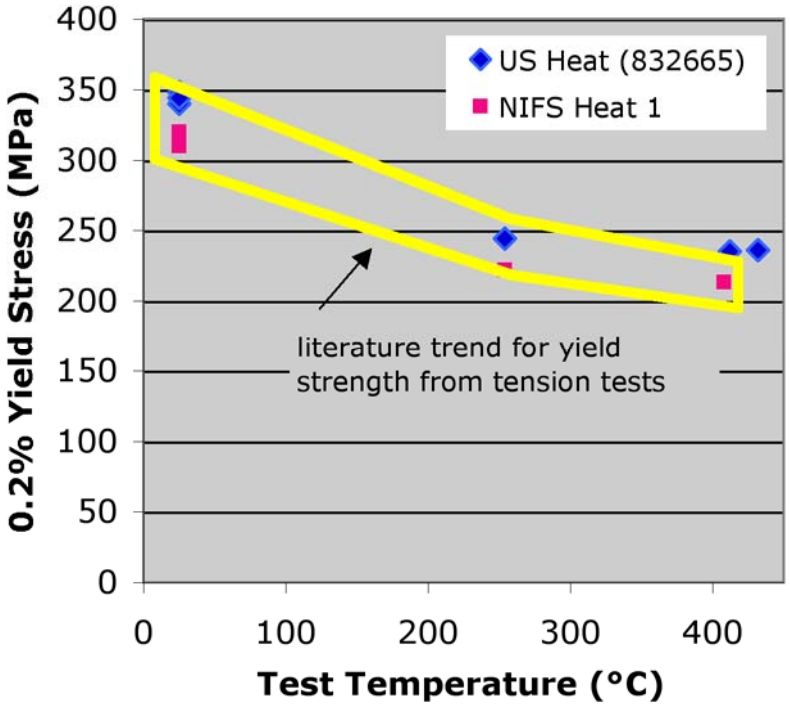

Fig. 3. Temperature dependence at 25°C, 250°C, and ~ 420°C of 0.2% offset yield stress for unirradiated V-4Cr-4Ti.

Discussion

Yield stress values from the literature for uniaxial tensile tests on heat 832665 are 315–355 MPa at 25°C, 220–260 MPa at 250°C, and 195–235 MPa at 400°C [8,9,11,12]. NIFS-1 yield stress values in tension were not found, but the NIFS-2 heat has a yield strength of around 300 MPa at 25°C [17]. Yield stress values from heat 832665 and the NIFS-1 heat measured in compression fall within the range of values in the literature for these materials in tension as expected (Fig. 3) because polycrystalline vanadium with a random grain orientation should have isotropic deformation properties. Figure 3 graphically shows that the elevated temperature compression yield stress is about 30% lower than the room temperature compression yield stress. Heat 832665 may be consistently stronger than the NIFS-1 heat due to heat 832665 having higher oxygen content [7,18]. Strain serrations as exhibited in CA06 (heat 832665) are seen in uniaxial tensile data from 300–750°C [9], but were not seen in some other published V-4Cr-4Ti tensile traces [12]. Dynamic strain aging causes the strain serrations.

Necking does not occur in compression tests, so uniform elongation cannot be measured to compare with tensile data. The PLSH exponent, however, can be used to compare deformation behavior in a compression test to deformation behavior in a tensile test. If there is a sufficient amount plastic strain during the test where the deformation along the length of the compression test specimen is uniform (i.e., minimal barreling for some part of the plastic deformation during the compression test), and if the true stress versus true plastic strain data fit well to the PLSH equation, then the PLSH exponent should be equal to the true uniform elongation (TUE) measured from an equivalent tensile test. The TUE from

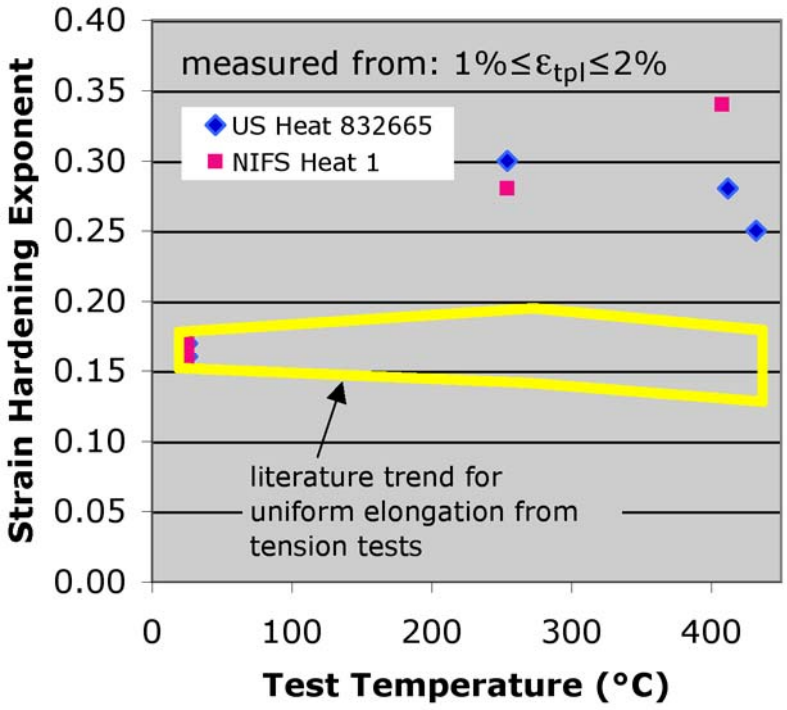

Fig. 4. Temperature dependence at 25°C, 250°C, and ~ 420°C of the strain hardening exponent for unirradiated V-4Cr-4Ti.

tensile data can be calculated from the engineering uniform elongation values in the literature using $\varepsilon_{UE} = \ln(e_{UE}+1)$ where ε_{UE} is the true uniform elongation and e_{UE} is the engineering uniform elongation. Literature values of uniform elongation for heat 832665 are 0.14–0.20 at 25°C and 250°C and 0.13–0.18 at 400°C [8,11,12]. Literature values for NIFS-1 are 0.18–0.2 for temperatures between 25°C and 400°C [19]. The TUE values are thus 0.13–0.18 at 250°C and 0.12–0.17 at 400°C for heat 832665 and approximately 0.18 for the NIFS-1 heat between 25°C and 400°C. A comparison of the measured PLSH exponent values from the compression tests with literature values of TUE from tensile tests are showing in Fig. 4. For the 25°C compression tests, the PLSH exponent ranged from 0.16–0.18 which is in good agreement with the TUE values calculated from tensile data in the literature. For the compression tests at elevated temperature, the PLSH values were considerably higher than the TUE values calculated from tensile data in the literature. The reason for this is not clear and will be investigated further.

Conclusions

Compression tests were performed on unirradiated V-4Cr-4Ti as part of a larger program to better understand the deformation behavior of irradiated V-4Cr-4Ti after irradiation. The yield stress in compression from two unirradiated heats of V-4Cr-4Ti are similar to the yield stress values in tension reported in the literature. The PLSH exponents from compression tests at 25°C are in agreement with TUE values from the literature, but at elevated temperature, the PLSH exponents were higher than the literature values for the TUE from tensile tests. This will be investigated.

Future Work

These results will be used to compare with future compression test studies on neutron irradiated V-4Cr-4Ti alloys.

References

[1] R. J. Kurtz, K. Abe, V. M. Chernov, D. T. Hoelzer, H. Matsui, T. Muroga, and G. R. Odette, “Recent progress on development of vanadium alloys for fusion,” J. Nucl. Mater. 329–333 (2004) 47–55.
[2] T. Muroga, T. Nagasaka, K. Abe, V. M. Chernov, H. Matsui, D. L. Smith, Z.-Y. Xu, and S. J. Zinkle, “Vanadium alloys – Overview and recent results,” J. Nucl. Mater. 307–311 (2002) 547–554.
[3] H. Tsai, L. J. Nowicki, M. C. Billone, H. M. Chung, and D. L. Smith, “Tensile and impact properties of vanadium-base alloys irradiated at low temperatures in the ATR-A1 experiment,” Fusion Materials Semiannual Progress Report 23 (1997) 70–76.
[4] D. J. Alexander, L. L. Snead, S. J. Zinkle, A. N. Gubbi, A. F. Rowcliffe, and E. E. Bloom, “Effects of irradiation at low temperature on V-4Cr-4Ti,” Fusion Materials Semiannual Progress Report 20 (1996) 87–95.
[5] T. S. Bray, H. Tsai, L. J. Nowicki, M. C. Billone, D. L. Smith, W. R. Johnson, and P. W. Trester, “Tensile and impact properties of V-4Cr-4Ti alloy heats 832665 and 832864,” J. Nucl. Mater. 283–287 (2000) 633–636.
[6] K. Natesan, W. K. Soppet, and M. Uz, “Effects of oxygen and oxidation on tensile behavior of V-4Cr-4Ti,” J. Nucl. Mater. 258–263 (1998) 1476–1481.
[7] N. J. Heo, T. Nagasaka, T. Muroga, and H. Matsui, ”Effect of impurity levels on precipitation behavior in the low-activation V-4Cr-4Ti alloys,” J. Nucl. Mater. 307–311 (2002) 620–624.
[8] A. N. Gubbi, A. F. Rowcliffe, W. S. Eatherly, and L. T. Gibson, “Effects of strain rate, test temperature and test environment on tensile properties of vanadium alloys,” Fusion Materials Semiannual Progress Report 20 (1996) 38–52.
[9] A. F. Rowcliffe, S. J. Zinkle, and D. T. Hoelzer, “Effect of strain rate on the tensile properties of unirradiated and irradiated V-4Cr-4Ti,” J. Nucl. Mater. 283–287 (2000) 508–512.
[10] E. V. van Osch and M. I. de Vries, “Irradiation hardening of V-4Cr-4Ti,” J. Nucl. Mater. 271&272 (1999) 162–166.
[11] A. F. Rowcliffe, D. T. Hoelzer, and S. J. Zinkle, “High temperature tensile properties and deformation behavior of V-4Cr-4Ti,” Fusion Materials Semiannual Progress Report 26 (1999) 25–32.
[12] M. C. Billone, “Revised ANL-reported tensile data for unirradiated and irradiated (FFTF, HFIR) V-Ti and V-Cr-Ti alloys,” Fusion Materials Semiannual Progress Report 23 (1997) 3–61.
[13] L. L. Snead, S. J. Zinkle, D. J. Alexander, A. F. Rowcliffe, J. P. Robertson, and W. S. Eatherly, “Summary of the investigation of low temperature, low dose radiation effects on the V-4Cr-4Ti alloy,” Fusion Materials Semiannual Progress Report 23 (1997) 81–98.
[14] S. J. Zinkle, L. L. Snead, A. F. Rowcliffe, D. J. Alexander, and L. T. Gibson, “Effect of irradiation temperature and strain rate on the mechanical properties of V-4Cr-4Ti irradiated to low doses in fission reactors,” Fusion Materials Semiannual Progress Report 24 (1998) 33–40.
[15] S. J. Zinkle, L. L. Snead, J. P. Robertson, and A. F. Rowcliffe, “Strain rate dependence of the tensile properties of V-(4-5%)Cr-(4-5%)Ti irradiated in EBR-II and HFBR,” Fusion Materials Semiannual Progress Report 23 (1997) 77–80.
[16] M. B. Toloczko and R. J. Kurtz, “Room temperature compression properties of two heats of unirradiated V-4Cr-4Ti,” Fusion Materials Semiannual Progress Report 36 (2004) 13–18.
[17] A. Nishimura, T. Nagasaka, and T. Muroga, "Fracture properties of high-purity V-4Cr-4Ti alloy (NIFS-HEAT-2) at room temperature," J. Nucl. Mater. 307–311 (2002) 571–575.
[18] D. L. Harrod and R. E. Gold, “Mechanical properties of vanadium and vanadium-based alloys,” International Metals Reviews 4 (1980) 163–221.
[19] K. Fukumoto, T. Yamamoto, N. Nakao, S. Takahashi, and H. Matsui, “High temperature performance of highly purified V-4Cr-4Ti alloy, NIFS-Heat 1,” J. Nucl. Mater. 307–311 (2002) 610–614.

2.0 CERAMIC COMPOSITE MATERIALS

ON He BUBBLES IN NEUTRON IRRADIATED SYLRAMIC™ TYPE SiC FIBERS–D. S. Gelles and G. E. Youngblood (Pacific Northwest National Laboratory)*

OBJECTIVE

The objective of this effort is to improve understanding of the effects of helium when it is produced in SiC/SiC composites during neutron irradiation in a fusion environment.

SUMMARY

Sylramic™ type SiC fibers, which contain at least 2.3 wt% B, were examined by TEM following neutron irradiation to dose levels of ~ 7 dpa in HFIR at 800°C and to ~ 1 dpa in ATR at 1090°C. At these radiation damage dose levels, transmutation of the boron-10 component effectively "dopes" the Sylramic™ type fibers with up to 10,000 appm helium. Following irradiation at 800°C, bubble development was too fine to reso72lve even by high resolution TEM. However, following irradiation at 1090°C helium bubble development was resolvable, but complex. A fine dispersion of 1-nm bubbles was observed within the SiC grains and a coarse, non-uniform distribution of irregular 25-nm bubbles was observed on grain boundaries. In addition, some unusual arrays of planar 2.5-nm thick bubbles were observed in the SiC grains and equiaxed bubbles were observed in the boride precipitate particles contained within the fiber microstructure. Not unexpectedly, helium retention and bubble formation in β-SiC depends on details of the polycrystalline microstructure as well as the irradiation conditions.

PROGRESS AND STATUS

Introduction

In a fusion reactor with SiC/SiC composite components, large levels of hydrogen and helium will be generated by transmutation of SiC. For instance, in an ARIES-IV first wall with a fast flux (E > 0.1 MeV) of 1.9 x 10^{19} m^2/s Heinisch predicts transmutation production ratios of 58 appm H/dpa and 161 ppm He/dpa for the C and Si components, respectively [1]. At those production rates, after one year the He concentration in SiC could be > 6000 appm in some regions. Since helium is insoluble in SiC, in the point-defect accumulation regime (at temperatures lower than ~ 800°C) swelling is enhanced by the additional accumulation of mostly small clusters of interstitial helium. At higher temperatures the helium clusters begin to coalesce (> 900°C), and are trapped by irradiation-induced vacancies. Together with irradiation-induced point defects, helium in the lattice is expected to degrade the thermal conductivity. At even higher temperatures when the vacancies become mobile (> 1000–1100°C in SiC), the helium is expected to stabilize vacancy clusters to form He-filled bubbles. Such helium-filled bubbles in SiC are expected to degrade mechanical properties. The degradation could be especially severe if the bubbles tend to orient and/or align along common layers such as grain boundaries or faulted planes.

Helium effects in metals and, in general, in other polycrystalline materials (including He diffusion and bubble nucleation under irradiation, dissociation at high temperatures, homogeneous nucleation in the bulk vs. heterogeneous nucleation at extended defects, bubble coarsening and coalescence, bubble pressure state, formation and growth of He platelets as well as possible effects on mechanical properties) are reviewed in Ref. [2]. Extensive single-, dual-, and or triple-beam accelerator irradiation experiments have been performed on SiC or SiC/SiC composites to examine synergistic radiation damage-helium and radiation damage-helium/hydrogen effects [3–5]. In particular, for fusion relevant helium-to-dpa ratios, Katoh observed significantly enhanced swelling in the 400–800°C temperature range for dual beam irradiations with 5.1 MeV Si^{+2}-ion and energy degraded 1.0m MeV He^{+}-ions [6]. However, for T > ~ 900°C similar saturated swelling levels both with and without helium co-implantation suggested a modification of the defect structure. The swelling for dual beam irradiation is greater than

*Pacific Northwest National Laboratory (PNNL) is operated for the U.S. Department of Energy by Battelle Memorial Institute under contract DE-AC06-76RLO-1830.

for neutron irradiations at comparable conditions, except that damage rates are on the order of 10^3 greater for the dual beam tests. Recent work by Chen et al. demonstrated that helium implantation to 2450 appm at ambient temperature produced platelets on the order of 10 nm in diameter lying on (0001) habit planes in hot-pressed hexagonal phase α-SiC [8,9]. Upon annealing to ~ 1500K, the platelets disintegrated into discs of bubbles as the Si and C atoms became mobile. A question that arose was whether similar bubble geometries or preferred locations would develop in β-SiC or, in particular, in fibers with primarily polycrystalline, cubic β-phase SiC grains that contain numerous faulted planes.

Several types of SiC fibers were irradiated at 800°C in the High Flux Isotope Reactor (HFIR) at Oak Ridge National Laboratory and at 1090°C in the Advanced Test Reactor (ATR) at Idaho Falls. One of the fiber types was Sylramic™, which contains a significant amount of boron doping. As boron can transmute to helium and lithium following capture of a low energy neutron, irradiated Sylramic™ fibers provide the opportunity to study effects of He production on SiC microstructures. However, such studies must be performed with the understanding that Li is also produced and that He and Li accumulate in separate spherical halo-like distributions around boride precipitate particles when the boron undergoes transmutation [10,11]. As in the accelerator experiments, the helium production rates during such "boron/helium-doping" experiments are expected to be orders of magnitude higher than for the helium production rates from Si and C transmutation in a fusion neutron energy spectrum. Furthermore, the He and Li recoil atoms themselves are energetic enough to contribute significantly to the overall radiation damage.

This report presents a detailed search by transmission electron microscopy (TEM) for helium bubbles in the boron-containing Sylramic™ type SiC fibers irradiated at 800 and 1090°C and, if formed, a microstructure examination of these bubbles.

Experimental Procedure

The composition of commercial Sylramic™ fiber in wt% is: Si (66.6), C (28.5), B (2.3), Ti (2.1), O (0.8), and N (0.4). Typical properties are: tensile strength (3.2 MPa), elastic modulus (380 GPa), diameter (10 μm), bulk density (3.0+ g/cc), C/Si ratio (1/1), and thermal conductivity at 323K (40–46 W/mK). The high degree of crystallinity and density lead to a high elastic modulus and thermal conductivity for this SiC fiber. The small diameter and relatively fine grain size allow this fiber to be readily woven into fabrics for composite 2D- or 3D-structures. Furthermore, the Sylramic™ fiber is thermally and chemically stable under ceramic matrix composite processing conditions up to ~ 1800°C. Developed by Dow Corning Corporation with support from NASA, Sylramic™ is primarily stoichiometric polycrystalline β-SiC. The 2.3 wt% boron exists primarily as crystalline precipitates of titanium diboride. The ~ 40-nm TiB_2 crystallites are uniformly distributed and typically are found at triple points of the 100–500 nm sized β -SiC grains [12]. The latter contains considerable twinning and stacking faults, primarily with {111} habit planes. Small amounts of B_4C (1 wt%) and BN also occur. The TiB_2, as well as minor amounts of B_4C and BN, limit grain growth during sintering of the green fiber.

Individual 50-mm long Sylramic™ SiC tows were encapsulated within Hexoloy™ sintered α-SiC protection tubes. Small vent holes in the tubes allowed gas exchange with the surrounding helium atmosphere. The specimens were irradiated in the HFIR as part of the HFIR-MFE-RB-14J experiment at 800°C (7.0 dpa) [13] or in the ATR as part of a similar experiment called "KAMET" at 1090°C (0.65 dpa) [14].

The transmutation of B proceeds as follows [15]. Natural He boron contains ~ 20% ^{10}B which can absorb a low energy neutron and transmute to ^{7}Li while releasing a α-particle. For 94% of the time, the ^{7}Li is in an excited state with recoil kinetic energy 0.840 MeV and the He atom recoils with a kinetic energy of 1.47 MeV. For the remaining 6% of the time, these atoms recoil with kinetic energies of 1.015 and 1.777 MeV, respectively. Stopping and Range of Ions in Matter (SRIM) calculations [16] for these conditions in SiC are given in Table 1.

Table 1 indicates that the bulk of the helium produced by transmutation will be deposited in a spherical halo about 3.4 μm from a ~ 40-nm TiB_2 particle with typical spacing between particles of 100–200 nm. Thus, the He (and Li) haloes formed about each TiB_2 particle contain ~ 10^5 other halo sources, and the overall He (and Li) deposition is expected to be fairly uniform within the SiC lattice. As mentioned, the relatively high recoil atom kinetic energies significantly contribute to the overall point-defect production in the fibers as well.

Table 1. SRIM calculations for Range and Straggle as a function of ion kinetic energy in SiC

Ion	Energy (MeV)	Fraction (%)	Range (μm)	Straggle (nm)
He	1.47	94	3.36	116
He	1.78	6	4.12	124
Li	0.84	94	1.79	110
Li	1.01	6	2.33	114

The helium content for the fiber specimens was determined by isotope-dilution gas mass spectroscopy (IDGMS) following vaporization in a resistance-heated graphite crucible. This method, developed to accurately measure low levels of helium in small liquid or solid samples, measures the absolute amount of ^{4}He released relative to a known quantity of added ^{3}He [17].

The ~ 10 μm diameter fibers were successfully thinned for electron microscopy by ion milling in a Precision Ion Polishing System (PIPS) from Gatan, Inc., operating with 5 KeV argon ions. A few fibers were glued between Mo washers using thermal setting epoxy, and then ion-milled in double modulation mode with the ion beam parallel to the fiber direction. This milling geometry tended to produce an elliptical cross-section from the circular fibers. It was found during preliminary preparation tests on unirradiated fibers that individual fibers were electron transparent when milled through to separation, but fiber vibration during examination prevented observation with high resolution. However, where fibers crossed, milling was sufficient to provide electron transparent regions without separation, and such regions could be examined at high resolution. Microstructure examinations by TEM were performed on a JEM 2010F operating at 200 KeV equipped with a Gatan parallel electron energy loss spectrometer (EELS) and an Oxford Instruments, Inc., X-ray spectrometer with INCA software.

Results

The helium concentrations of the Sylramic™ type SiC fibers and a monolithic sintered α-SiC (Hexoloy™ SA) are given in Table 2.

Table 2. Helium concentration in neutron irradiated SiC materials measured by IDGMS

Sample	Condition	Mass (mg)[a]	Meas. ^{4}He[b]	^{4}He Conc. (appm)[c]
J22	Unirradiated	1.412	0.073	0.34
Hexoloy™	800°C/7.0 dpa	0.694[d]	2.842[d]	1,350[d]
J22B,C	800°C/7.0 dpa	0.438[d]	7.566[d]	5,516[d]
KA44rA	500°C/0.95 dpa	1.116	34.06	10,040
KA44rB,C	“ “	0.166[d]	5.03[d]	9,946[d]
KA44r”A	1090°C/0.65 dpa	0.842	27.66	10,810
KA44r”B,C	“ “	0.155[d]	5.04[d]	9,982[d]

[a]Mass of specimen for analysis with uncertainty ±0.002 mg.
[b]Measured quantity of helium (x 10^{16} atoms) with uncertainty of ±1%.
[c]Helium concentration in atomic parts per million (appm) with respect to 3.04 x 10^{22} atoms/gm for SiC.
[d]Average values for duplicate samples B and C determined six years post-irradiation.

Samples labeled J22 were commercially available Sylramic™ fiber whereas samples labeled KA44 were a developmental version called Dow EPM. Helium contents in samples J22, KA44rA, and KA44r"A were originally analyzed in 1999. Helium contents in the remaining duplicate samples were analyzed in 2005. For the complete burn-up of the 20% ^{10}B component in Sylramic™ containing 2.3 wt% natural boron, 8330 appm helium should produced. The sintered monolithic Hexoloy sample contains 0.6 wt% natural boron (as B_4C precipitates); therefore about 2170 appm helium should be produced for complete burn-up of $^{10}\beta$.

By examining the data in Table 2, three conclusions can be reached regarding the helium contents remaining in the irradiated fibers. First, the KA44 fibers (Dow EPM irradiated at either 500 or 1090°C) retained helium contents ~ 20% in excess of the calculated 8330 appm for complete burn-up of the boron in Sylramic™ fiber. This suggests that the assumed boron content of 2.3 wt% in the Dow EPM (developmental Sylramic™) fiber was too low. Second, the similar helium contents determined for each irradiation temperature suggests that the produced helium is a saturation value even for doses of 0.65 dpa; and that no helium was lost at the higher irradiation temperature of 1090°C. Furthermore, the helium content values determined after storage of the fibers for six years decreased by only ~ 5% which suggests that the helium was retained within the irradiated fiber microstructure in a rather stable form. This may not be the case for the irradiated J22 (commercial Sylramic™) fiber where the measured helium contents are high, but nevertheless are about 34% less than the expected saturation value for complete $^{10}\beta$ burn-up. Regardless, there is sufficient helium in all of the irradiated fibers to carry out the main objective of this study, i.e., to examine the formation, distribution, and shape of helium bubbles formed in neutron irradiated polycrystalline SiC fibers with primarily β-SiC grains.

Microstructure of unirradiated Sylramic™ fiber

The microstructure of a commercial Sylramic™ fiber sample is shown in Fig. 1. It is polycrystalline, with a grain size greater than 100 nm and exhibits a twinned structure. Composition maps for this region showing outputs for B, C, Si, Ti, O, and a background signal that provides a measure of mass or thickness variation are shown in Fig. 2. The small particles rich in Ti do not account for all regions low in Si. However, the Ti rich regions account for regions of enhanced mass or thickness, and an association with O is indicated. Unfortunately, the B and C maps contain little information due to the low energy peaks associated with these elements. However, EELS examination did show B associated with regions containing high Ti, verifying the presence of TiB_2.

800°C irradiation

Following irradiation at 800°C, evidence for helium accumulation could not be identified. Examples at sufficient magnification to see 1-nm bubbles are given in Fig. 3, with no clear evidence for bubbles. In both examples, the image is under-focused at ~ 500 nm so that bubbles should show white with a black outline. Composition maps were generated similar to those shown in Fig. 2. A mosaic was made to identify large TiB_2 particles in thin areas at the edge of the sample and regions ~ 3 um from the largest particles were examined in detail, without improved success at imaging He bubbles. Apparently, the helium is distributed on too fine a scale for successful bubble imaging after the 800°C irradiation.

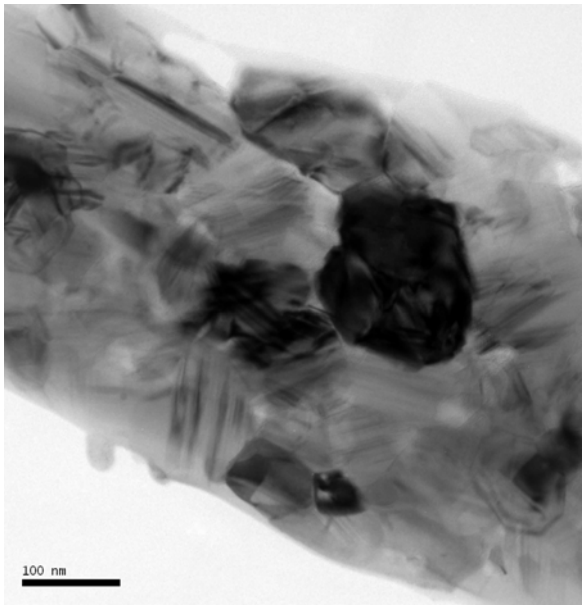

Fig. 1. An unirradiated Sylramic™ fiber thinned by ion milling.

1090°C irradiation

Following irradiation at 1090°C, bubbles were present in

two forms: uniformly distributed small bubbles at high density and non-uniformly distributed larger bubbles at low density. Low magnification examples of the general microstructure are provided in Fig. 4 where large bubbles on the order of 25 nm in diameter appear to be associated with grain boundaries. However, bubble shapes often are unusual, characteristically becoming pits after being distorted during preparation due to association with foil surfaces.

Examples of bubble structures at higher magnification are given in Fig. 5(a-d). Figure 5a is an under-focused image at high magnification showing a high density of small white bubbles with bubble diameters of ~ 1 nm. Figures 5b, c, and d show more complex, larger bubbles, apparently associated with grain structure of a different character. However, the fine bubbles away from the regions with complex structure are visible in the under-focused condition in Fig. 5c and in the over-focused condition in Fig. 5b. Several examples of complex bubbles were examined in stereo, which confirmed that these structures were captured within the SiC fiber and were not surface artifacts. The bubbles shown at the particle interface in Fig. 5b are of complex shape, and the bubbles in Figs. 5c and 5d appear to be planar bubbles with at least two configurations. Figure 5c shows the specimen tilted so that bubbles in the center of the array are on edge, which is an indication that these bubbles are as thin as 2.5 nm. Therefore, within the crystalline grains of Dow EPM fibers helium bubbles are formed on a very fine scale, (~ 1nm) and are barely resolvable after irradiation at 1090°C. However, bubble accumulation at grain boundaries often develops as large as 25 nm. Bubble structure characteristic of planar bubbles in α-SiC are also found. Attempts to demonstrate that planar bubble arrays were in fact in grains of β-SiC were unsuccessful, and in one case were found to be present in a B_4C grain.

Discussion

The results of this study indicate that relatively large quantities (up to 10,000 appm) of helium were distributed on a very fine scale after neutron irradiation of boron-doped Sylramic™-type SiC fibers. Following irradiation at 800°C, bubbles could not be resolved. Following irradiation at 1090°C, bubbles could be resolved at high magnification but within the SiC grains they were only about 1 nm in diameter. However, much larger bubbles (up to 25 nm in diameter) were discovered at grain boundaries.

The large complex planar bubble arrays shown in Figs. 5c and d are not expected to be representative of β-SiC. It is more likely that they are associated with the boride additions, as demonstrated by one example where such bubbles were found to be within a B_4C grain.

The present work on bubbles in Sylramic™ type fibers can be compared with earlier work on dense, pressureless sintered monolithic Hexoloy™ SA with equiaxed grains of 4–6 μm in diameter of hexagonal phase α-SiC [14]. Hexoloy™ SA contains less natural boron than the Sylramic-type fibers (0.6 wt% B added as B_4C to aid sintering). The present KA44 Dow EPM fibers with about four times as much boron as in Hexoloy, also generated about four times more helium than did the Hexoloy when the two materials were irradiated side-by-side in the same experiment (see Table 2). Nevertheless, the Hexoloy™ material exhibited a well-developed, dense array of 50-nm bubbles uniformly decorating grain boundaries. The bubbles were hexagonal in cross section and quite flat. So, relatively large bubbles were formed on the grain boundaries of both SiC materials, but the bubbles were larger, more densely packed and appeared only on the grain boundaries in the Hexoloy™ α-SiC. This evidence suggests that helium is trapped and dispersed on a much finer scale in the fine-grained, Sylramic™ fibers with faulted β-SiC grains as compared to the much larger-grained Hexoloy™ α-SiC with a limited fault microstructure.

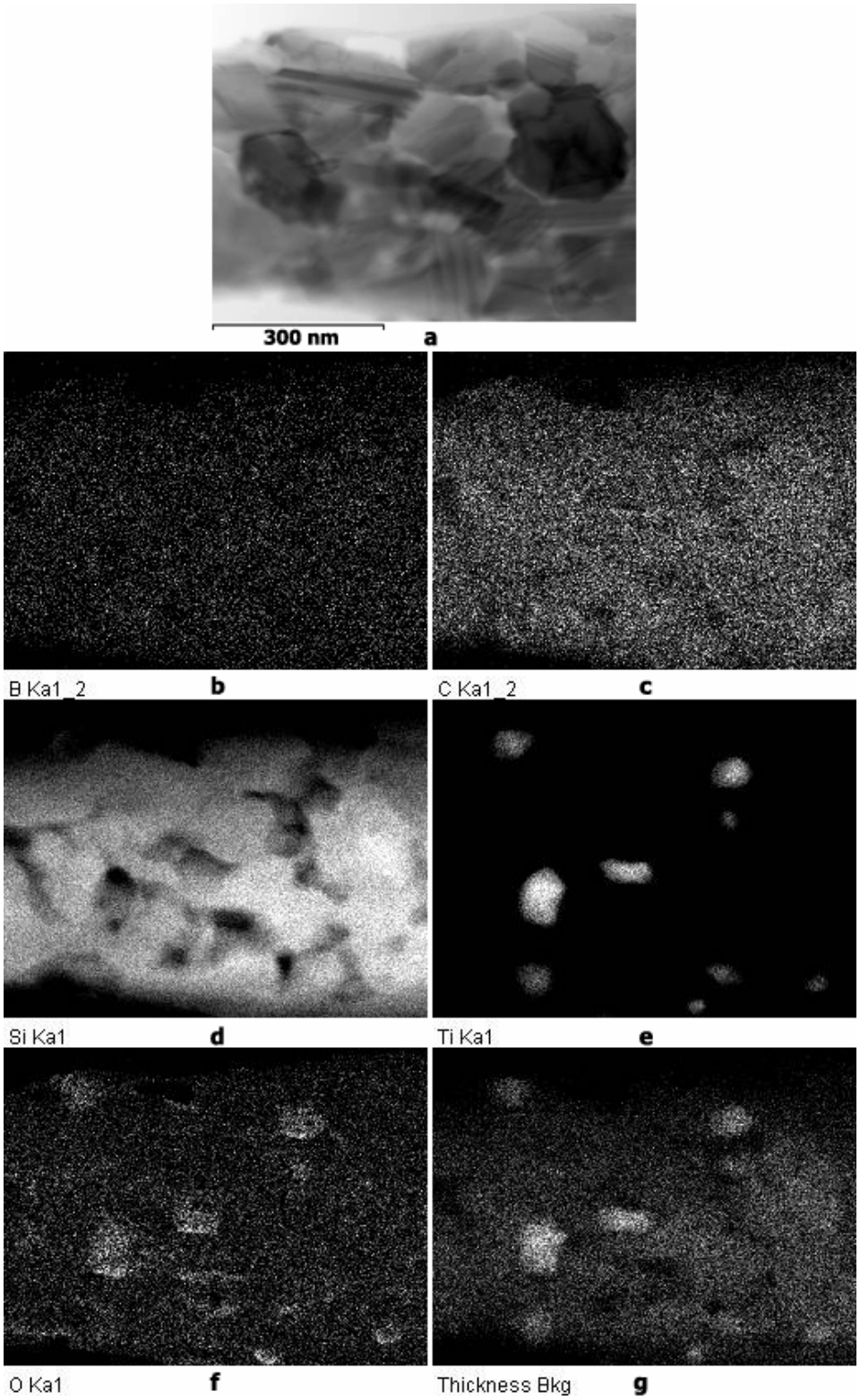

Fig. 2. Composition maps for Sylramic^{TM} fiber showing a region of interest and B, C, Si, Ti, and O windows as well as a background window effectively mapping mass or thickness.

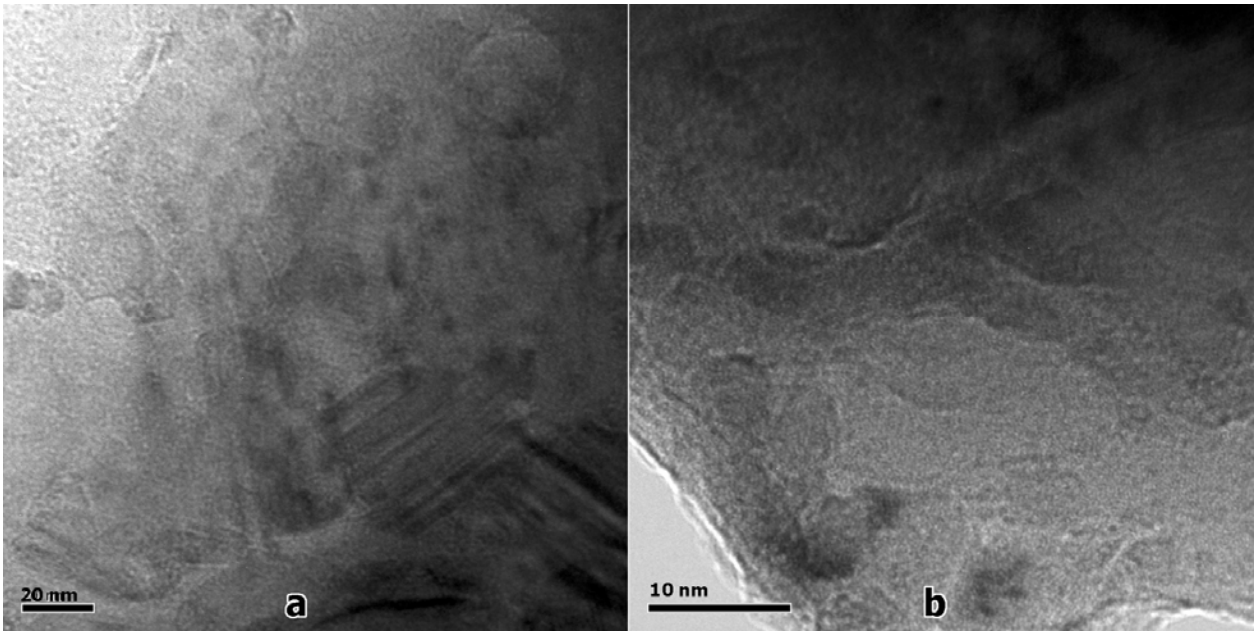

Fig. 3. Examples of microstructure in a Sylramic™ fiber at high magnification following irradiation at 800°C illustrating an unsuccessful attempt to identify fine helium bubbles.

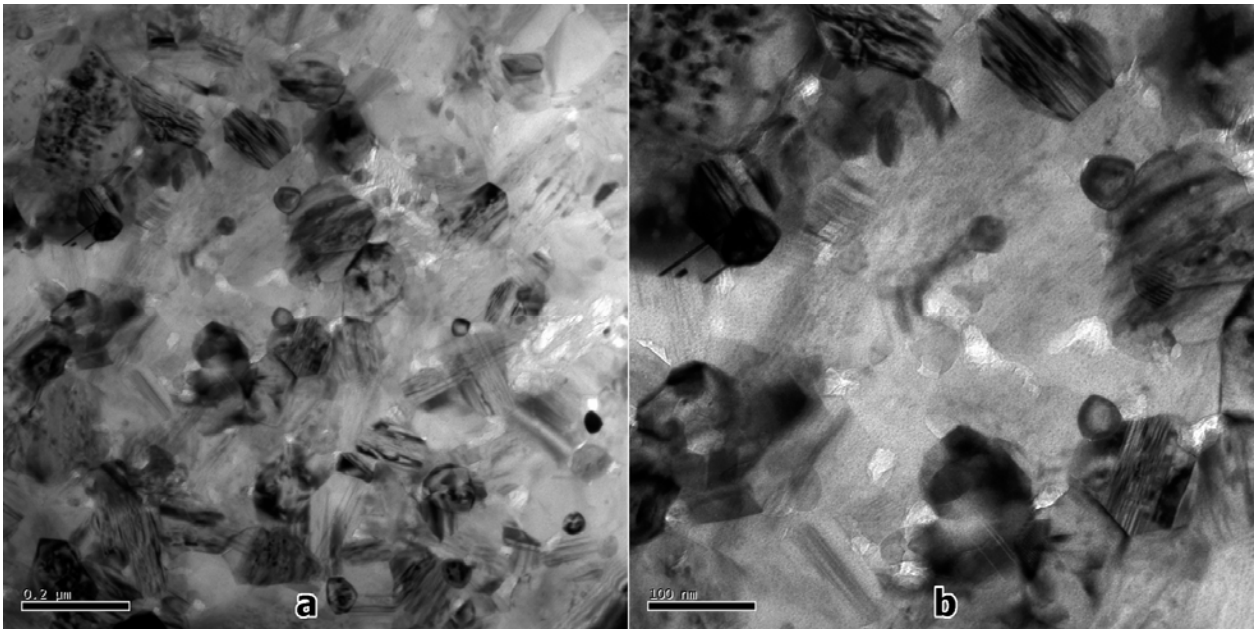

Fig. 4. Dow EPM (Sylramic™ type) fibers at low magnification following irradiation at 1090°C showing coarse helium bubble structure associated with grain boundaries and second phase particles.

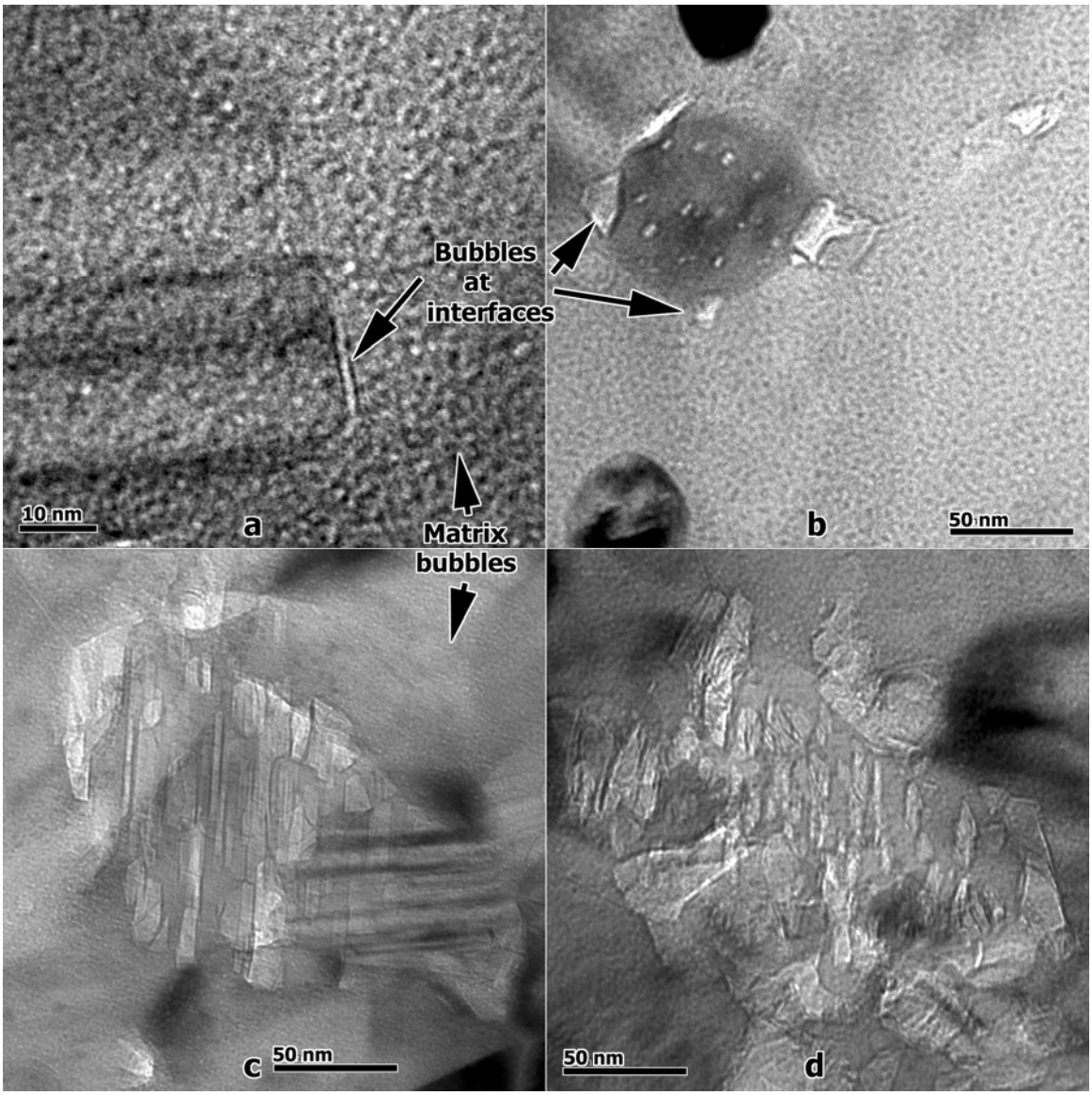

Fig. 5. Bubbles in the Dow EPM (Sylramic™ type) SiC fibers at higher magnification following irradiation at 1090°C showing bubble structures.

Ozawa et al. examined the microstructural evolution of SiC/SiC composites (made with Tyranno™-SA fiber reinforcement) using TEM after Si^{2}+ with/without He+ ion irradiation at 1273/1673K [18]. In the dual-ion irradiations at 1673K (100 dpa, 60 appm He/dpa), helium bubbles (d < 5nm) were densely formed on {111} faulted planes in the fiber and in the chemical vapor infiltrated (CVI) SiC matrix. Furthermore, lens-shaped cavities (major diameter 20–50 nm) were formed on grain boundaries of the matrix. Although the experiments by Ozawa were carried out at higher irradiation temperature and with dual ion bombardment, the similar helium bubble evolutions exhibited by Sylramic™-type SiC fibers Tyranno™ to the SA is striking.

Conclusions

The effect of helium production from boron additions has been studied in Sylramic™ type SiC fibers neutron irradiated at 800 and 1090°C. It was found that polycrystalline β-SiC may absorb He on a fine scale so that bubbles are too small to resolve following irradiation at 800°C and is only ~ 1 nm in diameter in the matrix following irradiation at 1090°C. However, some larger bubbles are found at grain boundaries and sometimes within the TiB_2 particles following irradiation at 1090°C. Nevertheless, the fine dispersion of a considerable amount of helium throughout the β-SiC grains with a highly faulted microstructure indicates that β-SiC may be uniquely able to survive the high levels of helium expected to be generated in SiC in a fusion environment.

Future Work

The effort will be continued as opportunities become available.

Acknowledgements

B. M. Oliver at PNNL provided the helium analysis of the SiC materials.

References

[1] H. L. Heinisch, Fusion Materials Semiannual Progress Report for Period Ending June 30, 2000, DOE/ER-0313/28, p. 98.
[2] H. Trinkhaus and B. N. Singh, J. Nucl. Mater. 323 (2003) 229.
[3] S. Nogami et al., J. Nucl. Mater. 283–287 (2000) 268.
[4] T. Taguchi et al., J. Nucl. Mater. 307–311 (2002) 1135.
[5] A. Hasegawa et al., J. Nucl. Mater. 329–333 (2004) 582.
[6] Y. Katoh, H. Kishimoto, and A. Kohyama, J. Nucl. Mater. 307–311 (2002) 1221.
[7] H. Kishimoto et al., Ceram. Trans. 144 (2002) 343–352.
[8] J. Chen, P. Jung, and H. Trinkaus, Phys. Rev. Letters 82 (1999) 2709.
[9] J. Chen, P. Jung, and H. Trinkaus, Phys. Rev. B 61 (2000) 12923.
[10] D. S. Gelles and F. A. Garner, J. Nucl. Mater. 85–86 (1979) 689.
[10] A. Kumar and F. A. Garner, Radiat. Effects 82 (1984) 61.
[11] J. Lipowitz, J. A. Rabe, A. Zangvil, and Y. Xu, Ceram. Eng. Sci. Proc. 18:3 (1997) 147.
[12] A. L. Qualls, DOE/ER-0313/28 (2000) 241.
[13] D. J. Senor, G. E. Youngblood, L. R. Greenwood, D. V. Archer, D. L. Alexander, M. C. Chen, and G. A. Newsome, J. Nucl. Mater. 317 (2003) 145.
[14] B. A. Oliver, private communication.
[15] G. R. Greenwood, private communication.
[16] H..Farrar and B. M. Oliver, J. Vac. Sci. Technol. A4 (1986) 1740.
[17] K. Ozawa, S. Kondo, T. Hinoki, K. Jimbo, and A. Kohyama, Fusion Sci. Technol. 47 (2005) 871.

EFFECT OF NEUTRON IRRADIATION ON TENSILE PROPERTIES OF UNIDIRECTIONAL SILICON CARBIDE COMPOSITES–Y. Katoh, T. Nozawa, L. L. Snead, and T. Hinoki (Oak Ridge National Laboratory)

OBJECTIVE

The objective of this work was to determine the effects of neutron irradiation in chemically vapor-infiltrated Hi-Nicalon™ Type-S SiC/SiC composites. A unidirectional reinforcement architecture was employed in order to better investigate the effects of irradiation on constitutive mechanical properties of the continuous fiber-reinforced composites. A miniature tensile test procedure developed for the irradiation effect studies by the authors was utilized.

SUMMARY

Tensile strength properties of unidirectionally reinforced Hi-Nicalon™ Type S SiC fiber, CVI SiC-matrix composites with either PyC or multilayered $(PyC/SiC)_n$ interphase was characterized after neutron irradiation to the maximum fluence of 7.7 x 10^{25} n/m^2 at 380 and 800°C in High Flux Isotope Reactor at Oak Ridge National Laboratory. The stress/strain behavior of the multilayered interphase composites remained unmodified after irradiation. The PyC interphase composite improved the ultimate tensile stress and the strain to failure by neutron irradiation, in slight expense of the proportional limit stress. Potential mechanisms for these changes include the irradiation creep-induced misfit stress mitigation, reduced interfacial friction, and the differential swelling among individual composite constituents. Substantial difference in irradiation effect on non-linear deformation of SiC/SiC composites is expected between unidirectional and multi-dimensional architectures.

PROGRESS AND STATUS

Introduction

Silicon carbide (SiC) continuous fiber-reinforced SiC-matrix composites (SiC/SiC composites) are the promising candidate materials for the advanced blanket design concepts for fusion reactors [1,2]. Those blanket concepts assume the SiC/SiC wall and/or channel as the pressure boundary for helium and/or lead-lithium cooled structures, or as the insulating insert for the lead-lithium flow channels [2–4]. One of the primary common requirements for such applications is that the SiC/SiC components retain their mechanical integrity under a combined loading of high flux neutrons and the substantial internal / external stresses. For example, many of the conceptual advanced blanket design works assume the maximum design stresses of ~ 200 MPa for SiC/SiC blanket structures [3]. Even for the flow channel insert applications where the expected external stress level is small, the magnitude of thermal stress can reach ~ 100 MPa depending on design parameters [5]. Recent studies support that the non-irradiated strength of the advanced SiC/SiC composites satisfies these requirements, and neutron irradiation may not significantly deteriorate the strength [6].

Historically the effect of neutron irradiation on the strength of SiC/SiC composites has been evaluated primarily by three-point or four-point flexural tests. It was well understood that a flexural test is suitable only for the purpose of screening-type experiments, as the flexural strength values can not be deconvoluted to intrinsic mechanical properties of fibrous composites [9]. However, a testing standard for tensile properties of ceramic matrix composites had not been available until ASTM standard C1275 was published in year 2000. Moreover, the test standard and generally accepted testing guidelines required multiple specimens each of which is substantially larger than can be accommodated in typical irradiation capsules. Recently, effort focusing on the establishment of a miniature test specimen technology for the tensile properties of ceramic matrix composites successfully lead to provide recommendation of small specimen geometries and test procedures for the irradiation effect studies [8].

It is well perceived that the flexural strength of near-stoichiometric SiC fiber-reinforced, chemically vapor-

infiltrated SiC-matrix composites, or advanced radiation-resistant CVI SiC/SiC composites, undergoes little or no degradation by neutron irradiation to ~ 8 dpa at 300–800°C [9,10]. In this work, the effects of neutron irradiation in similar SiC/SiC composites were evaluated utilizing the miniature tensile test procedures developed for the irradiation effect studies. Also, a unidirectional reinforcement architecture was employed in order to better investigate the effects of irradiation on constitutive mechanical properties of the continuous fiber-reinforced composites.

Experimental Procedure

The materials used were CVI SiC-matrix composites unidirectionally reinforced with Hi-Nicalon™ Type S near-stoichiometric SiC fibers. To facilitate the pseudo-ductile fracture, pyrolytic carbon (PyC) and multilayered $(PyC/SiC)_n$ coatings were applied onto the fiber as the fiber-matrix interphases. Typical fiber volume fraction and the composite porosity are ~ 30% and ~ 16%, respectively. Attributes of the materials studied are summarized in Table 1. These materials are identical to those used in the previous studies and the specimens were taken from the same plates [10].

The miniature straight tensile bar specimens of 50mm x 4mm x ~ 1.5mm were neutron-irradiated in two facilities at High Flux Isotope Reactor (HFIR) at Oak Ridge National Laboratory (Oak Ridge, TN, USA); to 1.8 x 10^{25} n/m^2 (E > 0.1 MeV, the same shall apply hereinafter) at 380°C in the peripheral target position rabbit facility, and to 7.7 x 10^{25} n/m^2 at 800°C in RB-14J removable beryllium reflector facility.

The tensile tests were performed at room temperature, incorporating incremental unloading / reloading sequences but in otherwise following the general guidelines in ASTM Standard C1275-00. The crosshead displacement rate was 0.5mm/min. A pair of strain gauges attached at the gauge section centers on both faces was used to determine both the average and the bending strains. The maximum fractional bending strain in successful tests appeared to be less than ~ 10%. The average strain was used for analysis of tensile properties. The proportional limit stress (PLS) was defined as the stress at 5% stress deviation from the extrapolated tangent modulus fit [11].

Results

In Figs. 1 (A) and (B), tensile stress/strain relationship is compared for non-irradiated and irradiated samples of the PyC and multilayered interphase composites, respectively. It is immediately noticed that no significant deteriorating irradiation effect on strength took place in either composite. The apparent feature of non-irradiated PyC interphase composite is the general failure at the stress slightly beyond the proportional limit, whereas some of the irradiated PyC interphase samples exhibit the ultimate tensile stresses which largely exceed the proportional limit stresses. It should also be noted that the strain to failure for the irradiated PyC interphase composite is substantially larger than that for the non-irradiated composite. As to the multilayered interphase composite, no significant difference in apparent stress/strain relationship is observed between the non-irradiated and the irradiated conditions.

The ultimate tensile stress of the unidirectional composites is plotted in Fig. 2 (A) as a function of neutron

Table 1. List of materials studied

Material	Fiber	Interphase	Matrix	V_f (%)	Density (g/cm^3)	Porosity (%)
UD-HNLS/PyC	Hi-Nicalon™ Type-S	$PyC^{520\text{-}720nm}$	SiC^{CVI}	~ 30	~ 2.6	~ 17
UD-HNLS/ML	Hi-Nicalon™ Type-S	$5x(PyC^{20nm}/SiC^{100nm})$	SiC^{CVI}	~ 30	~ 2.7	~ 15

dose. Data from an irradiation experiment in Japan Materials Test Reactor (JMTR, Oarai, Japan) for the identical materials were included [12]. The error bars represent the standard deviations in Fig. 2 (A) and the following figures. Although the statistical uncertainty may not be eliminated when comparing between particular data points, it is reasonable to admit the slight irradiation-induced strength enhancement, as all the irradiated average strength values are higher than the non-irradiated strength value for the identical material.

(A)

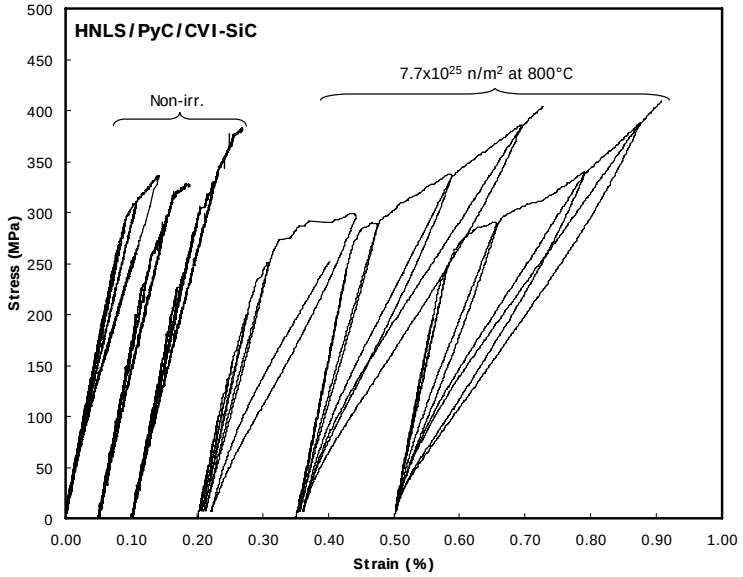

(B)

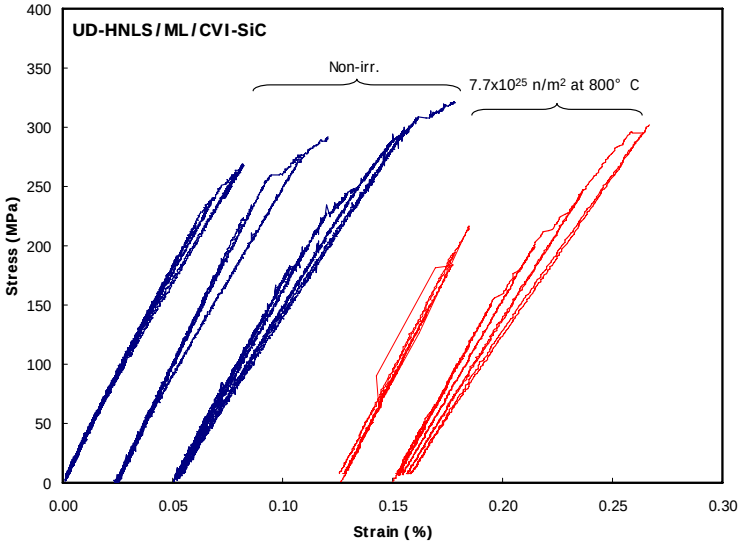

Fig. 1. Tensile stress - strain curves for non-irradiated and irradiated unidirectional Hi-Nicalon™ Type S composite with ~ 720 nm - thick PyC interphase (A) and multilayered $(PyC^{20nm} / SiC^{100nm})_5$ interphase (B).

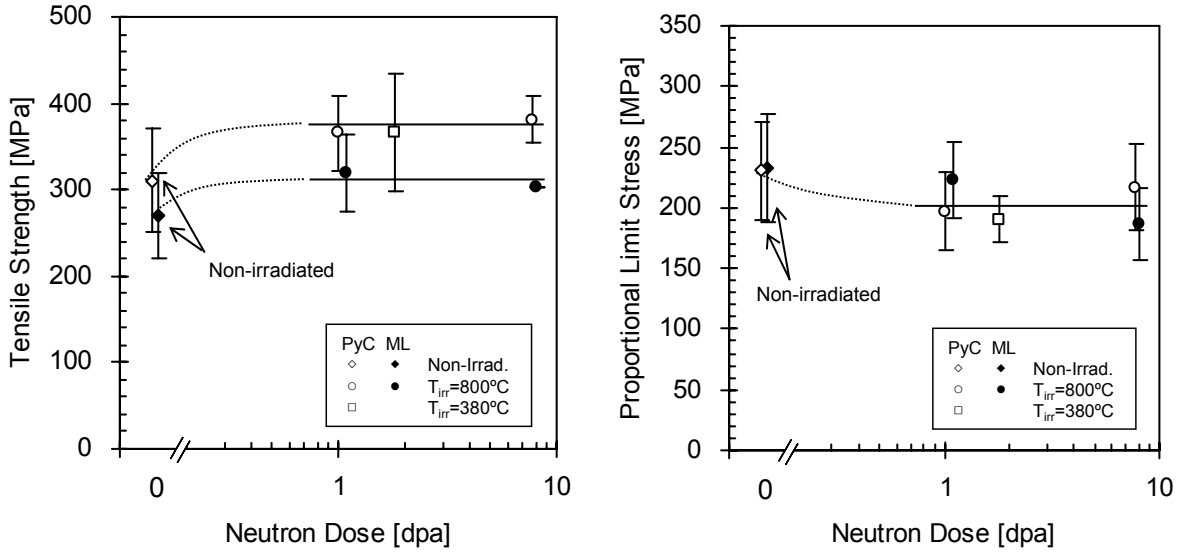

Fig. 2. Effect of neutron irradiation dose on ultimate tensile stress (A) and proportional limit tensile stress (B) of unidirectional Hi-Nicalon™ Type S composites. Error bars represent standard deviations.

In Fig. 2 (B), the influence of neutron dose on the proportional limit tensile stress is presented. The proportional limit stress did not appear to be very sensitive to neutron irradiation, but is likely to slightly decrease after irradiation.

The tensile properties measured are summarized in Table 2. The irradiation effect on the strain to failure for the PyC-interphase composite, which is consistent with the observation in Fig. 1 (A), is noticeable. The modification of tangent moduli was not statistically significant. For unidirectional composites, the longitudinal tangent modulus is determined only by the elastic moduli of the fiber and the matrix, both comprise of beta-phase SiC in the materials studied. The expected change in elastic modulus of beta-phase SiC by irradiation in this temperature range is a few to several percent [13]. Therefore, it is reasonable with this data scatter not to admit the tangent modulus change.

Table 2. Summary of non-irradiated and irradiated tensile properties.
Numbers in parentheses represent standard deviations.

Material	Condition	E (GPa)	UTS (MPa)	PLS (MPa)	ε_f (%)
UD-HNLS/PyC	Non-irradiated	357 (30)	311 (60)	231 (42)	0.16 (0.06)
	1.8 x 10^{25} n/m^2 @ 380°C	354 (23)	366 (67)	197 (33)	0.40 (0.11)
	7.7 x 10^{25} n/m^2 @ 800°C	320 (11)	381 (26)	217 (36)	0.38 (0.02)
UD-HNLS/ML	Non-irradiated	375 (18)	271 (49)	232 (45)	0.09 (0.03)
	7.7 x 10^{25} n/m^2 @ 800°C	356 (34)	302	186 (30)	0.12

Discussion

The most important result obtained in this work is the demonstrated insensitivity of tensile strength of the advanced SiC/SiC composites to neutron irradiation. However, significant effect of irradiation on the tensile behavior of the PyC-interphase composite beyond the proportional limits was observed. The apparent irradiation effect features on tensile behavior of the PyC-interphase composite are 1) the extended non-linear deformation beyond the proportional limit, 2) the slightly reduced proportional limit stress, and 3) the enlarged width of the unloading - reloading hysteresis. The increased ultimate stress and the strain to failure are primarily the consequences of the extended non-linear deformation.

The width of the unloading/reloading hysteresis loop at the half peak stress ($\delta\varepsilon_{1/2}$) can be related with the interfacial sliding stress (τ) and the mean matrix crack spacing ($\bar{d}$) by the following equation [14].

$$\delta\varepsilon_{1/2} = \frac{b_2\left(1-a_1 f\right)^2 \sigma_p{}^2}{8 f^2 \tau E_m} \cdot \frac{r}{\bar{d}} \tag{1}$$

where f is fiber volume fraction, σ_p is the peak stress, E_m is the matrix modulus, r is fiber radius, and a_1 and b_2 are the Hutchinson-Jensen parameters [15]. According to this equation, the enlarged hysteresis loop width implies the lower sliding stress and/or higher crack density, since other parameters do not significantly change by irradiation. Since the strength degradation of PyC interphase is anticipated, it is reasonable to assume that reduced interfacial friction potentially contributed to the observed hysteresis loop widening. However, a detailed interfacial shear properties analysis in the companion work by Nozawa et al. did not indicate a significant irradiation-induced change in the interfacial friction for the identical material [16]. Therefore, the hysteresis loop widening may have been caused by the higher matrix crack density in the irradiated samples.

The matrix cracking stress (σ_{mc}) can be given by the equations below [17,18].

$$\sigma_{mc} = \sigma_{mc}^0 - \sigma_T \tag{2}$$

$$\sigma_{mc}^0 = \left[\frac{6\tau\gamma_m}{r} \cdot \frac{V_f{}^2 E_f E_c{}^2}{\left(1-V_f\right)E_m{}^2}\right]^{1/3} \tag{3}$$

where σ_{mc}^0 is the matrix cracking stress in an internal stress-free condition, σ_T is misfit stress defined in Ref. [17], γ_m is matrix fracture energy, and E_f and E_c are Young's moduli of fiber and composite, respectively. The matrix fracture energy stays unchanged or possibly increased by irradiation [13,19], but it is likely that the extent of potential increase is small, since the proposed primary toughening mechanism for the chemically vapor deposited SiC is associated with cleavage fracture of large grains and therefore may not effectively operate for the highly fine-grained microstructures in the SiC matrix deposited by CVI. Assuming all other parameters, including the interfacial sliding stress, in Eq. 3 would not be significantly influenced, σ_{mc}^0 can be insensitive to neutron irradiation.

The misfit stress in an as-infiltrated condition is originated from the mismatch in coefficient of thermal expansion (CTE) between the fiber and the matrix. The manufacturer-claimed CTE of ~ 5.1 x 10^{-6} K^{-1} (20–500°C) for Hi-Nicalon™ Type S fiber is slightly larger than that for vapor-deposited SiC. This should result in compressive axial component of misfit stress for the matrix, thus increases apparent matrix cracking stress and the proportional limit stress. Since the irradiation temperatures in this study are lower than the matrix infiltration temperature of 1100–1200°C, the misfit stress will be relaxed by the irradiation creep deformation of both the fibers and the matrix, leaving reduced misfit stress when the specimens are cooled down to room temperature. Thus irradiation creep can mitigates the internal stress and consequently lower the matrix cracking stress.

The matrix crack density is ideally proportional to matrix damage parameter (D) in the following definition [20].

$$D = \frac{E_c - E^*}{E^*} \tag{4}$$

where E^* is the tangent modulus of the unloading curve. In Fig. 3, the matrix damage parameters for non-irradiated and irradiated PyC-interphase composites are compared as a function of the peak tensile stress. The lower onset stress and the larger slope for the irradiated samples clearly indicate the increased matrix cracking susceptibility. It is also noted in Fig. 3 that the matrix crack saturation is almost reached for the irradiated samples, while the non-irradiated samples fail before the crack saturation. The tensile failure of composites before the matrix crack saturation often implies excess interfacial friction. Although the measured interfacial friction change was not significant, it is possible that a minor change in the friction contributed to the observed enhanced non-linear deformation of the irradiated samples. However, this does not mean that the applied interphase was too strong for this composite system, because the external tensile stress required for introduction of matrix cracks is much lower in woven architectures, which are used for practical applications.

From Fig. 3, it is obvious that the similar matrix crack density occurs at substantially different stress levels in non-irradiated and irradiated samples. For example, matrix damage parameter of 0.5 occurs at ~ 280 MPa in irradiated conditions, whereas it occurs at ~ 330 MPa in a non-irradiated condition. When the hysteresis behavior is compared at these peak stress levels for respective conditions, the nearly closed irradiated loops contrast the widely open non-irradiated loops. This implies the radiation-induced mitigation of compressive internal stress in the matrix, rather than the unlikely substantial reduction in interfacial friction discussed earlier. In fact, the magnitude of compressive matrix stresses roughly estimated from the tensile regression lines decrease from 78 ±21 MPa non-irradiated to 34 ±24 MPa irradiated. Irradiation can also mitigate the axial tensile residual stress in the fibers through irradiation creep, in the same way as reducing the compressive residual stress in the matrix, thus cause prolonging

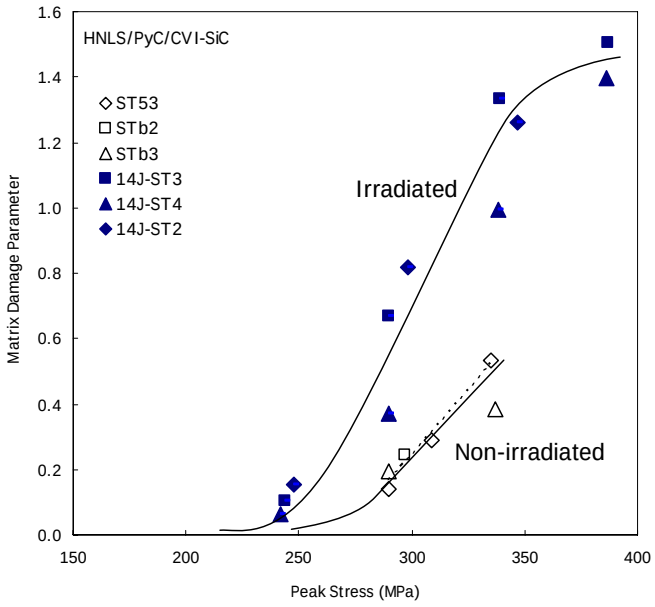

Fig. 3. Effect of neutron irradiation on evolution of matrix damage parameter with increasing peak tensile stress.

the apparent failure strain of the fibers. Therefore, the observed irradiation effect on the extended non-linear deformation of the PyC-interphase composites may be attributed to 1) reduced residual stresses in matrix and fibers by irradiation creep and 2) possibly reduced interfacial frictional stress. Potential differential swelling among the matrix, interphase, and fibers, which was not investigated in this work, may have also contributed to the macroscopic irradiation effects in the composites.

The most likely reason for the unmodified tensile behavior for the multilayered interphase composite is that the higher interfacial friction combined with the high matrix cracking stress, which is particular with the unidirectional reinforcement architecture, urged the premature composite failure even after irradiation. The single fiber push-out measurement and analysis support that both the interfacial debond and frictional stresses for the multilayered interphase are substantially higher than those for the PyC interphase [16].

Conclusions

Neutron irradiation to the maximum fluence of 7.7 x 10^{25} n/m^2 at 380 and 800°C did not impose deteriorating effect on tensile strength of unidirectional Hi-Nicalon™ Type S SiC fiber-reinforced, CVI SiC-matrix composites with either PyC or multilayered $(PyC/SiC)_n$ interphase. The tensile stress/strain behavior of the multilayered interphase composites remained unmodified after irradiation. The PyC interphase composite improved the ultimate tensile stress and the strain to failure in slight expense of the proportional limit stress. Potential mechanisms for these changes include the irradiation creep-induced misfit stress mitigation, reduced interfacial friction, and the differential swelling among individual composite constituents. Substantial difference in irradiation effect on non-linear deformation of SiC/SiC composites is expected for between unidirectional and multi-dimensional architectures.

References

[1] B. Riccardi, L. Giancarli, A. Hasegawa, Y. Katoh, A. Kohyama, R. H. Jones, and L. L. Snead, J. Nucl. Mater. 329–333 (2004) 56–65.
[2] L. Giancarli, H. Golfier, S. Nishio, R. Raffray, C. Wong, and R. Yamada, Fusion Eng. Des. 61–62 (2002) 307–318.
[3] A. R. Raffray, R. Jones, G. Aiello, M. Billone, L. Giancarli, H. Golfier, A. Hasegawa, Y. Katoh, A. Kohyama, S. Nishio, B. Riccardi, and M. S. Tillack, Fusion Eng. Des. 55 (2001) 55–95.
[4] M. Abdou, D. Sze, C. Wong, M. Sawan, A. Ying, N. B. Morley, and S. Malang, Fusion Sci. Technol. 47 (2005) 475–487.
[5] C. P. C. Wong, V. Chernov, A. Kimura, Y. Katoh, N. Morley, T. Muroga, K. W. Song, Y. C. Wu, and M. Zmitko, "ITER Test Blanket Module Functional Materials," presented at the 12th International Conference on Fusion Reactor Materials, December 4–9, 2005, Santa Barbara.
[6] Y. Katoh, A. Kohyama, T. Hinoki, and L. L. Snead, Fusion Sci. Technol. 44 (2003) 155.
[7] A. G. Evans and D. B. Marshall, Acta Metall. 37 (1989) 2567–2583.
[8] T. Nozawa, Y. Katoh, A. Kohyama, and E. Lara-Curzio, Fifth International Energy Agency Workshop on SiC/SiC Ceramic Composites for Fusion Energy Application, PNNL-SA-37623, San Diego (2002) 74–86.
[9] T. Hinoki, L. L. Snead, Y. Katoh, A. Hasegawa, T. Nozawa, and A. Kohyama, J. Nucl. Mater. 307–311 (2002) 1157–1162.
[10] L. L. Snead, Y. Katoh, A. Kohyama, J. L. Bailey, N. L. Vaughn, and R. A. Lowden, J. Nucl. Mater. 283–287 (2000) 551–555.
[11] Y. Katoh, T. Nozawa, and L. L. Snead, J. Am. Ceram. Soc. 88 (2005) 3088–3095.
[12] T. Nozawa, K. Ozawa, S. Kondo, T. Hinoki, Y. Katoh, L. L. Snead, and A. Kohyama, J. ASTM Int. 2 (2005) 12884-1-13.
[13] Y. Katoh and L. L. Snead, J. ASTM Int. 2 (2005) 12377-1-13.
[14] A. G. Evans, J.-M. Domergue, and E. Vagaggini, J. Am. Ceram. Soc. 77 (1994) 1425–1435.
[15] J. W. Hutchinson and H. M. Jensen, Mech. Mater. 9 (1990) 139–163.
[16] T. Nozawa, Y. Katoh, K. Ozawa, L. L. Snead, and A. Kohyama, "Strength of Neutron Irradiated SiC/SiC Composite with Multilayer SiC/PyC Interface," presented at the 12th International Conference on Fusion Reactor Materials, December 4–9, 2005, Santa Barbara.

[17] E. Vagaggini, J.-M. Domergue, and A. G. Evans, J. Am. Ceram. Soc. 78 (1995) 2709–2720.
[18] W. A. Curtin, J. Am. Ceram. Soc. 74 (1991) 2837–2845.
[19] L. L. Snead, T. Hinoki, and Y. Katoh, Fusion Materials, DOE/ER-0313/33 (2002) 49–57.
[20] M. Y. He, B. X. Wu, A. G. Evans, and J. W. Hutchinson, Mech. Mater. 18 (1994) 213–229.

SWELLING OF SiC AT INTERMEDIATE AND HIGH IRRADIATION TEMPERATURES—L. L. Snead, Y. Katoh, and S. Connery (Oak Ridge National Laboratory)

OBJECTIVE

The objective of this work is to define through experimental evidence the swelling behavior of stoichiometric SiC under neutron irradiation in the void swelling regime.

SUMMARY

This paper presents results from a neutron irradiation campaign on CVD SiC carried out in the High Flux Isotope Reactor. Materials were irradiated in a range of temperature from 200–1600°C and from a fraction of a dpa to ~ 6 dpa. Data on swelling and room temperature thermal conductivity are presented. The swelling behavior below ~ 800°C agrees well with the literature values. Data in the range of 1000–1600°C indicates a non-saturated swelling as the dose is increased from 2 dpa to 6 dpa, with increasing swelling with increasing irradiation temperature. Any peak in void swelling apparently occurs at irradiation temperature > 1600°C (> 0.6 T_M.) Near 1000°C, volumetric swelling increases from ~ 0.2% to ~ 0.6% as dose increases from ~ 2 dpa to ~ 6 dpa. The maximum swelling was found to be ~ 1.5% at the maximum dose and temperature of this study, ~ 6 dpa and ~ 1600°C. Room temperature thermal conductivity data over the entire temperature range are presented and a direct correlation between the thermal defect resistance and swelling is seen for materials irradiated at temperature less than 800°C. Above 1000°C the correlation between swelling and thermal defect resistance breaks down indicating a changing microstructure at high temperature to a microstructure less effective at scattering phonons on a swelling-normalized basis.

PROGRESS AND STATUS

Introduction

The neutron-induced swelling and degradation in thermal conductivity of silicon carbide (SiC) has been well studied for low and intermediate temperatures (~ 20–1000°C). Originally this material was investigated in support of nuclear fuel coating [1–9] and more recently for various nuclear applications such as structural SiC composites [10-23]. Before proceeding, it is important to distinguish neutron-induced effects in high purity materials, such as single crystal and most forms of chemically vapor deposited (CVD) SiC, with those of lower purity forms such as hot pressed, sintered, liquid phase converted, or polymer-derived SiC. It is well understood that the presence of significant impurity levels in these materials lead to unstable behavior under neutron irradiation [12,15,24,25], as compared to stoichiometric materials, which exhibit remarkable radiation tolerance. The present paper only utilizes materials and previously published data that are stoichiometric near theoretical density SiC.

Previous work describing the dimensional swelling and thermal conductivity behavior of SiC for irradiation temperatures in excess of 1000°C are quite limited [1,2,4,18], and as some authors note, suffer from uncertainty as to the irradiation temperature. The purpose of this paper is to accurately determine the swelling behavior and thermal conductivity reduction for fully dense stoichiometric SiC at doses to ~ 6 displacements per atom (dpa) for irradiation temperatures up to 1600°C.

Experimental

Materials evaluated in this paper are CVD SiC manufactured by Rohm & Haas and single crystal 6H-SiC produced by Cree, Inc. Manufacturer information for the CVD SiC describes a face centered cubic β-SiC of density 3.21 g/cc (theoretical is 3.217) and grain size of 5 microns. The chemical purity measurements by gas discharge mass spectroscopy and neutron activation yields > 99.9995 % SiC (metals basis.) It is likely that gaseous elements such as nitrogen exist in the ppm range. The single crystal material is a true

single crystal α-type 6H structure with purity exceeding that of the CVD SiC with a reported doping level of 4×10^{17} nitrogen atoms/cm^3.

Two fission reactor irradiation campaigns on SiC were carried out in the core region of the High Flux Isotope Reactor (HFIR) at the Oak Ridge National Laboratory. The respective peak thermal and fast neutron flux of the core is ~ 2.5×10^{19} (thermal) and 9×10^{18} n/m^2-s (E > 0.1 MeV). The irradiations are described as follows:

2.1 Rabbit Capsule Irradiation

In the first campaign a series of small capsules (rabbit capsules) were irradiated in the hydraulic tube of the HFIR. In these capsules 6 mm diameter samples of variable thickness (typically 3–8 mm) were loaded inside a graphite holder and welded under an inert gas inside the aluminum outer capsule. The sample thickness was selected based on an assumed post-irradiation thermal diffusivity to give a relevant rise time according to ASTM 1461 [26]. The sample irradiation temperatures were varied by a combination of variable gap thickness between the holder and the inner diameter of the aluminum capsule, and the type of capsule gas used (helium, neon, or argon.) The irradiation temperature of the rabbit capsules was measured by isochronal annealing of SiC temperature monitors while observing the thermal conductivity change. Application of such a technique is described elsewhere and has been shown to be accurate to 800°C and for irradiation doses as low as 0.001 dpa [27]. The irradiation temperature and neutron fluence for these capsules ranged from 200–800°C and 0.01 to 4×10^{25} n/m^2 (E > 0.1 MeV), respectively. Throughout this paper an equivalence of 1×10^{25} n/m^2 (E > 0.1 MeV) = 1 dpa is assumed.

2.2 Fixed-Core Irradiation

The second irradiation campaign includes data from the first two in a series of three fixed-core capsules irradiated in HFIR in the temperature range of 900–1600°C. The peak fast neutron fluences for the two fixed-core capsules discussed here are ~ 2 and ~ 6×10^{25} n/m^2 (E > 0.1 MeV, ~ 2 and 6 dpa, respectively). Each capsule contained ten sub-capsules, individually containing many specimens. The specimens were nominally 5.8 mm in diameter with varied thicknesses. A subset of subcapsules from the 6 dpa capsule had 3 mm thick samples appropriate for thermal conductivity measurement. The samples were loaded in contact with a high-purity graphite holder and the capsule environment was high purity argon. On both ends of the sub-capsules cylinder were threaded graphite caps that included eight cylindrical wells each containing a melt-wire. The melt wires were pure materials or binary alloys specifically blended to achieve a select melting temperature. For a given sub-capsule the design temperature was achieved by varying the gas gap between the outside of the sample holder and the inner diameter of the capsule containment. The maximum subcapsule irradiation temperature was then determined by viewing the melt-wires post-irradiation. The melt wires were arrayed to compensate for either an overestimation or underestimation of the true temperature of the sub-capsules. Typical intervals between melt-wires were ~ 20–40°C. A temporal variation in temperature within a sub-capsule is expected due to the radiation-induced dimensional change of the Poco AXF-5Q holder (thus changing the gap between the sample holder and capsule containment). No change in temperature due to variation in reactor power is expected due to the exceptionally steady power history of the HFIR reactor during the irradiations. The error bars associated with the temperature estimation herein are a combination of the melt-wire intervals and the changing gas gap.

2.3 Measurement Techniques

Sample densities were measured using the density gradient column technique [28] utilizing a mixture of tetrabromethane and methylene iodide and certified, calibrated floats. A typical gradient column ranged approximately 0.1 g/cc over ~ 1 meter of column height. The experimental uncertainty in density measurement was estimated to be 0.003%. The density shown for the highest dose fixed core capsule is made up of two to three CVD SiC samples from each subcapsule. The density of samples from

individual subcapsules was identical in many cases and therefore indistinguishable as plotted. All samples were soaked in hydrofluoric acid for 30 minutes and rinsed in alcohol prior to immersion to remove any surface oxide on the SiC. However, for all but the highest irradiation temperature, no surface reaction was observed and no sample mass loss was detected following irradiation or acid bath.

The room temperature thermal conductivity (K) was calculated using the measured thermal diffusivity (α), measured density (ρ), and the assumed specific heat (C_p) of 667 J/kg-K as follows: K=□ □ C_p. The thermal diffusivity of every specimen was measured before and after irradiation using an Anter Systems Flashline 5000 with a solid-state detector. The conversion from diffusivity to conductivity assumed a specific heat unchanged by irradiation. This common assumption is known to be valid for graphite [29] though has not been thoroughly demonstrated for ceramics.

Results

The irradiation-induced microstructural evolution of CVD SiC is fairly well understood and has been reviewed recently by Katoh [30]. The contribution of the defects themselves to the swelling in SiC is less well understood, especially at elevated temperatures. Below several hundred degrees Celsius the observable microstructure of neutron irradiated SiC is described as containing "black dots," which are most likely tiny clusters of self-interstitial atoms in various indeterminate configurations. For irradiation temperatures less than about 150°C, accumulation of strain due to the self-interstitial atoms leads to a critical level above which the crystal becomes amorphous. This has been shown for both self-ion irradiation and under fast neutron irradiation [31–33]. As shown by Katoh [32], the swelling at 50°C under self-ion irradiation increases linearly with dose until amorphization occurs. The swelling of neutron-amorphized SiC has been reported to be 10.8% for 70°C irradiation [33]. However, there is evidence that the density of amorphous SiC will depend on the conditions of irradiation (dose, temperature, etc.) [34].

For temperatures above the critical amorphization temperature the swelling saturates by a few dpa, with a steady decrease in the saturation swelling with increasing irradiation temperature. At very high doses [35], and/or higher temperatures such as 900–1400°C [4,18,36], Frank faulted loops of interstitial type become the dominant defects observed by transmission electron microscopy. Under self-ion irradiation at 1400°C, the development of Frank loops into dislocation networks through unfaulting reactions at high doses is reported [36]. The volume associated with dislocation loops in irradiated SiC has been estimated to be smaller than 0.1% [37,38].

At temperatures where vacancies are sufficiently mobile, vacancy clusters can be formed. Three-dimensional cavities (or voids) are the only vacancy clusters known to commonly develop in irradiated SiC. The lowest temperature at which void formation was observed under neutron irradiation is 1250°C [39]. Senor reported the lack of void production after neutron irradiation to 0.9 x 10^{25} n/m^2 at 1100°C, though voids were observed after subsequent annealing at 1500°C for 1 hr [18]. Under self-ion irradiation, voids start to form at 1000°C at very low density and become major contributors to swelling at irradiation conditions of 1400°C at > 10 dpa [37]. The work by Senor implies limited vacancy mobility prohibits observable void production at 1100°C for a neutron dose up to 0.9 dpa [18]. However, positron annihilation and electron paramagnetic resonance studies have shown that the silicon vacancy in cubic SiC becomes mobile at 800–900°C [40,41]. Therefore, it would not be surprising for void swelling takes place at as low as ~ 1000°C at high doses, particularly for low damage rate irradiations.

For the materials of this study, the non-irradiated density of CVD SiC at 20°C was 3.2101 g/cc and that of single crystal 3.2107 g/cc. The density of the non-irradiated samples was quite uniform within the samples studied, typically within the 0.003% experimental error. Figure 1 gives data for swelling of both the CVD and single crystal SiC materials irradiated in the fixed-core capsule as a function of irradiation temperature along with historical data on stoichiometric, near full density CVD SiC. Data on swelling from the rabbit capsule irradiations are not included here because the majority of samples were irradiated to

fluences less than saturation swelling. Error bars on temperature have been included for all the high-temperature data from this experiment, and in some cases those of the literature data. Error bars on swelling have also been included, though the measurement error for density in some cases is such that the error bars are not resolvable. It is noted that the CVD SiC data of Blackstone and Voice [1] is excluded due to the presence of free silicon and low density of that material. From the figure, it is seen that near 1000°C a swelling of ~ 0.2 % and 0.6% has been measured for both CVD SiC and single crystal SiC at ~ 2 and ~ 6 dpa, respectively. Clearly the swelling at 1000°C has not saturated by 2 dpa. As the irradiation temperature moves above 1000°C the data indicates a continual swelling increase to the maximum temperature of ~ 1600°C. This finding is somewhat surprising given the apparent mobility of the silicon vacancy above 1000°C found experimentally in cubic SiC (the CVD SiC of this study is highly faulted FCC) [40,41].

Figure 1 includes historical data for swelling above 1000°C [2,4,18,33,39,42]. Specifically, Senor [18] reports swelling for the same type of CVD SiC irradiated in this study. His maximum dose, irradiation temperature and swelling data were ~ 1 dpa, ~ 1100 ± 30°C, and 0.36 ± 0.02%. This level of swelling is considerably higher than the ~ 0.2% swelling at 2 dpa, ~ 1100°C of the present work and is actually covered on Fig. 1 by the data irradiated to 6 dpa. Also seen on the figure is the high temperature swelling of Price [2,4,39]. The Price data, which are in the dose range of about 4–8 dpa, is in fair agreement with the measured swelling of this study. The highest swelling material (~ 1250°C, ~ 6 and 10 dpa) shows the largest discrepancy, though if the true irradiation temperature were at the rightmost part of the error bar, this data would also be more consistent with the present work. It is also noted that the Price material may have had some excess silicon leading to a higher swelling as compared to stoichiometric material. There does not appear to be a difference in swelling between the highly faulted FCC β-SiC and the single crystal HCP α-SiC in the present study.

As mentioned earlier, the microstructural evolution of irradiated SiC is fairly well understood, at least for temperatures up to ~ 1100°C. The swelling near the critical amorphization temperature (~ 150°C) is classically described as the differential strain between single interstitial, or tiny interstitial clusters, and the contraction of immobile vacancies. As the temperature increases above the critical amorphization temperature the number of defects surviving the cascade are reduced and the mobility of both silicon and carbon interstitials becomes significant. For temperature approaching ~ 1000°C microstructural studies have noted the presence of both Frank loops and tiny voids indicating limited mobility of vacancies. The apparent increase in swelling in the 1000–1600°C range, and the assumed production of voids, is interesting considering the maximum irradiation temperature of this study is ~ 0.60 T_m of the homologous temperature (T_M) for SiC. It is noted that the melting temperature is somewhat variable in the literature. Here we have assumed the value of Olesinski [43] of 25–45°C where stoichiometric SiC transforms into C + liquid phase. This value of 0.65 T_m is high when viewed in comparison to FCC metals systems where void swelling typically begins at ~ 0.35 T_m, goes through a maximum value, and decreases to nil swelling by ~ 0.55 T_m. (It is noted that the melting and dissociation temperature of SiC is somewhat variable in the literature. Even considering this variability the previous statement is still accurate.) If, as the swelling data seems to indicate, the voids in SiC are continuing to grow in SiC irradiated to 1600°C the energies for diffusion of one or both the Si and C vacancy must be quite high, as are the binding energies for clustered vacancies. This has been shown through theoretical work in the literature [44–47]. However, it is noted that the defect energetics from this body of work, and in particular those of the Si and C vacancy, SiC vary widely. Perhaps the work of Bockstedte [45] following an ab-initio approach, is the most accurate yielding a ground state migration energy for Si and C vacancies of 3.5 and 3.4 eV, respectively. It was also noted by Bockstedte [45] that the charge state of the vacancy will effect the migration energy. Specifically the carbon vacancy in the +1 and +2 charge state increases from 3.5 to 4.1 and 5.2 eV, respectively, and that of silicon in the +1 charge state increases from 3.4 to 3.6 eV. Several papers discuss the vacancy and vacancy cluster mobility measured experimentally. The silicon monovacancy has been shown to be mobile below 1000°C. Using photoluminescence Sorman [48] and Wagner [49] find the Si vacancy disappearing above 750°C. Using electron spin resonance the carbon vacancy is shown to anneal above 1400°C [50]. Using isochronal annealing and positron lifetime analysis Lam [46] has shown a carbon-silicon vacancy

complex to dissociate above ~ 1500°C for the same 6H single crystal materials studied here.

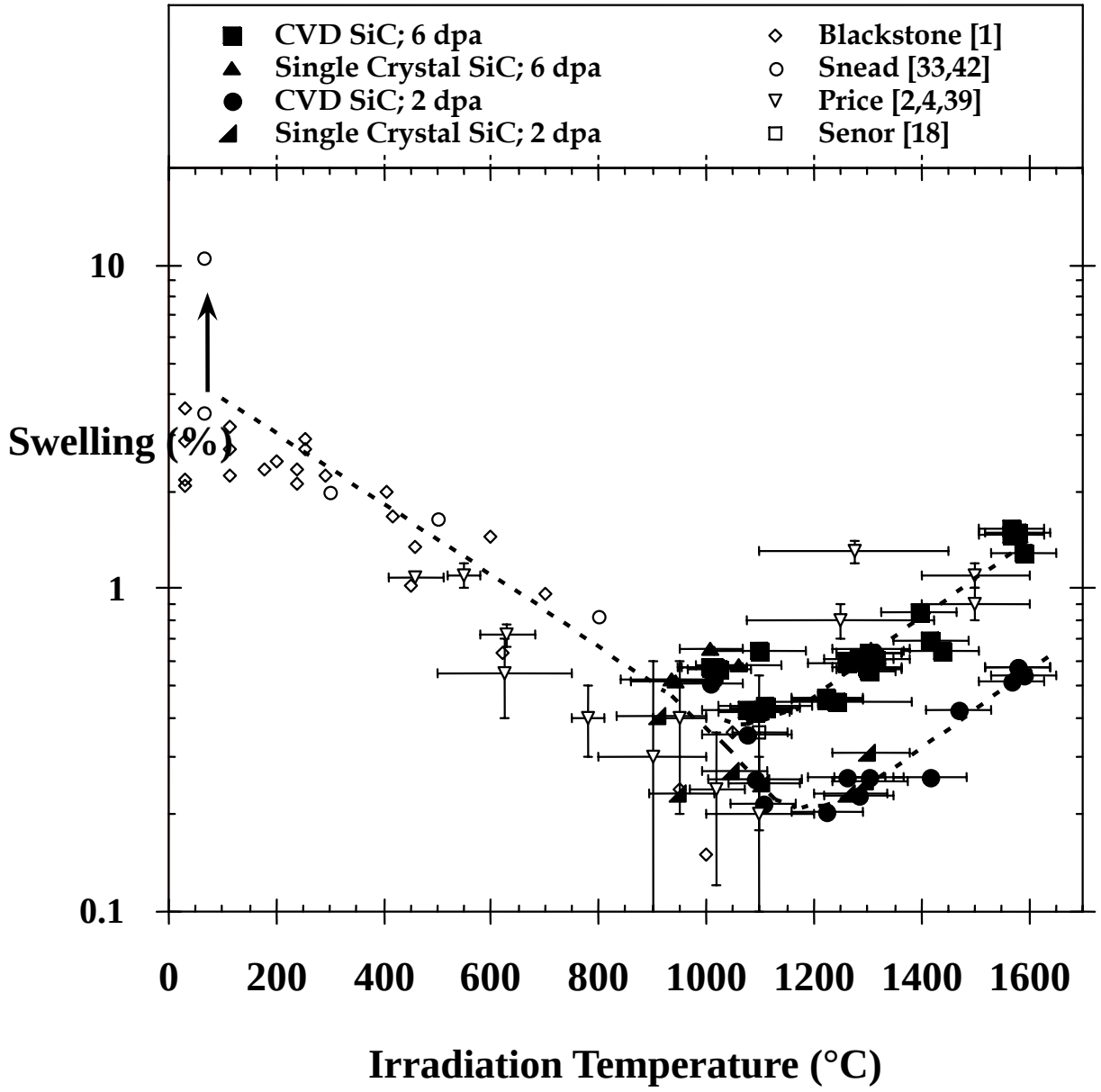

Fig. 1. Volumetric swelling of SiC as a function of neutron irradiation temperature.

Room temperature thermal conductivity for CVD SiC is given in Fig. 2 for the 6 x 10^{25} n/m^2 (E > 0.1 MeV) capsule as a function of irradiation temperature. Also included in Fig. 2 are literature data on Rohm-Haas CVD silicon carbide irradiated in this dose range for irradiation temperatures < 800°C. The degradation in thermal conductivity, for T < 800°C is certainly due to phonon scattering from small vacancy clusters in the crystal and can be considered saturation values [13].

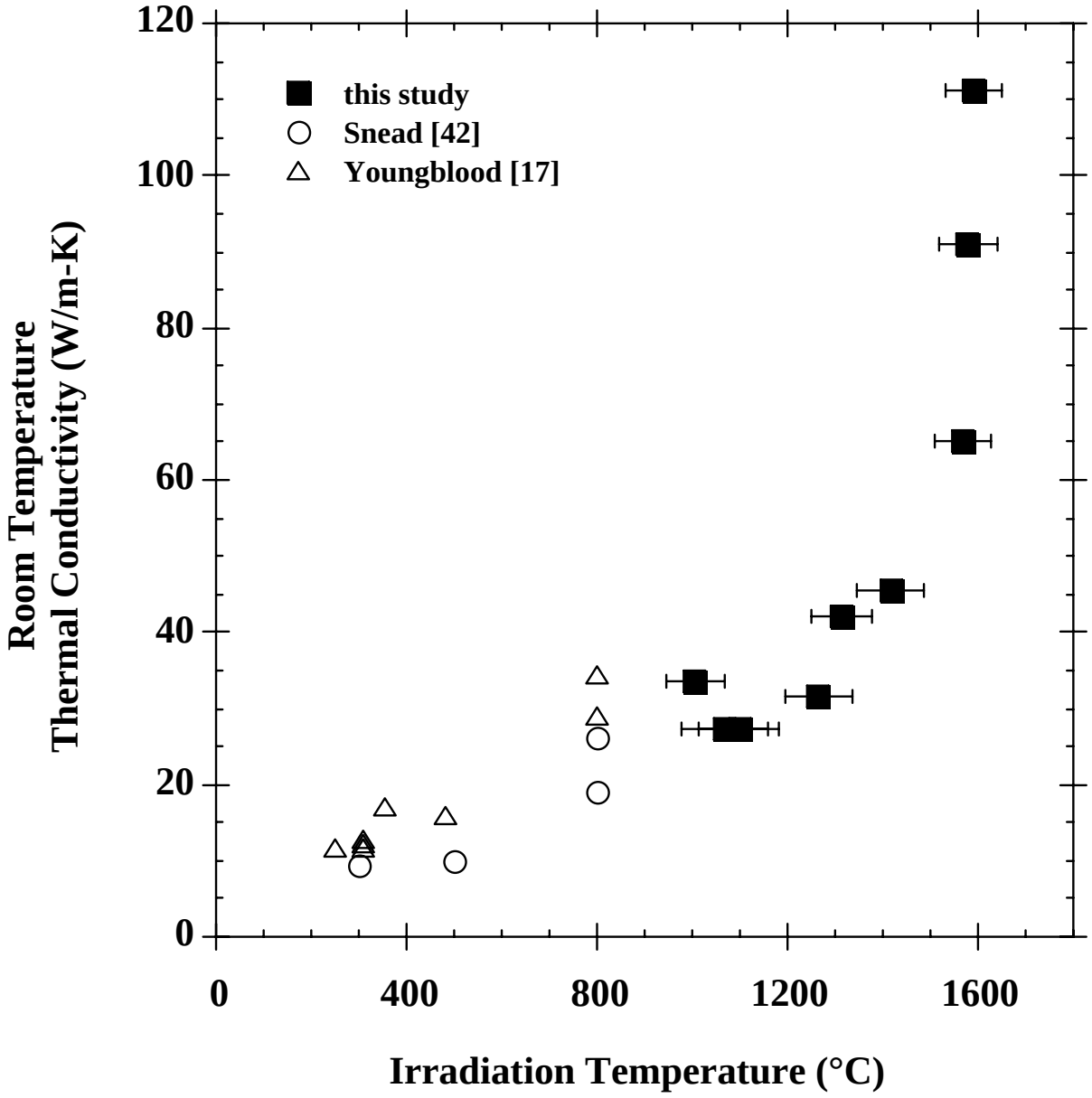

Fig. 2. Room temperature thermal conductivity of SiC irradiated in the 4–8 dpa range as a function of irradiation temperature.

The non-irradiated room temperature thermal conductivity in the current study is 327 ± 25 (one standard deviation) W/m-K. It is noted that significant plate-to-plate and intra-plate thermal conductivity variability exists for this particular grade of CVD SiC [13,23]. For irradiation temperature at or above 1100°C the thermal conductivity (Fig. 2) is seen to dramatically increase. This is attributed to the lack of the small vacancy clusters at this temperature, having been annihilated by migrating interstitials or formed into larger defects that are less effective at scattering phonons. The phonon scattering at such high temperature is now likely dominated by larger defects less effective in scattering phonons on a volumetric basis. For the highest irradiation temperature of this study (1590 ± 60°C) the as-irradiated room temperature thermal conductivity is ~ 111 W/m-K, or about 34% of the non-irradiated value.

Based on the previous work of Price [4] on the high-temperature swelling behavior CVD SiC it is expected that the current data presented in Fig. 2 do not represent saturation values in thermal conductivity. In his work, swelling continued to increase in the 1250–1500°C irradiation temperature range to about 10 dpa. It is most likely that the defects dominating the as-irradiated thermal conductivity at temperatures > 1000°C are a combination of Frank loops and voids. In particular, voids are expected to continue to evolve in the high-temperature range causing increased swelling and reduction in thermal conductivity. Recent work by Senor [18] indicated a continued degradation in room temperature thermal conductivity for Rohm & Haas CVD SiC in the 0.5–1 dpa range at 1100°C. No data exists above 10 dpa at these elevated temperatures. No conclusion can be drawn from this study relative to the continued degradation in thermal conductivity with increased dose since thermal conductivity measurements have not been completed at both doses. However, it is noted that a single sample from the lower dose capsule (~ 2 dpa, ~ 1579 ± 60°C) yielded a value of 90.5 W/m-K, very similar to the 6 dpa, 1579°C sample.

The nature of the microstructural development in the transition from the intermediate to high irradiation temperature range, as mentioned earlier, is fairly well understood. Moreover, a program of TEM and positron annihilation planned for the materials discussed here should demonstrate quantitatively the defect evolution. However, it can be shown that there is a clear change in the defects controlling the thermal conductivity through the simple analysis of “thermal defect resistance” [51]. The thermal defect resistance is defined as the difference in the reciprocal of the irradiated and non-irradiated thermal conductivity ($1/K_{rd} = 1/K_{irr} - 1/K_{non\text{-}irr.}$) This term can be related directly to the defect type and concentration present in irradiated ceramics [51]. Figure 3 gives a compilation of data from this study for both thermal conductivity and thermal defect resistance as a function of swelling. Data from previous works are not considered. As seen from the plot, as swelling increases the thermal conductivity rapidly degrades from its non-irradiated value of 327 ± 25 W/m-K to a saturation value of about 10 W/m-K. However, by plotting the same data as thermal defect resistance a clear linear relationship with swelling is seen for irradiation temperature where swelling is attributed to interstitial strain and mobility, in this case for material irradiated from 200–800°C. This data is the bulk of the data from the rabbit capsule irradiations. At these temperatures, vacancies are considered to have very limited mobility and form at most very tiny clusters. The implication here is that the small vacancies or vacancy complexes dominating phonon scattering are correlated with the interstitial strain causing swelling at T_{irr} < 800°C. Figure 4 shows a weak beam dark field TEM image of CVD SiC irradiated at 300°C (left) and 800°C (right) to approximately 7 dpa in a related study [30]. Both microstructures reveal the presence of what is generally referred to as black dots, though the 800°C microstructure has a loop diameter of ~ 3 nm, or three times that of the 300°C irradiated microstructure. Additionally the loop density has decreased by about an order of magnitude as these defect coarsen. It is interesting to note that the correlation between swelling and thermal defect resistance is independent of the coarsening microstructure shown in Fig. 4. It is further noted that the swelling-thermal defect resistance relationship can serve to estimate the thermal conductivity reduction of SiC by the simple measurement of swelling.

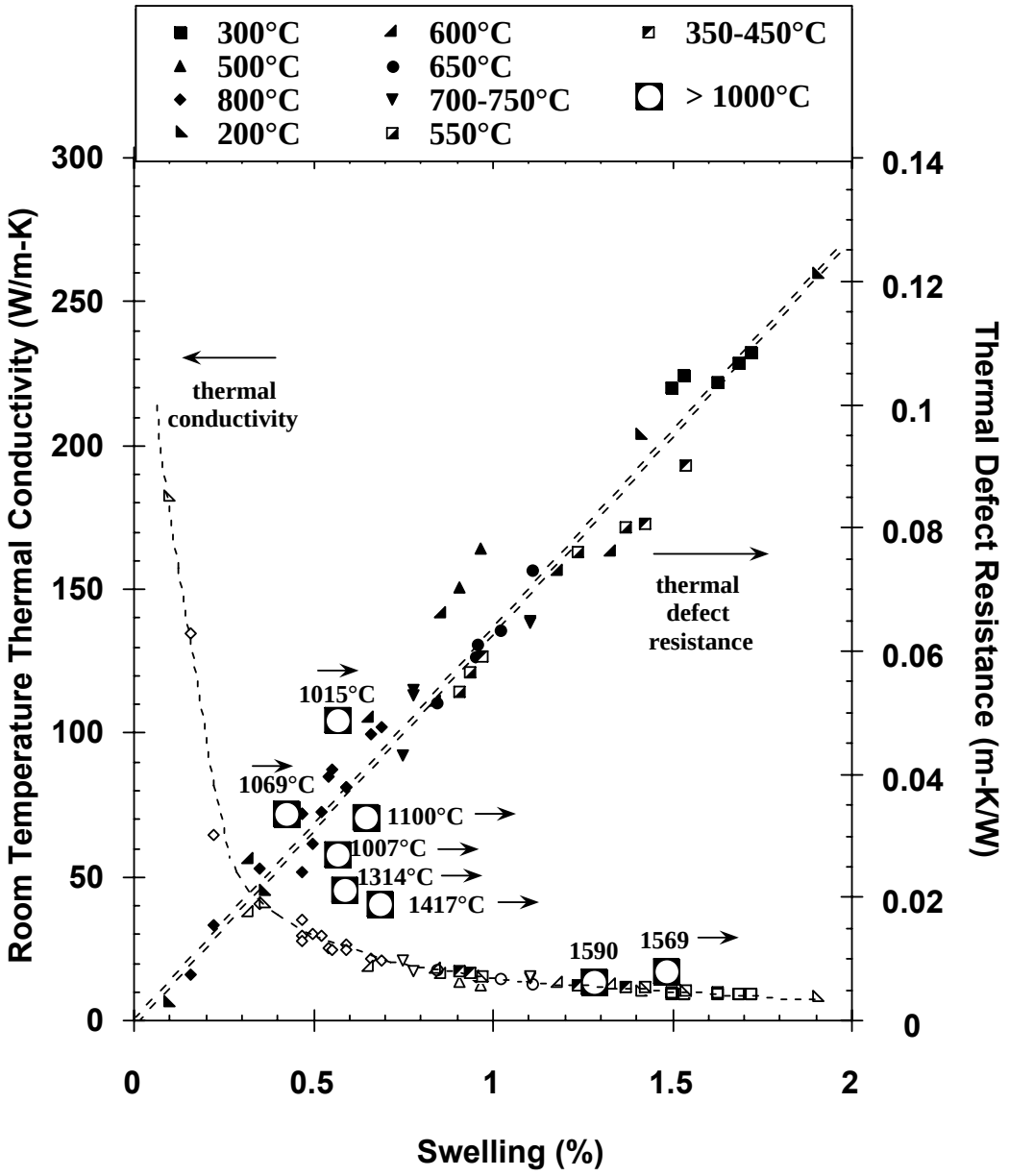

Fig. 3. Room temperature thermal conductivity and thermal defect resistance as a function of swelling of SiC. Irradiations at greater than 1000°C are 6 dpa data. Open symbols related to those in legend refer to thermal conductivity. Legend symbols refer to thermal defect resistance.

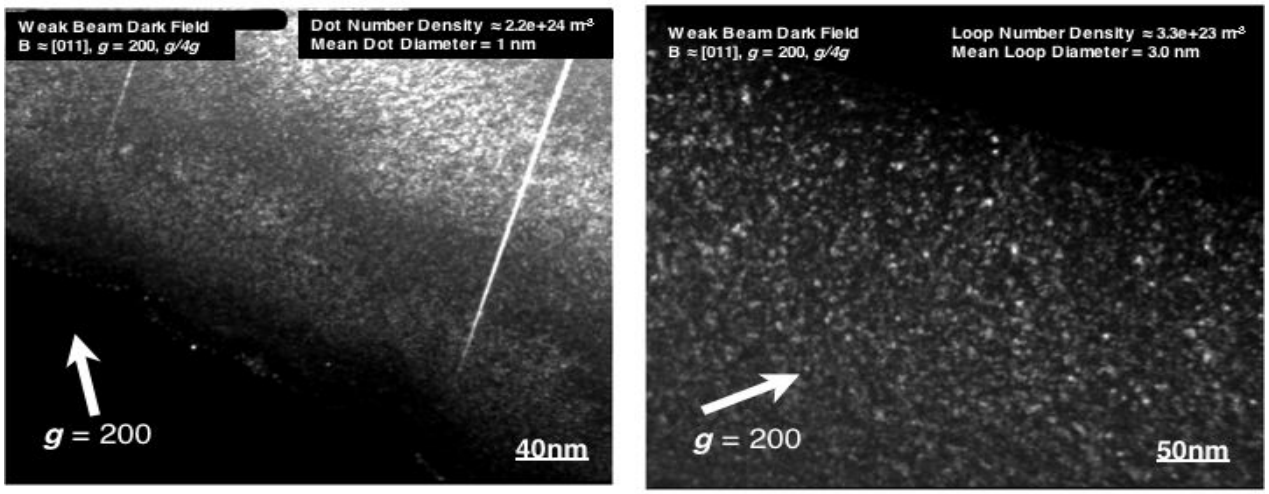

Fig. 4. TEM image of CVD SiC irradiated to ~ 7 dpa at 300°C (left) and 800°C (right) [30].

The correlation between swelling and thermal defect resistance does not hold as the irradiation temperature increases above 1000°C. On Fig. 3, the largest symbols refer to the 6 dpa CVD SiC irradiated in the fixed core capsules. On the plot the irradiation temperature is plotted to the right of the symbol. For materials irradiated in the 1015 to 1100°C range the thermal defect resistance roughly fall within the scatter band of the thermal defect resistance data. However, as the irradiation temperature is increased above ~ 1100°C the thermal defect resistance clearly falls below the "correlation line" with the material irradiated at higher temperature exhibiting much lower phonon scattering. The fact that the 1015–1100°C irradiated materials are consistent with the correlation line may be fortuitous. However, the reduced thermal defect resistance for the higher-swelling, higher-temperature irradiated materials clearly indicates that the defects dominating thermal conductivity are much less effective on a volume normalized basis in scattering phonons. The assertion that voids would be less effective phonon scattering center is not new, having been theoretically explained by Klemens and others [52].

Conclusions

Data have been presented for swelling and thermal conductivity of high-purity CVD SiC over the irradiation temperature range of 200–1600°C. Below about 800°C data on swelling is consistent with literature data. A robust set of data has been presented for irradiation above 1000°C indicated that swelling continues to increase as the irradiation dose is increased from 2 to 6 dpa. Moreover the swelling at 1000°C is ~ 0.2 percent at 2 dpa and ~ 0.6 percent at 6 dpa. While no conclusion can be made with this data relative to saturation in swelling at 1000°C, it is likely that the swelling at this irradiation temperature is due to a combination of tiny clusters and Frank loops. However, it is also possible that part of the swelling at 1000°C is due to voids. If this is the case the material will continue to swell for higher irradiation doses at 1000°C. For temperature greater than 1100°C the swelling of SiC appears to increase with increasing

irradiation temperature up to 1600°C with the level of swelling scaling with the dose for the 2 and 6 dpa irradiations. The swelling appears to be increasing even for the highest temperature irradiation achieving greater than 1.5% swelling at ~ 1575°C. There does not appear to be a difference in swelling between the highly faulted 3C β-SiC and the single crystal 6H α-SiC.

A direct correlation between the thermal defect resistance and swelling of SiC in the irradiation temperature range of 200–800°C has been shown. This dependence appears to be independent of irradiation temperature indicating that the defects controlling both swelling and thermal conductivity are the same independent of the temperature-driven coarsening of the observable SiC microstructure. Evaluation of the thermal conductivity on this basis also will be useful in predicting the thermal conductivity of SiC simply on the basis of swelling. For irradiation temperatures > 1000°C, the correlation between thermal defect resistance and swelling breaks down indicating that the small vacancy cluster evolve to large structures (such as voids) that are less effective phonon scattering centers per unit volume.

Acknowledgements

The authors would like to thank Marie Williams for her assistance with thermal diffusivity experiments and Stas Golubov for enlightening discussion. Additionally, the authors are thankful to Katey Lenox, Dennis Heatherly, and Bob Sitterson for their efforts in carrying out the irradiation and post-irradiation examinations. This research was sponsored by the Office of Fusion Energy Sciences, U.S. Department of Energy, under contract DE-AC05-00OR22725 with UT-Battelle, LLC. Additional support was provided by the Department of Energy through a Nuclear Energy Research Initiative grant.

References

[1] R. Blackstone and E. H. Voice, J. Nucl. Mater. 39 (1971) 319.
[2] R. J. Price, J. Nucl. Mater. 33 (1969) 17.
[3] R. Price, Nucl. Technol. 35 (1977) 320.
[4] R. J. Price, J. Nucl. Mater. 48 (1973) 47.
[5] W. Primak, L. H. Fuchs, and P. P. Day, Phys. Rev. 103 *(*1956) 1184.
[6] M. Balarin, Phys. Status Solidi 11 (1965) K67.
[7] N. F. Pravdyuk et al., Properties of Reactor Materials and the Effects of Radiation Damage Proceedings, D. J. Littler (ed.), Butterworths, London (1962).
[8] R. P. Thorne, V. C. Howard, and B. Hope, Proc. Br. Ceram. Soc. 7 (1967).
[9] R. Stevens, Philos. Mag. 25 (1972) 523.
[10] J. C. Corelli et al., J. Am. Ceram. Soc. 66 (1983) 529.
[11] H. Miyazaki et al., J. Nucl. Sci. Technol. 29 (1992) 656.
[12] R. Matthews, J. Nucl. Mater. 51 (1974) 203.
[13] L. L. Snead, J. Nucl. Mater. 329–333 (2004) 524.
[14] L. L. Snead, J. Nucl. Mater. 326 (2004) 114.
[15] G. W. Hollenberg et al., J. Nucl. Mater. 219 (1995) 70.
[16] D. J. Senor et al., Fusion Technol. 30 (1996) 943.
[17] G. E. Youngblood, D. J. Senor, and R. H. Jones, “Thermal diffusivity/conductivity of irradiated monolithic CVD-SiC," Fusion Materials Semiannual Progress Report DOE/ER-0313/33 (2002) 27.
[18] D. J. Senor et al., J. Nucl. Mater. 317 (2003) 145.
[19] W. Dienst et al., J. Nucl. Mater. 174 (1990) 102.
[20] T. Iseki et al., J. Nucl. Mater. 170 (1990) 95.
[21] C. W. Lee, F. J. Pineau, and J. C. Corelli, J. Nucl. Mater. 108–109 (1982) 678.
[22] H. Suzuki, T. Iseki, and M. Ito, J. Nucl. Mater. 48 (1973) 247.
[23] G. E. Youngblood, D. J. Senor, and R. H. Jones, J. Nucl. Mater. 329–333 (2004) 507.
[24] L. L. Snead, T. Hinoki, and Y. Katoh, “Strength of neutron irradiated silicon carbide and silicon carbide composite,” Fusion Materials Semiannual Progress Report DOE/ER-0313/33 (2002) 49.
[25] G. Newsome et al., Journal of Nuclear Materials (submitted).
[26] ASTM Standard Test Method for Thermal Diffusivity by the Flash Method E 1461-01.

[27] L. L. Snead, A. M. Williams, and A. L. Qualls, “Revisiting the use of SiC as a Post Irradiation Temperature Monitor,” ASTM STP 1447, M. L. Grossbeck (ed.), The Effects of Radiation on Materials: 21st International Symposium (2003).
[28] ASTM D1505-85, Standard Test Method for Density of Plastics by Density Gradient Technique (1985).
[29] J. W. H. Simmons, Radiation Damage in Graphite, Pergamon Press, Vol. 102 (1965).
[30] Y. Katoh et al., Journal of Nuclear Materials (accepted).
[31] L. L. Snead and S. J. Zinkle, "Threshold irradiation dose for amorphization of silicon carbide," in *Microstructure Evolution During Irradiation*, I. M. Robertson, G. S. Was, L. W. Hobbs, and T. D. d. l. Rubia, (eds.), Materials Research Society, Pittsburgh, 439 (1997) 595.
[32] Y. Katoh, H. Kishimoto, and A. Kohyama, J. Nucl. Mater. 307–311 (2002) 1221.
[33] L. L. Snead et al., Nucl. Instrum. Methods Phys. Res. Sect. B 141 (1998) 123.
[34] L. L. Snead and S. J. Zinkle, Nucl. Instrum. Methods Phys Res. Sect. B 191 (2002) 497.
[35] T. Yano et al., J. Nucl. Mater. 253 (1998) 78.
[36] S. Kondo et al., J. Fusion Sci. Technol. No. 2 (2003) 181.
[37] Y. Katoh et al., “Current Status and Critical Issues for Development of SiC Composites for Fusion Application,” International Conference on Fusion Reactor Materials 12, Santa Barbara, Calif., Journal of Nuclear Materials (submitted).
[38] S. Kondo, International Conference on Fusion Reactor Materials 12, Santa Barbara, Calif., Journal of Nuclear Materials (submitted).
[39] R. J. Price, J. Nucl. Mater. 46 (1973) 268.
[40] H. Itoh, N. Hayakawa, and I. Nashiyama, J. Appl. Phys. 66 (1989) 4529.
[41] A. Kawasuso, H. Itoh, and D. Cha, Appl. Phys. A: Mater. Sci. Processing 67 (1998) 209.
[42] L. L. Snead et al., J. Nucl. Mater. 307–311 (2002) 1141.
[43] R. W. Olesinski and G. J. Abbaschian, Bull. Alloy Phase Diagrams 5 (1984) 486.
[44] H. C. Huang et al., Model. Simul. Mater. Sci. Eng. 3 (1995) 615.
[45] M. Bockstedte, A. Mattausch, and O. Pankratov, Phys. Rev. B 68 (2003) 20521.
[46] C. H. Lam et al., Mat. Res. Soc. Symp. Proc. 792 (2004) R3.19.1.
[47] J. Li, L. Porter, and S. Yip, J. Nucl. Mater. 255 (1998) 139.
[48] E. Sorman et al., Phys. Rev. B 61 (2000) 2613.
[49] M. Wagner et al., Phys. Rev. B 66 (2002) 144214.
[50] L. A. d. Balona and J. H. N. Lousber, J. Phys. C, Solid State Phys. 3 (1970).
[51] L. L. Snead, S. J. Zinkle, and D. P. White, J. Nucl. Mater. 340 (2005) 187.
[52] P. G. Klemens and D. F. Pedraza, Carbon 32 (1994) 735.

ELECTRICAL CONDUCTIVITY OF SiC/SiC—G. E. Youngblood, E. Thomsen, and G. Coffey (Pacific Northwest National Laboratory)*

OBJECTIVE

The primary objective of this fusion materials research effort is to support component design and future testing for the International Tokamak Experimental Reactor (ITER).

SUMMARY

In this report, experimental measurements of the transverse electrical conductivity (EC) for a conventional 2D-SiC/CVI-SiC are presented that indicate that the desired EC-goals for operation of a Flow Channel Insert (FCI) made with this material can be achieved.

Several 2-probe DC and AC and 4-probe DC methods for measuring the electrical conductivity (EC) of various SiC forms as a function of temperature up to 800°C were examined. A 2D-SiC/SiC composite made by the isothermal chemical vapor infiltration (ICVI) process with Hi-Nicalon™ type S fabric and a thin pyrolytic-carbon (PyC) interphase was used as a reference material. To estimate the influence of the PyC interphase on the EC, conductivity measurements were made in the in-plane direction for as-received composite and for composite with the PyC removed by oxidation. Also, the EC was measured for monolithic CVD-SiC and for bare bundles and single filaments of SiC fiber types Nicalon™ S and Tyranno™ SA as well as for the transverse direction of our reference SiC/SiC.

For temperatures above 500°C, a temperature range relevant for operation of an FCI in an ITER blanket test module, EC-values for both bare SiC fiber and fiber bundles and monolithic CVD-SiC exceed the desired upper limit of 20 S/m for such an application. However, repeated measurements of the transverse EC for our reference 2D-SiC/ICVI-SiC composite exhibit EC-values less than ~ $1/10^{th}$ the 20 S/m value. If true, this is an important, very surprising discovery. The EC for the in-plane direction is ~ 100 times that in the transverse direction; hence, the EC for our reference 2D-SiC/ICVI-SiC is very anisotropic, a condition that in general is characteristic of 2D-CVI-SiC composites.

PROGRESS AND STATUS

Introduction

The design of a Dual Coolant Blanket Module (DCBM) is being considered as one element of the U. S. "ITER Mission." Within the flow channels of a DCBM, a key component is a Flow Channel Insert (FCI) that provides electrical and thermal insulation between the flowing, hot liquid Pb-Li metal and the helium-cooled ferritic steel channel walls. FCIs basically are free-floating channels with walls of typical thickness ~ 5 mm, individual channel cross-sections of about 0.08 m^2 and with lengths in meters. Although structurally relatively simple, the total volume of FCI-material required could be large.

A ceramic, fiber-reinforced silicon carbide composite (SiC/SiC) has been proposed as a promising high temperature, radiation and corrosion resistant material for construction of FCIs [1]. To carry out the required FCI-functions, the SiC/SiC material should have relatively low and uniform transverse electrical (EC) and thermal conductivity (TC). According to preliminary models, in the envisioned 500–800°C temperature operating range for an FCI the desired values are ~ 20 S/m and 2 W/mK, respectively [2]. The low and uniform transverse EC-values are required to reduce the induced MHD pressure drop within the FCI channels and to maintain a flow balance among the neighboring channels. In our first report, analysis of EC and TC for various SiC and SiC/SiC forms suggested that an architectural or

*Pacific Northwest National Laboratory (PNNL) is operated for the U.S. Department of Energy by Battelle Memorial Institute under contract DE-AC06-76RLO-1830.

"engineering" composite design solution would be necessary to achieve the desired transverse EC and TC goals for 2D-SiC/SiC [3].

Experimental Procedure

Materials

Monolithic CVD-SiC (polycrystalline □-SiC with density 3.21 g/cc and with impurity content < 5 wppm) was obtained from Morton Advanced Materials (now Rohm and Haas, Woburn, MA) [4]. A very high purity bar sample with reduced nitrogen impurity, obtained from Y. Katoh at Oak Ridge National Laboratory, also was examined. Beta-SiC is a wide band gap (~ 2.3 eV) semi-conducting material. By doping with n-type elements, its EC can be increased to ~ 10^4 S/m at room temperature [5].

Single filaments and as-received fiber bundles of two types of polycrystalline, near stoichiometric SiC fibers were examined: Hi-Nicalon™ type S and Tyranno™ SA. A 2D-SiC/SiC composite (made by GE Power Systems in 2002) with either six or eight plies of 2D-5HS weave type S fabric and an ICVI-SiC matrix was used as our reference material. The fabric lay-up was coated with a relatively thin (110 nm) pyrolytic-carbon (PyC) layer prior to matrix infiltration. The bulk density was 2.69 g/cc and the nominal overall fiber content was 40%. Further characterization of this composite material is given in Ref. [6].

4-Probe and 2-Probe DC Methods

Figure 1 shows a schematic diagram of our automated EC measurement system. A type S thermocouple placed within ~ 1 mm of the sample was used to monitor the sample temperature. A programmable computer (Labview™) controls the temperature (RT to 1000°C) in a closed end alumina tube furnace, the atmosphere mass flow (dry argon, argon plus 3% hydrogen or air), and the potentiometric measurements made with a Solartron™ 1480 Multistat. The 1480 was used to control and record cyclic voltamagrams (DC current vs. voltage), generally for a ±0.1volt range at 5 mV/sec. Over this range, the voltamagrams were always linear and the sample resistance could be calculated from the voltamagram slopes. The sample EC was then calculated from the measured resistance and the sample geometry factor when assuming uniform linear current flow.

A standard 4-probe method, as depicted in Fig. 1, was used for all bar samples (typically 15 x 1-4 x 2 mm^3). Gold lead wires were attached to various types of bar samples (CVD-SiC and in-plane SiC/SiC composite, as well as fiber bundles) by twisting a loop around the bar or fiber bundle. Gold paste was applied to make sample-to-wire contact. For the relatively thin disc-shaped samples (CVD-SiC or transverse SiC/SiC composite, typically 9 mm dia x 2 mm thick), a less reliable 2-probe method had to be used. Disc surfaces were carefully cleaned with dilute HF, rinsed with sonicated deionized water, and air-dried prior to applying

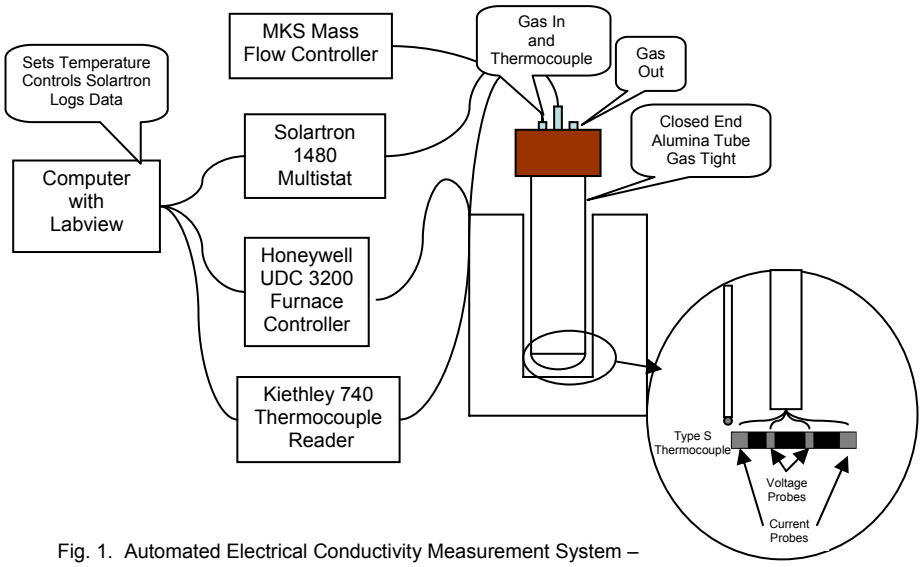

Fig. 1. Automated Electrical Conductivity Measurement System – RT to 1000°C, atmosphere controlled.

gold electrodes to both disc faces by vacuum evaporation using a conventional SEM sample coating system. Gold wire leads were spot-welded to gold foil on top of gold gauze contacts that were then pressed onto the gold-coated disc faces by an external spring-loaded push rod. The HF and water rinse was also given to the fiber bundles prior to mounting.

In the 4-probe potentiometric method, no current flows through the inner voltage contacts on a bar sample, so there is no contact resistance. In the 2-probe potentiometric method, the measured voltage drop includes contact resistances between each vacuum-coated gold electrode and the SiC disc sample face. For reliability, efforts were taken to reduce this contact resistance to well below the actual sample resistance. A typical resistance value for our 9-mm diameter reference SiC/SiC disc samples was 20Ω at 800°C. Therefore, the contact resistance should be maintained < 0.6 Ωcm^2 to reliably keep the error in the resistance measurements to < 5%.

Initially, a 2-probe AC impedance method was examined in an attempt to estimate the contact resistance. This method was not appropriate for these materials, so was abandoned.

Results

Monolithic CVD-SiC

In Fig. 2, temperature dependent EC(T)-values for three different CVD-SiC samples are compared with the EC-values (□) for a commercially available sintered □-SiC sample (Hexoloy™ SA) [7,8]. As expected, the EC(T)-values increase with increasing temperature. Apparent activation energies (E_a) were derived from a linear least squares data fit to □ = $□_o exp(-E_a/kT)$ in an Arrhenius plot for the low temperature 20–400°C range and are given in the legend.

Bare SiC fiber

In Fig. 3, 4-probe EC(T)-values (solid symbols) for bundles of Nicalon™ type S and Tyranno™ SA fibers are compared to data for these same fibers measured by Scholz (solid lines) [9]. Room temperature 2-probe EC-values for single filaments of these two fiber types are indicated with open symbols.

2D-SiC/SiC

In Fig. 4, 4-probe in-plane EC(T)-values for a bar are compared to 2-probe transverse EC(T)-values for a disc of our reference 2D-SiC/SiC. For the latter case, measurements were made on two different discs nominally fabricated in the same manner, one with six plies and the other with eight plies of Nicalon™ type S fabric. The transverse EC(T)-values had a similar temperature dependence, but were more than two orders of magnitude less than the in-plane EC(T)-values, which ranged from > 300 S/m at RT up to ~ 500 S/m at 800°C.

Discussion

In Fig. 2, order of magnitude variation of EC-levels for nominally similar high-purity, dense polycrystalline CVD-SiC reflects the dominant influence of type and even small levels of impurity in this wide band-gap semi-conducting material, at least in the RT-1000°C test range. The E_a-values (0.12 to 0.19 eV) are characteristic of n-type extrinsic conduction for the CVD-SiC. Note that the EC (logarithmic scale) at 500°C for the n-type extrinsic CVD-SiC samples is about X20 the EC at room temperature. The Hexoloy™ SA □-SiC material contains boron (a p-type dopant in SiC) as a sintering aid. Its EC-values are less than 10^{-4} S/m up to 200°C, but increase rapidly with increasing temperature because of its high E_a (0.78 eV).

In Figs. 2–4, for reference the 500°C and 20 S/m dashed lines form a window (lower right-hand corner) that encloses the range of EC(T)-values desired for FCIs. All the EC-values for high-purity monolithic SiC lie above this window, although a few of the lower temperature EC-values are very near the upper limit. It appears that special processes will be necessary to attain the desired low EC-values for nominally pure and dense SiC in the FCI operating range.

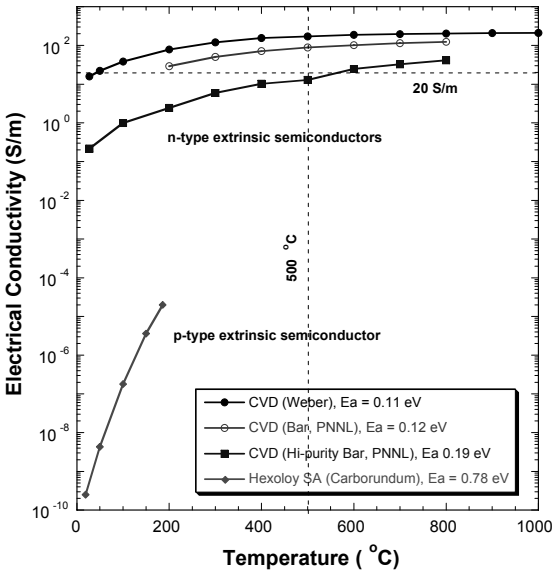

Fig. 2. Electrical conductivity of monolithic SiC.

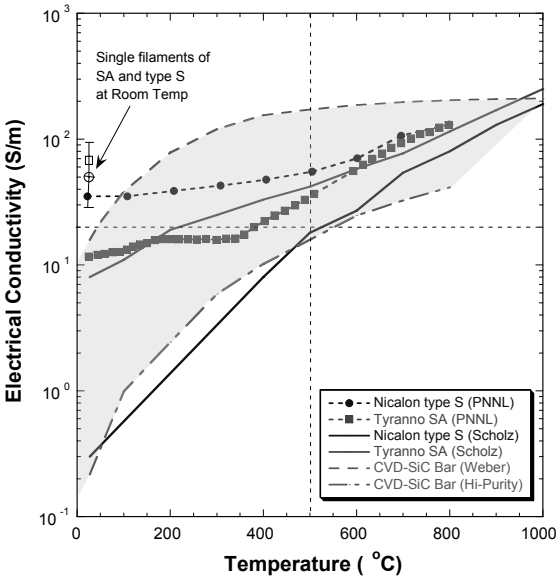

Fig. 3. Electrical conductivity of bare SiC fiber bundles and single filaments of Nicalon™ type S and Tyranno™ SA.

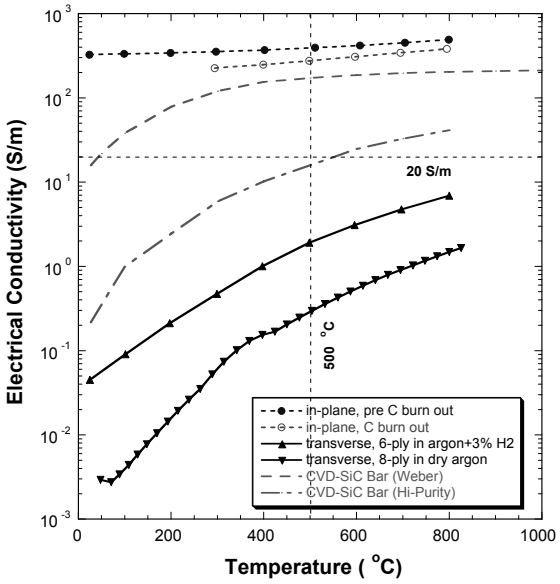

Fig. 4. Anisotropic electrical conductivity of 2D-Nic S/ICVI-SiC composite.

In Fig. 3, for reference the range of EC(T)-values from Fig. 2 for the high-purity CVD-SiC are shown in grey between dashed lines, and the FCI-window is again indicated. Although the EC-values for these two fiber types generally increase with increasing temperature, the temperature dependence did not fit an Arrhenius equation, so E_a-values were not estimated. The EC for a bare Nicalon™ type S bundle at 500 and 800°C was 50 and 130 S/m, respectively. Above 500°C, the EC-values for a Tyranno™ SA bundle were only slightly lower. Again, the EC(T)-values for polycrystalline SiC fiber appear to lie above the FCI-window.

For the Tyranno™ SA fiber, very close correspondence of EC(T)-values with Scholz data were obtained. However, for the type S fiber EC(T)-values were considerably greater than the Scholz data for this fiber. It is very easy for a thin layer of electrically insulating silicon dioxide to form on SiC, which may have been responsible for the much lower EC-values observed by Scholz. Our HF treatment should have removed any oxide layers if they were present, so we are confident that this new EC-data is more representative of the Nicalon™ type S fiber.

The ±40% error bars for the 2-probe data at room temperature represent the standard deviation for measurements on at least 20 different filaments for each fiber type. Apparently, the EC for polycrystalline SiC fibers is far from homogeneous between different filaments or along the lengths of the same filament. This again reflects the sensitive dependence of the EC on the type, amount and distribution of even small amounts of impurities in SiC.

Referring to Fig. 4, the EC-values for our reference 2D-SiC/SiC in the in-plane direction exceeded 300 S/m and were well above the FCI-window. To examine the influence of the thin, but highly conductive PyC interphase in our reference composite, the EC(T)-values were re-measured for the same in-plane bar sample after the PyC fiber coatings had been “burned out” by oxidation in air (1.5 hrs at 800°C in situ). For this condition, the EC decreased ~ 30%, which is reasonable for removal of the thin PyC layers along the fiber component lying parallel to the conductivity direction. The relatively high EC-values for the in-plane direction reflect the dominant contribution of the highly conductive PyC fiber coatings. The coatings are thin and represent only ~ 2% of the sample volume. Nevertheless, they are continuous and provide effective parallel electrically conductive pathways for 1/2 of the fiber component.

In contrast, measurements of the transverse EC for two different samples of our reference 2D-SiC/SiC composite exhibit EC-values less than ~ $1/10^{th}$ the desired 20 S/m upper limit, so lie well within the FCI-window. The EC for this 2D-SiC/SiC made by a conventional ICVI-process electrically is highly anisotropic with ratio σ_x/σ_z > 100. This condition likely is characteristic of CVI-processing of 2D-SiC/SiC.

Simple parallel/series models based on constituent EC-values and geometry cannot explain these results. One possible explanation for this seemingly fortuitous result is that during ICVI-infiltration of a SiC fabric layer preform many intersecting interfaces are formed by the SiC growth rings surrounding the individual SiC filaments as the rings coalesce. Observations of matrix growth interfaces have been made with polarized light for thin sections of similar material [10]. Many of these interfaces lie perpendicular to the transverse conduction direction, and may act as numerous thin electrically insulating layers in series with the SiC fiber and matrix components. The individual SiC fibers and their PyC coatings are separated one from another by the interfaces, which then very effectively reduce the overall transverse EC. The number of these growth ring interfaces is reduced by a factor of ~ 1/2 for the in-plane direction of a 2D-SiC/SiC, in which case the highly conductive PyC coatings as well as 1/2 of the SiC fiber filaments provide many continuous parallel conductive pathways.

Conclusion

For temperatures above 500°C, EC-values for both bare SiC fiber and monolithic CVD-SiC exceed 20 S/m, the desired upper limit for EC in the transverse direction for an FCI. Nevertheless, repeated measurements for a 2D-Nic S/CVI-SiC composite with a thin PyC interface made by a conventional

ICVI-process exhibit transverse EC-values less than 1/10th the 20 S/m value. If true, this is an important, very surprising discovery. The desired EC-goals required to reduce MHD pressure drop likely can be achieved for an FCI constructed with 2D-SiC/CVI-SiC.

Future Work

To examine the reliability of our 2-probe transverse EC method, 2- and 4-probe measurements will be made on a unidirectional SiC/SiC and compared for both transverse and in-plane directions.

References

[1] M. Abdou, et al, "U.S. Plans and Strategy for ITER Blanket Testing," Fus. Sci. and Tech., 47 (3), 475, 2005.
[2] N.B. Morley, et al, "Current Understanding of Feasibility of SiC/SiC Composites for Flow Channel Inserts in Dual Coolant Pb-17Li Blankets," presented at TBM meeting, June 4, 2004, UCLA.
[3] G.E. Youngblood, R.J. Kurtz and R.H. Jones, "Development of SiC/SiC for Application as a Flow Channel Insert," pp. 3-8, in Fusion Materials Semiannual Progress Report (FMSPR) for period ending Dec. 31, 2004. DOE-ER-0313/37.
[4] Technical Bulletin #107, Morton Advanced Materials, Woburn, MA, 1994.
[5] Yu Goldberg, M. Levinshstein and S. Rumyantsev, pp 93-147 in *2001 Silicon Carbide (SiC), Properties of Advanced Semiconductor Materials*, John Wiley and Sons, Inc., New York, 2001.
[6] G.E. Youngblood and R.H. Jones, "Characterization of a 2D-SiC/SiC Composite made by ICVI with Hi-Nicalon™ Type S Fabric," pp. 34-40, in FMSPR for period ending June 30, 2003, DOE-ER-0313/34.
[7] W. Weber, unpublished data.
[8] Carborundum Technical Bulletin, Saint-Gobain Ceramics, 2003.
[9] R. Scholz, F. dos Santos Marques and B. Riccardi, "Electrical Conductivity of Silicon Carbide Composites," J. Nucl. Mater. 307-311 (2002) 1098.
[10] Cover of the proceedings for the "5th IEA Workshop on SiC/SiC Ceramic Composites for Fusion Energy Applications," April 12-13, 2002, San Diego, CA.

THE EFFECT OF NEUTRON IRRADIATION ON INTERFACIAL SHEAR PROPERTIES OF SILICON CARBIDE COMPOSITES WITH MULTILAYER INTERPHASE—T. Nozawa, Y. Katoh, and L. L. Snead (Oak Ridge National Laboratory)

OBJECTIVE

This study aims to evaluate shear properties at the fiber/matrix interface of silicon carbide (SiC) composites with the multiple pyrocarbon (PyC)/SiC interphase by the fiber push-out test technique. Specifically, the effect of neutron irradiation on interfacial shear properties was emphasized on.

SUMMARY

Fiber push-out test results indicate that neutron irradiation decreased both the interfacial debond shear strength and interfacial friction stress. The mechanism of interphase property decrease for the multilayer interphase composite is due primarily to the changing interfacial cracking path. The primary crack propagated within PyC before irradiation provided a very rough fiber surface, resulting in high interfacial shear properties. In contrast, the cracking at the comparatively smooth fiber/PyC interface upon irradiation significantly decreased the interfacial shear properties. The effects of irradiation-induced dimensional change, associated with microstructure and mechanical property changes, and irradiation creep need to be further investigated.

PROGRESS AND STATUS

Introduction

Silicon carbide matrix composites are candidate structural materials for nuclear fusion and advanced fission energy applications. Previous work [1] has shown that, even though fiber and matrix properties remain unchanged after neutron irradiation, the composite performance can potentially degrade. This potential degradation can be directly linked to change in interfacial properties and indirectly to the crystallinity of the SiC fiber. The high-performance fiber/matrix interphase is therefore important for further stability under neutron irradiation.

In non-nuclear applications, a multilayered interphase composed of sequences of very thin (< 50 nm-thick) PyC and SiC has several advantages. First, the very thin PyC layer enhances interfacial shear strength, resulting in improved debond strength [2]. Second, multilayered interfacial structures promotes multiple crack deflections between layers [3] and the resulting tortuous crack path contributes effectively as a toughening mechanism [4]. Additionally, the very thin layered structures are more resistant to oxidation [5]. However, a fundamental question is whether the irradiation-induced swelling of carbon layers, albeit very thin layers in multilayered interphase, will impact composite performance. Presently, no quantitative data are available to evaluate irradiation effects on interfacial shear properties.

Experimental Procedure

A unidirectional Hi-Nicalon™ Type-S fiber reinforced chemically vapor infiltrated (CVI) SiC matrix composite was fabricated. A multiple PyC/SiC interphase was formed on the fiber surface by the CVI technique. The multilayer interphase was composed of five layers of ~ 20 nm-thick PyC and four sub-layers of ~ 100 nm-thick SiC (Fig. 1).

Neutron irradiation was performed in the High Flux Isotope reactor (HFIR) at Oak Ridge National Laboratory as a part of the RB-14J capsule irradiation experiment. The neutron fluence was 7.7 dpa (assuming that 1 dpa corresponds to 1.0×10^{25} n/m^2 (E > 0.1 MeV)), and the irradiation temperature was 800°C.

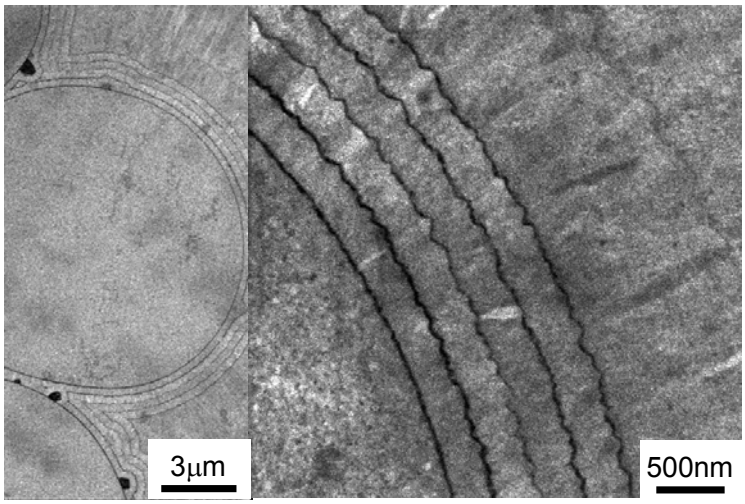

Fig. 1. Typical cross-sectional images of multilayer interphase SiC/SiC composites.

Interfacial shear properties were evaluated by the fiber push-out technique. The specimens were polished with a surface finish of < 1 μm by a standard metallographic technique. The sample thickness was ranged in 50~200 μm. Push-out tests were conducted using a nano-indentation test machine equipped with a Berkovich indenter tip. The loading rate was 0.05 s^{-1}. The pushed-out fiber surface was observed by scanning electron microscopy.

Push-out data were analyzed by non-linear shear-lag models [6, 7]. Two important push-out parameters: an interfacial debond shear strength, which is a critical shear stress to initiate a primary crack at the perfectly bonded interface, and an interfacial friction stress for the debonded interface were calculated from compressive stresses applied on the fiber surface at the debond initiation and the complete debonding, respectively (Fig. 2).

Results and Discussion

Interfacial debond shear strength

Figure 3 shows an experimental debond initiation stress with respect to the sample thickness and fitted curves were obtained using the double shear-lag model originally proposed by Hsueh [6]. Error bars correspond to ± one standard deviation. Interfacial debond shear strengths of 710 MPa (non-irradiated) and 590 MPa (irradiated) were obtained. In calculation, both PyC and SiC were assumed to be isotropic. Thermally-induced residual clamping stress was considered to be negligibly small. For simplicity, the effects of irradiation-induced swelling and irradiation creep were ignored because of uncertainity of irradiation effects on the constituents. Preliminary test results indicate that the slight decrease of the interfacial debond shear strength was obtained upon neutron irradiation up to 7.7 dpa at 800°C.

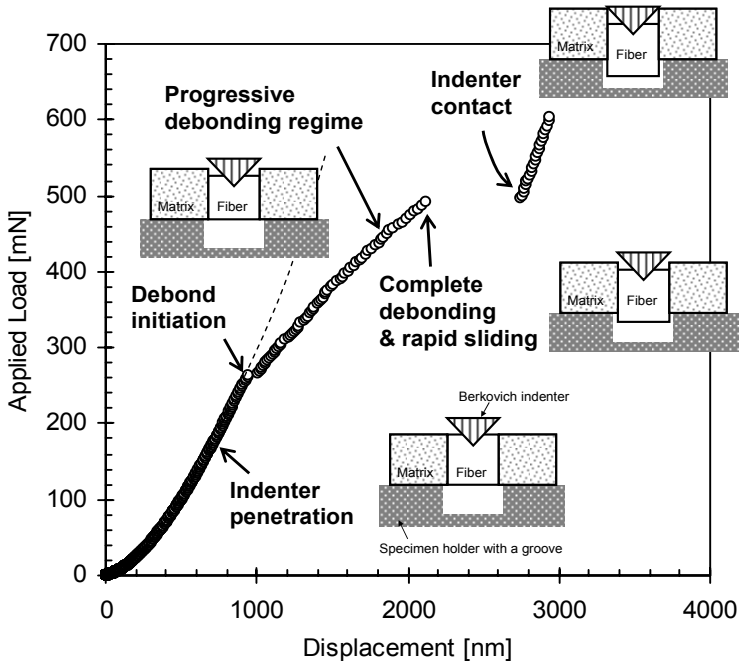

Fig. 2. Typical nano-indentation fiber push-out behavior of composites: 1) penetration of the sharp indenter tip, 2) crack pop-in, 3) progressive debonding regime, 4) complete debonding and rapid sliding, and 5) indenter contact with the SiC matrix.

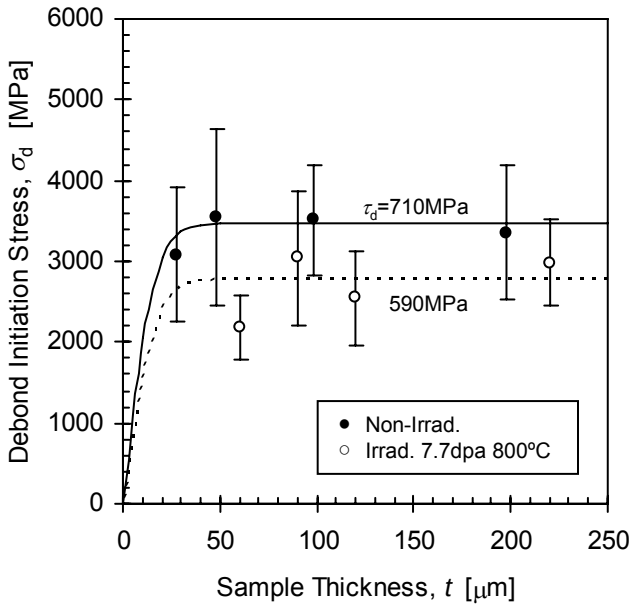

Fig. 3. Debond initiation stress vs. sample thickness, yielding interfacial debond shear strength of 710 MPa (non-irradiated) and 590 MPa (irradiated).

Interfacial friction stress

Figure 4 shows a complete debonding stress with respect to the sample thickness before and after neutron irradiation. According to the Shetty's model [7], for the very thin specimens, the complete debonding stress should be proportional to the sample thickness. Then, the slope of the figure gives estimates of interfacial friction stress: 288 MPa (non-irradiated) and 110 MPa (irradiated). Approximately 60% decrease was apparent in the multilayer interphase upon neutron irradiation up to 7.7 dpa at 800°C. However it is strongly emphasized that the interfacial friction stress of neutron-irradiated multilayer interphase composites was still sufficiently high.

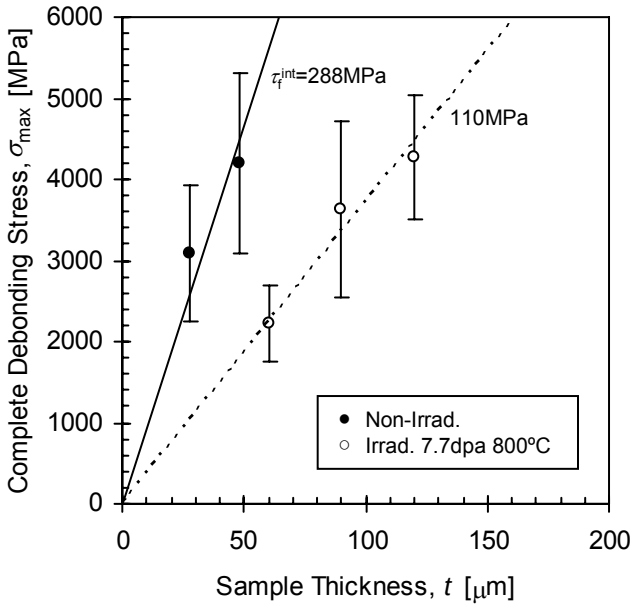

Fig. 4. Complete debonding stress vs. sample thickness, yielding interfacial friction stress of 288 MPa (non-irradiated) and 110 MPa (irradiated).

Effect of fiber surface roughness

Figure 5 shows typical micrographs of pushed out fiber surface. Apparently a rough fiber surface was observed before irradiation. The rough fiber surface indicates that the primary crack probably propagated within the PyC interphase, potentially providing very high clamping stress for the debonded interface. In contrast, the fiber surface for the neutron-irradiated composites, which was an original Hi-Nicalon™ Type-S fiber surface, was comparatively smooth. In this case, the primary crack might propagate at the fiber/PyC interface, resulting in the lower friction stress.

The primary mechanism for the changing interfacial cracking path induced by neutron irradiation is currently unknown. Irradiation-induced swelling, associated with the changes of mechanical property and microstructure, and irradiation creep may influence. The graphitic structure of the carbon interphase, which is preferred to form near the fiber surface, may also impact on interfacial shear properties and the irradiation effect.

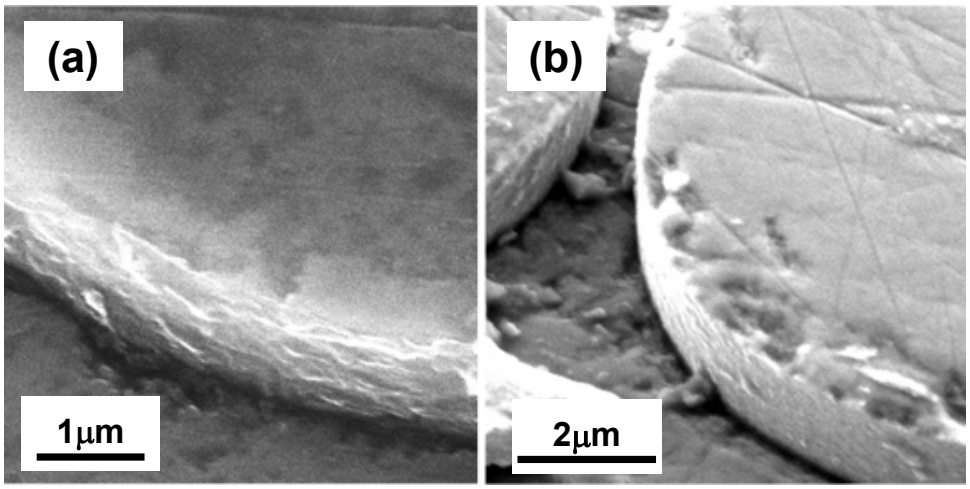

Fig. 5. Typical pushed-out fiber surface images of the multilayer interphase composites: (a) non-irradiated and (b) neutron irradiated up to 7.7 dpa at 800°C.

Acknowledgement

This research was sponsored by the Office of Fusion Energy Sciences, U.S. Department of Energy, under contract DE-AC05-00OR22725 with UT-Battelle, LLC.

References

[1] T. Nozawa, K. Ozawa, S. Kondo, T. Hinoki, Y. Katoh, L. L. Snead, and A. Kohyama, J. ASTM Int. 2 (2005) JAI12884.
[2] F. Rebillat, J. Lamon, and R. Naslain, J. Am. Ceram. Soc. 81 (1998) 2315.
[3] S. Bertrand, C. Droillard, R. Pailler, X. Bourrat, and R. Naslain, J. Eur. Ceram. Soc. 20 (2000) 1.
[4] C. Droillard and J. Lamon, J. Am. Ceram. Soc. 79 (1996) 849.
[5] R. Naslain, R. Pailler, X. Bourrat, S. Bertrand, F. Heurtevent, P. Dupel, and F. Lamouroux, Solid State Ionics 141–142 (2001) 541.
[6] C. H. Hsueh, Mater. Sci. Eng. A165 (1993) 189.
[7] D. K. Shetty, J. Am. Ceram. Soc. 71 (1988) C107.

COATINGS AND JOINING FOR SiC/SiC COMPOSITES FOR NUCLEAR ENERGY SYSTEMS—C. H. Henager, Jr., and Y. Shin (Pacific Northwest National Laboratory*), Y. Blum (SRI), L. A. Giannuzzi (FEI Company), and S. M. Schwarz (University of Central Florida and NanoSpective, Inc.)

OBJECTIVE

It is widely considered a weakness of SiC-SiC composites that they are not fully dense and can, as yet, only be fabricated into simple shapes that require development of attachment technologies in order to achieve more complex configurations. The implication of the lack of full density is that external coatings are required, both for hermeticity considerations [1] and for corrosion protection of the fine-grained SiC fibers and of the fiber-matrix interphase material [2]. Further, joining of simple shapes into more complex structures is also apparently required, particularly for fusion reactor first-wall vessels that cannot possibly be made as a single section [3]. Thus, a significant effort has gone into development and understanding of protective coatings and joining for SiC-SiC composites [1, 2, 4–12]. The purpose of this study is to help develop a wider range of coating and joining technologies for fusion.

SUMMARY

Coatings and joining materials for SiC/SiC composites for nuclear energy systems are being developed using preceramic polymers filled with reactive and inert powders, and using solid-state reactions with no polymers. Polymer-filled joints and coatings start with a poly(hydridomethylsiloxane) precursor, such that mixtures of Al/Al_2O_3/polymer form a hard oxide coating, coatings made with Al/SiC mixtures form a mixed oxide-carbide coating, while coatings made with SiC/polymer form a porous, hard carbide coating. Joints made from such mixtures have shear strengths range from 15 to 50 MPa depending on the applied pressure and joint composition. The strongest joints were obtained using tape cast ribbons of Si/TiC powders such that a solid state displacement reaction at 1473K using 30 MPa applied pressure resulted in shear strengths of 200 MPa, which exceeds the shear strength of SiC/SiC composite materials.

Preceramic polymers with inert and reactive fillers are being considered for SiC-SiC joining technologies [7, 13–15] and have performed adequately if not spectacularly as strong joints. A known difficulty with preceramic polymers is the mass loss, which can exceed 50%, on conversion to a ceramic phase. A slightly different approach has been considered here using a poly-hydridomethylsiloxane (PHMS) as a precursor to a polysiloxane that has the advantage of much lower mass loss on ceramic conversion compared to other systems [16, 17]. In addition, pyrolysis can be achieved at temperatures as low as 873K. PHMS, which is a low viscosity liquid, converts on heating to a Si-O-C phase but can be modified by side group additions to produce a more carbon-rich oxycarbide phase [18]. For the work here, however, we used PHMS with no side group additions but filled the polymer with SiC, Al, and Al_2O_3 powders, singly and in combination. The SiC powders are 0.7-μm average diameter pure SiC, the Al powders were in the form of flakes 1–2 μm in size, and the Al_2O_3 powders were submicron diameter. Powder loadings were in the range of 40% to 60% by volume and were processed in the form of liquid slurries with approximate viscosities of less than 10 cp using cyclohexane as a solvent.

Joining was accomplished by slurry application using a dropper with a nominal weight applied during curing at 423K in moist air. Figure 1 shows a batch of joints made in this manner. This was followed by pyrolysis with a nominal pressure of about 1 MPa in air at 1473K. One joint was also processed at 1073K in nitrogen without any applied pressure. Coatings were also synthesized using the same slurries by dip coating onto SiC-SiC composite coupons, as well as on 316 stainless steel coupons. Coatings were pyrolyzed at 1473K for SiC-SiC and at 1073K for the 316 steel. Joint strengths were tested in single-lap shear geometry at ambient temperature and results are shown in Fig. 1.

*Pacific Northwest National Laboratory (PNNL) is operated for the U.S. Department of Energy by Battelle Memorial Institute under contract DE-AC06-76RLO-1830.

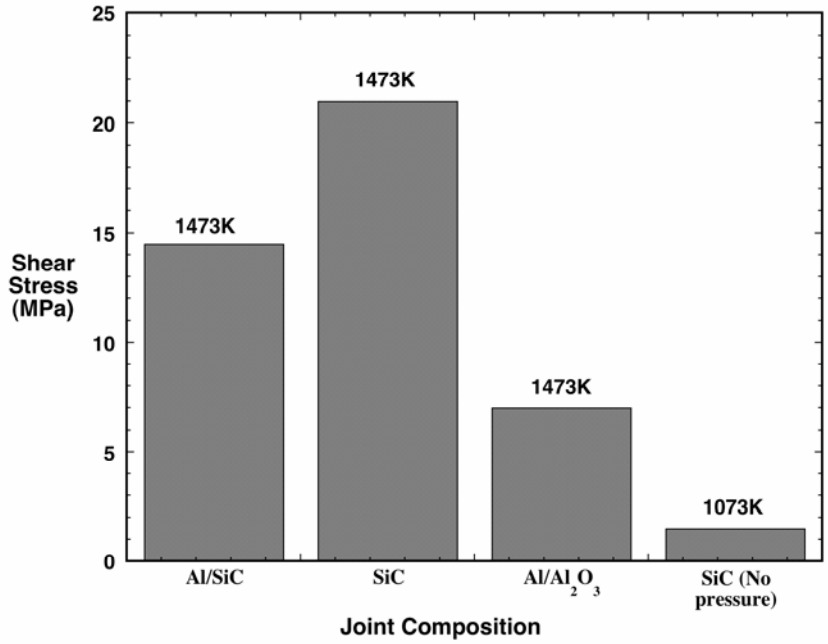

Fig. 1. Single-lap shear strength of PHMS joints processed in air at 1473K using 1 MPa pressure or in nitrogen with no applied pressure at 1073K.

Previous research at PNNL on solid state displacement reactions demonstrated that the reaction between TiC and Si produced an interwoven structure of Ti_3SiC_2, $TiSi_2$, and SiC, with the majority phases being the ternary Ti_3SiC_2 and SiC [19–22]. This reaction was used to make joints from tape cast powder mixtures of TiC and Si powders, which were 99.99% purity having average diameters less than 45 μm with a TiC:Si ratio of 3:2. Tapes were about 200 μm thick and were cut to shape and applied between either Hexaloy coupons or CVI SiC composite coupons[†]. Joints were formed by heating to 573K at 5K/min and holding for 2 hours for binder burnout with a nominal applied pressure followed by heating to 1573K at 10K/min and holding for 1 hour at 30 MPa applied pressure. Joints were tested in shear using a double-notch shear and sectioned for SEM examination.

Polymer slurry joints made with PHMS filled with SiC, Al/SiC, and Al/Al_2O_3 at 1473K using 1 MPa applied pressure exhibited reasonable strengths in single-lap shear testing at ambient temperatures of 21 MPa, 14.5 MPa, and 7 MPa. These joints possess reasonable shear strength values and are thin and dense after only 1 MPa applied pressure. No irradiation or other fusion relevant data exist for these joints, but they should be low activation based on their constituents. Compared to similar joints prepared by others, these have the distinction of being slightly stronger and easier to process. Polycarbosilane requires inert handling and higher conversion temperatures; however, it does convert to SiC whereas this polymer converts to a silicon oxycarbide, which may be a disadvantage in terms of creep strength and corrosion resistance. The high-temperature fracture and creep strength of these materials remains to be determined, but their ease of processing may make them amenable to field repair applications. The low strength of the joint processed at 1073K in nitrogen reveals that a small amount of pressure and temperatures in the 1400K range are required.

[†]Hi-Nicalon Type-S fibers from GE Power Systems with a 2D 8-harness satin weave architecture.

The solid-state reaction joints between TiC and Si resulted in high strength joints, with shear strengths in excess of 50 MPa[‡] as shown in Fig. 2. Almost more importantly, this shear fracture was observed to include some of the Hexaloy SiC and was not restricted to the joint material indicating very strong bonding. The reason for such strong bonding is that the SiC formed during the solid-state reaction between TiC and Si preferentially forms at the existing SiC interface, either the Hexaloy or SiC-SiC composite. This reaction formed SiC is epitaxial with the Hexaloy SiC and we are currently exploring this effect with regard to SiC-SiC composite joints. A further consideration is that Ti_3SiC_2 and SiC are low-activation materials and there is some evidence of pseudo plasticity in the Ti_3SiC_2 phase that might give these joints a measure of fracture resistance that a pure SiC joint would lack. Although, with this system care must be taken to prevent the formation of the brittle $TiSi_2$ phase if possible.

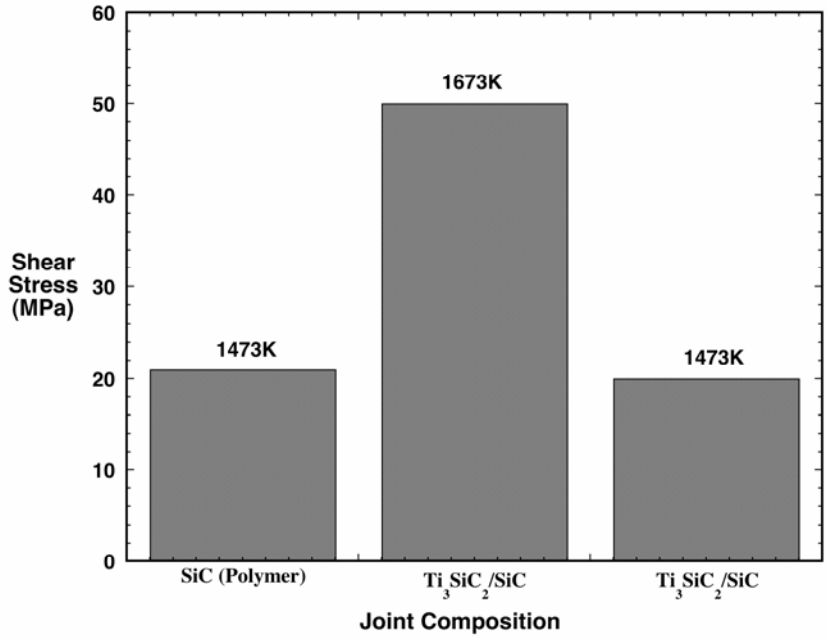

Fig. 2. Comparison of joint shear strengths for SiC-filled PHMS (single-lap) with solid-state reaction joints of TiC+Si to form Ti_3SiC_2/SiC joints (double-notch). Solid-state reaction joints are significantly stronger when processed at high temperatures and 30 MPa applied pressure.

New developments in preceramic polymers have been introduced to show that simple joints and coatings may be produced using simple materials and processing. Since fusion engineering is in its infancy and no single coating or joining technology is the clear favorite at this point, new technologies should continue to be developed to allow as much diversity in synthesis and processing as possible. This will ensure that many choices are available as required to meet the needs of ITER and other fusion projects. Solid-state joints appear to be very strong and, in comparison to reaction bonded joints, may have an advantage of no glassy phases or residual Si.

References

[1] T. Hino, Y. Hirohata, Y. Yamauchi, M. Hashiba, A. Kohyama, Y. Katoh, Y. Lee, T. Jinushi, M. Akiba, K. Nakamura, H. Yoshida, S. Sengoku, K. Tsuzuki, Y. Kusama, K. Yamaguchi, and T. Muroga, Plasma material interaction studies on low activation materials used for plasma facing or blanket component, J. Nucl. Mater. 329–333 (2004) 673.

[‡]Since the double-notch shear test involves some measure of stress concentration at the notches it is reasonable to expect that these measure values for the solid-state joints are an underestimate of the actual strength.

[2] B. A. Pint, K. L. More, H. M. Meyer, and J. R. DiStefano, Recent progress addressing compatibility issues relevant to fusion environments, Fusion Sci. Technol. 47 (2005) 851.
[3] A. R. Raffray, R. Jones, G. Aiello, M. Billone, L. Giancarli, H. Golfier, A. Hasegawa, Y. Katoh, A. Kohyama, S. Nishio, B. Riccardi, and M. S. Tillack, Design and material issues for high performance SiCf/ SiC-based fusion power cores, Fusion Eng. Des. 55 (2001) 55.
[4] S. Sharafat, N. Ghoniem, and S. Zinkle, Thermodynamic stability of oxide, nitride, and carbide coating materials in liquid Sn-25Li, J. Nucl. Mater. 329–333 (2004) 1429.
[5] L. L. Snead, T. Inoki, Y. Katoh, T. Taguchi, R. H. Jones, A. Kohyama, and N. Igawa, Silicon carbide composites for fusion reactor application, 10th International Ceramics Congress 2002, Part D, Adv. Sci. Technol. 33 (2003) 129.
[6] J. Sha, A. Kohyama, and Y. Katoh, Recent progresses and critical issues of SiCf/SiC composite under irradiation environments, Plasma Sci. Technol. 5(5) (2003) 1965.
[7] C. A. Lewinsohn, M. Singh, and C. H. Henager, Jr., Brazeless approaches to joining of silicon carbide -based ceramics for high temperature applications, Ceram. Trans. 138 (2003) 201.
[8] Y. Katoh, A. Kohyama, T. Hinoki, and L. L. Snead, Progress in SiC-based ceramic composites for fusion applications, Fusion Sci. Technol. 44 (2003) 155.
[9] R. H. Jones, SiCf/SiC composites for advanced nuclear applications, Ceram. Eng. Sci. Proc. 24 (2003) 261.
[10] T. Hino, T. Jinushi, Y. Hirohata, M. Hashiba, Y. Yamauchi, Y. Katoh, and A. Kohyama, Helium gas permeability of SiC/SiC composite developed for blanket component, Fusion Sci. Technol. 43 (2003) 184.
[11] M. Ferraris, P. Appendino, V. Casalegno, F. Smeacetto, and M. Salvo, Joining of ceramic matrix composites for fusion application, 10th International Ceramics Congress: 2002, Adv. Sci. Technol. 33 (2003).
[12] B. Riccardi, C. A. Nannetti, T. Petrisor, and M. Sacchetti, Low activation brazing materials and techniques for SiCf/SiC composites, J. Nucl. Mater. 307–311 (2002) 1237.
[13] C. A. Lewinsohn, R. H. Jones, P. Colombo, and B. Riccardi, Silicon carbide-based materials for joining silicon carbide composites for fusion energy applications, J. Nucl. Mater. 307–311 (2002) 1232.
[14] C. A. Lewinsohn, R. H. Jones, T. Nozawa, M. Kotani, Y. Katoh, A. Kohyama, and M. Singh, Silicon carbide based joining materials for fusion energy and other high-temperature, structural applications, Ceram. Eng. Sci. Proc. 22 (2001) 621.
[15] P. Colombo, B. Riccardi, A. Donato, and G. Scarinci, Joining of SiC/SiCf ceramic matrix composites for fusion reactor blanket applications, J. Nucl. Mater. 278 (2000) 127.
[16] Y. D. Blum and D. B. MacQueen, Modifications of hydrosiloxane polymers for coating applications, Surface Coatings International, Part B, Coat. Trans. 84 (2001) 27.
[17] Y. D. Blum, H. P. Chen, D. B. MacQueen, and S. M. Johnson, Modifications of preceramic polymers suitable for corrosion resistant and high temperature coatings, Materials Research Society Symposium Proceedings 576 (1999) 281.
[18] Y. D. Blum, D. B. MacQueen, and H.-J. Kleebe, Synthesis and characterization of carbon-enriched silicon oxycarbidesm, J. Eur. Ceram. Soc. 25 (2005) 143.
[19] C. Toy, E. Savrun, C. Lewinsohn, and C. Henager, Novel joining compounds in Ti-Si-C system, Ceram. Trans. 103 (2000) 561.
[20] R. Radhakrishnan, S. Bhaduri, and C. H. Henager, Jr., The reactive processing of silicides, J. Mater. 49 (1997) 41.
[21] C. H. Henager, Jr., and R. H. Jones, Joining SiC ceramics using displacement reactions, Ceram. Trans. 77 (1997) 117.
[22] R. Radhakrishnan, C. H. Henager, Jr., J. L. Brimhall, and S. B. Bhaduri, Synthesis of Ti_3SiC_2/SiC and $TiSi_2$/SiC composites using displacement reactions in the Ti-Si-C system, Scr. Mater. 34 (1996) 1809.

SWELLING AND TIME-DEPENDENT CRACK GROWTH IN SiC/SiC COMPOSITES—C. H. Henager, Jr. (Pacific Northwest National Laboratory)*

OBJECTIVE

Time-dependent and dose-dependent properties of SiC-composites include retained strength, dimensional stability, and creep-crack growth [1], which have been partly addressed by a dynamic crack growth model developed to predict composite lifetimes due to growth of internal cracks in these materials [2–4]. However, crack growth models have not been able to include dose-dependent swelling data until the development of a modified four-cylinder model [5]. The synthesis of these models will provide a more detailed understanding and improved predictive capabilities with respect to time-dependent mechanical properties of SiC-composites under neutron irradiation.

SUMMARY

Pacific Northwest National Laboratory (PNNL) was among the first to identify and study time-dependent bridging in ceramic composites [6–8] and we have proposed a crack growth mechanism map based on available experimental data as a function of temperature and oxygen partial pressure for continuous fiber composites with carbon interphases [4]. Once a relationship between crack-opening displacement and bridging tractions from crack-bridging elements is determined, a governing integral equation is obtained that relates the total crack opening, and the bridging tractions, to the applied load. The solution of this equation gives the force on the crack-bridges and the crack-opening displacement everywhere along the crack face [3]. This relation is rendered time-dependent by including appropriate bridging fiber creep laws and interface removal kinetics, if oxidation is an issue. For fusion environments, both thermal and irradiation-induced fiber creep are included but oxidation is not considered here. Since the frictional sliding stress, τ, is an input parameter for this dynamic model the results from our 4-cylinder model allow τ to be dose-dependent. The bridging model can be used to determine the effects of pyrocarbon type on composite mechanical properties in radiation environments.

A continuous fiber composite is simulated by four concentric cylinders [9]. The surrounding composite is the outermost cylinder, while the matrix, fiber coating, and fiber are the remaining cylinders, with the fiber being the innermost cylinder. The cylinders are subject to three independent boundary conditions; axisymmetric temperature change, $\Delta T(r)$, uniaxial applied stress, σ_{oz}, and biaxial applied stress, σ_{or}, where r and z are the radial and axial components referred to cylindrical coordinates (r, θ, z). Stress relaxation was not allowed during irradiation or during cooling from the fabrication temperature and all components remain elastic and perfectly bonded. The fiber, matrix, and surrounding composite were treated as isotropic materials, while the pyrocarbon coatings were considered to be transversely isotropic [10]. The boundary conditions for the four-cylinder problem and solution are presented in [9, 10] as the solution to eight simultaneous equations. Solution details when dose-dependent swelling terms are included in this model can be found in Ref. [5].

Several different cases were studied under simulated neutron irradiation at 1273K to 1473K using a dose rate of 10 dpa/year for a SiC-composite with SiC Type-S fibers. Time-dependent crack growth considering fiber creep under thermal and thermal plus radiation-induced was modeled under the assumptions of a constant sliding stress. This was then compared using the variable sliding stress results from the 4-cylinder model. For all models values of the domain radii for the 4-cylinder model were chosen to match microstructural information for CVI SiC/SiC composites. The fiber coating thickness was 100 nm, which is representative of pyrocarbon thicknesses. The stresses were computed out to 20 dpa, or 2 years of irradiation. Fiber thermal creep parameters for Hi-Nicalon Type-S SiC fibers were obtained from DiCarlo et al.†, while radiation-induced creep parameters were obtained from the work of Scholz and

*Pacific Northwest National Laboratory (PNNL) is operated for the U.S. Department of Energy by Battelle Memorial Institute under contract DE-AC06-76RLO-1830.

†Private communication from J. A. DiCarlo, NASA Glenn Research, James.A.DiCarlo@nasa.gov.

Youngblood [11] for Sylramic SiC fibers, which is a fine-grained SiC fiber comparable to the Type-S fiber. These creep parameters are shown in Table 1. The dynamic crack growth model reveals that Hi-Nicalon Type-S composites are thermal-creep resistant at 1273K but that using the assumed radiation-induced fiber creep law results in high crack growth rates, where the radiation-induced fiber creep is the dominant deformation mechanism. These crack growth results are shown in Fig. 1 for a composite bar in 4-point bending at 1273K to 1473K with an assumed crack in the bar loaded to 10 MPa$\sqrt{m}$ and with an assumed sliding stress value of 20 MPa. The sliding stress is then allowed to vary according for both HDIC and LDIC pyrocarbon interfaces of 100-nm thickness. For both pyrocarbon materials there is a dose at which "turn around" occurs in their swelling and growth curves. Initially there is densification of the pyrocarbon and net radial shrinkage, which acts to reduce the sliding stress. At "turn around," pyrocarbon shrinkage stops and net radial swelling begins, which acts to put the fiber-matrix interface into compression and increase the sliding stress. The sliding stress begins at 20 MPa at $t = 0$ and decreases with increasing tensile σ_{rr} but is not allowed to decrease below 5 MPa. These predicted crack growth curves are shown in Fig. 2. Crack growth is initially more rapid compared to the constant sliding stress case when this detail is included, but then begins to decrease after "turn around" as the sliding stress begins to increase with increasing dose. Although the total crack length is longer for the variable sliding stress case, the crack growth rate has dropped below the rate for constant sliding stress after a dose of about 10 dpa.

Table 1. Properties used in calculations (typical values)

Materials	Young's Modulus (GPa)		Poisson's ratio		CTE ($10^{-6}C^{-1}$)	
	Axial E_L	Transverse E_T	Axial ν_L	In-plane ν_T	Axial α_L	Transverse α_L
Type-S SiC fiber	420	420	0.2	0.2	4.0	4.0
SiC matrix	460	460	0.22	0.22	4.5	4.5
HDIC*	80	80	0.23	0.23	5	5
LDIC**	80	80	0.23	0.23	5	5

*High-density isotropic carbon
**Low-density isotropic carbon

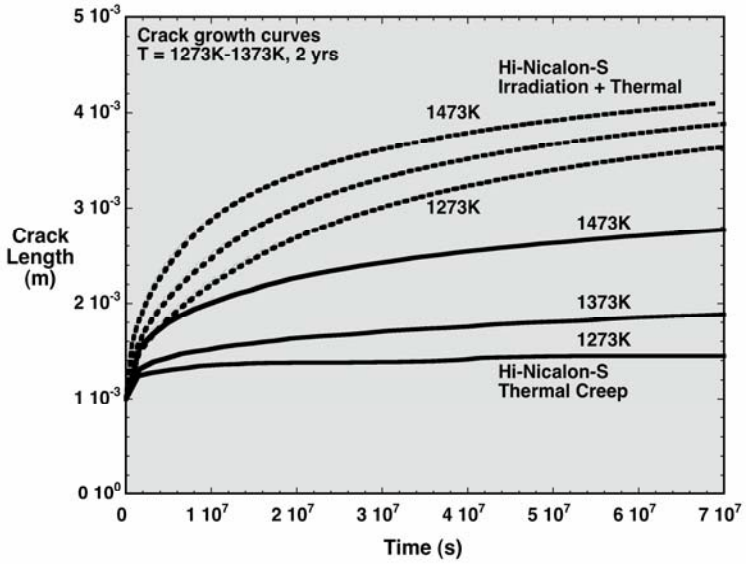

Fig. 1. Crack growth curves due to fiber thermal creep only (solid lines) or thermal plus radiation-induced creep (dashed lines) at 1273K to 1473K.

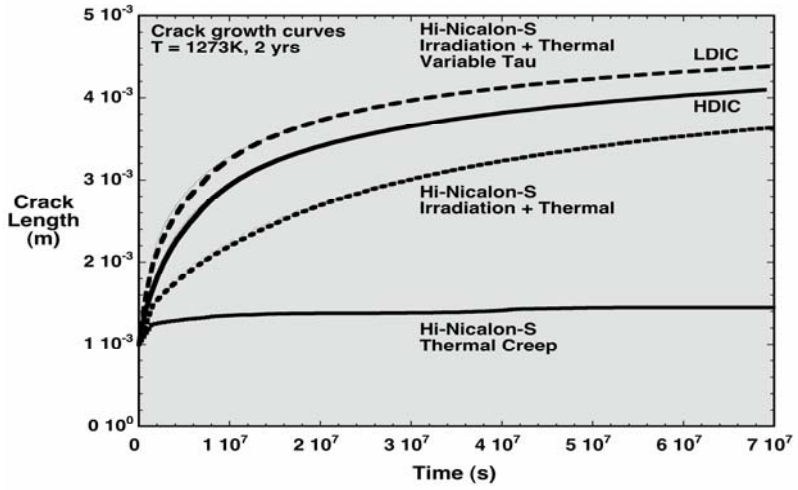

Fig. 2. Crack length as a function of time showing the effects of including a dose-dependent sliding stress in the dynamic crack modeling at 1273K. Total time in seconds is for 2 years or 20 dpa.

References

[1] L. L Snead, T. Inoki, Y. Katoh, T. Taguchi, R. H. Jones, A. Kohyama, and N. Igawa, Silicon carbide composites for fusion reactor application, 10th International Ceramics Congress 2002, Part D, Adv. Sci. Technol. 33 (2003) 129.

[2] C. H. Henager, C. A. Lewinsohn, and R. H. Jones, Subcritical crack growth in CVI SiCf/SiC composites at elevated temperatures: Effect of fiber creep rate, Acta Mater. 49 (2001) 3727.

[3] C. H. Henager, Jr., and R. G. Hoagland, Subcritical crack growth in CVI SiCf/SiC composites at elevated temperatures: Dynamic crack growth model, Acta Mater. 49 (2001) 3739.

[4] R. H. Jones and C. H. Henager, Jr., Subcritical crack growth processes in SiC/SiC ceramic matrix composites, J. Eur. Ceram. Soc. 25 (2005) 1717.

[5] C. H. Henager, E. A. Le, and R. H. Jones, A model stress analysis of swelling in SiC/SiC composites as a function of fiber type and carbon interphase structure, J. Nucl. Mater. 329–333 (2004) 502.

[6] C. H. Henager, Jr., R. H. Jones, C. F. Windisch, Jr., M. M. Stackpoole, and R. Bordia, Time dependent, environmentally assisted crack growth in Nicalon-fiber-reinforced SiC composites at elevated temperatures, Metall. Mater. Trans. A 27A (1996) 839.

[7] C. H. Henager, Jr., and R. H. Jones, Subcritical crack growth in CVI silicon carbide reinforced with Nicalon fibers: Experiment and model, J. Am. Ceram. Soc. 77 (1994) 2381.

[8] C. H. Henager, Jr., and R. H. Jones, High-temperature plasticity effects in bridged cracks and subcritical crack growth in ceramic composites, Mater. Sci. Eng. A 166 (1993) 211.

[9] Y. Mikata and M. Taya, Stress field in a coated continuous fiber composite subjected to thermo-mechanical loadings, J. Compos. Mater. 19 (1985) 554.

[10] C. M. Warwick and T. W. Clyne, Development of composite coaxial cylinder stress analysis model and its application to SiC monofilament systems, J. Mater. Sci. 26 (1991) 3817.

[11] R. Scholz and G. E. Youngblood, Irradiation creep of advanced silicon carbide fibers, J. Nucl. Mater. 283–287 (2000) 372.

3.0 FERRITIC/MARTENSITIC STEELS AND ODS STEELS

THE TRANSPORT AND FATE OF HELIUM IN MARTENSITIC STEELS AT FUSION RELEVANT HE/DPA RATIOS AND DPA RATES—R. J. Kurtz (Pacific Northwest National Laboratory*), G. R. Odette, T. Yamamoto (University of California, Santa Barbara), D. S. Gelles (Pacific Northwest National Laboratory), P. Miao (University of California, Santa Barbara), and B. M. Oliver (Pacific Northwest National Laboratory)

Extended abstract of a paper submitted to the Journal of Nuclear Materials as part of the proceedings of the 12th International Conference on Fusion Reactor Materials, Santa Barbara, California, December 4–9, 2005.

Experimental Procedure

The HFIR JP26 irradiation experiment contained a series of transmission electron microscopy (TEM) disks intended to study helium effects in ferritic/martensitic steels [1,2]. Table 1 lists specimens from that experiment chosen for examination. The Eurofer-97 disks were prepared with thin NiAl coatings so that irradiation would produce He by transmutation of the Ni and deposit that He uniformly in a thin layer ~ 6 to 8 μm thick adjacent to the coating. Yamamoto et al. [3] give details of the specimen design and preparation. Following irradiation, samples were prepared for TEM using a cross-section technique to show He effects in the implanted layer near the NiAl coating. The procedure involved mounting the TEM disk between two half cylinders of Cu wire with thermal setting epoxy and slicing the composite wire using a slow speed saw equipped with a diamond-impregnated blade to produce 3 mm disks, with the TEM slice supported between the half-cylinders of Cu. Each composite disk was then dimple ground to a central thickness of ~ 100 μm, and ion milled using a Gatan Precision Ion Polishing System. Ion milling was performed with 5 KV Ar ions to perforation so that the hole grew into the area of interest, followed by ion polishing at 2 KV for up to 1800 s to minimize Ar ion damage near the surface. Microstructural examinations were performed on a JEOL 2010F operating at 200 KeV in transmission with images recorded digitally.

Table 1. Summary of the NiAl coated Eurofer-97 transmission electron microscope discs irradiated in the JP26 experiment. Bold italic specimen numbers denote the samples examined in this study. The He concentrations are expected values based on pre-test calculations.

Nominal NiAl Thick., μm	300°C, 3.9 dpa		400°C, 3.9 dpa		500°C, 9 dpa	
	Spec. Nos.	[He], appm	Spec. Nos.	[He], appm	Spec. Nos.	[He], appm
0	R00, R01	0, 0	R10, R11	0, 0	R20, R21	0, 0
1	R02, R03	25, 23	R12, R13	24, 24	R22, R23	98, 98
2	R04, R05	41, 40	R14, R15	40, 40	R24, ***R25***	167, 169
4	***R06***, R07	89, 82	***R16***, R17	82, 81	R26, ***R27***	338, 372

Representative regions in the TEM images were selected for detailed analysis to determine the He bubble number densities and size distributions. Stereo pair images at ~ 500 nm underfocus were acquired so that the bubbles appeared white with a black outer ring. Foil thickness was measured from stereo pairs using a Hilger-Watts viewer for the center of each region analyzed. A square area centered on the thickness measurement location was analyzed for each specimen. The area analyzed was 0.05304, 0.1380, and 0.003812 μm^2 for specimens R16, R27, and R06, respectively. Grayscale TEM images were converted to black and white images, taking care not to change the shape or size of the bubbles during the conversion. Bubbles appear white against a black background in the converted images. A public domain software package was used to determine bubble area. Bubble diameters and size distributions were calculated from the area measurements assuming spherical bubbles.

*Pacific Northwest National Laboratory (PNNL) is operated for the U.S. Department of Energy by Battelle Memorial Institute under contract DE-AC06-76RLO-1830.

The He concentration was measured in two samples taken from specimen R25. One sample was abrasively polished to remove only the NiAl coating, and the other was abrasively polished to remove both the NiAl coating and enough of the Eurofer-97 to leave only the He implanted layer. Prior to analysis, each of these pieces was cut in half using a small wire cutter, then rinsed in acetone, and air-dried. The mass of each specimen was determined using a calibrated microbalance traceable to the National Institute of Standards and Technology. Mass uncertainty is estimated to be ± 0.001 mg.

The He content of each specimen was determined by isotope-dilution gas mass spectrometry following vaporization in a resistance-heated graphite crucible [4]. The absolute amount of ^{4}He released was measured relative to a known quantity of added ^{3}He "spike." The ^{3}He spike was obtained by expanding and partitioning a known quantity of gas through a succession of calibrated volumes [5]. The mass spectrometer was calibrated for mass sensitivity during each series of runs by analyzing known mixtures of ^{3}He and ^{4}He.

Results

Figure 1 gives TEM images showing the microstructure in the He implanted layer for specimen R06. This specimen was irradiated at 300°C to a dose of 3.9 dpa with a nominal 4 μm layer of NiAl. The expected implanted He concentration for this specimen is ~ 89 appm as shown in Table 1. The underfocus imaging conditions in Fig. 1a were selected to enhance bubble contrast to aid identification and measurement. In Fig. 1b, dislocation contrast imaging conditions were employed to determine if He bubbles are preferentially associated with dislocations. Detailed bubble size and number density analysis reveals that the mean bubble diameter is ~ 0.9 nm with a standard deviation (1σ) of 0.2 nm. The measured bubble number density is ~ 3.6 x 10^{23} m^{-3}. It should be noted the foil thickness measurement for R06 is uncertain. The value reported here is an average of the values for R16 and R27. Due to the very small sizes of the "black spot" defects produced at 300°C, it was difficult to determine the precise character of these defects. It is presumed they are small dislocation loops. The distribution of defects in Fig. 1b suggests that loop and/or void formation at 300°C may have been suppressed by the formation of a high-density of small He bubbles or clusters that served as point defect recombination centers. To explore this possibility the microstructure in the He implanted zone was compared to the microstructure in a He free region of the same specimen, see Figs. 2a and 2b. While the images in Figs. 2a and 2b were taken at different magnifications there was an indication that loop formation was suppressed in the He implanted zone. This indication needs to be further confirmed.

The bubble and dislocation microstructures observed in specimen R16 are presented in Figs. 3a and 3b, respectively. This specimen was irradiated at 400°C to a dose of 3.9 dpa. Similar to R06, the expected concentration of He in the implanted layer was ~ 82 appm. It is clear that much larger bubbles, at significantly lower number density, form at this temperature compared to 300°C. The mean bubble diameter is 3.0 nm with a standard deviation of 1.4 nm. This is roughly three times larger than at 300°C with a larger dispersion in bubble sizes. In addition, the bubble number density is 1.2 x 10^{22} m^{-3} which is about 30 times smaller than at 300°C. Dislocation loops of both a/2<111> and a<100> character were produced at 400°C. Careful examination of Fig. 3b suggests that He bubbles nucleated on pre-existing dislocations.

Figures 4a and 4b illustrate the bubble and dislocation microstructures found in specimen R27 irradiated at 500°C. This specimen received a dose of 9 dpa, consequently the expected He concentration is 372 appm. The largest He bubbles were observed at this irradiation temperature. The mean bubble diameter is 4.3 nm with a standard deviation of 1.6 nm. The mean bubble diameter increased more than 40% relative to R16, but the dispersion of bubble sizes was approximately the same. Bubble number density is slightly larger than for R16 at 1.5 x 10^{22} m^{-3}. While more than four times as much He was injected into this specimen compared to R06 and R16, the main effect was to increase bubble size rather than increase the number density. It is evident from Figs. 4a and 4b that bubbles are associated with

dislocations. The “pearls-on-a-string” spatial arrangements of bubbles clearly follow the pre-existing dislocation pattern.

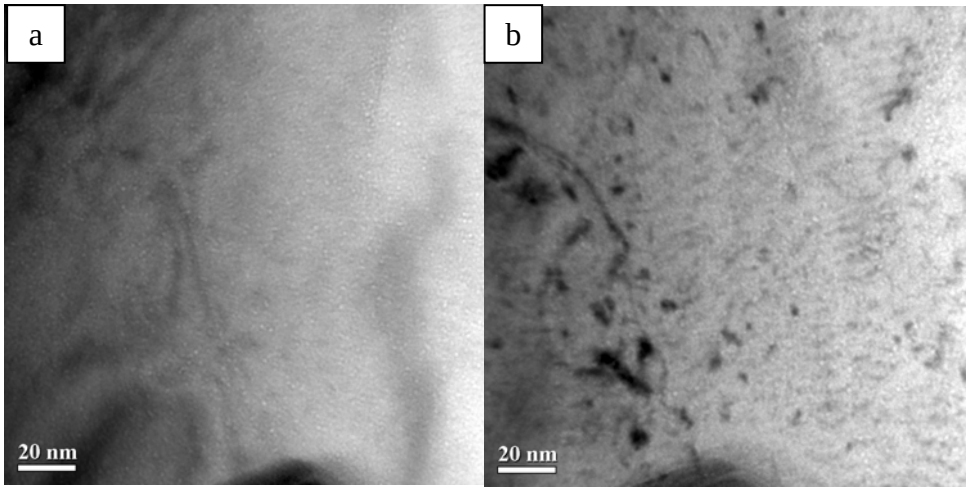

Fig. 1. TEM image showing a) the bubble microstructure and b) the dislocation microstructure for specimen R06 coated with 4 μm of NiAl and irradiated at 300°C to a dose of 3.9 dpa. The expected He concentration is 89 appm.

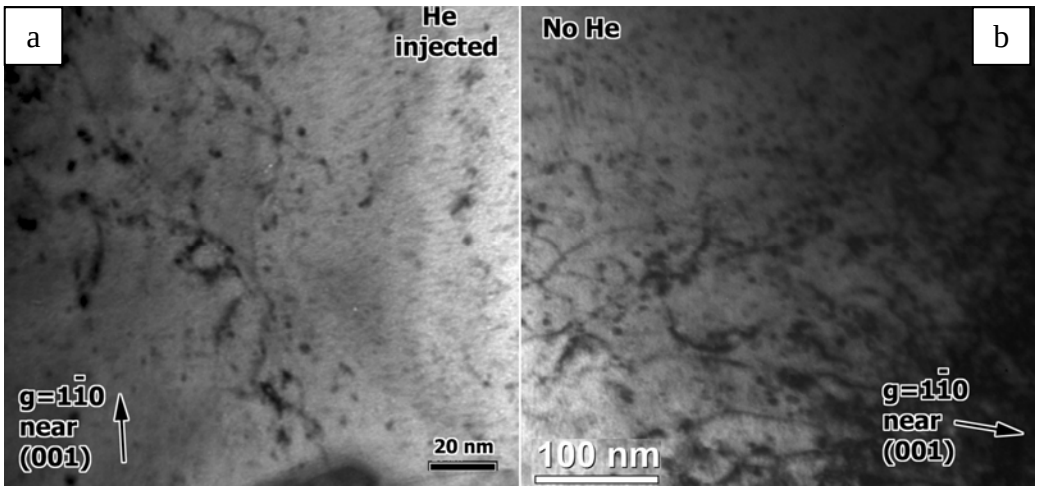

Fig. 2. TEM image showing the dislocation microstructures in specimen R06 in a) the He injected region near the NiAl coating and b) a region with no He injection far from the NiAl coating.

The results of the He measurements are given in Table 2 and are listed as total atoms of ^{4}He released and as ^{4}He concentrations in atomic parts per million (10^{-6} atom fraction). In Table 3, the samples consisting of only the He implanted layers are identified as R25A,B-thin and samples consisting of the full thickness TEM disc less the NiAl coating are designated as R25C,D-thick. Conversion from total He to He concentration was based on a calculated value of 1.07 x 1022 atoms/gram for Eurofer-97. It should be noted that this value, and the He concentrations obtained using it, are not very sensitive to small changes in material composition.

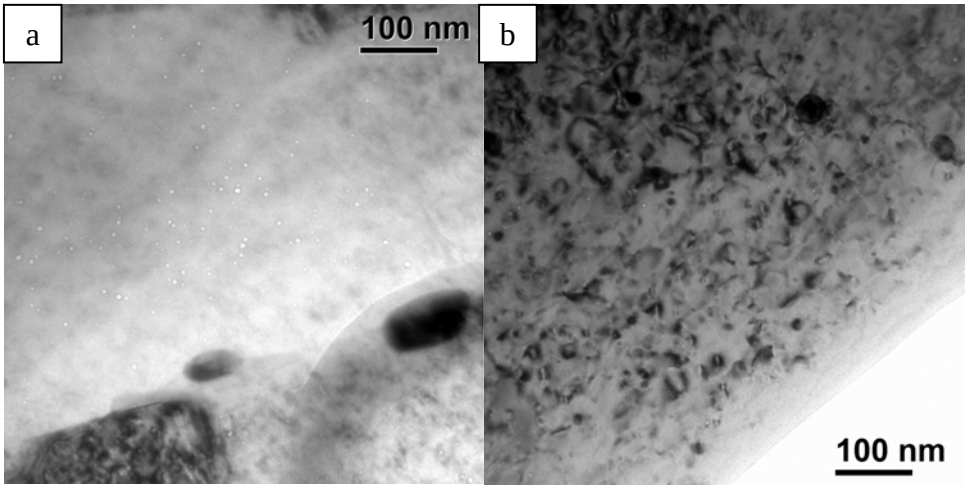

Fig. 3. TEM image showing a) the bubble microstructure and b) the dislocation microstructure for specimen R16 coated with 4 μm of NiAl and irradiated at 400°C to a dose of 3.9 dpa. The expected He concentration is 82 appm.

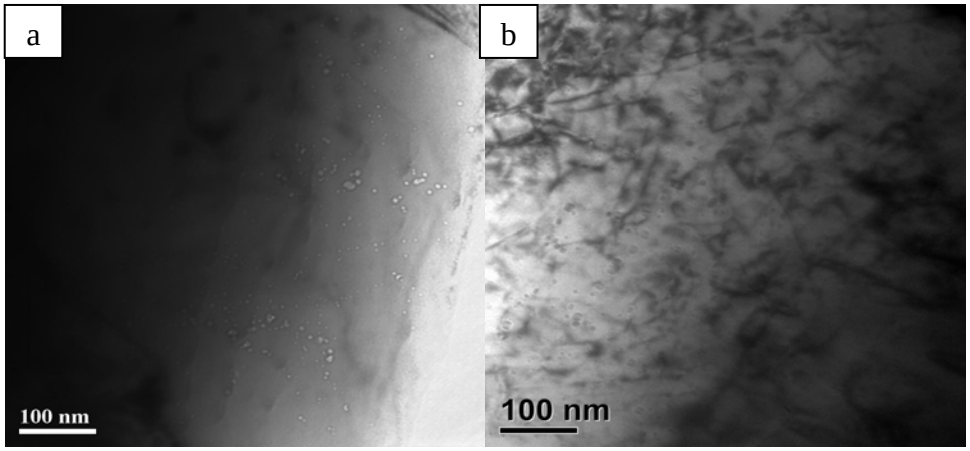

Fig. 4. TEM image showing a) the bubble microstructure and b) the dislocation microstructure for specimen R27 coated with 4 μm of NiAl and irradiated at 500°C to a dose of 9 dpa. The expected He concentration is 372 appm.

Table 2. The He concentration in R25 measured by a high-sensitivity isotope-dilution magnetic sector mass spectrometer. Specimens denoted as "thin" were prepared by sanding away the NiAl layer and enough of the Eurofer-97 to leave only the He implanted layer. Specimens denoted as "thick" were prepared by removing only the NiAl layer leaving both the implanted and unimplanted Eurofer-97.

Specimen ID	Mass[a], mg	Measured ^{4}He, 10^{14} atoms	He Concentration, appm[b]	
			Measured	Average[c]
R25A-thin	0.013	0.184	132	132 ± 0.0
R25B-thin	0.022	0.310	132	
R25C-thick	1.138	1.556	12.8	12.2 ± 0.9
R25D-thick	1.127	1.395	11.6	

[a]Mass of specimen for analysis. Mass uncertainty is ± 0.001 mg.
[b]Helium concentration in atomic parts per million (10^{-6} atom fraction) with respect to the total number of atoms in the specimen.
[c]Mean and standard deviation (1σ) of duplicate analyses.

Table 3. Measured He bubble sizes and number densities. He concentration calculated from the mean bubble radii and number densities. Note the MA957 specimen was examined in a companion study and included here for comparison to the Eurofer-97 results [3].

Specimen No.	Temp., °C	Foil thickness, nm	Mean bubble diameter, nm	Number density, m^{-3}	Calc. He conc., appm
R06	300	150*	0.9 ± 0.2	$3.6x10^{23}$	270
R16	400	130	3.0 ± 1.4	$1.2x10^{22}$	128
R27	500	170	4.3 ± 1.6	$1.5x10^{22}$	384
MA957	500	52	0.6 ± 0.3	$6.6x10^{23}$	131

*Foil thickness measurement is uncertain. The reported value is an average of the measurements for R16 and R27.

Mean He contents in the two samples were 132 appm for the thin specimens and 12.2 appm for the thick specimens. The 132 appm value is reasonably close to that calculated for the experiment (see Table 1). The lower He content in the thick samples represents dilution by the much lower He levels in the bulk material away from the implanted layer.

Absolute uncertainty (1σ) in the individual He atom results, determined from the cumulative uncertainties the isotope ratio measurement, and the spike size, is estimated to be ~ 1%. For the He concentrations, the sample mass normally contributes negligibly to the final uncertainty. However, for the thin specimens, additional mass uncertainty of ~ 6% is present due to the very small sample size. The estimated uncertainties are consistent with the variability observed in duplicate analyses.

Discussion

As summarized in Table 3, the mean bubble diameter increased systematically with increasing irradiation temperature, and the bubble density at 400 and 500°C was about 25 times smaller than at 300°C. Measurements of the He concentration in R25 correlate well with the concentration expected from pretest calculations (132 appm measured versus 169 appm predicted). Measurement of the He concentration in a full-thickness specimen that includes both the He injected zone and the He free region corroborate this result.

We recognize that the minimum bubble sizes observed are near the TEM resolution limit, so the precise nature of the bubble size distribution is uncertain below that limit. In addition, further work is needed to confirm that specimen preparation procedures, or the presence of surface oxides did not influence our measurements. To provide additional confidence in our results we calculated the He concentration in the

injected layer based on the measured average bubble sizes and number densities. We assume that all bubbles were in equilibrium at the irradiation temperature and that the bubble pressure, P, is given by:

$$P = \frac{2\gamma}{< r >} \quad (1)$$

where γ is the surface energy, which is taken to be ~ 2 J/m^2, and <r> is the mean bubble radius. A high-pressure equation-of-state [6] was used to determine the mole fraction of He in bubbles at pressure P. We also assume that all of the injected He is contained in the visible bubble population. The estimated He concentrations for R06, R16, and R27 are 270, 128, and 384 appm, respectively (see Table 3). Recall that the expected He levels are 89, 82, and 372 appm. Except for R06, the estimated He concentrations based on the measured bubble sizes and number densities agree very well with expected levels. Uncertainty in the foil thickness estimate for R06, coupled with the difficulty of accurately determining the mean bubble size and number density for the very small bubbles in R06, are likely responsible for the difference between the estimated He concentration and the expected value.

An objective of our research is to develop and test models of He trapping in ferritic alloys in order to design microstructures with optimal resistance to dimensional instabilities and mechanical property degradation due to He. It is informative to compare the efficiency of He trapping in a nanostructured ferritic alloy such as MA957 with a conventional RAFM alloy such as Eurofer-97. In a companion study to the present work [3], NiAl coatings were applied to TEM discs of MA957 and irradiated under the same conditions as R27. The measured bubble sizes and number densities for the MA957 specimen are included in Table 2 for comparison with the Eurofer-97 results. While the measured mean bubble size is below the TEM resolution limit, and therefore uncertain, the MA957 results clearly illustrate that a high-density of nano-scale Y-Ti-O particles effectively trapped He and dramatically suppressed bubble growth. Indeed, the measured bubble density is on the same order as the Y-Ti-O particle density. Considering the uncertainty in the bubble size and density measurements for the MA957 specimen, the calculated He concentration is in remarkable agreement with the expected value (see Table 3).

Conclusions

The He implanter layer concept has been demonstrated to be an effective experimental tool for producing controlled He-to-dpa ratios in Eurofer-97 TEM discs under neutron irradiation. Helium bubbles were found in the implanted region, adjacent to the NiAl layer, at all three irradiation temperatures, with estimated mean diameters of ~ 0.9, 3.0, and 4.3 nm at 300, 400, and 500°C, respectively. In addition, at 500°C, 10 nm faceted cavities were also observed, which may be voids. Minimum bubble sizes were near the TEM resolution limit for the specimen irradiated at 300°C. Loop and void formation at 300°C may have been suppressed by a high-density of small He bubbles serving as point defect recombination centers. At 400 and 500°C, pre-existing dislocations appear to be preferred He bubble nucleation sites. The addition of a high-density of nano-scale Y-Ti-O particles to a ferritic matrix effectively trapped He atoms and suppressed bubble growth. Additional work is needed to confirm that specimen preparation procedures or surface oxides did not influence these results.

References

[1] R. E. Stoller and H. Tanigawa, “Planning of the US-Japan JP-26 Experiment for Irradiation in the HFIR,” Fusion Materials Semiannual Progress Report for Period Ending June 30, 2003, DOE/ER-0313/34 (2003) 142.
[2] K. R. Thoms, D. W. Heatherly, S. H. Kim, R. G. Sitterson, and R. E. Stoller, “Assembly of the US-Japan JP-26 Experiment and Start of Irradiation in the HFIR,” Fusion Materials Semiannual Progress Report for Period Ending December 31, 2003, DOE/ER-0313/35 (2004) 250.
[3] T. Yamamoto, G. R. Odette, N. Hashimoto, D. T. Hoelzer, and H. Tanigawa, “The Transport and Fate of Helium in Nanostructured Ferritic Alloys at Fusion Relevant He/dpa Ratios and dpa Rates,” Journal of Nuclear Materials (submitted).
[4] H. Farrar and B. M. Oliver, “A Mass Spectrometer System to Determine Very Low Levels of Helium in

Small Solid and Liquid Samples," J. Vac. Sci. Technol. A4 (1986) 1740.
[5] B. M. Oliver, J. G. Bradley, and H. Farrar, "Helium Concentration in the Earth's Lower Atmosphere," Geochim. Cosmochim. Acta 48 (1984) 1759.
[6] R. E. Stoller and G. R. Odette, "Analytical Solutions for Helium Bubble Parameters Using a Hard Sphere Equation of State," J. Nucl. Mater. 131 (1985) 118.

MECHANICAL PROPERTIES OF IRRADIATED 9CR-2WVTA STEEL WITH AND WITHOUT NICKEL—R. L. Klueh and M. A. Sokolov (Oak Ridge National Laboratory)

OBJECTIVE

The objective of this work is to develop an understanding of the effect of transmutation helium on the irradiated mechanical properties of ferritic/martensitic steels for fusion applications and to use that knowledge to develop steels with improved properties.

SUMMARY

Tensile and Charpy specimens of normalized-and-tempered ORNL 9Cr-2WVTa reduced-activation steel and that steel composition containing 2% Ni (9Cr-2WVTa-2Ni) were irradiated at 376–405ºC in the Experimental Breeder Reactor (EBR-II) to 23–33 dpa. Steels were irradiated in two tempered conditions: 1 hr at 700ºC and 1 h at 750ºC. The mechanical properties before and after irradiation of the 9Cr-2WVTa-2Ni steel were quite similar to those of the 9Cr-2WVTa steel, indicating no adverse effect of the nickel. Neither of the steels showed excessive hardening or a large increase in ductile-brittle transition temperature.

PROGRESS AND STATUS

Introduction

Displacement damage by neutron irradiation of 9Cr reduced-activation martensitic steels below 425–450ºC hardens the lattice, causing an increase in strength and a decrease in toughness. The effect on impact toughness (embrittlement) is measured in a Charpy test as an increase in the ductile-brittle transition temperature (DBTT) and a decrease in the upper-shelf energy (USE).

Possible effects of helium on hardening and embrittlement are important because large amounts of transmutation helium will form in the ferritic/martensitic steel first wall of a fusion reactor. Nickel-doped 9 and 12 Cr steels have been irradiated in the mixed-spectrum High Flux Isotope Reactor (HFIR) to study the effect of helium on fracture [1]. Helium is formed in a mixed-spectrum reactor by a two-step transmutation reaction between ^{58}Ni and the thermal neutrons in the mixed-neutron spectrum. Irradiation of nickel-doped steels in HFIR causes the simultaneous production of displacement damage and helium in the steel matrix, thus simulating what will happen in a first wall. Results from such irradiation experiments at 400ºC have been interpreted to indicate an effect of helium on embrittlement [1].

More recent irradiation experiments of nickel-doped 9Cr reduced-activation steels at 170–270ºC indicated that nickel-doped steels hardened more than steels without the nickel [2,3]. These results indicated that nickel-doping should be used at $\lesssim$ 300ºC with caution. These hardening effects were well below temperatures where nickel-doped steels were used to indicate helium effects [1].

To more fully understand the effect of nickel, tensile and Charpy properties are reported for the reduced-activation steel ORNL 9Cr-2WVTa and this steel containing 2% Ni (9Cr-2WVTa-2Ni) after irradiation in the Experimental Breeder Reactor (EBR-II) at 376–405ºC.

Experimental Procedure

The nominal composition for the 9Cr-2WVTa steel in wt. % is: Fe-2.0W-0.25V-0.07Ta-0.10C; 9Cr-2WVTa-2Ni had this same composition but with a 2% Ni addition. The steels were produced from a 9Cr-2WVTa steel master alloy. Details on chemical composition, ingot preparation, and plate and sheet fabrication procedures have been published [5].

The steels were irradiated in the normalized-and-tempered condition; normalization involved austenitizing for 0.5 h at 1050ºC in a helium atmosphere, after which they were quickly cooled in flowing helium. Specimens were irradiated in two tempered conditions: 1 h at 700ºC and 1 h at 750ºC.

Tensile specimens 44.5-mm long with a reduced gage section of 20.3 x 1.52 x 0.76 mm were machined from normalized-and-tempered 0.76-mm sheet with gage lengths parallel to the rolling direction. Tests were conducted on irradiated and unirradiated specimens at 400ºC (near the irradiation temperature) in vacuum at a nominal strain rate of 4×10^{-4} s^{-1}.

One-third-size Charpy specimens measuring 3.3 x 3.3 x 25.4 mm with a 0.51-mm-deep 30º V-notch and a 0.05- to 0.08-mm-root radius were machined from normalized-and-tempered 6.4-mm plates. Specimens were machined with the longitudinal axis along the rolling direction and the notch transverse to the rolling direction (L-T orientation). Details of the test procedure for the subsize Charpy specimens have been published [6–8].

Two tensile and six Charpy specimens of each heat-treated condition were irradiated at 376 to 405ºC in the COBRA experiment in EBR-II. Specimens were irradiated to 5.1×10^{26} to 6.9×10^{26} n/m^2 (E > 0.1 MeV), which produced between 23 and 33 dpa. Calculated helium concentrations were between 3 and 6 appm, depending on the dose and composition.

Results

The yield stress [Fig. 1(a)] for 9Cr-2WVTa and 9Cr-2WVTa-2Ni steels given different tempers before and after irradiation indicated that there was little effect of irradiation on strength for the 9Cr-2WVTa for the 700ºC temper and on the 9Cr-2WVTa-2Ni for both tempering conditions. The yield stress of the 9Cr-2WVTa tempered at 750ºC increased after irradiation, but for both tempers, ultimate tensile strength showed little change for the 9Cr-2WVTa. For the 9Cr-2WVTa-2Ni, both the yield stress and ultimate tensile strength showed fairly large decreases-irradiation softening (Table 1).

The negative effect of irradiation on total elongation [Fig. 1(b)] was greater for 9Cr-2WVTa than 9Cr-2WVTa-2Ni. Total elongation of the 9Cr-2WVTa decreased after irradiation for both tempering conditions, but total elongation for the 9Cr-2WVTa-2Ni decreased slightly when tempered at 700ºC and increased when tempered at 750ºC, which reflects the irradiation softening. For both tempering conditions, uniform elongation of 9Cr-2WVTa-2Ni was relatively unchanged after irradiation, while that for 9Cr-2WVTa decreased by ≈ 60% (Table 1).

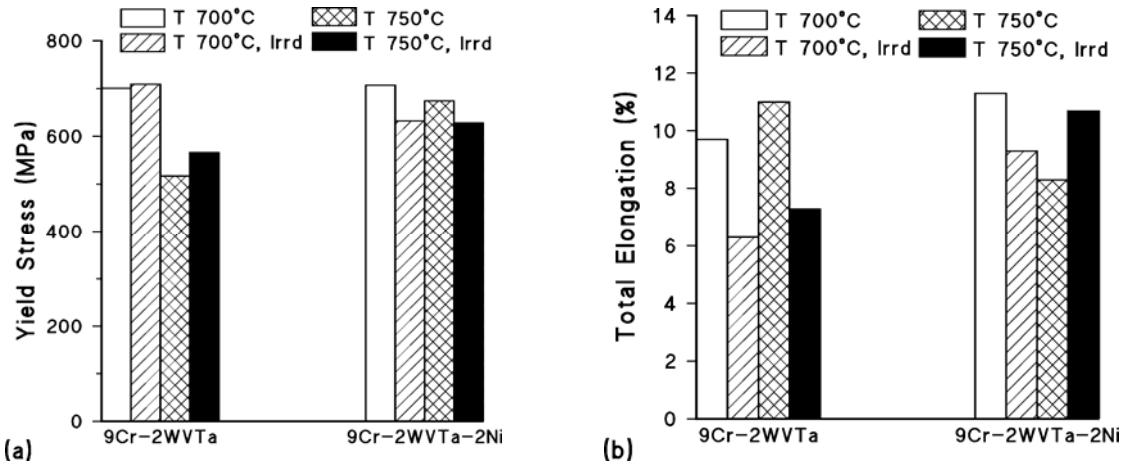

Fig. 1. (a) The yield stress and (b) total elongation of 9Cr-2WVTa and 9Cr-2WVTa-2Ni steels for two different tempering conditions before and after irradiation in EBR-II.

Table 1. Tensile data for unirradiated and irradiated steels tested at 400ºC

Steel	Temper	Irradiation	Strength (MPa)		Elongation (%)	
			Yield	Ultimate	Uniform	Total
9Cr-2WVTa	700ºC	Unirradiated	701	767	2.7	9.7
9Cr-2WVTa	700ºC	390ºC/32.6dpa	709	745	1.1	6.3
9Cr-2WVTa	750ºC	Unirradiated	517	603	3.3	11.0
9Cr-2WVTa	750ºC	390ºC/32.6dpa	567	598	1.3	7.3
9Cr-2WVTa -2Ni	700ºC	Unirradiated	707	798	2.7	11.3
9Cr-2WVTa -2Ni	700ºC	390ºC/32.6dpa	632	666	2.4	9.3
9Cr-2WVTa -2Ni	750ºC	Unirradiated	674	797	2.7	8.3
9Cr-2WVTa -2Ni	750ºC	390ºC/32.6dpa	629	670	3.1	10.7

Nickel has a beneficial effect on the Charpy transition temperature prior to irradiation, and in both heat-treated conditions, the nickel-containing steel had the lowest value (Table 2 and Fig. 2). For the two steels tempered at 700ºC, the 9Cr-2WVTa steel showed the larger shift in DBTT after irradiation; note, however, the 9Cr-2WVTa was irradiated at a lower temperature than the 9Cr-2WVTa-2Ni. For the steels tempered at 750ºC, the 9Cr-2WVTa showed a 17ºC decrease in DBTT after irradiation, while 9Cr-2WVTa-2Ni showed an increase of 39ºC. The final DBTT values for the 9Cr-2WVTa and 9Cr-2WVTa-2Ni were quite similar (-98 and -86ºC), because of the lower DBTT of the latter steel in the unirradiated condition.

Table 2. Charpy data for unirradiated and irradiated steels

Steel	Temper	Irrad. Temp	Dose	Uirrad. DBTT	Irrad. DBTT	DBTT Shift	Uirrad. USE	Irrad. USE
9Cr-2WVTa	700ºC	376ºC	23 dpa	-77ºC	-26ºC	51ºC	9.6 J	7.1 J
	750ºC	390ºC	33 dpa	-81ºC	-98ºC	-17ºC	14.0 J	9.0 J
9Cr-2WVTa-2Ni	700ºC	404ºC	26 dpa	-97ºC	-81ºC	16ºC	9.1 J	7.6 J
	750ºC	390ºC	33 dpa	-125ºC	-86ºC	39ºC	12.8 J	7.1 J

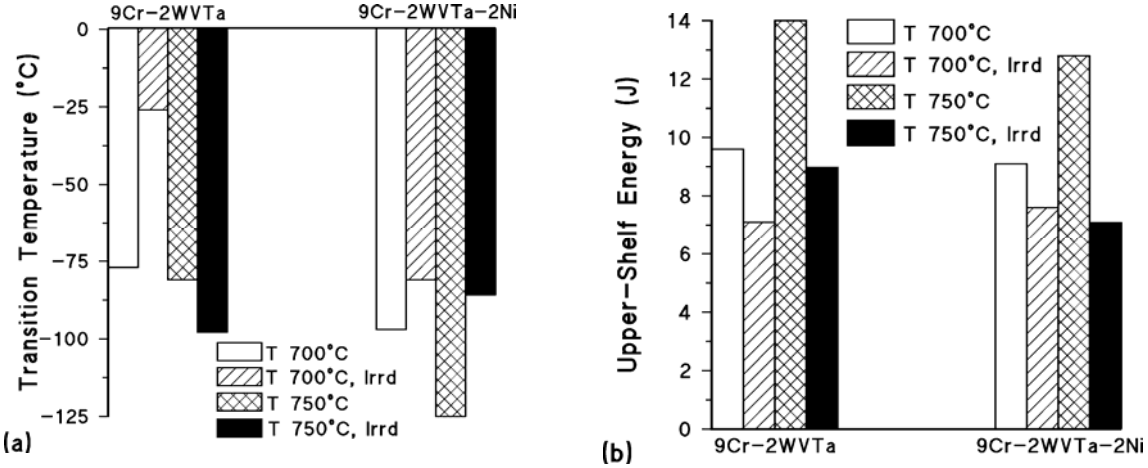

Fig. 2. (a) Transition temperature and (b) upper-shelf energy of 9Cr-2WVTa and 9Cr-2WVTa-Ni steels in unirradiated and irradiated conditions.

Before irradiation, the 9Cr-2WVTa and 9Cr-2WVTa-2Ni had relatively similar USE values [Fig. 2(b)] for similar tempers, with the values after the 750ºC temper being higher than after the 700ºC temper.

Irradiation caused a decrease in the USE, with the largest decreases occurring for the steels with the 750ºC temper. After irradiation, there was relatively little difference in the USE of the steels with and without nickel for similar tempers.

Discussion

It is well known that adding nickel, an austenite stabilizing element, to ferritic steel causes a reduction in Ac_1, the temperature where ferrite begins to transform to austenite when ferritic steel is heated. If the tempering temperature of the 9Cr steels is above Ac_1, then any austenite formed during tempering will transform to martensite during cooling, and the "normalized-and-tempered" steel will contain untempered martensite. It is known that 2% Ni lowers the Ac_1 below 750ºC for modified 9Cr-1Mo (9Cr-1MoVNb) and Sandvik HT9 (12Cr-1MoVW) [9], and because of the similarity of the commercial and reduced-activation steels, it is assumed Ac_1 for 9Cr-2WVTa-2Ni is below 750ºC. This was verified in the tensile tests (Table 1), where the presence of untempered martensite after the 750ºC treatment can be inferred from the unirradiated strength of the 9Cr-2WVTa-2Ni by comparing the strengths of this steel after the 700 and 750ºC tempers with the strengths of the steel without nickel [Fig. 1(a)].

The strengths after irradiation of 9Cr-2WVTa-2Ni tempered at 700 and 750ºC are less than the unirradiated strength (Table 1). There was no change in strength for the 9Cr-2WVTa steel due to irradiation after the 700ºC temper, but for this steel given the 750ºC temper, the yield stress increased slightly, with essentially no change in the ultimate tensile strength. In addition to the effect of nickel on strength, the effect on ductility is remarkable, especially for the steel tempered at 750ºC, where both uniform and total elongation increased after irradiation. This occurred despite the presence of untempered martensite in the microstructure of 9Cr-2WVTa-2Ni. As a further indication of the apparent beneficial effect of nickel, the uniform and total elongation in the nickel-containing steel with the 700ºC temper are significantly less affected by irradiation than the steel without nickel tempered at 700ºC.

The relatively minor hardening—and actual softening—was unexpected from previous experiments where steels with and without nickel were irradiated at ≈ 400ºC [10-12]. An explanation may be found in results from previous studies that found a peak in irradiation hardening with increasing fluence for reduced-activation steels [13] and for commercial-type Cr-Mo steels [14,15]. The previous results indicated that the reduction in irradiation hardening with increasing dose begins to approach the unirradiated value near 30 dpa, which is similar to the dose of the specimens irradiated in the present experiment. An explanation for the strength peak is that irradiation-enhanced recovery offsets irradiation hardening [15].

At first glance, it appears the Charpy properties of the 9Cr-2WVTa-2Ni are better than those of 9Cr-2WVTa after the 700ºC temper. However, this can probably be attributed to the higher irradiation temperature for 9Cr-2WVTa-2Ni—404ºC compared to 376ºC for 9Cr-2WVTa. The irradiation resistance of 9Cr-2WVTa-2Ni was not as good as 9Cr-2WVTa after the 750ºC temper, but even then, the DBTT for the nickel-containing steel was still -86ºC. Thus, after irradiation, not only was the 9Cr-2WVTa-2Ni with the 750ºC temper significantly stronger than 9Cr-2WVTa given a similar temper, it also had better ductility and excellent impact toughness relative to 9Cr-2WVTa. Further investigation of the effect of the untempered martensite in the steel is required.

As discussed earlier, nickel has been added to steels to study helium effects by comparing irradiation effects with and without the nickel addition in a fast reactor, such as EBR-II where very little helium forms, and in a mixed-spectrum reactor, such as HFIR where a transmutation reaction with ^{58}Ni and thermal neutrons produces much higher helium concentrations [1]. Previous irradiations of 12Cr-1MoVW steels with and without nickel indicated that there was no increased hardening or enhanced shift in DBTT for the steel with nickel when irradiated in FFTF, a fast reactor [16]. However, when irradiated in HFIR where over 200 appm He formed, a larger DBTT shift with little difference in hardening was observed for the nickel-containing steel. The additional DBTT shift was attributed to helium [1]. The results of the present fast-reactor irradiations indicated that the nickel did not cause increased hardening or embrittlement in reduced-activation 9Cr-2WVTa steels.

In recent years, data obtained from irradiations at 170–270ºC indicated the addition of nickel to 9Cr steel could produce excess hardening and a larger shift in DBTT, even in a reactor where no significant helium formed [2,3]. There was neither indication that the nickel-containing steel in the present experiment irradiated near 400ºC hardened excessively, nor that the there was a larger DBTT shift caused by the presence of nickel. It appears that irradiation test temperature may be the key cause of the difference in hardening behavior in tests that showed no hardening effect caused by nickel when irradiated in a fast reactor [16] and the tests that showed hardening [2,3]. The low-temperature nickel-enhanced irradiation hardening was attributed to finer defect clusters in the nickel-containing steels [3]. It is probable that such clusters are not stable at the higher temperatures of the present and previous tests [1,16].

Summary and Conclusions

ORNL 9Cr-2WVTa and the steel with 2% Ni were irradiated at 376–404ºC in EBR-II to 23–33 dpa (3–6 appm He). The steels showed little hardening in a temperature regime where hardening is normally observed. The limited hardening resulted in only minor changes in DBTT. Results indicated that there were no adverse effects of nickel, which is contrary to recent low-temperature irradiations that showed nickel causes excess hardening. Differences with these previous investigations are probably due to differences in irradiation temperatures (< 300ºC in previous work and 376–404ºC in present investigation). The minor hardening and minor change in Charpy properties may be an indication of the maximum in hardening with dose observed in ferritic steels that has been attributed to softening due to irradiation-enhanced recovery offsetting irradiation hardening.

References

[1] R. L. Klueh and D. J. Alexander, J. Nucl. Mater. 187 (1992) 60.
[2] R. Kasada, A. Kimura, H. Matsui, and M. Narui, J. Nucl. Mater. 258–263 (1998) 1199.
[3] A. Kimura, Report of IEA Workshop on Reduced-Activation Ferritic/Martensitic Steels, JAERI-Conf 2001-007, p. 348.
[4] R. L. Klueh and P. J. Maziasz, Metall. Trans. 20A (1989) 373.
[5] R. L. Klueh, D. J. Alexander, and M. Rieth, J. Nucl. Mater. 273 (1999) 146.
[6] D. J. Alexander, R. K. Nanstad, W. R. Corwin, and J. T. Hutton, in A. A. Braun, N. E. Ashbaugh, and F. M. Smith (eds.), Applications of Automation Technology to Fatigue and Fracture Testing, ASTM STP 1092, American Society for Testing and Materials, Philadelphia (1990) 83.
[7] D. J. Alexander and R. L. Klueh, in J. M. Molt (ed.), Charpy Impact Test: Factors and Variables, ASTM STP 1072, American Society for Testing and Materials, Philadelphia (1990) 179.
[8] M. A. Sokolov and R. K. Nanstad, in D. S. Gelles, R. K. Nanstad, A. S. Kumar, and E. A. Little (eds.), Effects of Radiation on Materials: 17th International Symposium, ASTM STP 1270, American Society for Testing and Materials, Philadelphia (1996) 384.
[9] R. L. Klueh, J. M. Vitek, and M. L. Grossbeck, in Effects of Radiation on Materials, ASTM STP 782, American Society for Testing and Materials, Philadelphia (1982), 648.
[10] R. L. Klueh and J. M. Vitek, J. Nucl. Mater. 132 (1986) 27.
[11] R. L. Klueh and J. M. Vitek, J. Nucl. Mater. 137 (1986) 44.
[12] R. L. Klueh and D. J. Alexander, Effects of Radiation on Materials: 18th International Symposium, ASTM STP 1325, American Society for Testing and Materials, Philadelphia (1999), 911.
[13] A. Kohyama, A. Hishinuma, D. S. Gelles, R. L. Klueh, W. Dietz, and K. Ehrlich, J. Nucl. Mater. 233–237 (1996) 138.
[14] R. L. Klueh and D. J. Alexander, J. Nucl. Mater. 253–258 (1998) 1269.
[15] V. S. Khabarov, A. M. Dvoriashin, and S. I. Porollo, J. Nucl. Mater. 233–237 (1996) 236.
[16] W. R. Corwin, J. M. Vitek, and R. L. Klueh, J. Nucl Mater. 149 (1987) 312.

NEW NANO-PARTICLE-STRENGTHENED FERRITIC/MARTENSITIC STEELS BY CONVENTIONAL THERMOMECHANICAL TREATMENT—R. L. Klueh and N. Hashimoto (Oak Ridge National Laboratory)

OBJECTIVE

The objective of this work is to develop new ferritic/martensitic steels for fusion applications.

SUMMARY

Martensitic steels are considered for structural applications for fusion power plants, but they are limited by strength to temperatures of 550–600ºC. For increased plant efficiency, steels for operation at 650ºC and higher are sought. Based on the science of precipitate strengthening, a thermo-mechanical treatment (TMT) was developed that increased the strength from room temperature to 700ºC of commercial nitrogen-containing steels and new steels designed for the TMT. At 700ºC an increase in yield stress of 80 and 200% was observed for a commercial steel and a new steel, respectively, compared to commercial steels after a conventional heat treatment. Creep-rupture strength was similarly improved. Depending on the TMT, precipitates in the steels were up to eight-times smaller at a number density four orders of magnitude greater than those in a normalized-and-tempered steel.

PROGRESS AND STATUS

Introduction

Reduced-activation ferritic/martensitic steels are at present considered to be the only viable structural material for fusion power plants [1]. A major shortcoming of the steels is high-temperature strength, which places a limit on maximum service temperature capability of 550–600ºC. This has led to work to develop oxide dispersion-strengthened (ODS) steels [2-4]. These steels, strengthened by small oxide particles, are produced by complicated and expensive mechanical-alloying, powder-metallurgy techniques, as opposed to conventional processing. This paper presents the science and technology of the development of new and different dispersion-strengthened steels using conventional processing techniques for applications at 650ºC and higher.

Concept of New Steels

For high elevated-temperature strength, it is necessary to “build” obstacles to dislocation motion into the matrix. In ODS steels, the obstacles are a high number density of small oxide particles. A normalized-and-tempered (N&T) reduced-activation or commercial 9 or 12% Cr elevated-temperature steel, such as commercial modified 9Cr-1Mo (nominal composition Fe-9.0Cr-1.0Mo-0.20V-0.08Nb-0.05N-0.10C, composition in wt %), consists of martensite laths (elongated subgrains with average width ≈ 0.25–0.5 μm) with a relatively high dislocation density (10^{13}-10^{15} m^{-2}); obstacles to dislocation motion are provided by precipitates on prior-austenite grain boundaries, on lath boundaries, and in the matrix. Dominant precipitates are “large” (60–200 nm) $M_{23}C_6$ particles located mainly on lath boundaries and prior-austenite grain boundaries. Smaller (20–80 nm) MX precipitates, which are present at a low number density, are thought to provide most of the precipitate strengthening. Figure 1 shows the microstructure for N&T modified 9Cr-1Mo steel with average particle size and number density of $M_{23}C_6$ estimated at 130–150 nm and 3-6 x 10^{19} m^{-3}, respectively, and MX estimated at 32 nm and 7-8 x 10^{18} m^{-3}, respectively [5].

Since the MX particles are the smallest and form in the matrix, most of the precipitation strengthening effect in 9–12Cr steels is attributed to them [6]. That strengthening effect is limited, however, because of their small number density and relatively large size. In nitrogen-containing high-temperature steels with vanadium and niobium, MX has been determined to be a combination of vanadium- and nitrogen-rich nitrides containing some carbon, niobium-rich carbides, and/or carbonitrides [7,8].

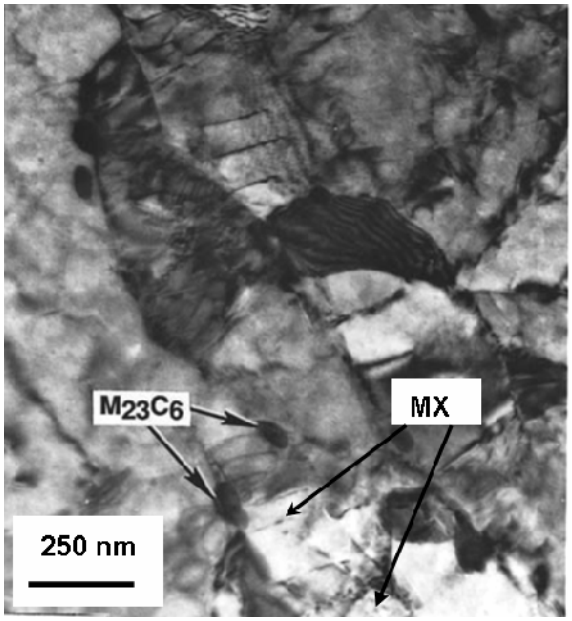

Fig. 1. Transmission electron microscopy photomicrograph of modified 9Cr-1Mo steel after a conventional normalizing-and-tempering heat treatment.

Since a strength contribution in nitrogen-containing steels is obtained from vanadium nitride, the objective of this work was to develop a steel that maximized the MX strengthening capability. Based on computational thermodynamics calculations, steel compositions were determined that have vanadium and nitrogen concentrations to produce a sufficient amount of precipitate for increased strength if precipitates have the correct size and number density. To produce such a distribution, it was reasoned that it would be necessary to provide heterogeneous precipitation sites on which a fine distribution of MX precipitates could form. Dislocations were the chosen sites, and they were introduced by hot working. A similar procedure was previously used to strengthen a steel with TiC as the MX precipitate [9,10].

Experimental Procedure

A thermomechanical treatment (TMT) was developed to produce a fine dispersion of nano-sized particles in nitrogen-containing steels. Because facilities were not available to produce nitrogen-containing steels, the TMT was first applied to 25.4-mm plates of nitrogen-containing commercial Cr-MoVNb-type steels. Later the process was used on small heats of steel compositions developed especially for the TMT.

The TMT involves heating the steel to 1050–1300ºC to convert ferrite to austenite and dissolve existing precipitates, after which it is cooled to a hot-working temperature (700–1000ºC). Hot rolling the plates introduces a high density of dislocations that act as nucleation sites for a fine distribution of MX (vanadium- or niobium-rich nitride and/or carbonitride) precipitates. Finally, the steel is annealed to grow precipitates to optimum size for hardening. Air cooling converts the austenite matrix to martensite.

Results and Discussion

Microstructure

The effect of a TMT on microstructure can be controlled by changing (1) austenitization temperature and time, (2) hot-working temperature, (3) amount of reduction by hot working, and (4) annealing temperature and time.

Application of a TMT to 25.4-mm-thick plate of modified 9Cr-1Mo produced a dramatically different microstructure from the N&T steel (Fig. 2). Transmission electron microscopy (TEM) indicated that, depending on the TMT, average MX particle size was up to four times smaller (7–8 nm) and the number density up to three orders of magnitude greater (2–9 x $10^{21}m^{-3}$) than for the N&T steel. Note that precipitates in Fig. 2 are somewhat larger, as they were chosen to demonstrate the high-number density; because of their size, they were easily viewed under bright-field conditions. The commercial 12% Cr steel HCM12A (Fe-12.0Cr-2.0W-0.40Mo-1.0Cu-0.30Ni-0.25V-0.05Nb-0.06N-0.10C) was given two versions of the new TMT, one rolled at 750ºC and the other at 800ºC (Fig. 3). In contrast to modified 9Cr-1Mo steel, no fine precipitates were visible by TEM. After tempering 1 h at 750ºC, however, fine precipitates (4.2 nm, 2.4 x $10^{21}m^{-3}$) were detected by dark-field TEM in the one rolled at 800ºC. Evidently, the higher vanadium and nitrogen in HCM12A resulted in precipitates that were too fine to observe by TEM. Evidently, tempering coarsened the precipitates in the steel rolled at 800ºC so they were visible by TEM.

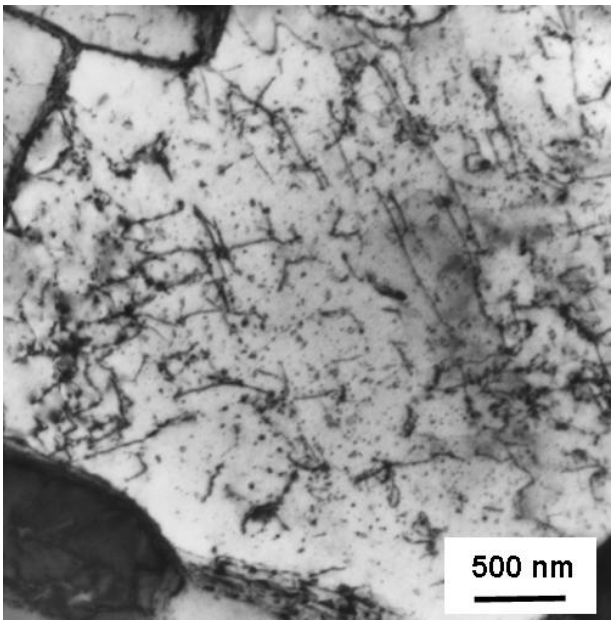

Fig. 2. Electron microscopy photomicrograph of modified 9Cr-1Mo steel after the new thermo-mechanical treatment.

Based on thermodynamic calculations, small (400-g) heats of new compositions were produced in an effort to maximize the effect of the TMT. Besides optimizing the precipitate distribution, another objective of the new steels was minimization of the number of large $M_{23}C_6$ particles lowering carbon. To demonstrate the effect of nitrogen, two new steels with nominal composition Fe-9.0Cr-1.0Mo-1.0Ni-0.30V-0.07Nb-0.05C were compared, one containing 0.035% N (9Cr-MoNiVNbN4) and the other 0.065% N (9Cr-MoNiVNbN5). For both, average MX precipitate size was smaller and number density greater than for the best achieved with modified 9Cr-1Mo given the TMT: about 4.0 nm, 1.0 x 10^{22} m^{-3} and 3.3 nm, 7.2 x 10^{22} m^{-3} for 9Cr-MoNiVNbN4 and 9Cr-MoNiVNbN5, respectively—about 8 times smaller at a number density almost four orders of magnitude greater than MX in N&T modified 9Cr-1Mo.

Mechanical Properties

Tensile properties were determined on modified 9Cr-1Mo after a TMT at 750ºC, and they were compared to average values for N&T steel. After the TMT, the 0.2% yield stress and ultimate tensile strength from room temperature to 800ºC were considerably greater than those for N&T modified 9Cr-1Mo steel, with the relative difference increasing with increasing test temperature. At 600 and 700ºC, the yield stress after the TMT was 61 and 88% greater than for the N&T steel. Total elongation after the TMT was less

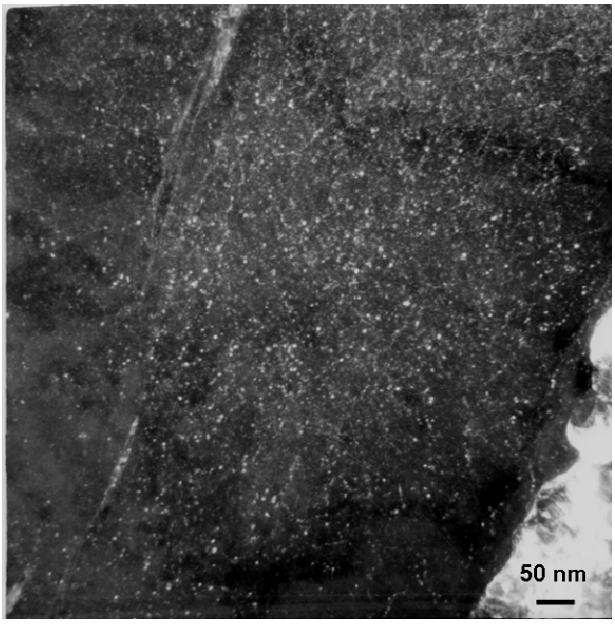

Fig. 3. Dark-field transmission electron microscopy image of the commercial 12% Cr HCM12A steel after a TMT plus temper.

than in the N&T condition, but given the normal trade off of strength and ductility, ductility was excellent with total elongations of 16 and 22% at 600 and 700ºC, respectively.

The 12% Cr steel HCM12A after the TMTs at 750ºC and 800ºC followed by a temper showed large increases in yield stress relative to N&T HCMA12A: 47 and 64% increases at 600 and 700ºC, respectively, with little difference between the two TMTs. An increase of 22% was observed at 800ºC. The strength of HCM12A with the TMT plus temper was greater than that of modified 9Cr-1Mo steel with just a TMT, a reflection of smaller precipitates at a higher number density in HCM12A. The strength up to 700ºC of HCM12A was greater than PM 2000, the best available commercial ODS steel (Fig. 4).

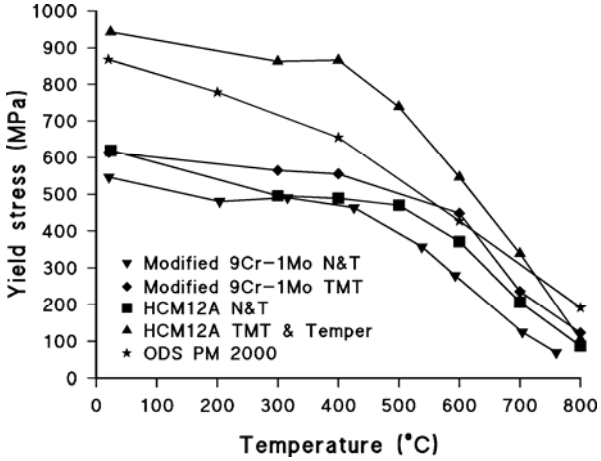

Fig. 4. Yield stress as a function of temperature for modified 9Cr-1Mo steel after a conventional normalize-and-temper (N&T) and a TMT for HCM12A after N&T and a TMT and temper, and for the best commercial ODS steel PM 2000.

To demonstrate the excellent strength properties of new steel compositions developed to take advantage of the TMT, yield stress of the new 9Cr-MoNiVNbN (0.042% N) composition was compared to an experimental ODS steel labeled 12YWT (Fe-12.0Cr-2.5W-0.4Ti-0.25Y_2O_3). The strength of this ODS steel was superior to that of available commercial ODS steels [4]. The TMT produced yield stress values comparable to those of 12YWT up to 700ºC [Fig. 5(a)]. Total elongations for 9Cr-1MoNiVNbN in the TMT condition and the TMT-and-tempered condition were also comparable to those of 12YWT [Fig. 5(b)].

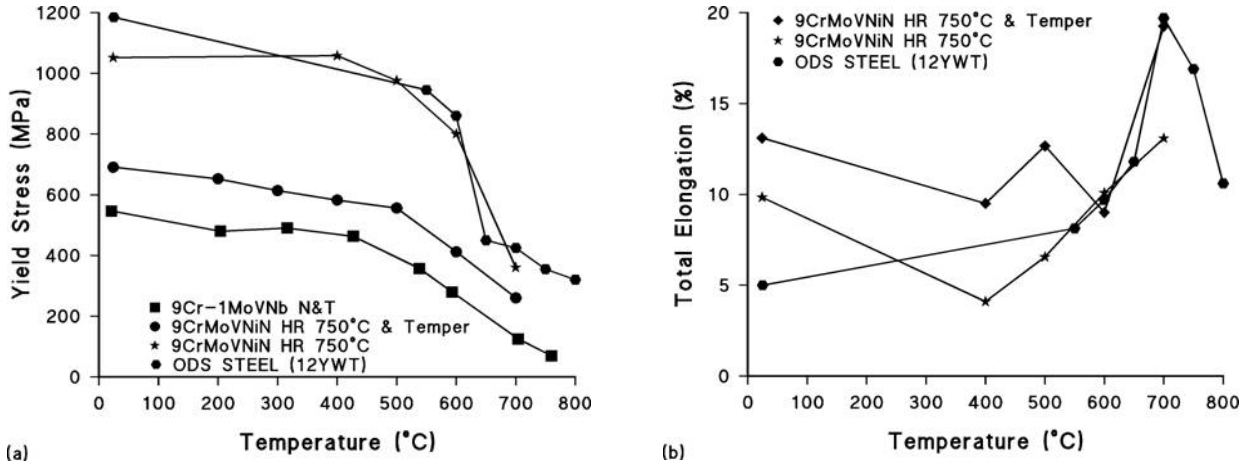

Fig. 5. (a) Yield stress and (b) total elongation of new 9CrMoVNiN steel after a TMT and after a TMT and temper compared to normalized and tempered (N&T) modified 9Cr-1Mo steel and the high-strength experimental ODS steel 12YWT.

In Fig. 6, creep curves for tests at 138 MPa at 650ºC are shown for modified 9Cr-1Mo after an N&T and a TMT. Rupture life for the steel with TMT was ≈ 80 times greater than for the N&T steel. Even with this large difference in strength, fracture ductility was excellent; total elongation was 21%.

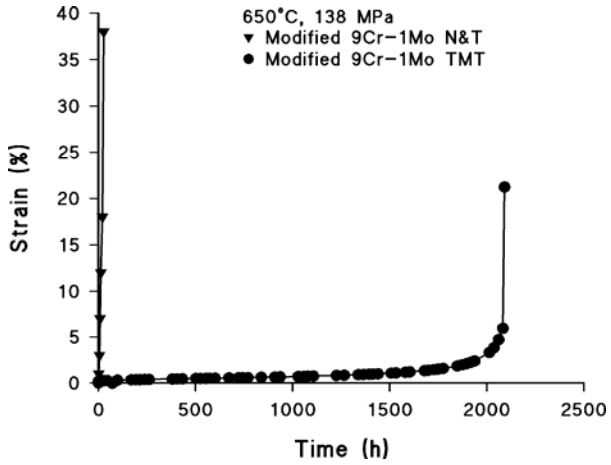

Fig. 6. Creep curves of modified 9Cr-1Mo in the normalized and tempered (N&T) condition and after a thermomechanical treatment tested at 138 MPa at 650ºC.

Creep rupture curves for modified 9Cr-1Mo after a TMT indicated a significant increase in strength relative to N&T modified 9Cr-1Mo [11] and the reduced-activation steels F82H [12] and EUROFER 97 [13] (Fig. 7). After the TMT, rupture life extrapolated to 10000 h was also about 80 times that of the N&T steel. Extrapolation to 100,000 h would give 10^5 h rupture stresses of ≈ 60 and ≈ 40 MPa for the TMT and N&T steels, respectively. Obviously, the validity of such extrapolations will depend on stability of the precipitates produced by the TMT, for which longer-time tests are required. As observed above, HCM12A and the new 9Cr-1MoNiVNbN had higher strengths after the TMTs than modified 9Cr-1Mo with a TMT, so they should have significantly higher creep strengths.

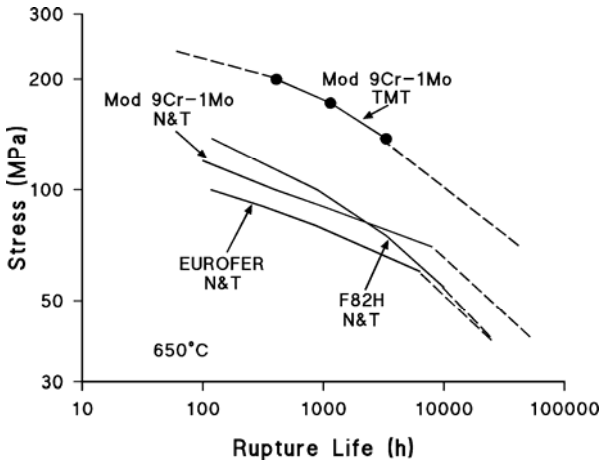

Fig. 7. Creep-rupture curves at 650ºC for modified 9Cr-1Mo steel after a conventional normalize and temper (N&T) and after three thermomechanical treatments.

It needs to be emphasized that although it was demonstrated that the commercial and new steels with TMT have excellent mechanical properties, further work is required to validate these materials for future applications. Likewise, larger heats of new steels with optimum compositions are required for the development of the steels to their ultimate potential.

Summary and Conclusions

A thermomechanical treatment procedure was devised to produce a dense dispersion of nano-scale MX precipitates in vanadium- and nitrogen-containing elevated-temperature steels. The new TMT involves three distinct steps, each of which involves a range of conditions that need to be optimized to produce the most favorable precipitate microstructure for elevated-temperature strength. Along with optimization of the new TMT process, steel compositions that fully exploit the TMT need to be developed further. The initial efforts on the small heats of new steels indicated that it is possible to develop compositions with properties that are significant improvements over the N&T commercial or reduced-activation ferritic/martensitic steels.

The high number density of precipitates produced by the new TMT using conventional processing methods is similar to particle number densities in the best commercial ODS steels produced by much more complicated and expensive powder-metallurgy/mechanical-alloying procedures. Although the nitrogen precipitates will not be as stable as the oxides in the ODS steels, dispersion strengthening by the nitrogen-rich MX precipitates should allow such steels to be used at 650–700ºC, a significant improvement over upper-use temperatures of 550–600ºC for N&T reduced-activation steels now available.

References

[1] R. L. Klueh and D. R. Harries, High-Chromium Ferritic and Martensitic Steels for Nuclear Applications, American Society for Testing and Materials, West Conshohocken, Pa. (2001).
[2] S. Ukai and M. Fujiwara, J. Nucl. Mater. 307–311 (2002) 749.
[3] A. Alamo, H. Regle, and J. L. Bechade, in Novel Powder Processing: Advances in Powder Metallurgy & Particulate Materials, Vol. 7, Metal Powder Industries Federation, Princeton, N.J. (1992) 169.
[4] R. L. Klueh, P. J. Maziasz, I. S. Kim, L. Heatherly, D. T. Hoelzer, N. Hashimoto, E. A. Kenik, and K. Miyahara, J. Nucl. Mater. 307–311 (2002) 773.
[5] N. Hashimoto and R. L. Klueh, J. Nucl. Mater. 305 (2002) 153.
[6] L. Lundin, S. Fällman, and H.-O. Andrén, Mater. Sci. Technol. 13 (1997) 233.
[7] M. Hättestrand, M. Schwind, and H.-O. Andrén, Mater. Sci. Eng. A 250 (1998) 27.
[8] V. Foldyna, Z. Kubon, V. Vodárek, and J. Purmenský, in R. Viswanathan, W. T. Bakker, and J. D. Parker (eds.), Proceedings of the 3rd EPRI Conference on Advanced Materials Technology for Fossil Plants, Gomer Press, Llandysul, Ceredigion, United Kingdom (2001) 89.
[9] R. F. Buck, Adv. Mater. Process. 150 (8) (1996) 27.
[10] R. L. Klueh, N. Hashimoto, R. F. Buck, and M. A. Sokolov, J. Nucl. Mater. 283–287 (2000) 697.
[11] G. Guntz, M. Julien, G. Kottmann, F. Pellicani, A. Pouilly, and J. C. Vaillant, The T91 Book, Vallourec Industries, France (1990) 52.
[12] K. Shiba, H. Tanigawa, T. Nakata, and Y. Kohno, Journal of Nuclear Materials (submitted).
[13] R. Lindau and M. Schirra, Fusion Eng. Des. 58–59 (2001) 781.

4.0 COPPER ALLOYS

EFFECT OF HEAT TREATMENTS ON PRECIPITATE MICROSTRUCTURE AND MECHANICAL PROPERTIES OF A CuCrZr ALLOY—D. J. Edwards (Pacific Northwest National Laboratory),* B. N. Singh (Risø National Laboratory, Denmark), and S. Tähtinen (VTT Industries, Finland)

EXTENDED ABSTRACT (presented at the 12th International Conference on Fusion Reactor Materials, Santa Barbara, California, December 4–9, 2005)

Experimental investigations have demonstrated that neutron irradiation of prime aged CuCrZr at temperatures below ~ 473K leads to a substantial increase in strength, formation of a tensile instability, and a severe loss of work hardening ability and uniform elongation [1, 2]. The precipitates in this alloy are unable to inhibit localized deformation via dislocation channeling in the irradiated materials, namely because the precipitates are small Guinier-Preston (G-P) zones too weak to effectively prevent or hinder dislocation motion once dislocations become mobile at stress concentrations. It was therefore decided to coarsen the precipitate microstructure by annealing the prime aged CuCrZr so that larger and hopefully stronger precipitates, albeit in lower density, might prove more effective at preventing the initiation of plastic flow localization by resisting dislocation motion. As a starting point, we hoped to achieve a precipitate microstructure in the over-aged CuCrZr that was coarsened to a level near that of the GlidCop Al25, that is, particles with an average size of ~ 7–8 nm with a density of ~ 10^{22} particles per m^{-3}.

A CuCrZr alloy (Cu-0.73%Cr-0.14%Zr) supplied by Outokumpu Oyj (Finland) was solution annealed at 1233K for 3 h, water quenched and then prime aged (PA) at 733K for 3 h. After prime ageing the specimens were given further heat treatments to modify the precipitate microstructure. In the first series, the prime aged specimens were annealed in vacuum at 873K for 1, 2, and 4 h. In the second series a number of prime aged specimens were annealed at 973K and 1123K for 4 h. All specimens were water quenched after final annealing at the various temperatures.

The microstructures of each heat treatment condition were characterized using a JEOL 2000FX transmission electron microscope (TEM). Specimen preparation and the imaging conditions used to characterize the microstructure of these samples have been described in previous work [1,2]. As expected, heat treatments after prime ageing led to significant coarsening of the prime aged precipitate microstructure. The annealing replaced the G-P zones with precipitates thought to be predominately incoherent Cr-rich particles, which are commonly observed in this alloy [3–6]. As the data presented in Table 1 shows, annealing for 1–2 hours at 873K produced a significant coarsening that was accelerated when the annealing time was increased to 4 hours. Increasing the annealing temperature to 973K for 4 hours produced an even lower density of larger precipitates, whereas annealing at 1123K appeared to solution anneal the material and remove all but the sub-micron Cr inclusions, which were probably present in the original solution annealed material.

Table 1. Measured size and densities of precipitates

Heat Treatment	Precipitate Size (nm)	Precipitate Density (x 10^{23} m^{-3})
Prime aged (PA)	2.2	2.6
PA + 873K/1 h	8.7	0.17
PA + 873K/2 h	9.4	0.18
PA + 873K/4 h	21.3	0.015
PA + 973K/4 h	46.4	0.007
PA + 1123K/4 h	Precipitates removed (effectively solution annealed)	----------

Because the over-aged condition of 873K at 1–4 hours yielded a reasonable density of larger, and presumably stronger, particles than found in the prime aged condition, samples given these two over-aging treatments were selected for inclusion in a neutron irradiation experiment. A number of tensile and fracture toughness specimens of the CuCrZr alloy in the prime aged condition and the 1 or 4 hour over-aging treatment were irradiated with fission neutrons in the BR-2 reactor at Mol (Belgium) at 373 and 573K to a displacement dose level of ~ 0.3 dpa (displacement per atom). The damage rate during irradiation was ~ 6 x 10^{-8} dpa s^{-1}.

The tensile and fracture toughness results shown in Figs. 1 through 4 demonstrate that the coarsening of the precipitates due to over-aging produced a significant decrease in the tensile strength and some increase in fracture toughness properties of the alloy. The irradiation at 333K to a dose level of ~ 0.3 dpa caused significant hardening both in the prime aged and over-aged specimens while severely reducing the ductility and work hardening. The tensile response and post-deformation microstructure of the irradiated alloy indicate that the lower density of larger particles produced by over-aging at 873K for one hour improved the plastic instability and led to some increase in the overall ductility. The over-aging heat treatment PA+873K/1 hr also improved the fracture toughness properties when compared to those of the prime aged CuCrZr alloy in irradiated conditions at 333 and 573K.

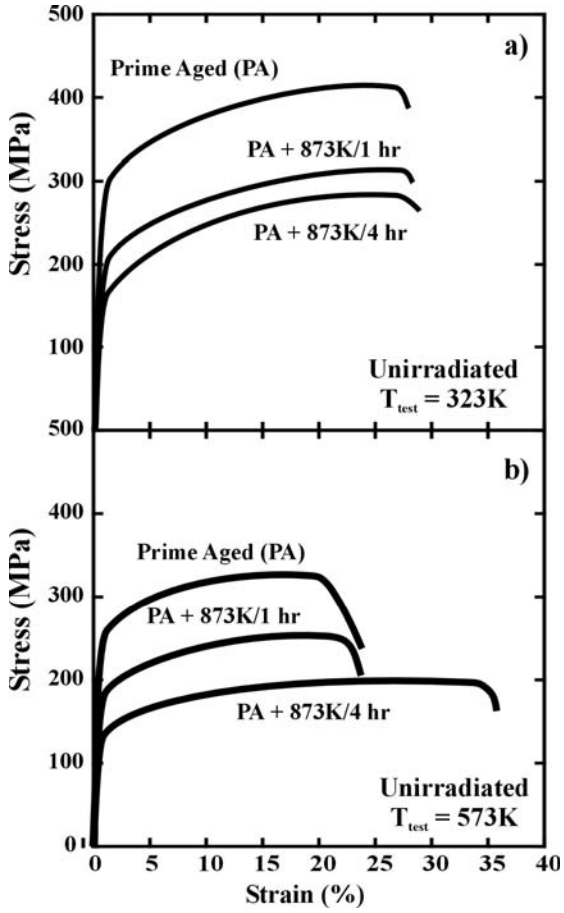

Fig. 1. Stress-strain curves for CuCrZr alloy in the prime-aged condition and after annealing at 873K for 1 and 4 hours and tensile tested at (a) 323K and (b) 573K.

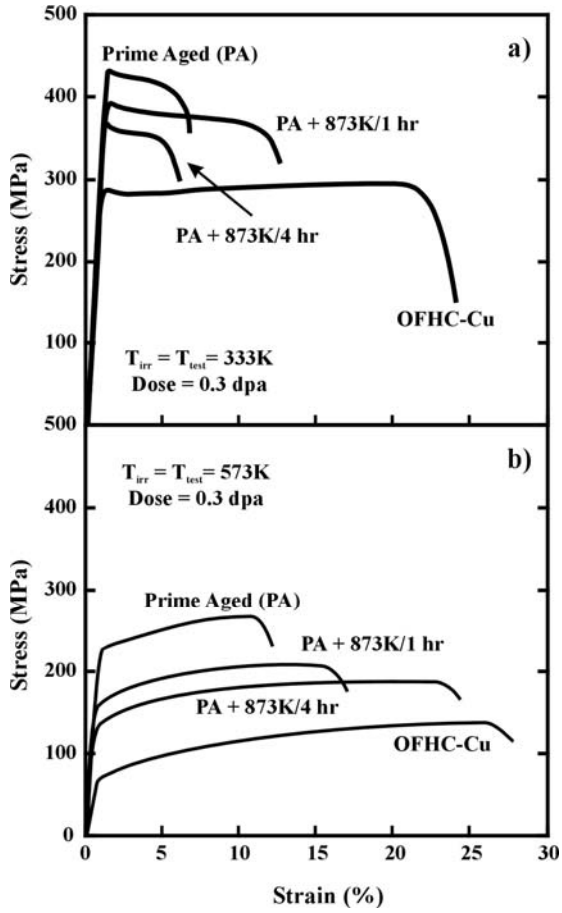

Fig. 2. Stress-strain curves for CuCrZr alloy irradiated to a dose level of ~ 0.3 dpa in the prime aged and over-aged at 873K for 1 h and 4 h conditions and tensile tested at (a) 333K and (b) 573K.

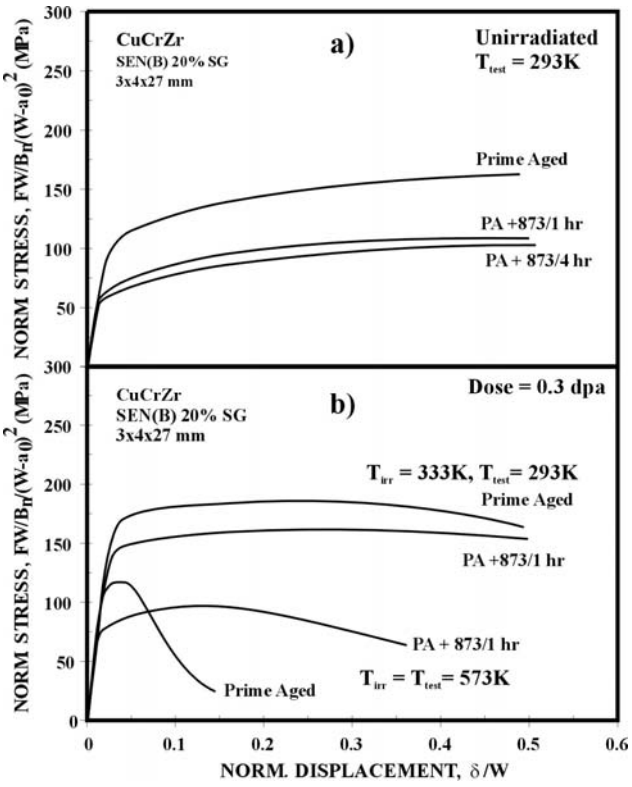

Fig. 3. Normalised load-displacement curves for CuCrZr alloy (a) in unirradiated and prime aged and over-aged (at 873K for 1 h and 4 h) conditions at 293K and (b) irradiated at 333K and 573K and tested at 293K and 573K, respectively, to a dose level of ~ 0.3 dpa in the prime aged and over-aged (at 873K for 1 h) conditions.

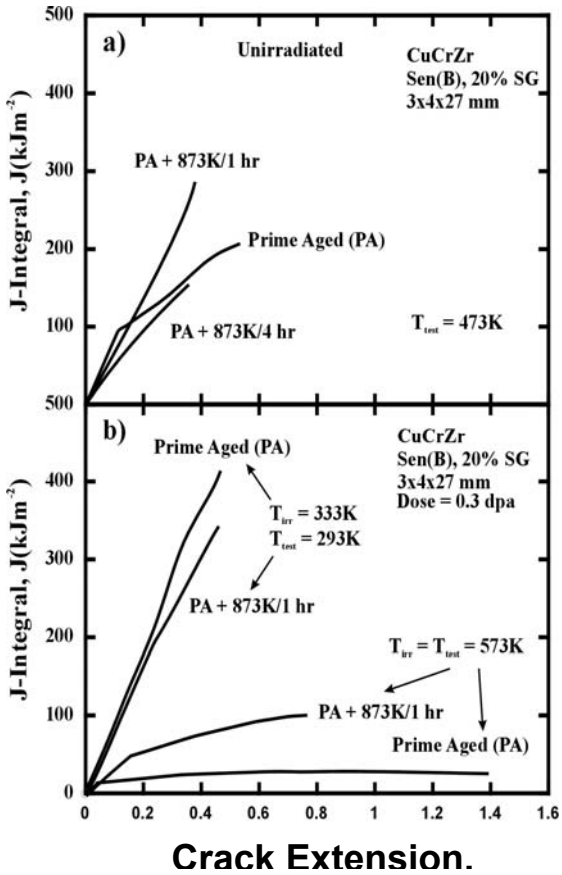

Fig. 4. Fracture resistance curves for CuCrZr alloy (a) in unirradiated and prime aged and over-aged (at 873K for 1 h and 4 h) conditions at 473K and (b) irradiated at 333K and 573K and tested at 293K and 573K, respectively, to a dose level of ~ 0.3 dpa in the prime aged and over-aged (at 873K for 1 h) conditions.

Despite these positive changes in the mechanical response, microstructurally the material was found to deform by a dislocation channeling in all of the conditions studied. These results suggest that some improvement in the mechanical response of irradiated CuCrZr can be realized if care is taken to alter the final thermomechanical treatment to introduce a precipitate dispersion that is coarser than that produced by prime ageing while still maintaining a sufficient precipitate structure to inhibit the motion of dislocations within the channels.

Acknowledgements

The present work was partly funded by the European Fusion Technology Programme. The authors wish to thank B. F. Olsen for his technical assistance. D. J. Edwards would like to thank Risø National Laboratory for the support and assistance during his visit. His work was partly supported by the U.S. Department of Energy under contract DE-AC06-76RLO 1830 with the Battelle Memorial Institute at the Pacific Northwest National Laboratory.

References

[1] B. N. Singh, D. J. Edwards, and P. Toft, J. Nucl. Mater. 238 (1996) 244.
[2] D. J. Edwards, B. N. Singh, P. Toft, and M. Eldrup, J. Nucl. Mater. 258–263 (1998) 978.
[3] B. N. Singh, D. J. Edwards, M. Eldrup, and P. Toft, J. Nucl. Mater. 249 (1997) 1.
[4] N. Y. Tang, D. M. R. Taplin, and G. L. Dunlop, Mater. Sci. Technol. 1 (1985) 270.
[5] Z. Rdzawski and J. Strobrawa, Scr. Metall. 20 (1986) 341.
[6] R. W. Knights and P. Wilkes, Metall. Trans. 4 (1973) 2389.

5.0 REFRACTORY METALS AND ALLOYS

FLOW AND FRACTURE BEHAVIOR OF MOLYBDENUM NEUTRON-IRRADIATED AT 80°C— M. Li, T. S. Byun, N. Hashimoto, L. L. Snead, and S. J. Zinkle (Oak Ridge National Laboratory)

SUMMARY

Low carbon arc cast (LCAC) molybdenum was neutron irradiated at 80°C in the high flux isotope reactor (HFIR) to fluences between 2×10^{21} and 8×10^{24} n/m^2 (E > 0.1 MeV), corresponding to nominal displacement doses of 7.2×10^{-5}, 7.2×10^{-4}, 7.2×10^{-3}, 7.2×10^{-2}, and 0.28 dpa. Tensile tests were performed on unirradiated and irradiated specimens at 100, 22, -25, and -50°C at a strain rate of 1.1×10^{-3} s^{-1}. The fracture surfaces of tensile-tested specimens were examined by scanning electron microscopy. The paper examined the temperature and dose dependence of yield stress, post-yield strain hardening and tensile ductility. The fracture modes of irradiated Mo were also discussed.

PROGRESS AND STATUS

Experimental Procedure

The material examined was low carbon arc cast (LCAC) molybdenum (Ingot No. 50814) provided by Bettis Atomic Power Laboratory. The nominal chemical composition is given in Table 1. Subsize SS-3 tensile specimens were electron-discharge-machined (EDM) from a cold-rolled 0.5 mm thick sheet. The geometry and dimensions of SS-3 tensile specimens are shown in Fig. 1. Following machining specimens were annealed at 1200°C for 1 h in a high vacuum and furnace cooled. The annealed microstructure has equaxied grains with a grain size of 70 μm. Before irradiation SS-3 tensile specimens were mechanically polished with 2400 grit SiC abrasive paper.

Table 1. The nominal chemical composition of LCAC Mo

Mo (%)	Fe (ppm)	Ni (ppm)	Si (ppm)	C (ppm)	O (ppm)	N (ppm)
> 99.95	100	2	100	100	15	20

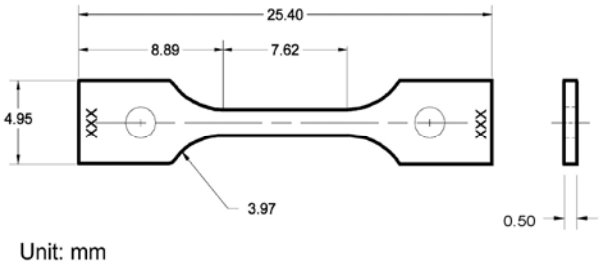

Fig. 1. Dimensions of SS-3 type sheet tensile specimens.

Irradiation of specimens was carried out in the hydraulic tube (HT) facility of the high flux isotope reactor (HFIR) at the ORNL. Four bare SS-3 tensile specimens were loaded in each perforated rabbit capsule allowing contact with the flowing coolant in the hydraulic tube to maintain the specimen temperature at ~ 80°C. Specimens were irradiated to neutron fluences of 2×10^{21}, 2×10^{22}, 2×10^{23}, 2×10^{24}, and 8×10^{24} n/m^2 (E > 0.1 MeV), corresponding to displacement damage levels of 7.2×10^{-5}, 7.2×10^{-4}, 7.2×10^{-3}, 7.2×10^{-2}, and 0.28 dpa. Tensile tests were conducted on unirradiated and irradiated specimens at -50, -25, 22, and 100°C on a screw-driven machine. All tensile tests were performed at a crosshead speed of 0.02 in/min, corresponding to a strain rate of 1.1×10^{-3} s^{-1}. Tensile tests at 20 and 100°C were conducted in air, and -25 and -50°C tests were carried out in a mixed air and cold nitrogen environment. Load and displacement data

were recorded and used to determine stress-strain curves and tensile properties. The engineering stress-strain curves were corrected by the theoretical Young's modulus of molybdenum to eliminate any discrepancy of tests from machine stiffness and specimen loading. The correction of stiffness was made using the following equation:

$$\varepsilon_p = \varepsilon_t - \varepsilon_e = \varepsilon_t - \frac{\sigma}{E_0}$$
$$\varepsilon_t^{corr} = \varepsilon_t - \frac{\sigma}{E_0} + \frac{\sigma}{E} \quad (1)$$

where ε_p is the plastic strain, ε_t the measured total strain, ε_e the measured elastic strain, ε_t^{corr} the total strain corrected by the Young's modulus, σ the applied stress, E_o the machine stiffness, and E the Young's modulus. The machine stiffness, E_o, was determined from the linear portion of the load-displacement curves. The corrected engineering stress-strain curves were checked by comparing the values of tensile properties such as yield stress, ultimate tensile strength, fracture stress and elongations obtained from the corrected curves and non-corrected curves. After tensile testing, fractographic examinations were performed by scanning electron microscopy (SEM).

RESULTS

Engineering Stress-Strain Curves

Tensile tests were carried out at 22 and 100°C on SS-3 tensile specimens irradiated to 7.2×10^{-5}, 7.2×10^{-4}, 7.2×10^{-3}, 0.072, and 0.28 dpa. Specimens irradiated up to 0.072 dpa were also tested at -25 and -50°C. Duplicated tests were performed on some dose conditions to estimate uncertainty of the data. The engineering stress-strain curves are shown in Fig. 2, and the tensile properties data are summarized in Table 2. The original stress-strain curves were shifted along the strain axis by 5% consecutively for clarity in the figure. It is seen that stress-strain curves have different characteristics at varied irradiation doses and test temperatures. Unirradiated specimens and low dose specimens (7.2×10^{-5}, 7.2×10^{-4} dpa) showed a prominent yield drop and yield elongation followed by significant strain hardening. As doses increased the yield elongation zone gradually disappeared. The flow curves were dominated by an extended plateau with negligent strain hardening after yield drop. As doses increased further, yielding began with a yield drop followed by a continuous load drop to fracture, indicating a lack of homogeneous deformation leading to plastic instability at yield. Some high dose specimens broke in a completely brittle manner at lower temperatures. Test temperatures affect the shapes of stress-strain curves as well. For unirradiated specimens, the yield elongation zone became more evident as temperature decreased. For specimens irradiated to 7.2×10^{-5} dpa, the yield elongation zone showed irregular features at low temperatures. For higher dose specimens, decrease in test temperature led to brittle fracture.

Radiation softening was observed in low dose specimens when tested at 22°C and lower. The yield stress reached a minimum at 7.2×10^{-4} dpa. Irradiation hardening became evident at ~ 0.01 dpa. The hardening effect increased significantly with increasing dose and approached to saturation at ~ 0.1 dpa. The hardening behavior is consistent with the microstructure development during irradiation. The detailed as-irradiated microstructure was described in a previous paper [1]. Similar softening and hardening behavior was observed in Tanaka's experiments [2]. Comparable hardening effect was found in neutron-irradiated mono-crystalline Mo [3], and a smaller hardening effect was observed in proton-irradiated Mo in stress-relieved condition [4]. Byun et al. [5] reported a decrease in the yield strength of powder metallurgy Mo above 0.001 dpa, which is likely due to premature failure caused by grain boundary embrittlement.

Significant hardening was accompanied by severe loss in tensile ductility. Uniform elongation dropped to less than 1% at a dose of 0.072 dpa even at 100°C. The more striking feature is the temperature dependence of embrittling behavior. Specimen failed elastically even at 0.0072 dpa when tested at -50°C.

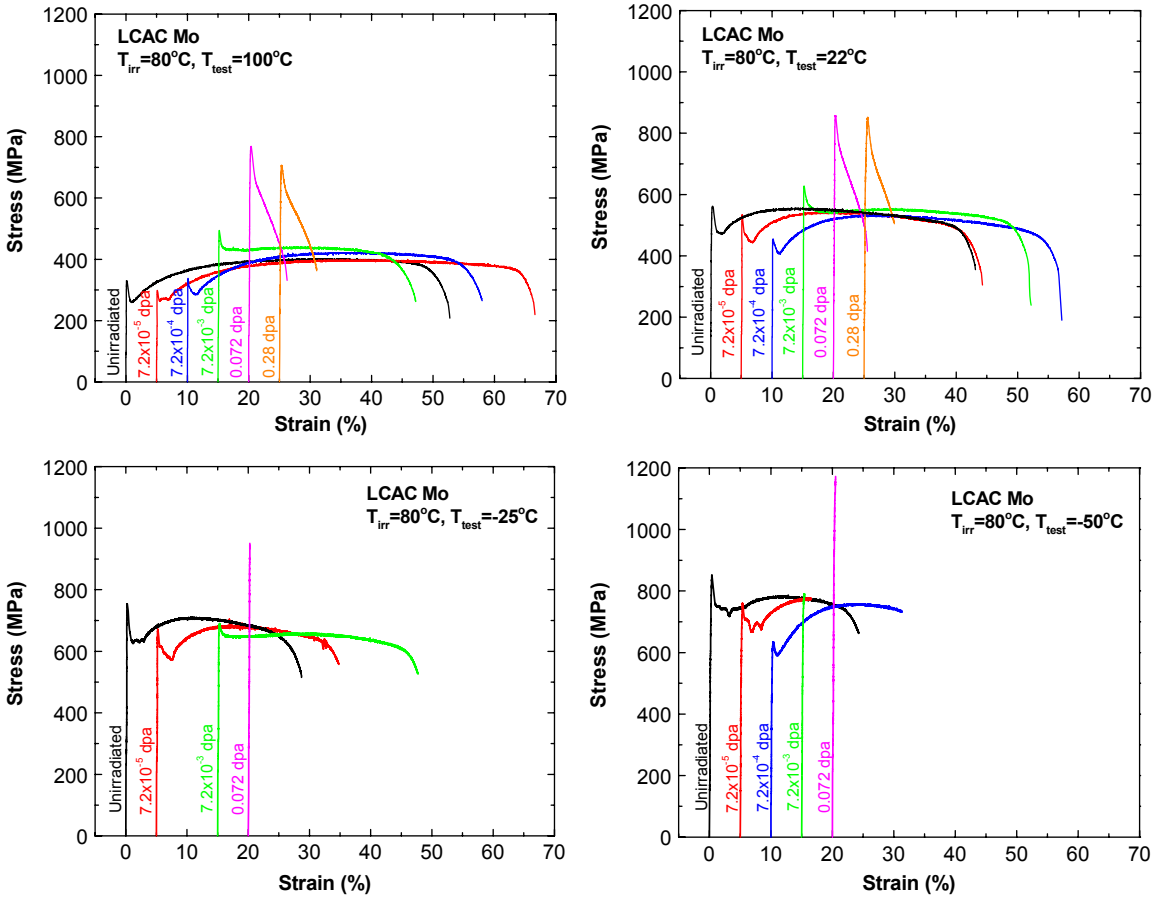

Fig. 2. Engineering stress-strain curves of unirradiated and irradiated LCAC Mo tested between -50 and 100°C.

Table 2. Tensile properties of unirradiated and irradiated LCAC Mo

Test Temp (°C)	Dose (dpa)	UYS (MPa)	LYS (MPa)	UTS (MPa)	UE (%)	TE (%)
22	Unirr	561.8	473.0	552.9	14.6	42.9
	7.2×10^{-5}	531.8	444.6	540.5	15.8	38.9
	7.2×10^{-4}	455.2	409.1	532.9	17.4	46.5
	7.2×10^{-4}	458.2	440.3	562.3	17.2	39.9
	7.2×10^{-3}	627.5	542.6	551.7	13.5	36.5
	7.2×10^{-2}	857.0	748.1	857.0	0.1	5.3
	0.28	796.8	680.3	796.8	0.2	4.9
	0.28	852.6	725.2	852.6	0.3	4.8
100	Unirr	330.8	259.5	402.1	33.2	52.3
	7.2×10^{-5}	298.5	272.4	397.0	31.8	61.3
	7.2×10^{-4}	337.6	291.1	422.0	27.1	47.9
	7.2×10^{-3}	494.5	434.2	440.2	13.0	32.1
	7.2×10^{-2}	768.1	655.6	768.1	0.2	6.2
	0.28	658.7	555.1	658.7	0.1	5.0
	0.28	706.2	621.0	706.2	0.2	6.0
-25	Unirr	694.7	631.6	697.6	11.3	29.2
	Unirr	754.3	633.5	710.1	10.9	28.5
	7.2×10^{-5}	668.9	572.0	680.6	12.8	29.6
	7.2×10^{-3}	690.3	645.5	657.4	13.9	32.6
	7.2×10^{-2}	951.1	951.1	951.1	0.0	0.0
-50	Unirr	849.8	740.4	783.6	11.4	24.1
	7.2×10^{-5}	760.4	669.4	775.1	11.3	11.3
	7.2×10^{-4}	633.8	593.5	757.7	14.2	21.0
	7.2×10^{-3}	790.5	790.5	790.5	0.2	0.2
	7.2×10^{-2}	1172.0	1172.0	1172.0	0.2	0.2

Temperature Dependence of Yield Stress

The yield stress of bcc metals exhibits strong temperature and strain rate dependence at low temperatures. The temperature and strain rate dependence of yielding can be affected by chemical and microstructural changes, and therefore by neutron irradiations. As all the tensile tests were performed at a single strain rate, only the temperature dependence of the yield stress is of interest in this paper. In discussion of temperature dependence of the yield stress, it is necessary to divide the yield stress into two components, an athermal component (practically no temperature dependence) and a thermal component (temperature dependent). Figure 3 shows the yield stress of unirradiated LCAC Mo as a function of test temperature along with the Mo

data from the literature [2,4,6,7]. Note that both annealed and stress-relieved heat treatments are included. The yield stress of Mo increases rapidly with decreasing temperature. The yield stress of annealed Mo apparently reached the athermal regime at 150–200°C (0.15–0.16 T_m), while stress-relieved Mo approached to the athermal regime at about room temperature (0.1 T_m). The difference in yield stress between annealed Mo and stress-relieved Mo is essentially temperature independent, i.e., athermal in nature. The yield stress of LCAC Mo examined in this study is relatively higher than the yield stress of recrystallized Mo studied by Tanaka [2] and by Hasson [7]. This difference is likely associated with material's processing, purity and strain rate. Note that the data reported by Hasson was for single crystal Mo of [110] orientation, and the values of critical resolved shear stress were multiplied by 3.06 so to compare with the yield stress of polycrystalline materials [8].

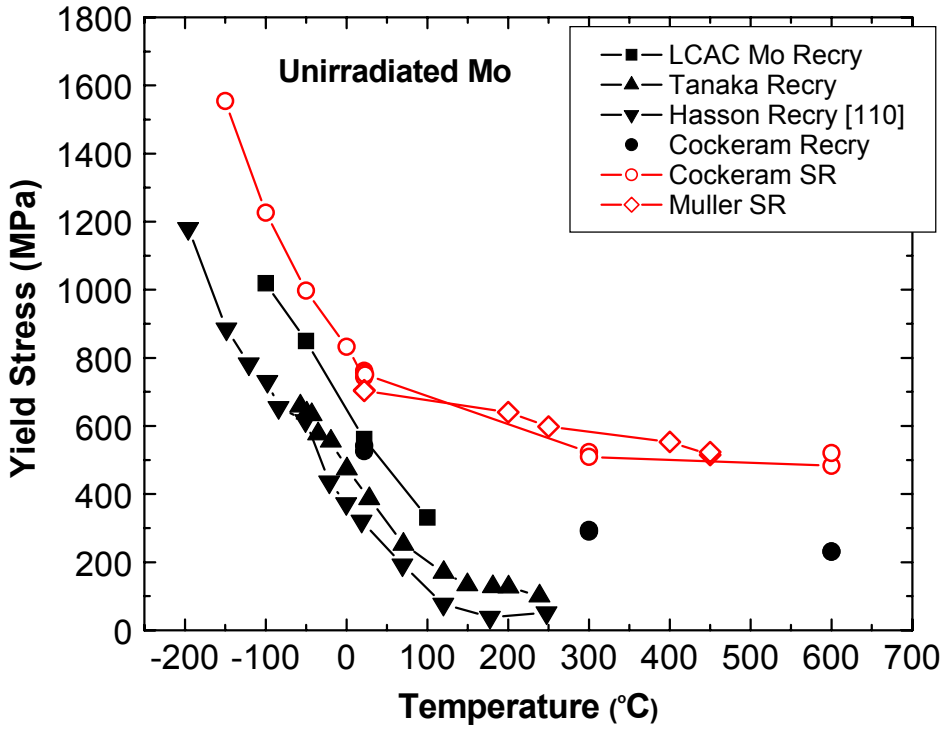

Fig. 3. Temperature dependence of the yield stress of unirradiated Mo.

The temperature-dependent yield stress of irradiated LCAC Mo are shown in Fig. 4 for low dose irradiations (< 0.001 dpa), along with the data reported by Tanaka et al. [2]. In this dose range, the yield stress and its temperature dependence were only slightly affected by irradiations. Reduced temperature dependence was observed both in this study and in Tanaka's work due to radiation-induced softening at low temperatures and hardening at high temperatures. The crossover of radiation softening and radiation hardening is ~ 70°C in the present work and ~ 50°C in Tanaka's experiments. Regarding the dose effect, the radiation softening effect was stronger at 7.2×10^{-4} dpa than at 7.2×10^{-5} dpa with a maximum reduction in yield stress of 16–20%. The decrease in temperature dependence of yielding implies that the irradiation effect was mainly thermal in nature, and the activation energy for thermally-activated dislocation glide was smaller in the irradiated material. There has been significant evidence of radiation-induced softening in bcc metals such as iron, niobium, molybdenum, vanadium, etc. The phenomena of softening caused by defect clusters from irradiation are similar to "alloy softening" in bcc-base alloys that was observed in the low temperature range below 0.15 T_m where obstacles can be overcome by a thermally-activated process [9]. Several models have been proposed to explain the softening effects in bcc metals. The generally-accepted model is the enhanced nucleation of double kinks in the vicinity of small defect clusters. TEM examinations and electrical resistivity measurements

on the specimens irradiated at 7.2×10^{-5} and 7.2×10^{-4} dpa revealed that there was a large population of small glissile defect clusters, and the interactions between these small defect clusters and screw dislocations may be responsible for the observed radiation softening.

The effect of neutron irradiations on the temperature dependence of the yield stress is significantly different at higher doses. Figure 5 shows the yield stress versus test temperature at doses of 0.0072, 0.072, and 0.28 dpa for LCAC Mo. Data reported by Tanaka et al. [2] and Hasson et al. [7] were also presented in Fig. 5 for comparison. Only radiation hardening was observed in the examined dose range, and the increase in yield stress is primarily athermal, which is in contrast to the thermal obstacles at low doses. TEM examinations revealed a high number density of dislocation loops uniformly-distributed in the matrix in the 0.0072 dpa specimen. As doses increased to 0.072 and 0.28 dpa a strong aggregation of dislocation loops occurred, forming rafts. The cluster mean size increased continuously with dose from 1.76 to 3.36 nm between 7.2×10^{-5} and 0.28 dpa with a broader size distribution at high doses. These visible dislocation loops can be effective hardening centers, impeding dislocation motions. When the hardening is superior, it will surpass any softening effects that are caused by small defect clusters or self-interstitial atoms and give an overall athermal hardening at low temperatures. Tanaka et al. estimated the thermal and athermal yield stress in neutron irradiated Mo specimens. His estimation indicated that the thermal component was decreased, while the athermal component increased with increasing doses. The overall effect of irradiation on temperature dependence of yielding is the result of these two combined reactions.

Temperature Dependence of Strain Hardening

Significant increase in yield stress of Mo was accompanied by drastic decrease in uniform elongation after neutron irradiations. The plastic flow was restricted due to loss of strain hardening capacity. The strain hardening behavior of neutron-irradiated Mo was investigated by examining the difference between yield stress (YS) and ultimate tensile strength (UTS). The UTS and YS are plotted in Fig. 6 as a function of test temperature for the unirradiated and irradiated Mo. As test temperature increases, both UTS and YS of unirradiated and irradiated Mo decrease. For the unirradiated Mo, the temperature dependence of ultimate tensile strength is much weaker than that of the yield stress. Moreover, in contrast to the yield stress, the ultimate tensile strength was not effectively altered by neutron irradiations. At lower doses (< 0.01 dpa) when the material has strain hardenability and some degree of uniform deformations irradiation-induced defect clusters evidently changed the temperature dependence of the yield stress but practically had no effects on the ultimate tensile strength. In other word, the yield stress of Mo depends both on test temperature and neutron dose, but the ultimate tensile strength is dependent only on test temperature at a given irradiation temperature. It is also interesting to note that the temperature dependence of the yield stress after low dose irradiations changed towards to the same temperature dependence of the UTS, due to softening effects at lower temperatures. In fact, the yield stress at 7.2×10^{-4} dpa has nearly the same temperature dependence as of the UTS. As doses increased to 7.2×10^{-3} dpa the material showed very limited strain hardening capability, and the temperature-dependent yield stress was very close to the UTS.

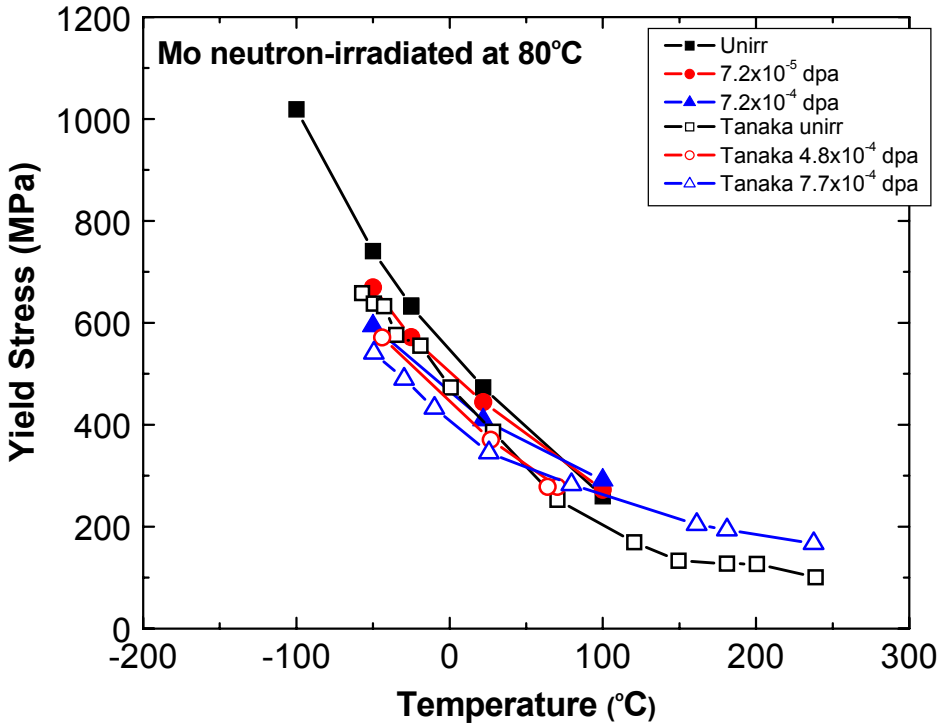

Fig. 4. Radiation effects on temperature dependence of the yield stress of Mo at low doses.

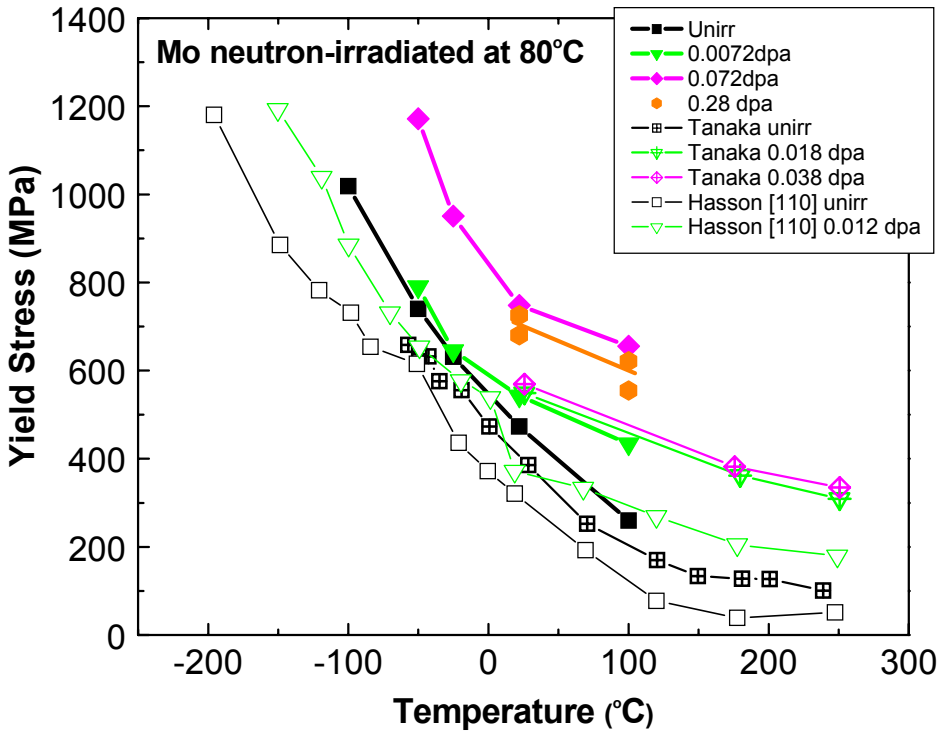

Fig. 5. Radiation effects on temperature dependence of yield stress of Mo at high doses.

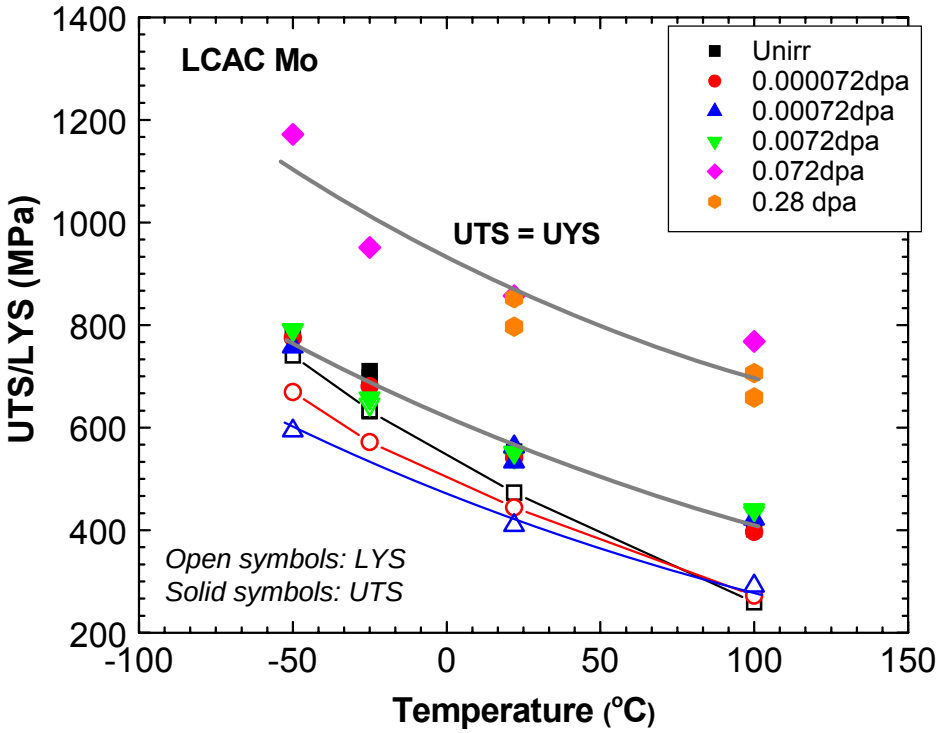

Fig. 6. Temperature dependence of ultimate tensile strength (UTS) of LCAC Mo.

Further irradiations (e.g., 0.072 and 0.28 dpa) caused significant increase in yield stress and complete loss of strain hardenability, leading to severe problems with flow localization and embrittlement. The strength-temperature curves moved upward without changing the temperature dependence, indicating strong athermal hardening. It is suggested that the strain hardening behavior of Mo depends on both doses and test temperature. The dose-independent UTS defines the strength limit where radiation-induced flow localization and embrittlement occurred.

The influence of neutron irradiations on the strain hardening behavior of Mo can be understood further by examining the true stress-true strain behavior. True stress-strain curves were calculated from engineering stress-strain curves up to the point at the onset of necking. The true stress-true strain curves for the unirradiated specimens tested between -50 and 100°C are compared in Fig. 7(a) and their corresponding strain hardening rate-stress curves are shown in Fig. 7(b). It is clear that the yield stress of Mo is very sensitive to temperature in the range of -50 and 100°C, and this difference in yield stress dominates the true stress-true strain curves. The strain hardening behavior shows temperature dependence as well. The strain hardening behavior is comparable at -25 and -50°C with the hardening rate decreasing with flow stress in a nearly linear fashion. At the low stress end around yielding the strain hardening rate decreased rapidly from an initial very high value. As temperature increased to 22°C both high and low stress ends exhibited an upward curvature with an intermittent linear hardening rate similar to low temperature behavior. The initial hardening rate at low stresses was also low relative to -25 and -50°C curves. When tested at 100°C, an extended continuous and gradually-decreasing hardening rate was observed after the linear portion of the curve. The upward tail at the low stress end disappeared at this temperature. For convenience we shall define the rapidly-decreasing low stress end as stage II, the linear portion as stage III and gradually-decreasing high stress end as stage IV.

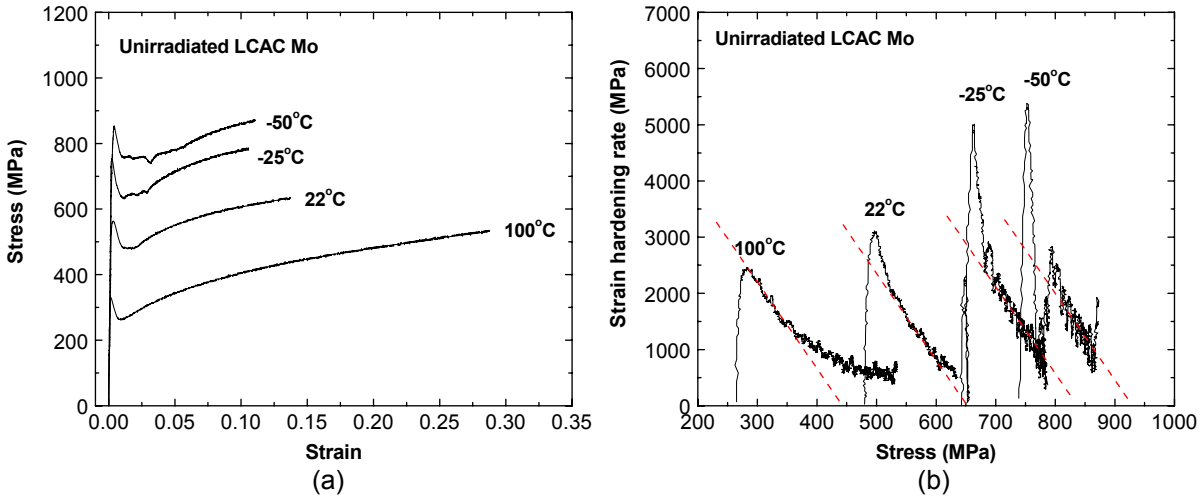

Fig. 7. Unirradiated Mo (a) true stress-true strain curves, (b) strain hardening rate-stress curves.

The true stress-true strain curves and the strain hardening rate–stress curves are shown in Figs. 8 and 9, respectively, for neutron-irradiated Mo. As there is no strain hardenability at any test temperature for specimens irradiated to 0.072 dpa and above, only the strain hardening behavior at 0.0072 dpa and below will be discussed. Note that the end point of strain hardening rate curves is the onset of plastic instability and it is where the hardening rate is equal to the flow stress, i.e., the true stress at necking, $d\sigma / d\varepsilon = \sigma$. The true stress at necking is also defined as the plastic instability stress (PIS) and it is found to be dose-independent parameter for metals and alloys [5,10–12]. It is seen that the plastic instability stress of Mo is independent of neutron irradiation condition but dependent only on test temperature. At 100°C and at doses of 7.2×10^{-5} and 7.2×10^{-4} dpa when slight radiation hardening was observed, the linear hardening behavior (stage III) of irradiated Mo was nearly the same as of unirradiated Mo, and the stage II around yielding varied with doses. As the dose increased to 7.2×10^{-3} dpa when significant radiation hardening occurred, the initial strain hardening rate around yield was very low (~ 800 MPa vs. ~ 3000 MPa for unirradiated Mo), and the hardening rate decreased with decreasing flow stress following the curve of unirradiated Mo and soon reached the PIS. When tested at 22°C, the strain hardening behavior of unirradiated Mo is again similar to unirradiated Mo but the stage II around yield is significantly different between unirradiated and irradiated Mo for low dose irradiations (7.2×10^{-5} and 7.2×10^{-4} dpa). At an intermediate dose (7.2×10^{-3} dpa), the hardening rate is very low, and the hardening rate curve is again overlapped with the curve of unirradiated Mo at high stress end, rapidly reaching the minimum hardening rate. At lower test temperatures, -25 and -50°C, for both unirradiated and irradiated Mo, only stage II and stage III in the hardening rate curves exist. Neutron irradiations at these low doses strongly affected strain hardening within small plastic strain range but had no effect on the dominant linear hardening behavior. In general, at low doses when radiation yield softening and slight hardening occurred, the hardening rate at yield is significantly affected by neutron irradiations. The linear hardening rate behavior is nearly the same for unirradiated and irradiated Mo. At intermediate doses when significant radiation yield hardening occurred and the material still had sufficient uniform elongation, the strain hardening rate was very low, and the hardening rate curve of irradiated Mo was overlapped with the stage III or IV of the unirradiated curve, and soon reached the minimum hardening rate, leading to necking. If the strain hardening rate is plotted as a function of true strain for all the unirradiated and irradiated test conditions, neutron irradiations at low doses (7.2×10^{-5} and 7.2×10^{-4} dpa) have practically no effects on the hardening rate curves except the difference around yielding in a very narrow plastic strain range. Neutron irradiation at an intermediate dose (7.2×10^{-3} dpa) gave almost a constant but very low hardening rate, and the hardening rate increased with decreasing test temperature between 100 and -25°C.

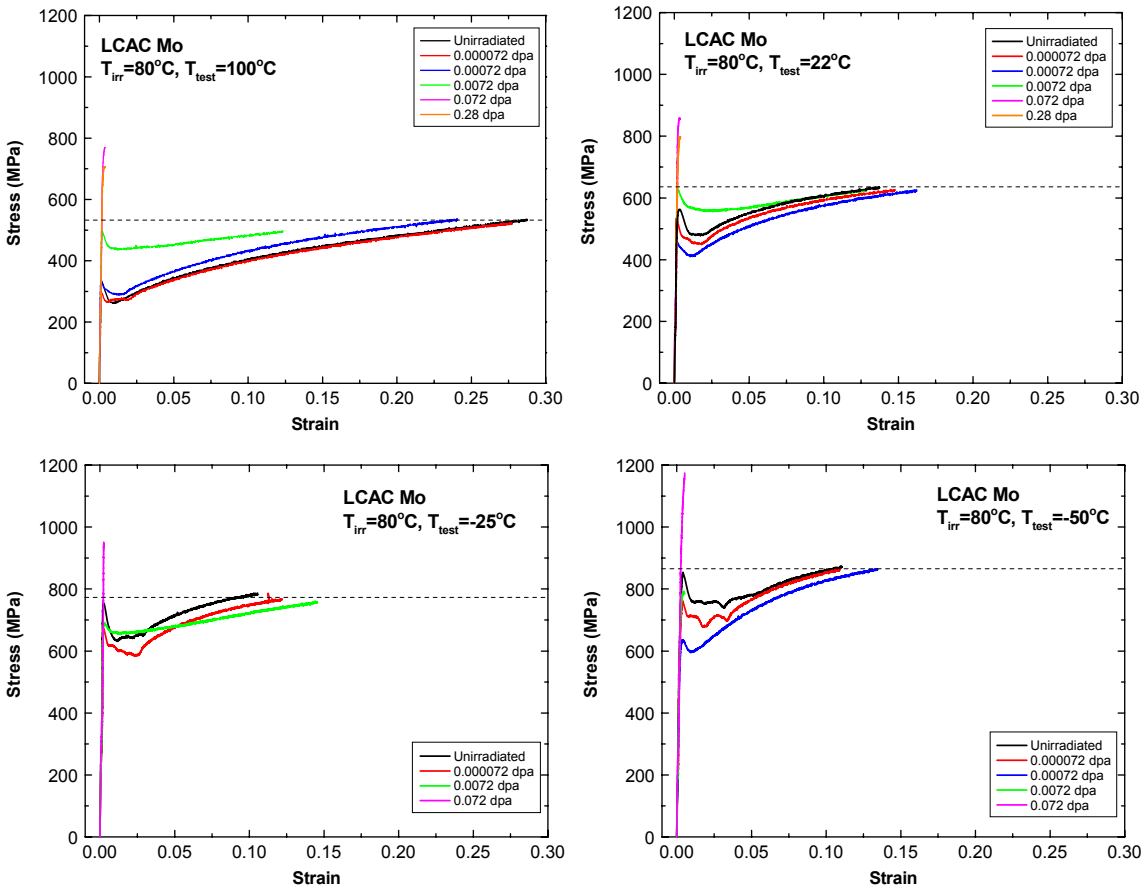

Fig. 8. True stress-true strain curves of unirradiated and irradiated LCAC Mo tested between -50 and 100°C.

The radiation effects on the post-yield strain hardening behavior has been studied widely on fcc metals (e.g., Cu, Ni, Au), model alloys and structural material such as austenitic stainless steels. Previous studies have found that the true stress-true strain curves of irradiated materials were superimposed on the curve of the unirradiated material after shifting the irradiated curves in strain. It was suggested that the strain hardening behavior is dose independent for fcc metals and alloys [11–13]. A remarkable similarity has been found in neutron-irradiated bcc Mo. The irradiated true stress-true strain curves for Mo match very well with the unirradiated curve after shifting the curves in strain to compensate radiation-induced increase or decrease in yield stress. The strain hardening behavior of molybdenum was not changed by irradiation by any means except the initial strain hardening at yielding. This finding is more significant for the Mo neutron irradiated at a moderate dose. The reduced strain hardening at low strains was restored at high strains so that the portion of stress-strain curves at larger strains for the irradiated Mo is superposed on the curve for the unirradiated Mo. This restoration of strain hardenability was suggested to be associated with activation of additional slip systems that assist dislocation network interaction and dislocation multiplication [14]. Strain hardenability capacity appears to be consumed as irradiation dose increases, leading to plastic instability and onset of necking at yield.

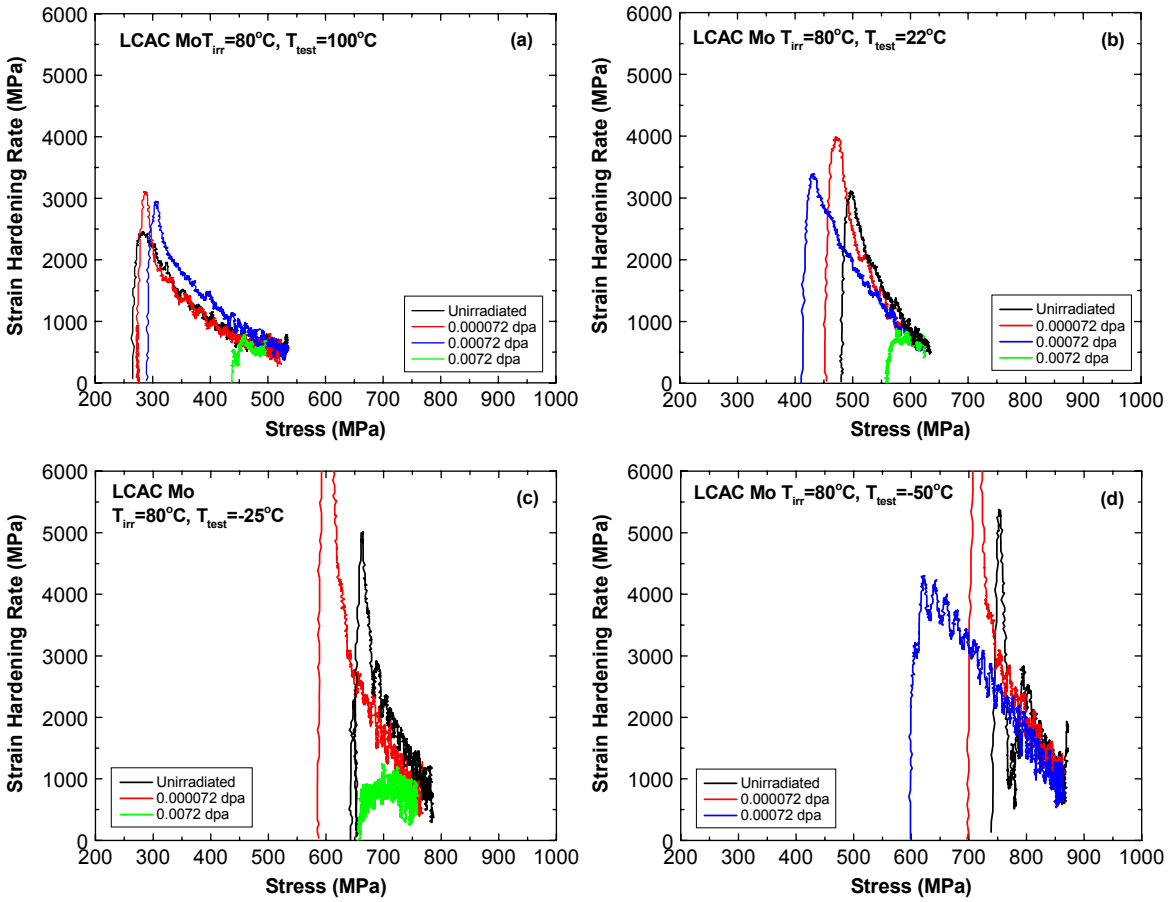

Fig. 9. Strain hardening rate-strain curves of unirradiated and irradiated LCAC Mo tested between -50 and 100°C.

Temperature Dependence of Ductility

Hardening in Mo resulting from low temperature neutron irradiations was accompanied by flow localization and embrittlement, as seen from the stress-strain curves (Fig. 2). Due to strong dose and temperature dependence of yield strength, drastic ductility loss occurred at low temperatures. Figure 10 shows the uniform elongation (UE), total elongation (TE) and reduction in area (RA) as a function of test temperature for LCAC Mo irradiated at five doses. The tensile elongations include the plastic portion only. The reduction in area was determined from low magnification (50×) SEM images of fracture surfaces of the tensile specimens. The projected cross section area at final failure was used to calculate the reduction in area (RA) for the unirradiated and irradiated Mo.

The unirradiated Mo has moderate temperature dependence of tensile ductility. The ductility decreased about 50% as the temperature decreased from 100°C to -50°C but still retained 11% uniform elongation at -50°C. After low dose irradiations (7.2×10^{-5} and 7.2×10^{-4} dpa), tensile ductility changed only slightly. Uniform elongation of irradiated Mo increased relative to unirradiated Mo when radiation softening occurred, and the temperature dependence of uniform elongation was slightly affected. The temperature dependence of ductility was drastically changed after irradiation at 0.0072 dpa. The uniform elongation and total elongation were nearly constant and retained good ductility between -25 and 100°C and then was reduced to < 1%. Interestingly, the reduction in area at 0.0072 dpa was similar to the unirradiated Mo at -25 and 100°C. Evidently irradiations at 0.0072 dpa increased the embrittling temperature of molybdenum. As doses increased

to 0.072 dpa and above, plastic instability occurred at all test temperature due to significant radiation hardening. Total elongation was about 5% at 22 and 100°C but dropped to < 1% below room temperature. The flow localization temperature increased from -50 to 100°C and the embrittling temperature increased from -50 to -25°C as doses increased from 0.0072 to 0.072 dpa. However, the temperature-dependent reduction in area of irradiated Mo was reduced only slightly at 22 and 100°C when the total elongation was strongly affected by irradiation hardening. At -50°C the reduction in area of unirradiated specimens was all below unirradiated specimens.

A strong correlation between the yield stress and uniform elongation has been reported for the irradiated 316SS by Wu et al. [11] and for copper alloys by Pan et al. [12]. To explore the correlation for the irradiated Mo, the yield stress and the plastic instability stress (PIS) are plotted in Fig. 11 in terms of uniform elongation for the unirradiated Mo and irradiated Mo to all doses. At a given test temperature the plastic instability stress of irradiated Mo is constant over the examined dose range. The PIS increased with decreasing test temperature. The PIS defines the stress level where onset of necking takes place at yield and it is solely dependent upon test temperature. Below the plastic instability stress, uniform elongation decreases with increasing yield stress. It is apparent that the reduction in uniform elongation with increasing yield stress is more gradual at a higher test temperature and much more dramatic as test temperature decreased. It is also noted that the minimum observed uniform elongation before flow localization is about 10% at all test temperatures, practically temperature-independent.

Temperature Dependence of Fracture

The fracture surfaces of unirradiated and irradiated specimens tested between -50 and 100°C were examined by scanning electron microscopy. Two major fracture modes were observed for all specimen conditions, i.e., ductile laminate fracture and brittle transgranular cleavage mixed with intergranular brittle fracture. Tensile tests at 100°C result in ductile laminate fracture for the unirradiated and all irradiated specimens. As test temperature decreased to room temperature, the unirradiated Mo failed still in a complete ductile mode, and the irradiated Mo showed different fracture modes depending on the irradiation dose. A transition from layered ductile fracture to transgranular cleavage and intergranular fracture was observed as dose increased. A mixed fracture mode of laminate fracture and transgranular cleavage was observed in the low dose specimens (0.000072 to 0.0072 dpa); at doses of 0.072 and 0.28 dpa transgranular cleavage and brittle intergranular separation became the single dominant fracture mode. Necking is still pronounced in all the specimen conditions at 22 and 100°C. When tested at lower temperatures, -25 and -50°C, nearly all the unirradiated and irradiated specimens showed complete transgranular cleavage and intergranular fracture. Necking was observed in the unirradiated and 0.000072 and 0.0072 dpa specimens tested at -25°C and in the unirradiated and 0.00072 dpa specimens tested at -50°C, but the reduction in area is significantly lower compared to those of 22 and 100°C specimens. No necking occurred in the 0.000072, 0.0072, and 0.072 dpa specimens at -50°C. In general the fracture mode of irradiated Mo depends both on irradiation dose and test temperature. Increase in test temperature and decrease in dose changed the mode of fracture from brittle to ductile.

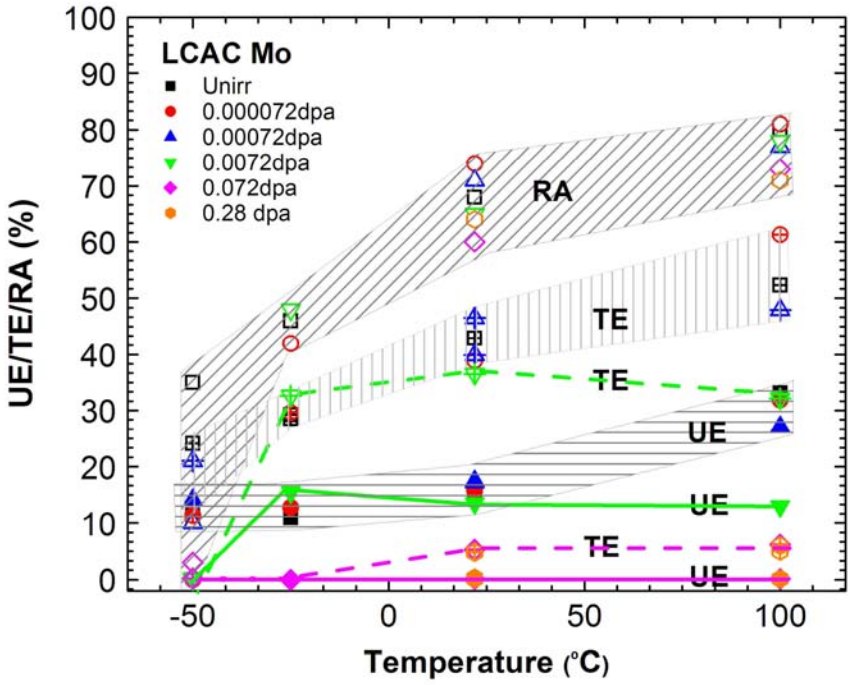

Fig. 10. Temperature dependence of uniform elongation (UE), total elongation (TE), and reduction in area (RA) of neutron-irradiated Mo.

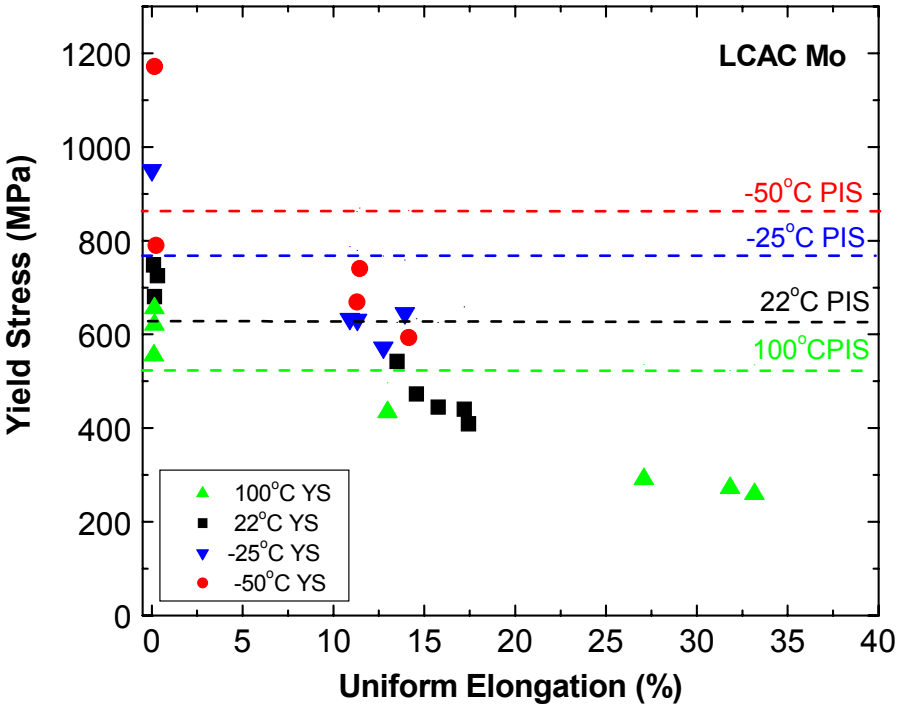

Fig. 11. The correlation between yield stress and uniform elongation of irradiated Mo.

Layered ductile fracture is commonly observed in neutron irradiated Mo [6,15]. Layered structure consists of a stack of thin deformed layers, and it may be associated with the maintained texture by cold rolling after annealing treatment. Grain boundary cracking is the major brittle fracture mode observed in neutron-irradiated, and it has been assumed to be associated with either grain boundary embrittlement by segregated impurity atoms [16] or grain boundary sliding and separation due to irradiation-induced hardening in the grain interior [17]. In the present work, brittle transgranular cleavage was the dominant fracture mode leading to severe reduction in ductility. Singh et al. [3] studied mono- and polycrystalline molybdenum and Mo-Re in order to clarify whether grain boundaries play an important role in irradiation-induced reduction in ductility, and they found that mono- and polycrystalline Mo and Mo-Re deformed in almost the same way after neutron irradiation. Singh et al. suggested that cracks may nucleate at internal or external flaws in the material and propagate without plasticity when the material is significantly hardened. Both their results and the evidence given in this study ruled out grain boundary segregation.

The fracture stress was calculated by the recorded fracture load divided by the cross-section area measured by SEM after failure, and the fracture stress and plastic instability stress are plotted as a function of test temperature in Fig. 12. It needs to be pointed out that the cross-section area determined from SEM images is the projected area. There were no corrections on angular distribution and surface roughness of the cross-section. There was no correction on triaxiality of stress state for the fracture stress calculation either. Fracture modes are also indicated for each irradiation and test condition. Transgranular cleavage fracture was categorized as types I, II, and III according to Gandhi and Ashby [18]. Cleavage I refers to a totally brittle cleavage failure from a pre-existing flaw when the stress is well below the general yield; cleavage II refers to an almost brittle fracture from a plasticity-nucleated crack below the general yield; cleavage III a brittle failure above general yield with measurable fracture strain. Both cleavage II and III fracture were observed in neutron-irradiated Mo. At 22 and 100°C when specimens failed either in a ductile mode or a cleavage mode with evident plasticity the fracture stresses are higher than the PIS, and no evident dose dependence of fracture stress is seen in the figures. Within scatter of data, the fracture stress is apparently constant between 22 and 100°C, as shown in the shaded band in Fig. 12. As test temperature decreased to -25°C, no ductile fracture was observed and the fracture stresses for both unirradiated and irradiated Mo are lower than the constant fracture stress at higher temperature. The fracture stresses at -50°C showed a large scatter of data. The fracture stress of 0.072 dpa specimen is essentially equal to the constant fracture stress at 22 and 100°C, while the unirradiated Mo showed a 200 MPa smaller fracture stress, nearly the same as the fracture stress at -25°C, and the specimens irradiated between 0.000072 and 0.0072 dpa had a fracture stress equal to the PIS at low doses. Recall that the reduction in area at -50°C for unirradiated and irradiated Mo also showed a large scatter of data. With the very high stress, very low ductility, large scatter of reduction in area, it is suggested that the fracture stress at -50°C is close to cleavage stress. What is not understood is if neutron irradiations really have any effects on fracture stresses for cleavage. It appears that the PIS is a more appropriate parameter than the fracture stress that describes the fracture mode at a given dose and test temperature. Neutron irradiations at high doses when plastic instability at yield or embrittlement occurred, the boundaries between fracture fields were shifted.

Acknowledgements

The research was sponsored by the Office of Fusion Energy Sciences, the U.S. DOE under contract DE-AC05-00OR22725 with ORNL, managed and operated by UT-Battelle, LLC. The material was provided by Brian Cockeram at Bettis Atomic Power Laboratory. The authors would like to thank J. L. Bailey, A. M. Williams, L. T. Gibson, and P. S. Tedder for their technical support.

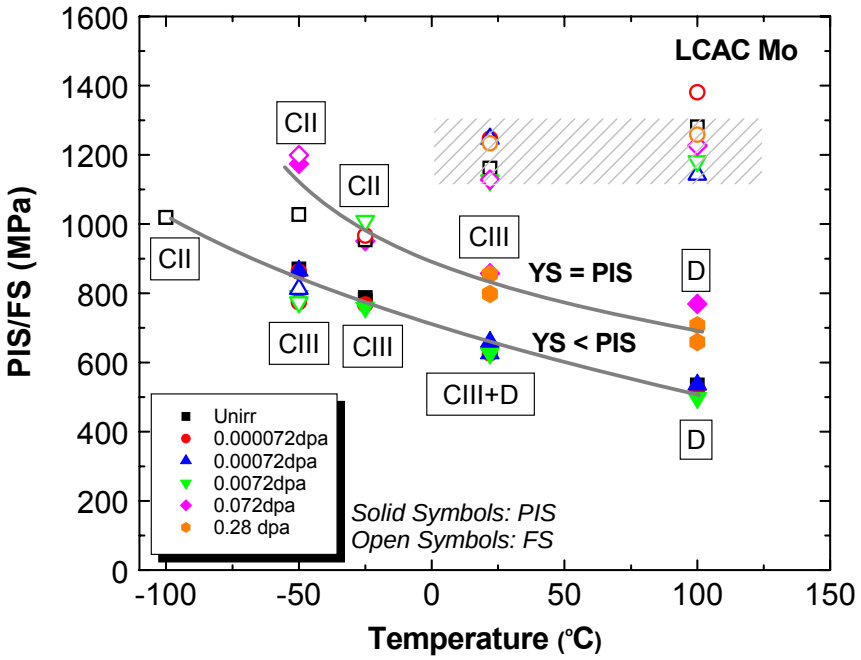

Fig. 12. Temperature dependence of plastic instability stress (PIS) and fracture stress (FS). Fracture modes are also indicated with CIII representing cleavage III, CII cleavage II, and D ductile fracture.

References

[1] M. Li, N. Hashimoto, T. S. Byun, L. L. Snead, and S. J. Zinkle, Journal of Nuclear Materials (ICFRM12).
[2] M. Tanaka, K. Fukaya, and K. Shiraishi, Tran JIM 20 (1979) 697.
[3] B. N. Singh, J. H. Evans, A. Horsewell, P. Toft, and G. V. Műller, J. Nucl. Mater. 258–263 (1998) 865.
[4] G. Műller, Ph.D. thesis, Ėcole Polytechnique Fėdėrale de Lausanne, 1997.
[5] T. S. Byun, K. Farrell, and N. Hashimoto, J. Nucl. Mater. 329–333 (2004) 998.
[6] B. V. Cockeram, J. L. Hollenbeck, and L. L. Snead, J. Nucl. Mater. 324 (2004) 77.
[7] D. F. Hasson, Y. Huang, E. Pink, and R. J. Arsenault, Metall. Trans. 5 (1974) 371.
[8] R. E. Stoller and S. J. Zinkle, J. Nucl. Mater. 283–287 (2000) 349.
[9] E. Pink and R. J. Arsenault, Low temperature softening in body-centered cubic alloys, Prog. Mater. Sci. 24 (1979).
[10] T. S. Byun and K. Farrell, Acta Mater. 52 (2004) 1597.
[11] X. Wu, X. Pan, M. Li, and J. F. Stubbins, J. Nucl. Mater. 343 (2005) 302.
[12] X. Pan, X. Wu, M. Li, and J. F. Stubbins, J. Nucl. Mater. 329–333 (2004) 1088.
[13] R. J. DiMelfi, D. E. Alexander, and L. E. Rehn, J. Nucl. Mater. 252 (1998) 171–177.
[14] S. J. Zinkle and Y. Matsukawa, J. Nucl. Mater. 329–333 (2004) 88.
[15] A. Hasegawa and K. Abe et al., J. Nucl. Mater. 233–237 (1996) 565.
[16] I. V. Gorynin et al., J. Nucl. Mater. 191–194(1992) 421.
[17] B. N. Singh et al., J. Nucl. Mater. 223 (1995) 95.
[18] C. Gandhi and M. F. Ashby, Acta Metall. 27 (1979) 1565.

6.0 AUSTENITIC STAINLESS STEELS

VOID SWELLING OF AISI 321 ANALOG STAINLESS STEEL IRRADIATED AT LOW DPA RATES IN THE BN-350 REACTOR—O. P. Maksimkin, K. V. Tsai, L. G. Turubarova, T. Doronina (Institute of Nuclear Physics) and F. A.. Garner (Pacific Northwest National Laboratory)

OBJECTIVE

The objective of this effort is to explore the response of Russian austenitic steels to irradiation in various fast reactors of the former Soviet Union, looking for insights on how Western steels of similar composition might behave. Of particular interest is the magnitude of void swelling that might occur for irradiation proceeding at relatively low irradiation temperatures and dpa rates that are relevant to ITER.

SUMMARY

In several recently published studies conducted on a Soviet analog of AISI 321 stainless steel irradiated in either fast reactors or light water reactors, it was shown that the void swelling phenomenon extended to temperatures as low as ~ 300ºC or less, when produced by neutron irradiation at dpa rates in the range 10^{-7} to 10^{-8} dpa/sec. Other studies yielded similar results for AISI 316 and the Russian analog of AISI 316. In the current study a blanket duct assembly from BN-350, constructed from the Soviet analog of AISI 321, also exhibits swelling at dpa rates on the order of 10^{-8} dpa/sec, with voids seen as low as 281ºC and only 0.65 dpa. It appears that low-temperature swelling occurs at low dpa rates in 300 series stainless steels in general, and also occurs during irradiations conducted in either fast or mixed spectrum reactors. Therefore it is expected that a similar behavior will be observed in fusion devices as well.

PROGRESS AND STATUS

Introduction

In a recently published study it was shown that in annealed 12X18H10T, the Soviet analog of AISI 321 stainless steel, void swelling inhabits a temperature regime with a lower limit just at or above 300^{o}C, when irradiated in the BN-350 fast reactor at dpa rates on the order of 10^{-7} to 10^{-8} dpa/s [1]. This study was conducted on an unfueled flow restrictor element removed from the breeder zone of the reactor. Limited comparison of swelling in the same steel following irradiation at comparable dpa rates in several light water reactors confirmed that void nucleation in general is limited to temperatures > 300ºC [2, 3]. Similar results were recently observed in 316-type stainless steels irradiated in Japanese and European PWRs [4, 5].

Previous fast reactors studies conducted in Western countries could not establish the lower temperature limit of swelling because the inlet coolant temperatures of all second-generation fast reactors in the West are in the range 365–380ºC. First-generation Western reactors such as EBR-I and DFR operated with lower inlet temperatures, but these reactors were decommissioned many years ago. In countries of the Former Soviet Union, however, there exist both first and second-generation fast reactors. One of these, the BN-350 fast reactor in Kazakhstan, was recently decommissioned. It had an inlet coolant temperature of 280ºC.

Following an earlier prediction concerning higher-than-expected swelling in PWRs [6,7] a number of recent studies by Garner and coworkers have shown that void swelling in austenitic stainless steels actually increases at lower dpa rates [8–15], often allowing the observation of the lower swelling temperature limit at much lower dpa levels. This increase in swelling arises primarily from a decrease in the duration of the transient regime of swelling at lower dpa rates. Both the flow restrictor component and the components from VVERs and PWRs experienced dpa rates that were much lower than those found inside the fueled regions of fast reactor cores.

Recently, it was shown that the Soviet analog of AISI 316 when irradiated as a hexagonal blanket assembly at relatively low dpa rates (on the order of 10^{-8} dpa/sec) in BN-350 also exhibits swelling at unexpectedly low levels, with voids seen as low as 281ºC and only 1.3 dpa. [14].

Another opportunity has recently arisen to provide additional confirmation concerning the generality of the lower temperature limit of void nucleation in austenitic stainless steels by examining another component from the BN-350 reactor that was irradiated at low neutron flux. This component was similar in irradiation history to that of the hexagonal blanket assembly constructed from the AISI 316 analog previously reported in reference [14].

Experimental Procedure

A hexagonal blanket assembly designated N-214(1) was irradiated in the reflector region of the BN-350 reactor, reaching a maximum of 12.6 dpa at an average maximum dpa rate of 3.8×10^{-8} dpa/sec averaged over its lifetime in reactor. The hexagonal duct with faces 50 mm wide and 2 mm thick was constructed from 12Cr18Ni10Ti stainless steel, a Soviet analog of AISI 321 steel, and was produced with the final thermal-mechanical treatment of the duct being 15–20% cold deformation followed by annealing at 800ºC for 1 hour.

The coolant temperature at the bottom of the assembly was 280ºC and the temperature at the top of the assembly was 430ºC. Specimens were chosen for examination between positions having calculated coolant temperatures between 281 and 333ºC. Since the inlet coolant temperature is controlled at 280ºC, the temperatures toward the bottom of the assembly are well-known, but may be uncertain by ±5ºC at the upper elevations examined in this experiment. Due to the thinness of the duct wall, the internal temperature of the duct was not raised significantly by gamma heating. Thus, the temperature of the steel is expected to be within 1–2ºC of the local coolant temperature at any elevation.

At the BN-350 site specimens with 10 mm height and 50 mm width were cut from the duct walls at various locations. Subsequent reduction of these specimens was conducted in a hot cell at INP-Almaty for microstructural analysis and microhardness measurements. Plate-shape specimens with sizes of 5×6 mm were prepared for metallography investigations, microhardness measurements and immersion density weighing.

The examination technique involved transmission electron microscopy (TEM), using a JEM-100CX electron microscope operating at 100 keV. The density was measured using a hydrostatic weighing technique employing a CEPN-770 electronic balance with methyl alcohol as the working liquid.

Disks of 3 mm diameter for microscopy studies were prepared from ≤ 300 μm sections cut from the mid-section of the duct face. Mechanical grinding and polishing with subsequent electrochemical polishing were used for final preparation of TEM disks. The irradiation conditions for specimens examined to date are shown in Table 1.

Table 1. Dose and temperatures over the height of the N-214(1) blanket assembly shroud

Distance from mid-plane, mm	N-214(1) / 12Cr18Ni10Ti		
	Dose, dpa	Dpa rate, 10^{-8} dpa/sec	Calculated temperature, ºC
-900	0.65	0.12	281
-375	7.3	1.36	294
0	12.3	2.3	313
+75	12.6	2.34	318
+375	7.3	1.35	333

Results and Discussion

The results of the density change measurements are shown in Table 2. There definitely appears to be swelling at relatively low levels that increase gradually with axial position and thereby increasing temperature. The presence of voids can not be directly inferred from these measurements alone, however, since precipitation may be occurring to produce all or some portion of these density changes.

The density of non-irradiated steel 12Cr18Ni10Ti was listed in previous studies on this steel to be 7.868g/cm^3. The point at -900 mm therefore indicates some densification has occurred. Note that this measurement was made after electrical polishing of the specimen. Another measurement made before polishing yielded 7.869g/cm^3, indicating that no net densification had occurred.

It is known that stainless steels, especially those of lower nickel content, tend to interact during long-term exposure with sodium such that near-surface compositional changes occur, sometimes leading to the formation of a ferritic layer on the surface [16–19]. Perhaps this phenomenon accounts for the difference in density between polished and unpolished specimens, with the net density changing upon removal of the ferrite layer.

Table 2. Hydrostatic weighing results

Distance from mid-plane, mm	Density, g/cm^3 (metallography specimen)	$\Delta\rho/\rho$, % (metallography specimen)
-900	7.888	-0.25
-375	7.856	0.15
0	7.852	0.20
+75	7.846	0.28
+375	7.817	0.65

The microscopy results, however, confirm the presence of void swelling in the range 281 to 333ºC, as shown in Table 3 and Figs. 1–3. Most significantly, it is seen that even at 0.65 dpa and 281ºC voids are clearly visible, adding additional support to the growing body of evidence that void swelling can extend down to unexpectedly low temperatures and doses if the atomic displacement rate is low enough.

Table 3. Microstructural data on cavities for irradiated stainless steel 12Cr18Ni10Ti

Distance from mid-plane, mm	Range for void sizes, nm	Mean void diameter, nm	Peak void diameter, nm	Void density, $\times 10^{15}$cm^{-3}	Swelling, %
-900	< 5–12	7.7	< 5nm / 5–10	0.84	0.03
-375	(1) < 10–15	11.6	10	0.47	0.05
0	(1) < 10–20	11.2	10	2.9	0.25
+75	< 8–18	9.0	8	8.2	0.33
+375	< 10–35	15.3	15	1.0	0.23

Once again it appears that irradiation of stainless steels at progressively lower dpa rates usually leads to swelling occurring at lower doses and temperatures than previously expected. Such observations have been hampered in previous Western studies by the high dpa rates used in those studies and the relatively high inlet temperatures of Western reactors.

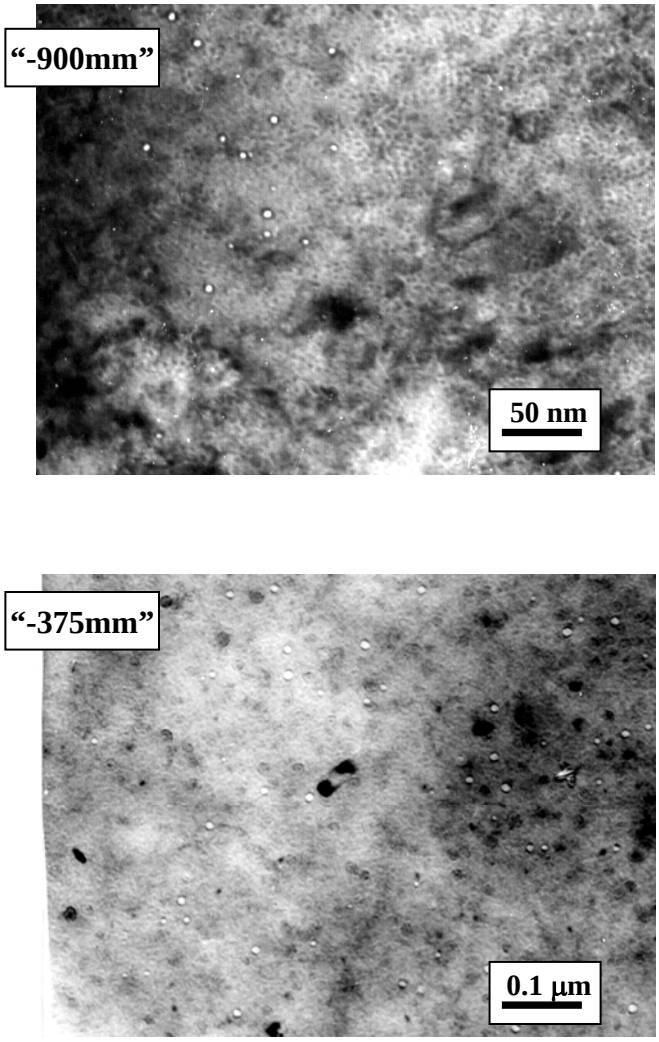

Fig. 1. Voids observed in 12Cr18Ni10Ti at 0.65 dpa, 281ºC (top) and 7.3 dpa, 294ºC (bottom) after irradiation in BN-350.

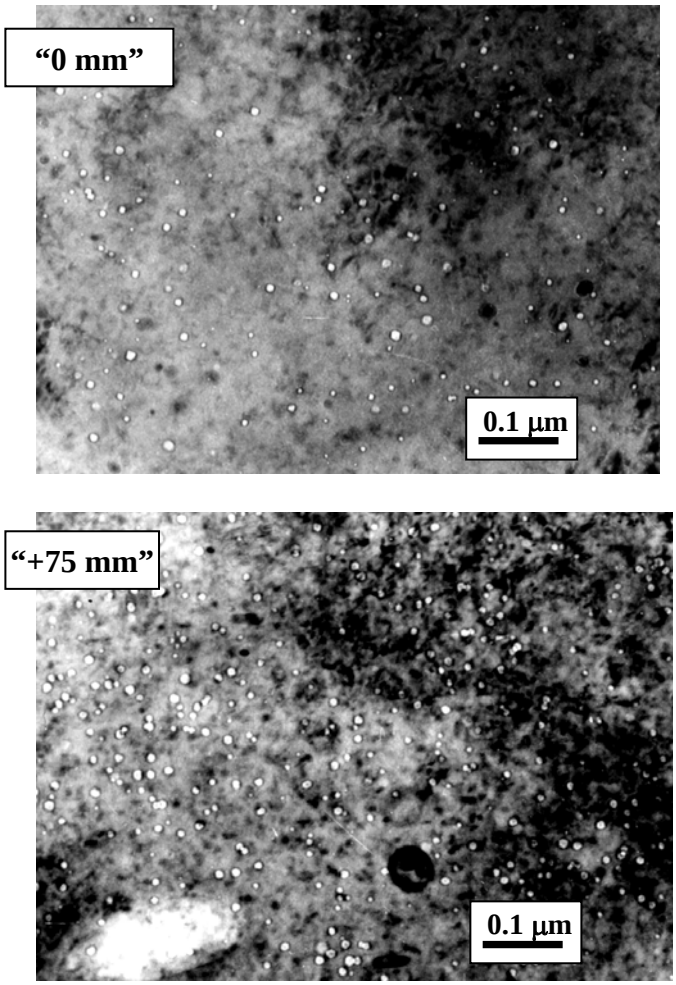

Fig. 2. Voids observed in 12Cr18Ni10Ti at 12.3 dpa, 313ºC (top) and 12.6 dpa, 318ºC (bottom) after irradiation in BN-350.

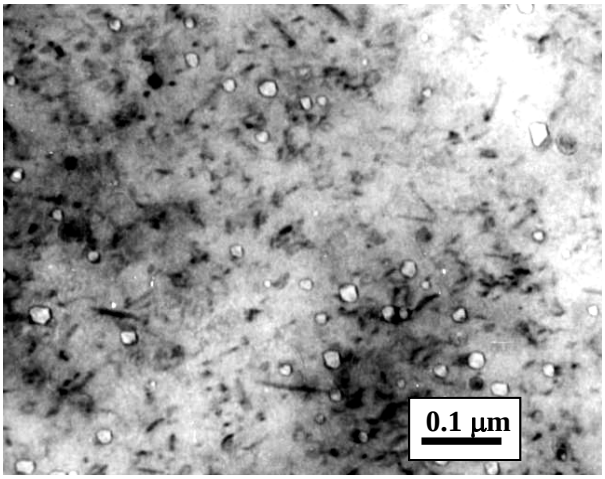

Fig. 3. Voids observed at +375 mm elevation in 12Cr18Ni10Ti duct at 7.3 dpa, 333ºC dpa after irradiation in BN-350.

It also appears that low-temperature swelling at low dpa rates occurs in all 300 series stainless steels in general, whether Western or Russian in composition. The fact that such behavior is observed during irradiations conducted in both fast and mixed spectrum reactors implies that it will be observed in fusion devices as well.

Acknowledgements

The Kazakh portion of this work was supported by the Ministry of Energy and Mineral Resources of the Republic of Kazakhstan, and under ISTC project number K-437. The US portion was jointly sponsored by the Materials Science Branch, Office of Basic Energy Sciences, and the Office of Fusion Energy, U.S. Department of Energy. The authors are indebted to Natalia A. Brikotnina of Interpreter and Translation Services for her assistance in the conduct and interpretation of this experiment, and for translation of the original Russian text into English.

References

[1] S. I. Porollo, Yu. V. Konobeev, A. M. Dvoriashin, V. M. Krigan, and F. A. Garner, “Determination of the Lower Temperature Limit of Void Swelling of Stainless Steels at PWR-relevant Displacement Rates,” 10th International Conference on Environmental Degradation of Materials in Nuclear Power Systems--Water Reactors, August 5–9, 2001, issued in CD format.

[2] V. S. Neustroev, V. K. Shamardin, Z. E. Ostrovsky, A. M. Pecherin, and F. A. Garner, “Temperature-Shift of Void Swelling Observed at PWR-Relevant Temperatures in Annealed Fe-18Cr-10Ni-Ti Stainless Steel Irradiated at High and Low Dpa Rates in BOR-60," International Symposium on "Contribution of Materials Investigation to the Resolution of Problems Encountered in Pressurized Water Reactors,” September 14–18, 1998, Fontevraud, France, pp. 261–269.

[3] V. S. Neustroev, V. N. Golovanov, V. K. Shamardin, Z. E. Ostrovskiy, and A. M. Pecherin,“ Radiation Phenomena in X18H10T Steel Irradiated in Different Reactors Under Conditions Close to the Operating Conditions of VVER Internals,” Proceedings of 7th Russian Conference on Reactor Material Science, September 8-12, 2003, in Russian.

[4] K. Fujii, K. Fukuya, G. Furutani, T. Torimaru, A. Kohyama, and Y. Katoh, “Swelling in 316 Stainless Steel Irradiated in a PWR,” 10th International Conference on Environmental Degradation of Materials in Nuclear Power Systems--Water Reactors, issued in CD format.

[5] N. I. Budylkin, T. M. Bulanova, E. G. Mironova, N. M. Mitrofanova, S. I. Porollo, V. M. Chernov, V. K. Shamardin, and F. A. Garner, “The Strong Influence of Displacement Rate on Void Swelling in Variants of Fe-16Cr-15Ni-3Mo Austenitic Stainless Steel Irradiated in BN-350 and BOR-60,” J. Nucl. Mater. 329–333 (2004) 621–624.

[6] F. A. Garner, L. R. Greenwood, and D. L. Harrod, "Potential High Fluence Response of Pressure Vessel Internals Constructed from Austenitic Stainless Steels," Proceedings of the Sixth International Symposium on Environmental Degradation of Materials in Nuclear Power Systems--Water Reactors, San Diego, August 1–5, 1993, pp. 783–790.

[7] F. A. Garner, "Materials Issues Involving Austenitic Pressure Vessel Internals Arising from Void Swelling and Irradiation Creep," Trans. Am. Nucl. Soc. 71 (1994) 190.

[8] F. A. Garner and M. B. Toloczko, "Irradiation Creep and Void Swelling of Austenitic Stainless Steels at Low Displacement Rates in Light Water Energy Systems," J. Nucl. Mater. 251 (1997) 252–261.

[9] D. J. Edwards, E. P. Simonen, F. A. Garner, B. A. Oliver, and S. M. Bruemmer, “Sensitivity of Microstructural Evolution Due to Temperature and Dose Gradients in Neutron-Irradiated 316SS,” J. Nucl. Mater. 317 (2003) 32–45.

[10] T. Okita, T. Sato, N. Sekimura, F. A. Garner, and L. R. Greenwood,” The Primary Origin of Dose Rate Effects on Microstructural Evolution of Austenitic Alloys During Neutron Irradiation,” J. Nucl. Mater. 207–211 (2002) 322–326.

[11] T. Okita, T. Sato, N. Sekimura, F. A. Garner, and W. G. Wolfer,“ Combined Effect of Temperature, Displacement Rate and Composition on the Neutron-Induced Swelling of Austenitic Alloys,” 11th International Conference on Environmental Degradation of Materials in Nuclear Power Systems--Water Reactors, August 2003, issued on CD format.

[12] V. S. Neustroev, V. K. Shamardin, Z. E. Ostrovsky, A. M. Pecherin, and F. A. Garner,"Temperature-Shift of Void Swelling Observed at PWR-Relevant Temperatures in Annealed Fe-18Cr-10Ni-Ti Stainless Steel Irradiated in the Reflector Region of BOR-60," Effects of Radiation on Materials: 19th International Symposium, ASTM STP 1366, M. L. Hamilton, A. S. Kumar, S. T. Rosinski, and M. L. Grossbeck (eds.), American Society for Testing and Materials (2000) 792–800.

[13] F. A. Garner, N. I. Budylkin, Yu. V. Konobeev, S. I. Porollo, V. S. Neustroev, V. K. Shamardin, and A. V. Kozlov,“ The Influence of DPA Rate on Void Swelling of Russian Austenitic Stainless Steels,” 10th International Conference on Environmental Degradation of Materials in Nuclear Power Systems--Water Reactors (2003) 647–656.

[14] O. P. Maksimkin, K. V. Tsai, L. G. Turubarova, T. Doronina, and F. A. Garner,“ Characterization of 08Cr16Ni11Mo3 Stainless Steel Irradiated in the BN-350 Reactor,” J. Nucl. Mater. 329–333 (2004) 625–629.

[15] S. I. Porollo, A. M. Dvoriashin, Yu. V. Konobeev, A. A. Ivanov, S. V. Shulepin, and F. A. Garner, “Microstructure and Mechanical Properties of Austenitic Stainless Steel 12X18H9T Irradiated in the Pressure Vessel of BR-10 at Very Low Displacement Rates,” progress report to be issued in the Fusion Materials Semiannual Progress Report, DOE/ER-0313/39, December 31, 2005.

[16] W. F. Brehm, “Interaction of Sodium with Breeder Reactor Materials,” in Diffusion Processes in Nuclear Materials, R. P. Agarwala (ed.), Elsevier Science Publishers B. V. (1992) 323–352.

[17] P. T. Nettley, I. P. Bell, K. Q. Bagely, D. R. Harries, A. W. Thorley, and C. Tyzack, “Problems in the Selection and Utilization of Materials in Sodium Cooled Fast Reactors,” BNES, Fast Breeder Reactors, Pergamon, Oxford (1967) 825–849.

[18] W. Charnock, C. P. Haigh, C. A. P. Horten, and P. Marshall, CEBG Research, November 1979, p. 3.

[19] I. I. Balachov, F. A. Garner, Y. Isobe, M. Sagisaka, and H. T. Tang, “NDE Measurements of Irradiation-induced Void Swelling,” Eleventh International Conference on Environmental Degradation of Materials in Nuclear Systems--Water Reactors (2003) 640–645.

MICROSTRUCTURE AND MECHANICAL PROPERTIES OF AUSTENITIC STAINLESS STEEL 12X18H9T AFTER NEUTRON IRRADIATION IN THE PRESSURE VESSEL OF BR-10 FAST REACTOR AT VERY LOW DOSE RATES—S. I. Porollo, A. M. Dvoriashin, Yu. V. Konobeev, A. A. Ivanov, and S. V. Shulepin (Institute of Physics and Power Engineering) and F. A. Garner (Pacific Northwest National Laboratory)

OBJECTIVE

The objective of this effort is to explore the response of Russian austenitic steels to irradiation in various fast reactors of the former Soviet Union, looking for insights on how Western steels of similar composition might behave. Of particular interest is the magnitude of void swelling that might occur for irradiation proceeding at relatively low irradiation temperatures and dpa rates.

SUMMARY

The internal components of various Russian reactors such as VVER-440 and VVER-1000 pressurized water reactors and the BN-600 fast reactor are usually made of Russian designation 18Cr-9Ni or 18Cr-10Ni-Ti austenitic stainless steel. In Western PWRs and BWRs, the AISI Type 304 steel with composition similar to 18Cr-9Ni steel is used for this purpose. Currently, the issue of reactor life extension is very important for both Russian and Western reactors of the PWR type. It has also been recognized that some problems encountered in PWRs, especially those associated with changes in dimension and mechanical properties, can also be expected to occur in water-cooled fusion devices.

Results are presented for void swelling and microstructure and mechanical properties of Russian 12X18H9T (0.12C-18Cr-9Ni-Ti) austenitic stainless steel irradiated as a pressure vessel structural material of the BR-10 fast reactor at ~ 350ºC to only 0.64 dpa, produced by many years of exposure at the very low displacement rate of only 1.9×10^{-9} dpa/s. In agreement with a number of other recent studies, it appears that lower dpa rates have a pronounced effect on the microstructure and mechanical properties. In general, lower dpa rates lead to the onset of swelling at much lower doses compared to comparable irradiations conducted at higher dpa rates.

PROGRESS AND STATUS

Introduction

Near-core internals of Russian power reactors (VVER-440, VVER-1000, BN-600) are made of type X18H9 or X18H9T (18Cr-9Ni or 18Cr-10Ni-Ti) austenitic stainless steels. In Western PWRs and BWRs, the steel AISI 304 (with chemical composition similar to 18Cr-9Ni) is used for such purposes. In addition, Soviet-design fast reactors also use 18Cr-10Ni-Ti as a pressure vessel material, whereas Western-design reactors use low-alloy ferritic steels.

Currently, the issue of plant life extension is very important to many Russian and Western reactors of PWR and BWR type, especially since much of the internals are not easily removable. It has also been recognized that many of the material issues confronting the PWR and BWR reactors will also be faced by water-cooled fusion reactors such as ITER.

Confident validation of reactor life extension requires reliable information on how the properties of structural materials of internal components will change with increasing neutron dose, especially at damage levels not yet reached by the component. In practice, this question is usually solved for pressure vessels by using surveillance samples, which are located at the reactor core periphery and therefore irradiated at higher neutron fluxes than is the vessel. For internal components of PWRs and WWERS, however, higher fluence data are usually needed at lower dpa rates than are available in the reactor type of interest. When available, such data are usually generated in higher flux reactors at dpa rates that are

much larger than that of water-moderated reactors. If the properties under consideration are flux-sensitive, then there is some problem in extrapolation to the component of interest.

Recently it became clear that data on surveillance samples are insufficient for Russian life extension efforts concerning austenitic pressure vessels. A similar insufficiency exists for in-core components. This problem is related to the impossibility to obtain data over a sufficiently wide range of dose rates to approximately the same dose that will allow quantification of a flux dependency. One approach to partially fill this need is to examine assemblies irradiated at the core periphery or other components located even farther from the core.

In the present paper are presented results of swelling and microstructure and mechanical properties investigations of Russian austenitic stainless steel 12X18H9T (0.12C-18Cr-9Ni-Ti) irradiated as the structural material of the BR-10 fast reactor vessel to a dose of only 0.64 dpa at the very low displacement rate of 1.9×10^{-9} dpa/s.

Experimental Procedure

Samples for investigation of microstructure and mechanical properties were cut from the first vessel of the BR-10 fast reactor, after the vessel was replaced by a new vessel in 1979. The first vessel was variable in width with a maximum outside diameter of 535 mm and a total length just over 4 m. At the location of fuel assemblies, the vessel has the outside diameter of 366 mm and wall thickness of 7 mm. The vessel material is 12X18H9T austenitic stainless steel in the solution treated condition. The nominal chemical composition of the steel is (wt. %): $C \leq 0.12$; $Si \leq 0.8$; $Mn \leq 2.0$; Cr at 17-20; Ni at 8-11; $Ti < 0.8$.

The first vessel was in operation for 20 years (July 1959 till October 1979) with three fuel cycle runs, the first two with PuO_2 fuel and the third with UC fuel. The total reactor operation during this period was 3930 days or 2562.6 effective full power days. The total neutron fluence accumulated by the vessel at the core midplane was 8.44×10^{26} n/m^2 corresponding to an exposure dose of 33.1 dpa (NRT). On the inside, the vessel was in contact with sodium coolant flowing from bottom to top, but on the outside, it was in contact with air contained in the gap between the vessel and a safety vessel. In the first and last cycles, the temperature of the vessel was 350ºC, but during the second cycle it was 430ºC.

To study the mechanical properties and microstructure, specimens were cut from the vessel at two elevations. Irradiation conditions for these elevations are shown in Table 1.

Table 1. Irradiation conditions for sections cut from the BR-10 reactor vessel

Place of specimen cutting	Distance from core midplane, mm	Total neutron fluence, 10^{26} n/m^2	Dose, dpa	Average irradiation temperature, °C	Dose rate, dpa/s
Level of basket bottom	-425	0.35	0.64	350	1.9×10^{-9}
Level of upper flange	+1890	…	…	80	...

One specimen was cut from the bottom level of the fuel basket, in which the lower ends of fuel assemblies were located. Another specimen was cut at the level of the upper flange of the first coolant circuit. This second specimen was effectively unirradiated but had been aged for 20 years at 80ºC.

Using a remote milling machine, strips with cross section 10 mm × 2 mm or 7 mm × 2 mm were cut from the original sections in an axial direction. Then from these strips, TEM specimens and flat specimens for measurements of short-term mechanical properties were prepared.

Mechanical properties were measured for flat samples having a gauge length of 12 mm and a cross section of 2 mm × 2 mm. The tests were carried out at temperatures of 25 and 350ºC. The test temperature of 350ºC equals the inlet coolant temperature in the core for the majority of reactor operation time and was approximately equal to the temperature of the reactor vessel at the basket bottom level. The initial strain rate employed was 1.4×10^{-3} s^{-1}. At each temperature, three or four tensile specimens were tested and the results averaged.

TEM specimens in the form of disks of 3 mm in diameter with a perforated central hole were prepared using a standard technique employing the two-jet-polishing "STRUERS" device. Microstructural investigations were performed at an accelerating voltage of 100 kV using a JEM-100CX electron microscope equipped with a lateral goniometer.

Results

The microstructure of the unirradiated steel at the level of upper flange is shown in Figs. 1 and 2. It is observed that the steel had the anticipated austenitic structure with a grain size of ~ 10–20 microns. Austenitic grains, in turn, are divided into subgrains by dislocation walls with sizes ranging from ~ 1 to 5 microns (Fig. 1). The average dislocation density is (4–5) × 10^{13} m^{-2}. In addition, twins, large TiC precipitates with mean diameter of 0.5 to 1 microns, and much smaller precipitates distributed uniformly and at much higher density within the grains (Fig. 2), were observed. The diameter of the small precipitates ranges from 50 to 60 nm, with their concentration at ~ 3×10^{19} m^{-3}. An analysis of micro-diffraction patterns obtained from these precipitates showed that these precipitates have the fcc-structure with the lattice parameter of 0.43 nm, identifying them as TiC carbides.

The microstructure of the irradiated steel from the cross section at the level of the basket bottom is shown in Figs. 3 and 4. Even at the low dose of 0.64 dpa, the microstructure has changed significantly, producing non-uniform spatial distribution of dislocation loops (Fig. 3) and voids (Fig. 4). Frank dislocation loops were found with a mean diameter of 33 nm and mean concentration of 3 × 10^{21} m^{-3} but which are arrayed in extended linear clusters, at concentrations higher compared with other regions (Fig. 3). The size of such arrays coincides with the size of sub-grains observed in the unirradiated steel, and thus, it can be assumed that the dislocation loops formed presumably on the dislocation walls separating the sub-grains.

The spatial distribution of voids is also rather non-uniform. Large voids are located mainly in zones having high loop concentration, i.e., in the former dislocation walls (Fig. 4). Smaller voids, however, are distributed nearly uniformly throughout the grain. The swelling of the steel equals 0.1%, with a mean void diameter of 11 nm and concentration of 6 × 10^{20} m^{-3}. Precipitates observed in the irradiated steel were essentially identical to those in the unirradiated steel.

The average values of ultimate strength, yield strength, and total and uniform elongation of specimens from the two cross sections of the BR-10 vessel are shown in Table 2.

From Table 2, it appears that irradiation of steel 12X18H9T at a temperature of 350ºC to 0.64 dpa has resulted in substantial strengthening and some ductility loss. The yield strength increased by 286 MPa at T_{test} = 25ºC, and by 223 MPa at T_{test} = 350ºC. The total elongation of the steel has decreased from 53.3% to 34.5% at T_{test} = 25ºC, and from 28.6% to 18.7% at T_{test} = 350ºC.

Table 2. Results of mechanical tests of flat samples from steel 12X18H9T

Cross section	Test temperature, ºC	Mechanical properties			
		Ultimate strength, MPa	Yield strength MPa	Total elongation %	Uniform elongation, %
Level of basket bottom	25	784	563	34.5	28.0
	350	585	445	18.7	12.8
Level of upper flange	25	553	277	53.3	47.7
	350	396	222	28.6	21.8

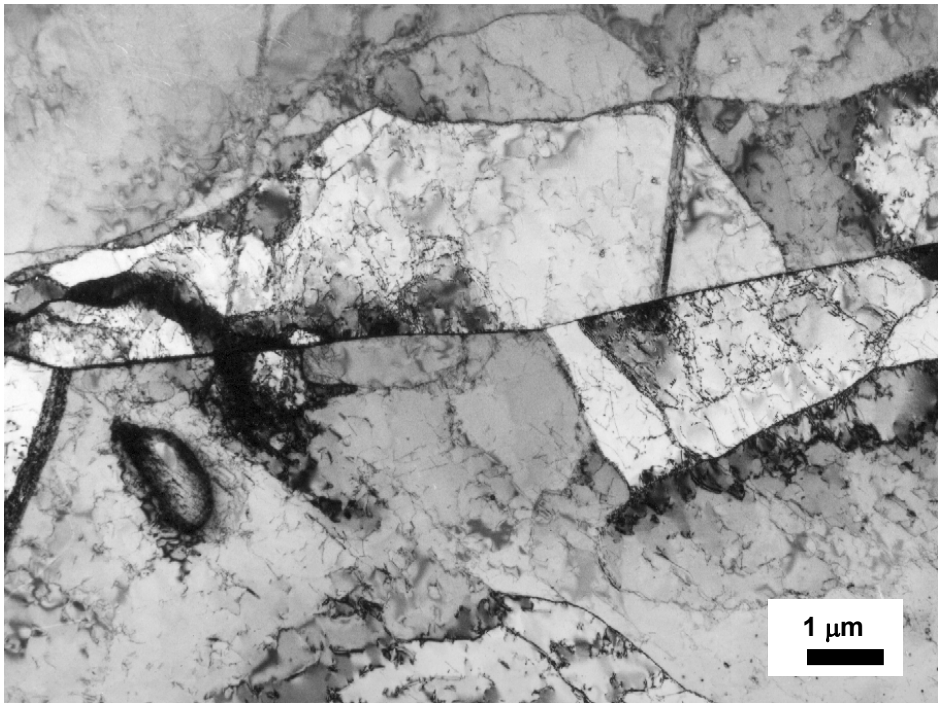

Fig. 1. Microstructure of the unirradiated steel 12X18H9T from the template cut out from the upper flange of the BR-10 reactor first vessel.

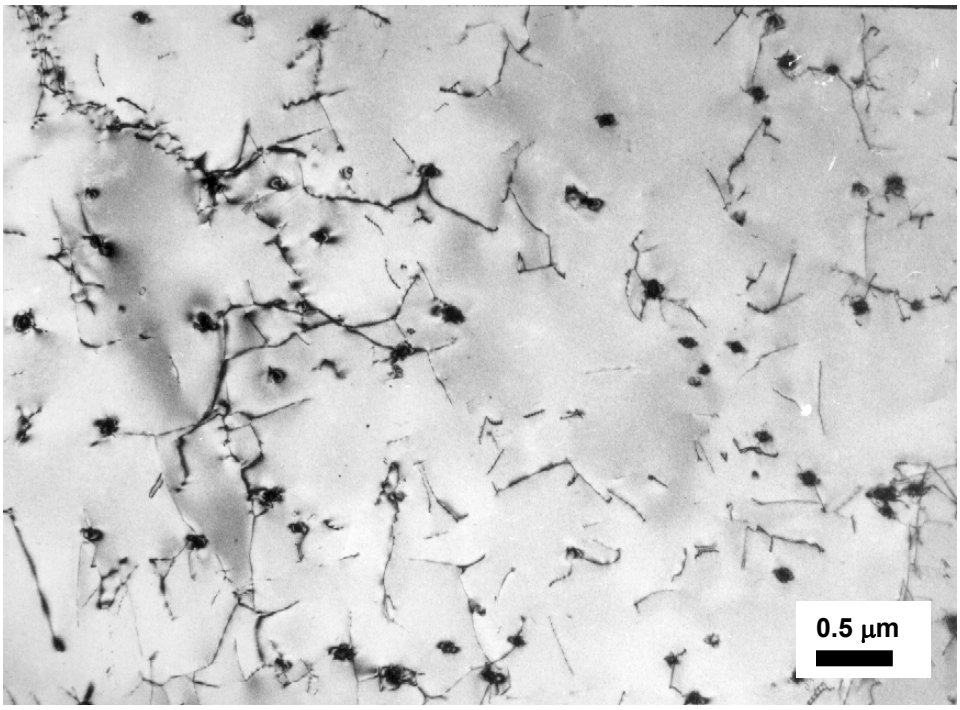

Fig. 2. Dislocations and TiC-precipitates unirradiated steel 12X18H9T (cross section of the BR-10 reactor vessel at the level of the upper flange).

Discussion

The cross section of the BR-10 vessel at the basket bottom level is quite remote from the reactor core. The dose of 0.64 dpa in this cross section has been accumulated in the vessel steel for 2563 effective full power days of reactor operation. Hence, the maximum dose rate in this cross section was equal to 0.64 dpa/2.2 $\times$ 10^8s = 2.9 $\times$ 10^{-9} dpa/s with an average dose rate of 1.9 $\times$ 10^{-9} dpa/s. In comparison, the dose rate at the center of the BR-10 core was 3.5 $\times$ 10^{-7} dpa/s. In the BN-600 fast reactor core this rate is even higher at 1.8 $\times$ 10^{-6} dpa/s [1]. The internals of Russian power reactors (VVER-440, VVER-1000) operate at considerably lower dose rates. Dose rates and doses accumulated in some internals during 30 years of operation are shown in Table 3.

As seen from Table 3, the dose rates in various internals of VVER-1000 and BN-600 are much higher than that of this steel in this current study but vary at least by one order of magnitude. Nevertheless, even at low dose rates some structural components of these reactors can accumulate rather high doses. If there exists a sensitivity to dose rate for either swelling or hardening, then there is considerable uncertainty associated with extrapolation of data from one dose rate situation to a different dose rate situation.

One can compare the swelling observed for the pressure vessel with that of wrappers and pin cladding of BR-10 fuel assemblies made from the same steel and irradiated at much higher dpa rates. The data base on swelling of the steel was obtained from examination of wrappers and fuel pins of the BR-10 reactor where the inlet sodium temperature was equal to 430ºC. For this comparison, only swelling data derived from bottom of the wrappers and claddings were selected in order to keep the temperature very close to 430ºC so there is very little uncertainty in the temperature. These in-core data are a subset of a larger data base later shown in Fig. 6 and were published in an earlier report [13].

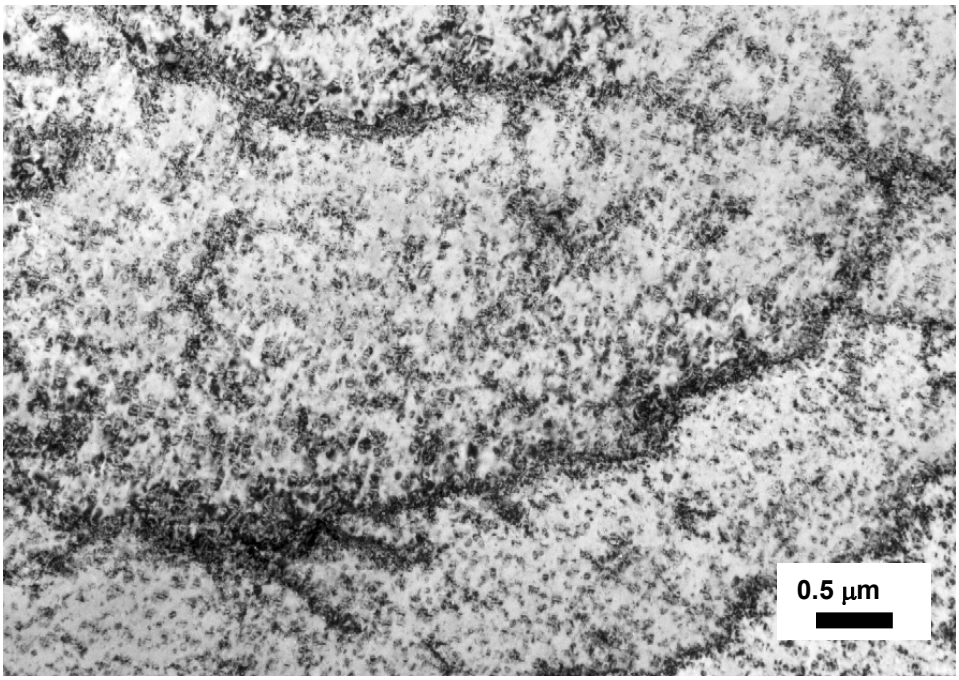

a)

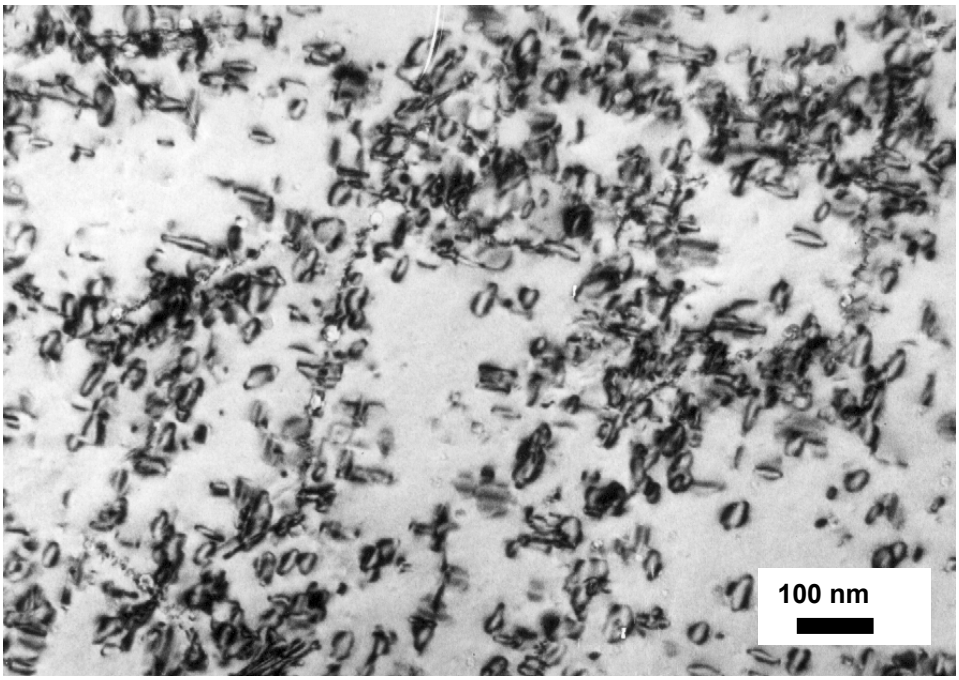

b)

Fig. 3. Dislocation loops in neutron irradiated 12X18H9T steel (cross section of theBR-10 reactor vessel at a level of the basket bottom): a) general view and b) dislocation loop arrays along previously existing sub-grain boundaries.

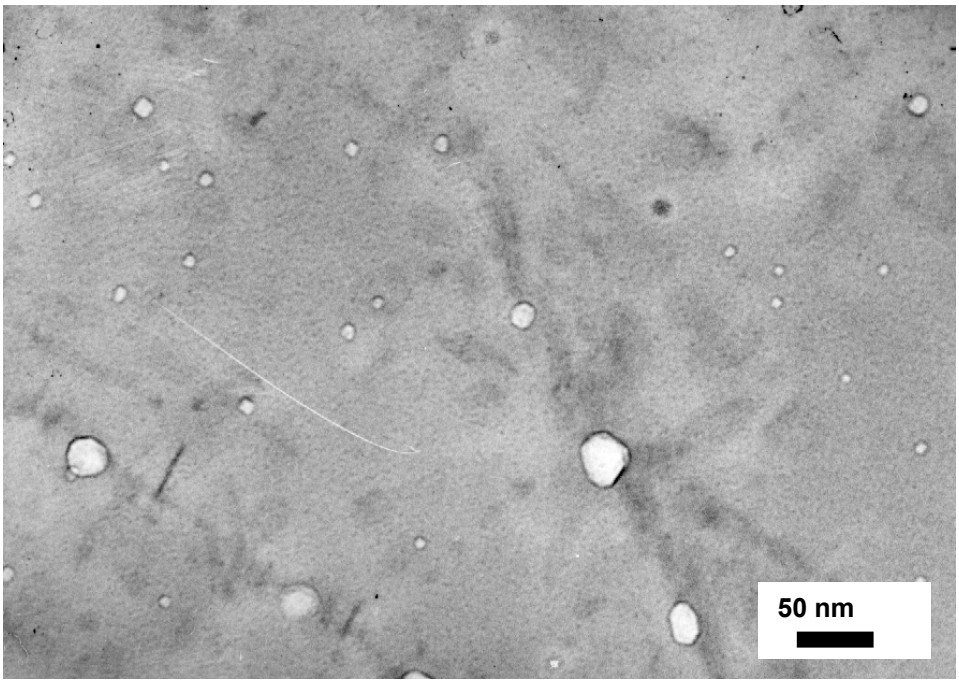

a)

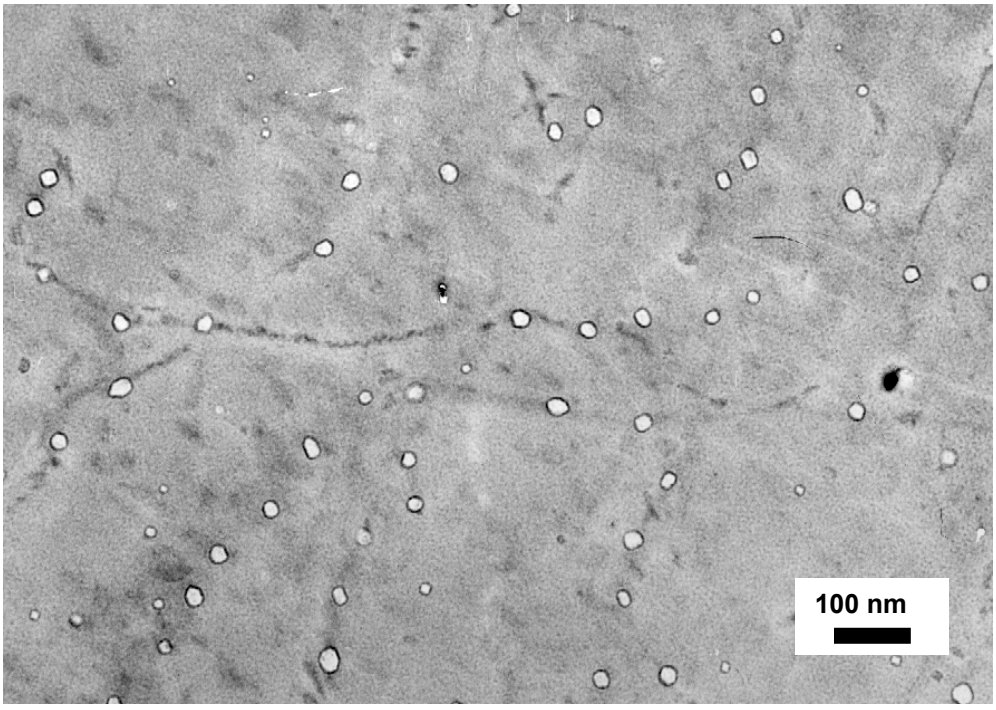

b)

Fig. 4. Voids in neutron irradiated 12X18H9T steel: a) large voids on pre-existing sub-grain boundaries and b) spatial distribution of smaller voids.

Table 3. Doses accumulated in various internals during 30 years of operation and dose rates

Structural component	Dose, dpa	Dose rate dpa/s	Reference
BN-600 fast reactor			
Subassembly sheath	35	4.5×10^{-8}	[2]
Guide tubes of control rods	15–18	$(1.9–2.3) \times 10^{-8}$	[2]
Collector bottom grid plate	2	0.6×10^{-8}	[2]
Reactor vessel	< 1	$< 0.13 \times 10^{-8}$	[2]
VVER-1000			
Baffle assembly	2–50	$(0.3–7.4) \times 10^{-8}$	[3]

The data for cladding and wrappers are shown in Fig. 5, together with the data for the vessel as a function of dose. It is seen from Fig. 6 that after the incubation dose of 4–7 dpa, the swelling of the wrapper and cladding at ~ 430ºC is an approximately linear function of dose with the swelling rate of 0.08 to 0.13 %/dpa. In general, one would expect that the vessel specimen, which spent two-thirds of its life at 350ºC, would swell less at lower temperatures, but the swelling of the vessel steel measured by microscopy is higher (~ 0.1% at only 0.64 dpa).

Since irradiation conditions for the vessel and reference fuel assemblies of BR-10 reactor differ primarily in dose rate but secondarily in temperature history, one can conclude with caution that a decrease of dose rate results in a reduction of transient period of swelling. A similar conclusion was reached following examination of AISI Type 316 fuel pin cladding after irradiation in the RAPSODIE and PHENIX fast reactors where the duration of incubation period decreases with decreasing the displacement rate [5]. The most significant observation is that voids can form at such a low dpa level, regardless of the temperature.

This rather surprising result is very consistent with a growing body of evidence that shows that a decrease in dose rate leads not only to an earlier onset of swelling with dose but also swelling that extends to lower-than-expected temperatures. Based on some earlier studies [4–5], Garner and coworkers predicted that austenitic steels serving as internal components in PWRs would exhibit unanticipated levels of void swelling [6–7]. Even more importantly, it was concluded that high dose data derived from in-core regions of high flux fast reactors would strongly under-predict the swelling that would arise at lower dpa rates characteristic of PWRs, BWRs, out-of-core regions of fast reactors, and many components of proposed fusion devices such as ITER.

A number of recent studies by Garner and coworkers have shown that void swelling in austenitic stainless steels strongly increases at lower dpa rates [8–16], often allowing the observation of the lower swelling temperature limit (~ 280ºC) at very low dpa levels. This increase in swelling arises primarily from a decrease in the duration the transient regime of swelling at lower dpa rates. As the dpa rate goes below ~ 10^{-8} dpa/sec the transient regime of swelling approaches zero dpa.

As noted earlier, a peculiarity of the irradiated microstructure is an inhomogeneous spatial distribution of dislocation loops and voids. The largest voids formed in regions of higher density of initial dislocations (i.e., in dislocation walls). The dislocation loop concentration is also higher in these regions. Surprisingly, within the limits of measurement accuracy, the mean loop diameter does not depend on the location of loops.

Addressing the change of mechanical properties, as a result of irradiation to a rather low dose of 0.64 dpa, the strength of the vessel steel increased significantly. The yield strength measured at 25ºC has increased from 277 MPa (unirradiated steel) to 563 MPa, i.e., increased by 103%. The steel ductility has also changed; the total elongation has decreased from 53.3% to 34.5%, i.e., by 18.8%.

Irradiation hardening and ductility loss at low temperatures of austenitic stainless steels in the solution treated condition has been observed many times [17–19]. The change of yield strength with dose initially occurs very quickly. At doses in the 0.5–1.0 dpa range, the yield strength of a material increases strongly, and usually reaches a saturation level at < 10 dpa. Therefore the observed strength change of the BR-10 vessel steel is similar to the behavior of other austenitic stainless steels.

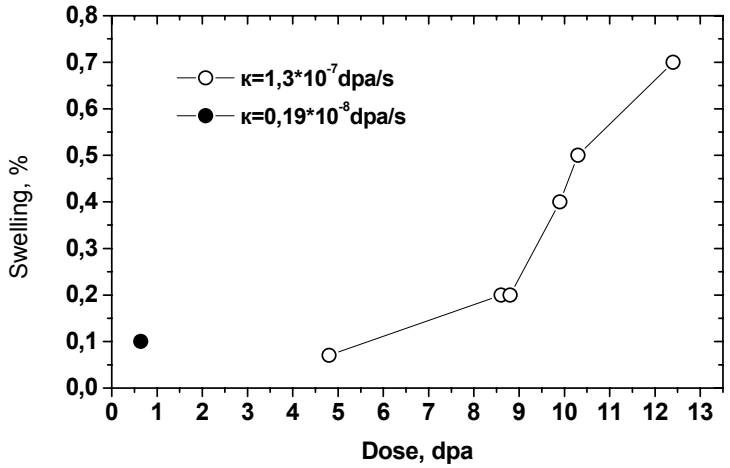

Fig. 5. Dependence of steel 12X18H9T swelling on dose. Light circles - wrappers of fuel assemblies and fuel pin claddings of BR-10 reactor at 430ºC, black circle - vessel specimen with 350-430-350ºC history. The displacement rates are shown in the figure for both sets of specimens.

It is of interest to compare the change of the yield strength of 12X18H9T steel with microstructural changes occurred under irradiation. Pre-existing straight dislocations have disappeared completely under irradiation with dislocation loops and voids taking their place without any changes in the precipitate structure, which is the same in both cases.

In this case, by assuming an additive superposition of different dislocation barriers, the change of yield strength of the steel can be written as follows:

$$\Delta\sigma = MGb[\alpha_v(d_vN_v)^{1/2} + \alpha_l(d_lN_l)^{1/2} - \alpha_d\rho_d^{1/2}] \quad (1)$$

where the Taylor factor M = 3.06; G=78.7; GPa (at 25ºC) is the shear modulus; b = 0.25; nm is the Burgers vector; α_v, α_l, and α_d are the barrier constants for voids, dislocation loops, and dislocations, respectively; d_v and d_l are the mean diameters of voids and dislocation loops; N_v and N_l are the concentrations of voids and dislocation loops, respectively; ρ_d is the density of straight dislocations.

Using the microstructural data for d_v, dl, N_v, N_l, and ρ_d to obtain the value of $\Delta\sigma$ from Eq. (1), one concludes that when the values of barrier constants known from the literature (α_v = 1.0, α_l = 0.33, and α_d = 0.20) are assumed, the calculated increase of yield strength is 267 MPa compared to the measured value of 286 MPa. If there is any significance to this relatively small difference, the discrepancy may arise from the non-uniform spatial distribution of voids and loops in the irradiated steel, but such conjecture is entirely speculative.

Finally, it should be noted that most previous perceptions concerning the lower boundary of void swelling and the flux-dependence of the lower temperature limit of swelling were established using reactors with relatively high inlet temperatures, such as 350ºC in BR-10 and 365–370ºC in FFTF and EBR-II. As shown

in Fig. 6, when swelling data on the same steel are compiled from reactors with different inlet temperatures and from data derived from both fueled and unfueled zones, then the apparent lower limit of swelling moves toward the lowest inlet temperature. Thus the previously published BR-10 in-core data imply that swelling ceases between 400 to 430ºC, but swelling actually develops down to significantly lower temperatures, as seen in both the vessel specimen and in specimens taken from the reflector region of BN-350 with its lower inlet temperature of 280ºC.

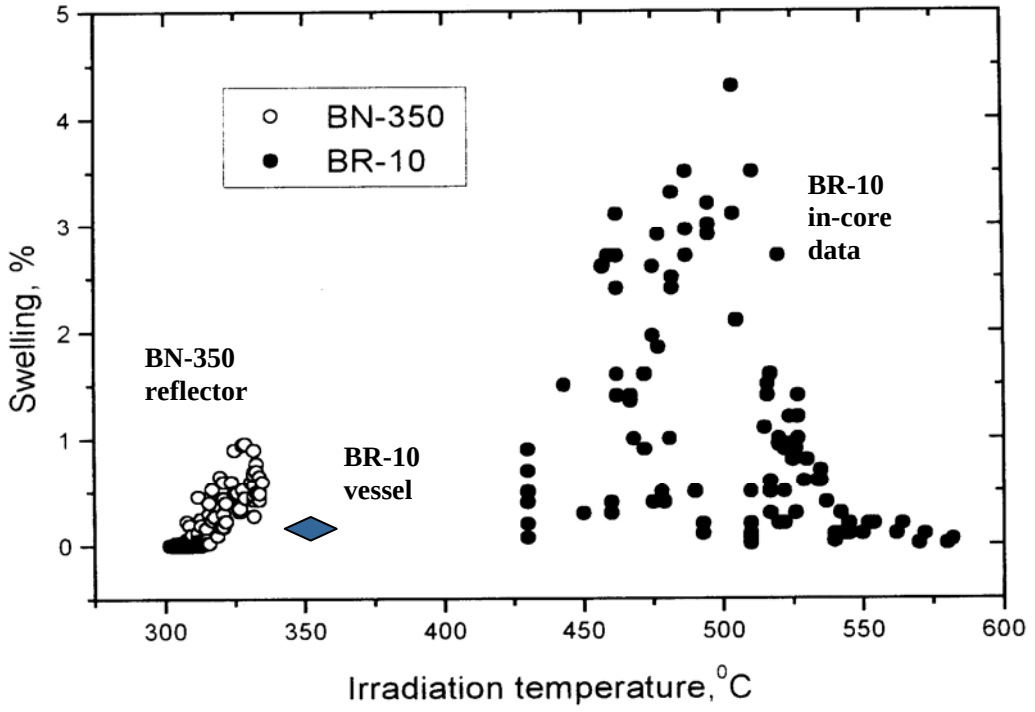

Fig. 6. Comparison of swelling data on annealed austenitic steel 18Cr-10Ni-Ti derived from three separate sources in two fast reactors [13]. The BR-10 data shown at 430ºC was presented earlier in Fig. 5. The added datum of the BR-10 vessel is shown at 350ºC only for convenience.

Conclusions

Examination of the microstructure, swelling, and short-term mechanical properties of the BR-10 reactor first vessel steel (12X18H9T) after irradiation to 0.64 dpa at a very low displacement rate of 1.9 × 10-9 dpa/s leads to the following conclusions:

1. Neutron irradiation under such conditions results in a significant reduction of the swelling incubation dose to < 1 dpa as compared with incubation dose of 4–7 dpa in cladding and wrapper materials of BR-10 reactor at a dose rate of ~ 1.3×10^{-7} dpa/s.

2. The spatial distribution of both dislocation loops and voids in the irradiated steel is non-uniform and appears to be caused by the initial non-uniformity of dislocation structure.

Irradiation resulted in hardening accompanied with a ductility loss.

Acknowledgements

This work was supported by the Russian Foundation for Basic Research under the Project # 04-02-17278. The U.S. portion was jointly sponsored by the Materials Science Branch, Office of Basic Energy Sciences, and the Office of Fusion Energy, U.S. Department of Energy.

References

[1] B. A. Vasiljev, A. I. Zinovjev, A. I. Staroverov, V. V. Maltsev, and A. N. Ogorodov, “Status and possibility of fuel and structural materials experimental irradiation in BN-600 reactor, Stages of BN-600 reactor core development,” Proceedings of a technical committee meeting, “Influence of high dose irradiation on core structural and fuel materials in advanced reactors,” Obninsk, Russia, June 16–19, 1997, pp. 37–46.

[2] A. I. Kiryushin, V. A. Rogov, A. I. Zinovyev, and V. A. Dolgov, “Provisions for BN reactors for low dose irradiation of materials,” Proceedings of a specialists meeting, “Influence of low dose irradiation on the design criteria of fixed internals in fast reactors,” IAEA-TECDOC-817, Gif-sur-Yvette, France, December 1–3, 1993, pp. 39-50.

[3] V. M. Troyanov, Yu. I. Likhachev, M. Ya. Khmelevsky et al., “Evaluation and analysis of thermo-mechanical behavior of internals of WWERs taking into account irradiation effects,” Proceedings of 5th Russian Conference on Reactor Materials Science, Dimitrovgrad, Russia, September 8–12, 1997, Vol. 2, Part I, pp. 3–18.

[4] D. L. Porter and F. A. Garner, “Swelling of AISI Type 304L Stainless Steel in Response to Simultaneous Variation in Stress and Displacement Rate,” Effects of Radiation on Materials: Twelfth International Symposium, ASTM STP 870, F. A. Garner and J. S. Perrin (eds.), American Society for Testing and Materials, Philadelphia (1985) 212–220.

[5] J. L. Seran and J. M. Dupouy, “The swelling of solution annealed 316 cladding in RAPSODIE and PHENIX,” Effects of Radiation on Materials: Eleventh Symposium, ASTM STP 782, H. R. Brager and J. R. Perrin (eds.), American Society for Testing and Materials (1982) 5–16.

[6] F. A. Garner, L. R. Greenwood, and D. L. Harrod, "Potential High Fluence Response of Pressure Vessel Internals Constructed from Austenitic Stainless Steels," Proceedings of the Sixth International Symposium on Environmental Degradation of Materials in Nuclear Power Systems--Water Reactors, San Diego, August 1–5, 1993, pp. 783–790.

[7] F. A. Garner, "Materials Issues Involving Austenitic Pressure Vessel Internals Arising From Void Swelling and Irradiation Creep," Trans. Am. Nucl. Soc. 71 (1994) 190.

[8] F. A. Garner and M. B. Toloczko, "Irradiation Creep and Void Swelling of Austenitic Stainless Steels at Low Displacement Rates in Light Water Energy Systems," J. Nucl. Mater. 251–252 (1997).

[9] D. J. Edwards, E. P. Simonen, F. A. Garner, B. A. Oliver, and S. M. Bruemmer, “Sensitivity of Microstructural Evolution Due to Temperature and Dose Gradients in Neutron-Irradiated 316SS,” J. Nucl. Mater. 317 (2003) 32.

[10] T. Okita, T. Sato, N. Sekimura, F. A. Garner, and L. R. Greenwood, “The Primary Origin of Dose Rate Effects on Microstructural Evolution of Austenitic Alloys During Neutron Irradiation,” J. Nucl. Mater. 207–211 (2002) 322.

[11] T. Okita, T. Sato, N. Sekimura, F. A. Garner, and W. G. Wolfer, “Combined Effect of Temperature, Displacement Rate and Composition on the Neutron-Induced Swelling of Austenitic Alloys,” 11th International Conference on Environmental Degradation of Materials in Nuclear Power Systems--Water Reactors, August 2003, issued on CD format.

[12] V. S. Neustroev, V. K. Shamardin, Z. E. Ostrovsky, A. M. Pecherin, and F. A. Garner, “Temperature-Shift of Void Swelling Observed at PWR-Relevant Temperatures in Annealed Fe-18Cr-10Ni-Ti Stainless Steel Irradiated in the Reflector Region of BOR-60," Effects of Radiation on Materials: 19th International Symposium, ASTM STP 1366, M. L. Hamilton, A. S. Kumar, S. T. Rosinski, and M. L. Grossbeck (eds.), American Society for Testing and Materials (2000) 792–800.

[13] F. A. Garner, N. I. Budylkin, Yu. V. Konobeev, S. I. Porollo, V. S. Neustroev, V. K. Shamardin, and A. V. Kozlov, “The Influence of DPA Rate on Void Swelling of Russian Austenitic Stainless Steels,”

10th International Conference on Environmental Degradation of Materials in Nuclear Power Systems--Water Reactors (2003) 647–656.

[14] O. P. Maksimkin, K. V. Tsai, L. G. Turubarova, T. Doronina, and F. A. Garner, “Characterization of 08Cr16Ni11Mo3 Stainless Steel Irradiated in the BN-350 Reactor,” J. Nucl. Mater. 329–333 (2004) 625.

[15] O. P. Maksimkin, K. V. Tsai, L. G. Turubarova, T. Doronina, and F. A. Garner, “Void swelling of AISI 321 analog stainless steel irradiated at low dpa rates in the BN-350 reactor, Fusion Reactor Materials Semiannual Progress Report, July 2005 (submitted); ICFRM-12 (submitted).

[16] V. S. Neustroev, V. N. Golovanov, V. K. Shamardin, Z. E. Ostrovsky, and A. M. Pecherin, “Irradiation phenomena in X18H10T steel irradiated in different reactors under conditions relevant to operation conditions of internals of VVERs,” Proceedings of 6th Russian Conference on Reactor Materials Science, Dimitrovgrad, Russia, September 11–15, 2000, Vol. 3, Part I, pp. 3–23.

[17] G. R. Odette and G. E. Lucas, “The effects of intermediate temperature irradiation on the mechanical behavior of 300-series austenitic stainless steels,” J. Nucl. Mater. 179–181 (1991) 572.

[18] G. E. Lucas, “The evolution of mechanical property change in irradiated austenitic stainless steels,” J. Nucl. Mater. 206 (1993) 278.

[19] D. J. Edwards, E. P. Simonen, F. A. Garner, L. R. Greenwood, B. M. Oliver, and S. M. Bruemmer, “Influence of irradiation temperature and dose gradients on the microstructural evolution in neutron-irradiated 316SS,” J. Nucl. Mater. 317 (2003) 32.

7.0 MHD INSULATORS, INSULATING CERAMICS, AND OPTICAL MATERIALS

COMPATIBILITY OF MULTI-LAYER, ELECTRICALLY INSULATING COATINGS FOR THE VANADIUM-LITHIUM BLANKET—B. A. Pint and J. L. Moser (Oak Ridge National Laboratory), A. Jankowski and J. Hayes (Lawrence Livermore National Laboratory)

OBJECTIVE

The objective of this work is to demonstrate that a multi-layer, electrically-insulating coating will be an acceptable solution to reduce the magneto hydrodynamic (MHD) force in the first wall of a lithium cooled blanket. Coatings of Er_2O_3 or Y_2O_3 with an overlying coating of vanadium have been fabricated by physical vapor deposition. Coatings have demonstrated acceptable as-received resistivity at 800°C and at 600°C in contact with Li. When the Y_2O_3 coating was completely covered with a 10μm vanadium layer, it survived exposure to Li at 800°C without degradation. The interaction between V alloys and Li at 800°C is now the critical compatibility issue and a loop test is being planned. New ceramic materials based on the Y-Ti-O system also are being explored.

SUMMARY

Multi-layer coatings are being investigated to reduce the MHD pressure drop in a lithium-cooled blanket. As the fabrication process is improved, the performance of the coatings is improving with adequate as-deposited and in-situ resistance, and good compatibility being demonstrated in a recent capsule test. The compatibility of a thin (10-100μm) vanadium overlayer is now critical to coating durability. Initial experiments showed no dissolution of V-4Cr-4Ti after 1,000h at 800°C although the specimens were embrittled after exposure. A planned monometallic loop experiment will help verify the compatibility of V-4Cr-4Ti in Li at 700°C. New insulating ceramic materials are being investigated with $Y_2Ti_2O_7$ showing some promise for this application.

PROGRESS AND STATUS

Introduction

A self-cooled lithium blanket concept is an attractive concept for a fusion reactor because of lithium's tritium breeding capability and excellent heat transfer characteristics. Due to compatibility issues with conventional alloys[1-2] and SiC[3], vanadium alloys[4-6] are the most likely structural materials for this concept. One of the critical issues for this, and any liquid-metal concept, is the need to reduce the pressure drop associated with the magnetohydrodynamic (MHD) force due to the high magnetic field in the reactor.[7-8]

One solution to the MHD problem is to apply an electrically insulating coating to decouple the structure wall from the liquid metal.[9] The coating must be thin, durable and have a high electrical resistivity. It also must be almost crack-free to prevent shorting.[10,11] For many years, the idea of a "self-healing" CaO insulating coating was promoted and investigated.[12-15] However, thermodynamic and experimental results suggested poor long-term stability.[16] Therefore, the current focus of the U.S. program on reducing the MHD pressure drop is on durable multi-layer coatings or a flow-channel insert.[16,17] Both of these solutions has been previously proposed,[8,18,19] however, little experimental verification has been conducted. Therefore, multi-layer coatings have been fabricated for screening and qualification testing. With a multi-layer coating, the compatibility between the V or V alloy overcoat and Li becomes more critical and this issue is being investigated, including plans for a loop experiment. Finally, new ceramic Y-Ti-O candidate coating materials are being explored.

Experimental Procedure

Multi-layer coatings were fabricated on 15mm diameter V-4Cr-4Ti substrates using electron-beam physical vapor deposition (EB-PVD) at Lawrence Livermore National Laboratory (LLNL). Coatings were either Er_2O_3 or Y_2O_3 with vanadium overlayers. The resistivity of as-received coatings was measured in vacuum at temperatures up to 800°C, and specimens were sectioned by focused ion beam (FIB) thinning and examined by scanning electron microscopy (SEM). Bowl shaped V-4Cr-4Ti specimens (5 cm diameter, ~1 mm thickness) provided by NIFS in Japan were coated by the same process for measuring the in-situ resistivity in contact with Li (~0.5g placed in the bowl) at temperatures up to 600°C.[20] The unit was designed to measure resistance of a coating on a bowl shaped specimen filled with 0.5g of Li at temperatures up to 600°C in an Ar-filled glove box (to minimize Li reaction with O and N). Springs hold the bowl in contact with an alumina disk and a Mo heater.

The compatibility of V-4Cr-4Ti specimens with and without coatings was investigated by conducting capsule experiments using a Mo inner capsule and a type 304 stainless steel outer capsule. High-purity, unalloyed Li (5g) was added to each capsule. The capsules were exposed isothermally at 800°C in resistively heated box furnaces. To explore new materials, mixtures of Y_2O_3 and TiO_2 powder were mixed in a ball mill, cold compacted and sintered in air at temperatures up to 1600°C. The phase composition was checked using x-ray diffraction (XRD).

Results and Discussion

X-ray diffraction of the as-deposited EB-PVD coatings on V-4Cr-4Ti substrates showed that the coatings were poly-crystalline Er_2O_3 when deposited with a substrate temperature of >950 K. However, at lower substrate deposition temperatures, additional phases were detected, possibly ErO_6. The first batch of coatings had a 2µm vanadium overlayer which only covered the center of the Er_2O_3 coating. Due to the roughness of the underlying oxide, the vanadium layer was convoluted and not likely fully dense [17]. Figure 1 shows the resistivity of an 8µm EB-PVD Er_2O_3 coating as a function of temperature. The

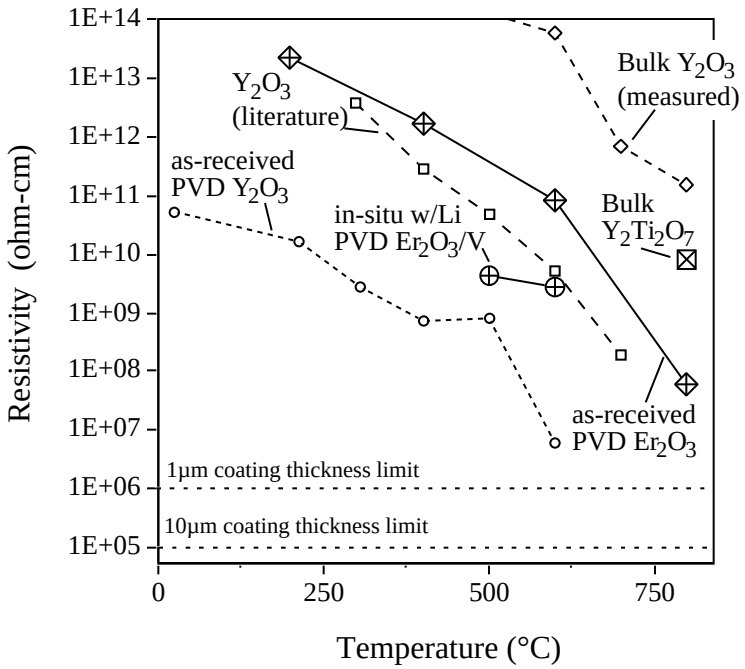

Fig. 1. Resistivity as a function of temperature for as-received EB-PVD Er_2O_3 and Y_2O_3 coatings compared to literature and measured values for bulk Y_2O_3 and bulk $Y_2Ti_2O_7$.

resistivity was higher than the first batch of 12μm thick EB-PVD Y_2O_3 coatings[16] and well above the minimum requirements.[9,12] One specimen from this batch was exposed to Li in a capsule test for 1000h at 800°C. The coating was highly degraded. Thus, neither a single layer of Y_2O_3 or Er_2O_3 is likely to meet the durability goals.

In order to better test the multi-layer concept, a second batch of coatings was produced with a 10-14μm vanadium overlayer which completely covered the ~10μm thick Y_2O_3 or Er_2O_3 oxide layer. The surface morphology of the vanadium outer layer is shown in Fig. 2. Because the vanadium overlayer was in contact with the V-4Cr-4Ti substrate, it was not possible to measure the resistivity of the as-deposited coatings in this batch but it is expected that the as-deposited resistivity would be similar to prior batches. One coated coupon from this batch was exposed to Li in a capsule test for 100h at 800°C and survived with a minor mass gain (0.16 mg/cm^2) which is consistent with other exposures (see next section). In order to measure the post-test coating resistivity, the outer V layer needs to be partially machined away in order to isolate it from the V-4Cr-4Ti substrate. This procedure is currently being developed.

In both batches, bowl-shaped specimens were fabricated for in-situ testing. Previously it was reported that the coatings from the first batch, 8μm Er_2O_3 alone and 11μm Er_2O_3 + 2μm V, were tested in-situ to 500°C but shorted when the Li became liquid at ~180°C.[17] After the Li was removed by cleaning with ethanol or by vacuum distillation, both coatings degraded and essentially were removed where the Li was in contact with the coating. The rapid degradation may have been due to the less-stable ErO_6 phase being present in the coatings. The second batch of materials included one bowl with 18μm Er_2O_3 + 10μm V and another with 16μm Y_2O_3 and 14μm V. The Y_2O_3/V coated bowl was heated to 500°C without Li and the resistance was too high to be measured by the multimeter in the glove box. (>10MΩ) When the Li was added, the specimen showed high resistivity up to 250°C but then shorted during heating to 500°C. As before, after vacuum distillation to remove the Li, the coating was degraded where the Li was in contact with the coating. The Er_2O_3/V coated bowl showed a resistance of 8MΩ at 500°C with no Li. When Li was added, a similar resistance was measured at 500°C and 600°C. The resistance values were converted to

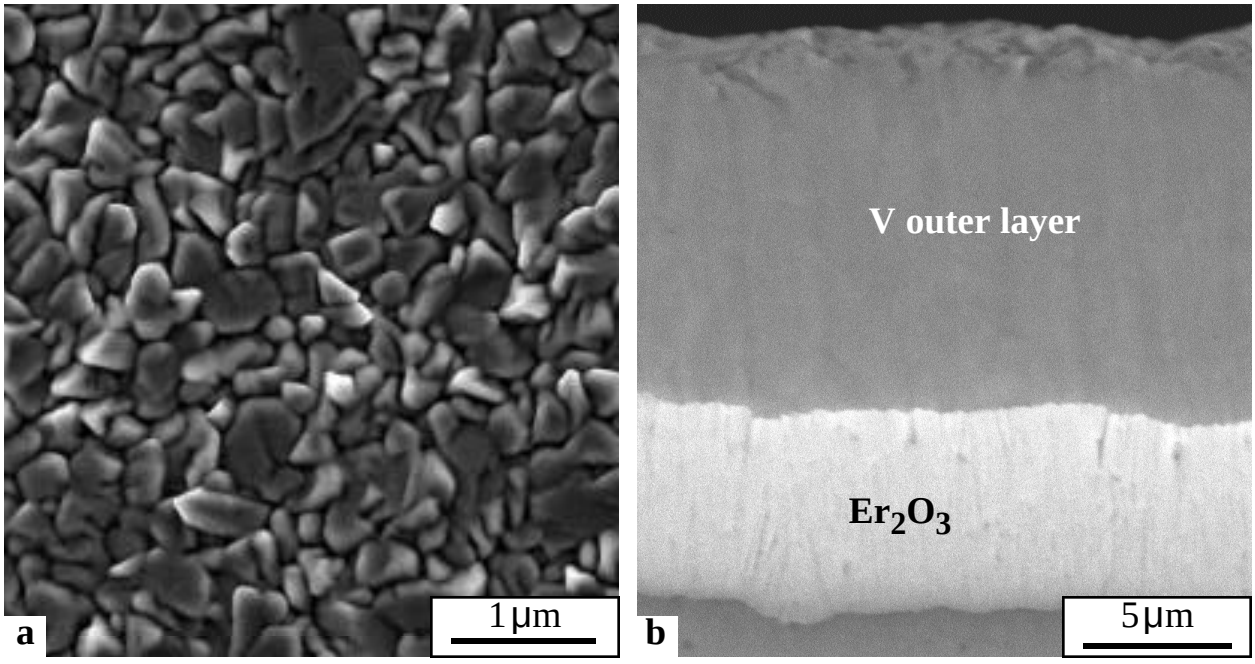

Fig. 2. SEM secondary electron images (a) plan-view of the as-received EB-PVD Y_2O_3/V coating showing the outer V coating morphology and (b) FIB-section of the as-received EB-PVD Er_2O_3/V coating.

resistivity and are shown in Fig. 1. The resistance dropped from 7.8 to 4.3MW when the bowl was held for 24h at 500°C but this was partially attributed to the Li evaporation and reaction in the glove box atmosphere. While these results were positive, the coating delaminated where it was in contact with Li after cleaning (Fig. 3).

Vanadium-lithium compatibility. Solutions to the MHD problem which use multi-layer coatings or a flow channel insert[17] rely on excellent long-term compatibility between the vanadium overlayer and Li since this layer would be restricted to <100µm.[21] A brief summary of the vanadium-lithium compatibility literature[22] showed a wide range of results with no systematic study of the effects or relative importance of alloying elements and Li impurities. Ideally, a monometallic loop with relatively high purity Li and V specimens is needed and this experiment is currently being planned with V-4Cr-4Ti tubing ordered for loop construction.

Previous testing of ceramic specimens in Li was conducted with V alloy capsules and no V was detected in the Li after exposures for up to 1,000h at 800°C.[23] The results of a recent capsule experiment using V-4Cr-4Ti tensile specimens (SS-3 type) and a relatively inert Mo capsule are summarized in Fig. 4. The mass gains can be explained due to the uptake of C and N in the system.[17] However, the drop in room temperature ductility from ~30% total elongation to 0-5% was unexpected and could be related to the C and N uptake or H uptake during cleaning in methanol or to the formation of X-Li-N compounds.[24] The other important observation from this experiment was that neither V, Cr or Ti was detected in the Li after the test (Table 1). The high Mo content after the test was unexpected but very little Mo was detected on the specimens using Auger electron spectroscopy.[17] Additional experiments are needed to better understand this system.

New ceramic materials. While Er_2O_3 and Y_2O_3 are the primary electrically insulating materials being investigated, it would be desirable to have a ceramic that was more compatible with Li in case of degradation of the V overlayer. All of the realistic binary compound oxides have been considered, thus ternary or higher compounds are now being examined. There has been significant recent interest in the formation of stable Y-Ti-O particles in dispersion-strengthened steels.[25] While there is little thermodynamic information available for these compounds,[26] the possibility of a ternary oxide inhibiting the formation of $LiYO_2$[27] is worth investigating.

Fig. 3. Photograph of the Er_2O_3/V coated specimen after exposure to Li. A pool of liquid Li was in the center of the bowl at up to 500°C.

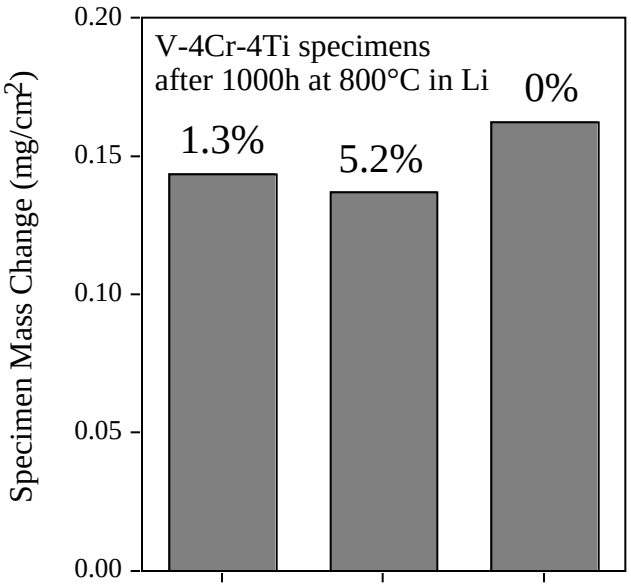

Fig. 4. Specimen mass gains for three V-4Cr-4Ti tensile specimens exposed to Li for 1000h at 800°C in a Mo capsule and the total elongation at room temperature after exposure.

Coupons (~1cm diameter, 3mm thick) of $Y_2Ti_2O_7$ were fabricated and found to be single phase by XRD. An initial resistance measurement showed a reasonably high value at 800°C (Fig. 1). Coupons with a 1:1 mixture of Y_2O_3 and TiO_2 did not form Y_2TiO_5 as expected, but instead XRD showed a mixture of Y_2O_3 and $Y_2Ti_2O_7$. The compatibility of bulk $Y_2Ti_2O_7$ in Li will be examined before coatings are fabricated.

Table 1. Chemical composition using inductively coupled plasma (metals), combustion (C), micro-Kjeldhal (N) and neutron activation (O) analyses of the starting Li and the Li after the 800°C 1000h capsule exposure (in ppmw)

Test	Al	Ba	C	Ca	Cr	Cu	Fe	Mg	Mo	N	Na	O	Si	Ti	V	Zn
Starting	<20	18	95*	20	<3	<5	<10	10	<8	65†	30	950*	<20	<3	<3	4
800°C	<30	17	**<50**	30	**<3**	6	10	<10	**89**	<100	30	**1400**	30	**<3**	**<3**	6

* average of 5 analyses

† vendor specification, <100 by analysis

References

[1] J. H. DeVan, J. Nucl. Mater. 85-86 (1979) 249.
[2] O. K. Chopra, D. L. Smith, P. F. Tortorelli, J. H. DeVan, and D. K. Sze, Fusion Technol. 8 (1985) 1956.
[3] T. Yoneoka, S. Tanaka, and T. Terai, Mater. Trans. 42 (2001) 1019.
[4] R. J. Kurtz, K. Abe, V. M. Chernov, V. A. Kazakov, G. E. Lucas, H. Matsui, T. Muroga, G. R. Odette, D. L. Smith, and S. J. Zinkle, J. Nucl. Mater. 283-287 (2000) 70.
[5] T. Muroga, T. Nagasaka, K. Abe, V. M. Chernov, H. Matsui, D. L. Smith, Z.-Y. Xu, and S. J. Zinkle, J. Nucl. Mater. 307-311 (2002) 547.
[6] R. J. Kurtz, K. Abe, V. M. Chernov, D. T. Hoelzer, H. Matsui, T. Muroga, and G. R. Odette, J. Nucl. Mater. 329-333 (2004) 47.
[7] I. R. Kirillov, C. B. Reed, L. Barleon, and K. Miyazaki, Fusion Eng. Des. 27 (1995) 553.
[8] L. Barleon, V. Casal, and L. Lenhart, Fusion Eng. Des. 14 (1991) 401.
[9] S. Malang, H. U. Borgstedt, E. H. Farnum, K. Natesan, and I. V. Vitkovski, Fusion Eng. Des. 27 (1995) 570.
[10] L. Bühler, Fusion Eng. Des. 27 (1995) 650.
[11] A. Y. Ying and A. A. Gaizer, Fusion Eng. Des. 27 (1995) 634.
[12] J. H. Park and T. F. Kassner, J. Nucl. Mater. 233-237 (1996) 476.
[13] K. Natesan, M. Uz, and S. Wieder, J. Nucl. Mater., 283-287 (2000) 1277-1281.
[14] D. L. Smith, K. Natesan, J. H. Park, C. B. Reed, and R. F. Mattas, Fusion Eng. Des. 51-52 (2000) 185.
[15] D. L. Smith, J. Konys, T. Muroga, and V. Evitkhin, J. Nucl. Mater. 307-311 (2002) 1314.
[16] B. A. Pint, P. F. Tortorelli, A. Jankowski, J. Hays, T. Muroga, A. Suzuki, O. I. Yeliseyeva, and V. M. Chernov, J. Nucl. Mater. 329-333 (2004) 119.
[17] B. A. Pint, J. L. Moser, and P. F. Tortorelli, Fusion Engineering and Design (in press).
[18] Y. Y. Liu and D. L. Smith, J. Nucl. Mater. 141-143 (1986) 38.
[19] I. V. Vitkovsky et al., Fusion Eng. Des. 61-62 (2002) 739.
[20] B. A. Pint, K. L. More, J. L. Moser, A. Jankowski, and A. Suzuki, DOE-ER-0313/37 (2005) 101.
[21] D.-K. Sze, private communication (2003).
[22] B. A. Pint, K. L. More, H. M. Meyer, and J. R. DiStefano, Fusion Sci. Technol. 47 (2005) 851.
[23] B. A. Pint, J. H. DeVan, and J. R. DiStefano, J. Nucl. Mater. 307-311 (2002) 1344.
[24] P. Hubberstey and P. G. Roberts, J. Nucl. Mater. 155-157 (1988) 694.
[25] S. Ukai and M. Fujiwara, J. Nucl. Mater. 307 (2002) 749.
[26] P. F. Tortorelli, B. A. Pint, and T. M. Besmann, DOE-ER-0313/36 (2004) 81.
[27] T. Terai, T. Yoneoka, H. Tanaka, A. Suzuki, S. Tanaka, M. Nakamichi, H. Kawamura, K. Miyajima, and Y. Harada, J. Nucl. Mater. 233-237 (1996) 421.

INVESTIGATION OF Pb-Li COMPATIBILITY FOR THE DUAL COOLANT TEST BLANKET MODULE—
B. A. Pint, J. L. Moser, and P. F. Tortorelli (Oak Ridge National Laboratory, USA)

OBJECTIVE

The objective of this task is to assess the long-term, high-temperature compatibility of various materials with Pb-Li. One proposed fusion reactor concept uses SiC/SiC composites with a self-cooled Pb-17Li blanket. Another concept uses a SiC/SiC flow channel insert with a dual coolant of He and Pb-Li at ~800°C. This concept also requires tubing material to carry the Pb-Li between the first wall and the heat exchanger. As a first step in the evaluation process, monolithic SiC and potential tubing and coating materials are being exposed to Pb-17Li in capsule tests at 700°-1200°C.

SUMMARY

Static Pb-17Li capsule tests were performed on monolithic SiC specimens and Al-containing alloys. Both systems showed little or no dissolution in Pb-Li likely due to the formation of a protective surface oxide which was expected to be stable based on thermodynamic evaluations. For SiC, Si was detected in the Pb-Li only at the highest test temperatures (2,000h at 1100°C and 1000h at 1200°C). The addition of Al to Fe- or Ni-base alloys resulted in a significant decrease in the amount of dissolution after 1000h at 700° and 800°C compared to type 316 stainless steel. Chemical vapor deposited (CVD) aluminide coatings on type 316 substrates significantly reduced the dissolution rate at 800°C. With or without pre-oxidation, Al-containing alloys or coatings formed an Al_2O_3 surface layer. These results demonstrate that aluminide coatings could protect a conventional Fe- or Ni-base tubing alloy to carry Pb-Li between the first wall and the heat exchanger. Future work will need to include testing in a flowing system with a thermal gradient to fully determine the compatibility of these materials.

PROGRESS AND STATUS

Introduction

Among the proposed test blanket module (TBM) concepts for ITER, one possibility is a dual coolant (He and Pb-Li) system using advanced ferritic steels as the structural material and a silicon carbide composite as a flow channel insert.[1,2] Although the TBM design will operate at <500°C, thereby limiting compatibility problems, ultimately this concept would be more attractive with a maximum operating temperature of 700-800°C. In this temperature range, critical compatibility issues need to be addressed. Recent effort has been focused on the compatibility of ferritic-martensitic steels in Pb-Li at 400-600°C.[3,4] However, there has been less work examining SiC/SiC composites and corrosion-resistant coatings needed at higher temperatures.

The compatibility of SiC/SiC composites with Pb-17Li is of interest as a flow channel insert to reduce both corrosion and the MHD pressure drop and as a higher temperature (1000°-1100°C) structural material.[5] SiC dissolves readily in Li at <500°C.[6] However, the activity of Li is much lower in Pb-17Li (e.g., 1.2×10^{-4} at 500°C)[7] such that the native surface oxide on SiC, SiO_2, is stable. The same argument applies for Al-containing alloys or coatings that could form a protective external Al_2O_3 in Pb-Li.[8] Coatings are of interest for tubing materials to carry Pb-Li from the first wall to the heat exchanger at ~700°C. While a SiC flow channel insert could protect the steel walls from Pb-Li dissolution, it is unlikely this strategy could be used through the entire flow path. Contact of Fe- or Ni-base, alloys with flowing Pb-Li at this temperature would result in unacceptably high dissolution rates.[3,4,9] Although the use of refractory metals is one option,[10] fabrication and durability of Nb or Mo tubing could be an issue. A protective coating could allow a conventional Fe- or Ni-base tubing alloy to be used.

Baseline compatibility data is being developed using static capsule tests and model materials. Studying monolithic SiC avoids issues with composites, such as fiber interfaces and porosity. Initially, a range of Al-containing alloys were studied. Based on positive results at 700°C, CVD aluminide coatings on type 316 stainless steel substrates were tested at 800°C. Both sets of experiments show promising results, consistent with the thermodynamic assessment.

Experimental Procedure

Capsule tests with static PbLi (detailed elsewhere[11]) were performed on dense, monolithic, high-purity (99.9995%) chemical vapor deposited (CVD) β-SiC specimens (3 x 8 x 12 mm) with a density of 3.21g/cm^3. To avoid unwanted reactions, the SiC specimen and Pb-Li were contained in CVD SiC capsules and welded Mo intermediate capsules. The 1200°C experiment used an outer capsule of alloy 602CA (Ni-26at%Cr-9Fe-5Al). In all tests, the capsules were loaded with high purity (99.9999%) Pb shot and Li in an argon-filled glove box. Specimen mass was measured before and after exposure on a Mettler-Toledo balance with an accuracy of ±0.04 mg. Exposures were performed in resistively heated box furnaces.

The chemical composition of the Al-containing alloys tested at 700° and 800°C are shown in Table I. A Fe_3Al composition was selected as being similar to aluminide coatings formed on Fe-base alloys[12-14] and a Ni-42Al composition is similar to the composition of a CVD aluminide coating on a Ni-base alloy.[15] In addition, an oxide dispersion strengthened (ODS) FeCrAl (Plansee alloy PM2000) was tested as this alloy, or similar commercial tubing alloys (e.g. Kanthal alloy APMT),[16] could be used without a coating. The 1.5mm thick specimens had a surface area of 4-5 cm^2 and were polished to a 600grit SiC finish. The alloy specimens were not pre-oxidized before testing at 700°C but were pre-oxidized for 2h at 1000°C in 1 atm dry O_2 before exposure at 800°C. Two specimens of type 316 stainless steel were CVD aluminized for 4h at 1050°C in a laboratory scale reactor and then immediately annealed for 2h at the same temperature.[13,14] These conditions produce a coating approximately 200μm thick with an Al-rich outer layer, ~$(Fe,Ni)_3Al$, about 20μm thick. All metal specimens were ultrasonically cleaned in acetone and methanol prior to suspending the specimens in a welded Mo (or steel) capsule using Mo (or steel) wire.

After exposure, the specimens were soaked in a mixture of acetic acid, hydrogen peroxide and ethanol for 24-72h to remove any residual Pb-Li. The composition of the Pb-Li after testing was determined by inductively coupled plasma analysis and combustion analysis. Post-test surfaces were examined using Auger electron spectroscopy (AES), x-ray photoelectron spectroscopy (XPS) and secondary electron microscopy (SEM). Cross-sections of the metal specimens were examined using electron probe microanalysis (EPMA).

Table 1. Alloy chemical compositions (atomic% or ppma) determined by inductively coupled plasma analysis and combustion analysis

Material	Fe	Ni	Cr	Al	O	C	N	S	Other
316SS	65.1	8.9	19.9	0.02	490	3360	2380	68	1.94Si,1.67Mn, 1.38Mo,0.21Cu
ODS FeCrAl	67.8	0.02	20.0	10.6	7430	340	210	50	0.44Ti,0.23Y 0.04Si, 0.04Mn
Fe-28Al-2Cr+Zr	70.0	<	2.0	27.9	70	400	<	46	0.026Zr, 0.005Hf
Ni-42.5Al	<	57.3	<	42.6	40	380	<	<	<

< indicates below the detectability limit of <0.01% or <0.001% for interstitials

Results and Discussion

SiC Specimens. Three capsule experiments with monolithic SiC specimens exposed have recently been completed: 5,000h at 800°C, 2,000h at 1100°C and 1,000h at 1200°C. A summary of the mass change results for the most recent capsule tests and previous tests[11,17] is shown in Table 2. A statistically significant mass gain was observed after 5,000h at 800°C while the other tests showed smaller mass gains or losses. Limited reaction at 800°C is consistent with previous results.[18,19] No change in the specimen surface was visible. However, as with the earlier tests, a small amount of powdery black residue was left on the specimen surface. This was identified as C by AES with trace amounts of Pb and Li detected by XPS.

The composition of the Pb-Li after exposure is shown in Table 3. Although previous tests had shown no detectable Si after exposures for 1,000h at 800°C and 1100°C, Si was detected after 2,000h at 1100°C and 1,000h at 1200°C. (The amount does not necessarily correspond to the specimen mass change because the capsule was made of the same CVD SiC.) The presence of Si in the Pb-Li indicates that some dissolution occurred at the higher temperatures and suggests that SiC may be limited to <1100°C in flowing Pb-Li. These Si levels are still less than the 2100ppma (350ppmw) that was reported from EPMA of Pb-Li after an 800°C exposure.[19] The O, C and N contents increased after each exposure, however, some contamination could occur during post-test handling. Capsule experiments are being planned with SiC/SiC composite specimens. More interaction may be expected with the SiC fibers or the fiber-matrix interface, however, it is anticipated that a dense CVD SiC seal coat will cover the outer layer of any SiC composite components.[5]

Metallic Specimens. Table 4 shows the mass losses for the Al-containing alloys exposed for 1,000h at 700°C in Pb-17Li compared to the mass loss for type 316 stainless steel in three different types of

Table 2. Mass change of CVD SiC specimens after exposure in Pb-17Li

Temperature	Time	Mass Change (mg)	(mg/cm^2)
800°C	1,000h	-0.02 ±0.04	-0.01 ±0.01
	5,000h	+0.10	+0.03
1100°C	1,000h	-0.02	-0.01
	2,000h	+0.02	+0.01
1200°C	1,000h	+0.04	+0.01

Table 3. Chemical composition using inductively coupled plasma and combustion analysis of the starting Pb and the Pb-Li after capsule exposures at the indicated temperatures and times (in ppma except for Li in atomic%)

Test	Li	Si	C	O	N	Al	Cr	Fe	Mo	Ni	Y
Starting	n.d.	<40	<170	1270	<40	<8	<4	<4	<2	<4	<2
1,000h exposure											
800°C	17.49%	<30	1850	4090	100	6	<3	6	<2	<3	<2
1100°C	16.27%	<30	1160	3550	90	<6	<3	6	<2	<3	<2
1200°C	15.62%	**370**	2690	16620	450	<20	<10	<10	<5	<10	<6
2,000h exposure											
1100°C	15.99%	**185**	1025	7890	200	<60	<30	<30	<20	<30	<20
5,000h exposure											
800°C	18.55%	<60	650	2580	90	<20	<10	<10	<5	<10	<6

Table 4. Mass change of specimens after 1000h at 700°C in Pb-17Li

Specimen	Capsule	Mass Change (mg)	Mass Change (mg/cm^2)
316SS	316SS	-3.1	-0.67
316SS	Fe	-26.2	-5.72
316SS	Mo	-17.4	-3.79
ODS FeCrAl	Mo	-1.4	-0.20
Fe-28Al-2Cr+Zr	Mo	-1.0	-0.25
Ni-42.5Al	Mo	-0.4	-0.09

capsules.[20] Compared to type 316 stainless steel, more than an order of magnitude reduction in the amount of dissolution was observed. The lowest mass loss for a 316SS specimen was in the 316SS capsule. This can be understood based on the fundamental flux equation governing dissolution in a liquid metal like Pb-Li:

$$J_i = k\,(C_i^S - C_i) \qquad [1]$$

where J_i is the flux of species i into (positive) or from (negative) the liquid metal, C_i^S is the solubility of i in the Pb-Li and C_i is the instantaneous concentration of i in the liquid. In a capsule experiment, dissolution continues until the liquid metal is saturated, i.e. $C_i^S = C_i$. Therefore, with a 316SS capsule, the predominant dissolution of Ni and Cr would reach saturation quickly due to the large surface area of the capsule itself (relative to the specimen). This correlates well with the high levels of Ni, Mn and Cr observed in the Pb-Li from this capsule, Table 5. In contrast, with a Fe or Mo capsule all of the Ni and Cr needed to reach saturation would come from the 316SS specimen. Thus the higher mass losses for these tests are expected.

All of the specimens were characterized after exposure and Figures 1-4 give examples of those findings. Figure 1 shows a polished cross-section of the type 316 stainless steel specimen after exposure. As expected, there is an outer layer depleted in both Cr (Figure 1b) and Ni (Figure 2). The mass loss corresponds to a ~5µm loss in metal, with Ni and Cr being selectively removed, which is consistent with this observation. The Mo-rich precipitates in the outer layer (Figure 1c) are not likely from the Mo capsule, but from the alloy itself, Table 1. Figure 3 shows a similar Mo map from the 316SS specimen exposed in a carbon steel capsule at 700°C. Similar Mo-rich particles are present in the outer layer without an external source of Mo.

No depletion layer was observed in the NiAl specimen although selective removal of Ni would be expected. However, a slight depletion in Al was observed near the surface that may be due to Al diffusing outward

Table 5. Chemical composition using inductively coupled plasma and combustion analysis of the starting Pb and the Pb-Li after capsule exposures at 700°C for 1000h (in ppma except for Li in atomic%)

Test	Li	Fe	Cr	Ni	Mn	Si	Al	Mo	C	O	N	S
Starting	n.d.	<4	<4	<4	<4	<40	<8	<2	<170	1270	<40	<50
316SS (SS)	16.4%	60	**160**	**740**	**380**	<60	<60	<20	1420	4810	160	320
316SS (FS)	17.3%	30	<30	90	30	<60	<60	<20	970	3346	40	110
316SS (Mo)	17.4%	<30	<30	90	<30	<60	<60	<20	1590	7440	60	903
FeCrAl (Mo)	17.9%	30	<30	<60	<30	<60	<60	<20	1260	4140	90	370
Fe_3Al (Mo)	16.5%	<30	<30	<60	<30	<60	<60	<20	1520	14860	320	110
NiAl (Mo)	18.2%	840	<30	30	<30	<60	<60	20	1200	10310	370	1100

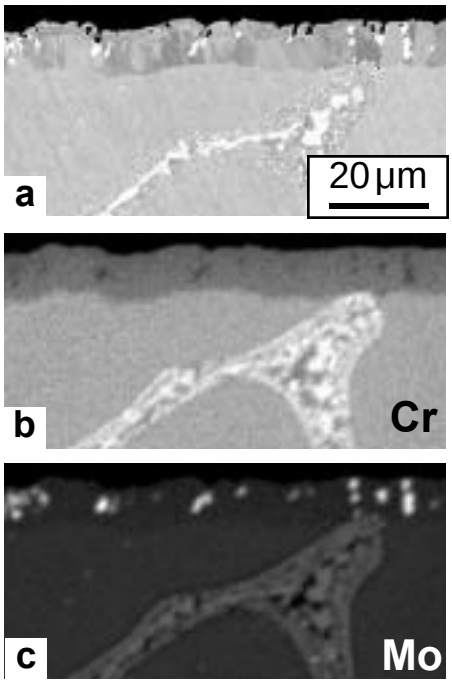

Fig. 1. (a) Secondary electron image of a polished cross-section of type 316 stainless steel after exposure in a Mo capsule for 1,000h at 700°C in Pb-17Li. X-rap maps of the same region show the concentration of (b) Cr and (c) Mo. The Cr- and Mo-rich second phase in the steel is likely sigma or a laves phase.

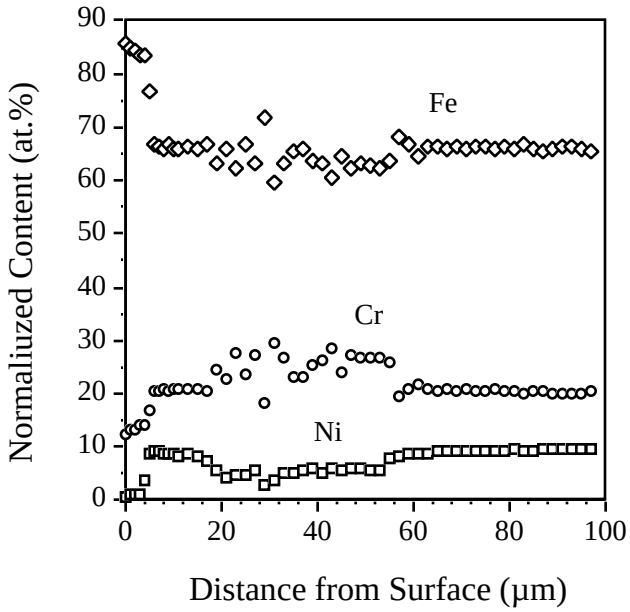

Fig. 2. Composition line profile of a polished cross-section of type 316 stainless steel after exposure for 1,000h at 700°C in Pb-17Li. The Ni and Cr are depleted from the outer region shown in Figure 1a.

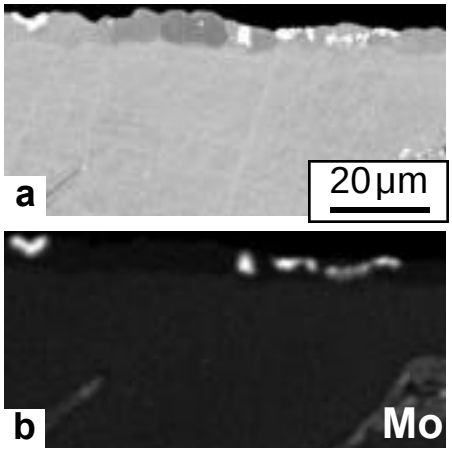

Fig. 3. (a) Secondary electron image of a polished cross-section of type 316 stainless steel after exposure in a carbon steel capsule for 1,000h at 700°C in Pb-17Li. X-rap maps of the same region show the concentration of (b) Mo.

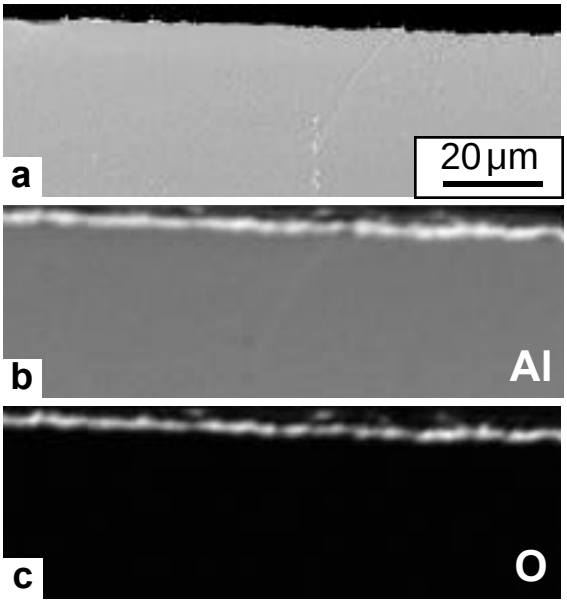

Fig. 4. (a) Secondary electron image of a polished cross-section of Ni-42Al after exposure for 1,000h at 700°C in Pb-17Li. X-rap maps of the same region show the concentration of (b) Al and (c) O.

Table 6. Mass change of specimens after 1000h at 800°C in Pb-17Li with a Mo capsule

Specimen	Pre-oxidation	Mass Change (mg)	Mass Change (mg/cm^2)
316SS	none	-79.51	-17.30
316SS + CVD Al	none	- 1.55	- 0.34
316SS + CVD Al	2h at 800°C	- 1.93	- 0.43
ODS FeCrAl	2h at 1000°C	+ 1.58	+ 0.24
Fe-28Al-2Cr+Zr	2h at 1000°C	- 1.55	- 0.37
Ni-42.5Al	2h at 1000°C	-12.12	- 2.72

to form a surface Al_2O_3 layer, Figures 4b and 4c. Similar oxide layers, although less distinct, were observed on the FeCrAl and Fe_3Al specimens. This is a relatively low temperature for the formation of a continuous alumina layer. With the lower Al contents in FeCrAl and Fe_3Al, these specimens may not have been able to form an alumina layer as quickly. The higher mass losses for these materials (Table 4) may be associated with the longer time needed to form a protective alumina layer by gettering O from the Pb-Li.

Table 6 shows the initial mass change results for a series of capsules run for 1,000h at 800°C. In this case, all of the capsules were Mo and the Al-containing alloys and one of the aluminized 316SS specimens were pre-oxidized, Table 6. Compared to the uncoated 316SS specimen, the aluminized 316SS specimens showed dramatically lower mass losses. Pre-oxidizing the coating for 2h at 800°C to form an alumina layer did not have a beneficial effect on dissolution. The Al-containing alloys also showed lower amounts of dissolution. The mass gain for the ODS FeCrAl specimen may be due to entrapped metal, however, the specimen appeared unaffected by the exposure. The Fe_3Al specimen had one ~3mm area where the oxide was removed causing some degree of mass loss. This selective attack area may be due to incomplete initial mixing of the Pb and Li. Lithium would quickly attack alumina and any of these alloys at 800°C. The highest mass loss was for NiAl where ~90% of the oxide appeared to be spalled after exposure. One reason for the higher mass loss may be that Ni dissolves more readily than Fe in PbLi. Another factor is that this alloy did not contain a reactive element addition (e.g. Y, Zr, Hf, etc.) which improves the adhesion of the alumina layer formed during pre-oxidation, Table I. Spallation of the alumina could have allowed more attack for this specimen. This experiment could be repeated with Hf-doped NiAl specimen to test this hypothesis.

Future work will eventually include flowing liquid metal experiments with a temperature gradient. Static capsule experiments can only be expected to produce a limited assessment of the compatibility issue because saturation inhibits further dissolution, Equation 1. Since low-cost quartz loops have been used for testing Bi-Li,[21] the possibility of constructing Pb-Li loops out of quartz was investigated by testing Pb-17Li in a quartz ampule at 800°C. The post-test PbLi chemistry is being measured to determine if any dissolution of the quartz occurred during this exposure.

References

[1] P. Noajitra, L. Buhler, U. Fischer, S. Malang, G. Reimann, and H. Schnauder, Fusion Eng. Des. 61-62 (2002) 449.
[2] M. Abdou, D. Sze, C. Wong, M. Sawan, A. Ying, N. B. Morley, and S. Malang, Fusion Sci. Technol. 47 (2005) 475.
[3] G. Benamati, C. Fazio, and I. Ricapito, J. Nucl. Mater. 307-311 (2002) 1391.
[4] J. Konys, W. Krauss, Z. Voss, and O. Wedemeyer, J. Nucl. Mater. 329-333 (2004) 1379.
[5] B. Riccardi, L. Giancarli, A. Hasegawa, Y. Katoh, A. Kohyama, R. H. Jones, and L. L. Snead, J. Nucl. Mater. 329-333 (2004) 56.

[6] T. Yoneoka, S. Tanaka, and T. Terai, Mater. Trans. 42 (2001) 1019-1023.
[7] P. Hubberstey, J. Nucl. Mater. 247 (1997) 208.
[8] P. Hubberstey, T. Sample, and A. Terlain, Fusion Technol. 28 (1995) 1194.
[9] T. Flament, P. Tortorelli, V. Coen, and H. U. Borgstedt, J. Nucl. Mater. 191-194 (1992) 132.
[10] H. Feuerstein, H. Gräbner, J. Oschinski, and S. Horn, J. Nucl. Mater. 233-237 (1996) 1383.
[11] B. A. Pint, L. D. Chitwood, and J. R. DiStefano, DOE/ER-0313/35 (2003) 13.
[12] N. V. Bangaru and R. C. Krutenat, J. Vac. Sci. Technol. B2 (1984) 806.
[13] Y. Zhang, B. A. Pint, J. A. Haynes, I. G. Wright, and P. F. Tortorelli, Oxid. Met. 62 (2004) 103.
[14] Y. Zhang, B. A. Pint, G. W. Garner, K. M. Cooley, and J. A. Haynes, Surf. Coat. Technol. 188-189 (2004) 35.
[15] Y. Zhang, W. Y. Lee, J. A. Haynes, I. G. Wright, B. A. Pint, K. M. Cooley, and P. K. Liaw, Met. Trans. 30A (1999) 2679.
[16] B. Jönsson, R. Berglund, J. Magnusson, P. Henning, and M. Hättestrand, Mater. Sci. Forum, 461-464 (2004) 455.
[17] B. A. Pint J. L. Moser, and P. F. Tortorelli, Fusion Engineering and Design (in press).
[18] F. Barbier, Ph. Deloffre, and A. Terlain, J. Nucl. Mater. 307-311 (2002) 1351.
[19] H. Kleykamp, J. Nucl. Mater. 321 (2003) 170.
[20] B. A. Pint, P. F. Tortorelli, and J. L. Moser, DOE-ER-0313/38 (2005) 89.
[21] J. R. DiStefano and O B. Cavin, Report # ORNL/TM-5503, Oak Ridge National Laboratory, Oak Ridge, TN (1976).

8.0 BREEDING MATERIALS

No contributions.

9.0 RADIATION EFFECTS, MECHANISTIC STUDIES, AND EXPERIMENTAL METHODS

THE INTERACTION OF HELIUM ATOMS WITH SCREW DISLOCATIONS IN α-Fe—H. L. Heinisch, F. Gao, and R. J. Kurtz (Pacific Northwest National Laboratory)*

OBJECTIVE

The objective of this research is to understand the fate of He atoms produced in metals and alloys by fusion neutron induced transmutation reactions. In the present work the migration energies, binding energies, and diffusion mechanisms of He atoms in and near screw dislocations in α-Fe are studied using atomic-scale simulations.

EXTENDED ABSTRACT

This report is based on information presented at ICFRM-12, December 4–9, 2005, and a publication to be published in the Journal of Nuclear Materials.

SUMMARY

Formation energies, binding energies, and migration energies of interstitial He atoms in and near the core of an a/2<111> screw dislocation in α-Fe are determined in atomistic simulations using conjugate gradient relaxation and the Dimer method for determining saddle point energies. Results are compared as a function of the proximity of the He to the dislocation core and the excess interstitial volume in regions around the dislocation. Interstitial He atoms have binding energies to the screw dislocation that are about half the magnitude of binding energies to the a/2<111>{110} edge dislocation in α-Fe. Migration energies of interstitial He atoms for diffusion toward the dislocation and for pipe diffusion along the dislocation are about the same magnitude for the screw and edge dislocations, despite a significant difference in their migration mechanisms. Interstitial He atoms diffuse along the dislocation cores with a migration energy of 0.4–0.5 eV.

PROGRESS AND STATUS

Introduction

A detailed study of how He interacts with dislocations and other microstructural features is needed to develop improved kinetic Monte Carlo and rate theory models for prediction of long-time material behavior in the high helium environment of fusion reactor materials. Molecular statics, molecular dynamics and the dimer method of potential surface mapping are being used to study the fate of He atoms in the vicinity of dislocations in alpha-iron, which we consider to be a first-order model for ferritic steels. We report here on the calculations of formation energies of He atoms in interstitial positions about a screw dislocation, as well as the migration energies for "pipe diffusion" of He atoms trapped within the dislocation core. A comparison of the interactions of interstitial He with screw and edge dislocations is discussed.

Computer Simulations

An a/2<111> screw dislocation was created along the axis of a cylindrical cell of body-centered cubic Fe, oriented as in Fig. 1(a). The dislocation was introduced by displacing the atoms according to the anisotropic elastic displacement field of the dislocation, then relaxing the entire model with fixed boundary conditions. The model is periodic along the dislocation line. Binding energy calculations were performed for He atoms placed at substitutional and interstitial positions in the dislocation-distorted lattice in an array of positions at various distances from the dislocation line. Conjugate gradient relaxations were performed to determine the relaxed configurations of the He and surrounding Fe atoms, as well as the energy of the relaxed configuration. In all cases the set of interatomic potentials due to Ackland [1], Wilson and

*Pacific Northwest National Laboratory (PNNL) is operated for the U.S. Department of Energy by Battelle Memorial Institute under contract DE-AC06-76RLO-1830.

Johnson [2]and Beck [3] were used for the Fe-Fe, Fe-He, and He-He interactions, respectively. Excess volumes associated with lattice sites in the vicinity of the dislocation were determined using the "Voronoi volume" atomic volume technique [4].

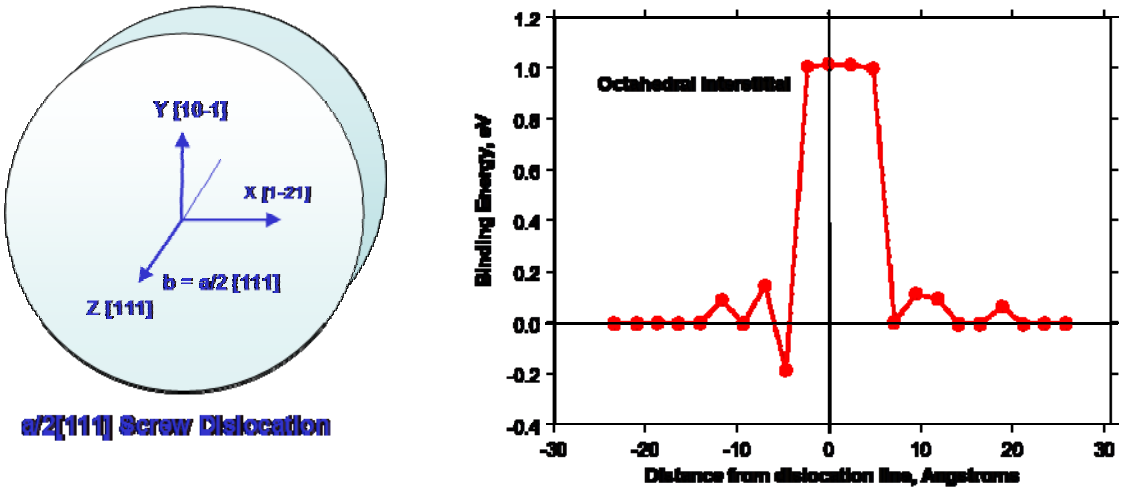

(a) (b)

Fig. 1. a) The orientation of the computational cell for the a/2<111> screw dislocation in α-Fe. The dislocation line and Burgers vector lie along [111] (the z-direction, out of the page) and b) binding energies of relaxed interstitial He atoms as a function of their distance from the center of the screw dislocation along the [1 -2 1] direction (x-axis).

The Dimer method [5] was used to determine saddle point energies for possible transitions of interstitial He atoms to other locations, starting from a number of relaxed He atom positions about the dislocation. The Dimer results give the migration energies and saddle point atom configurations for He interstitials as they migrate from one equilibrium position to another. In a single run the Dimer method can find saddle points for more than one transition from a given starting configuration, not just the transition of lowest energy. Thus, it is useful for locating unexpected and competing transitions, which can be especially important in exploring a complicated potential energy landscape such as near a dislocation or grain boundary.

Results

The binding energies of interstitial He atoms to the screw dislocation are shown in Fig. 1b, plotted as a function of their initial unrelaxed positions at octahedral sites (somewhat distorted in the core region) along a line through the center of the dislocation. The Helium atoms relaxed within their octahedral interstitial positions, and they have maximum binding energies of about 1.0 eV, relative to octahedral He in the perfect Fe lattice. Helium atoms placed farther away from the dislocation core also relax to positions near their original octahedral interstitial sites, and they have significantly smaller binding energies that decrease with distance from the dislocation. The binding energy of interstitial He to the a/2<111> screw dislocation is less than half the maximum binding energy of interstitial He to the a/2[111] {110} edge dislocation [6]. Also, unlike octahedral interstitial He in and near the edge dislocation, there are no locations near or in the screw dislocation core where octahedral interstitial He atoms spontaneously assume a crowdion configuration. Undoubtedly, this is related to the much smaller excess volume associated with the screw dislocation.

The Dimer method was used to determine the migration pathways and migration energies for diffusion of a He interstitial initially placed at various octahedral interstitial positions about the screw dislocation, chosen with regard to the symmetry of the dislocation stress field and the core field, as shown in Fig. 2a. Interstitial He atoms within a radius of about 0.3 nm from the center of the dislocation migrate as octahedral interstitials along the screw dislocation with a migration energy of E_m ~ 0.4–0.5 eV. See Fig. 2b. He atoms within a radius of up to 1.0 nm from the center of the dislocation migrate preferentially toward the center of the screw dislocation with a migration energy of E_m ~ 0.2–0.4 eV. Thus, there is a cylindrical region about the screw dislocation within which interstitial He atoms are attracted to the dislocation. The interstitial He atoms become trapped near the dislocation, but they can easily migrate along the dislocation.

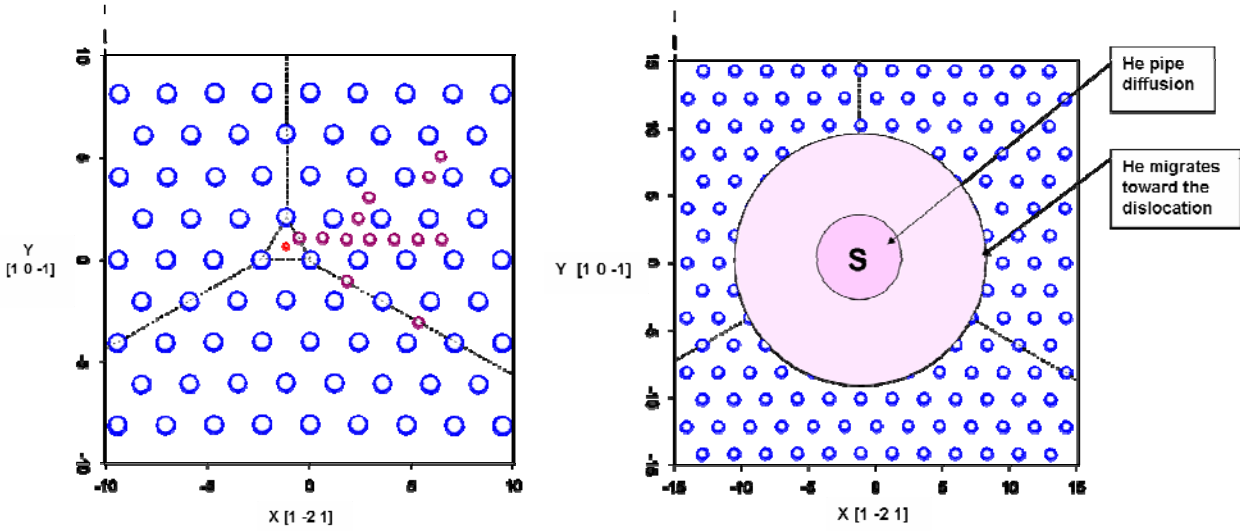

(a) (b)

Fig. 2. a) Locations of the initial positions of a single interstitial He atom prior to relaxation. The large circles are Fe atom rows, and the small circles are the various initial He atom positions. The dislocation line is along the z axis (into the page) at the center of the dashed triangle. The z-components of all the He locations are approximately the same. Dimensions of the axes are in Angstrom units. b) The cylindrical volumes centered on the screw dislocation line (into the page) within which an interstitial He atom migrates preferentially toward the dislocation and migrates along the dislocation, i.e., pipe diffusion.

Conclusions

The results of these simulations indicate that interstitial He atoms are attracted to and trapped at <111> screw dislocations in α-Fe. Within about 1 nm from the screw dislocation core He atoms migrate as octahedral interstitials preferentially toward the dislocation core, and in this form He atoms can migrate along the dislocation with a migration energy of 0.4–0.5 eV.

References

[1] G. J. Ackland, D. J. Bacon, A. F. Calder, and T. Harry, Philos. Mag. A75 (1997) 713.
[2] W. D. Wilson and R. D. Johnson, Interatomic Potential and Simulation of Lattice Defects, Plenum (1972) 375.
[3] D. E. Beck, Mol. Phys. 14 (1968) 311.
[4] G. Voronoi and J. Reine, Angew. Math. 134 (1908) 198.
[5] G. Henkelman and H. Jónsson, J. Chem. Phys. 111 (1999) 7010.
[6] H. L. Heinisch, F. Gao, R. J. Kurtz, and E. A. Le, Journal of Nuclear Materials (in press).

KINETIC MONTE CARLO STUDIES OF THE REACTION KINETICS OF CRYSTAL DEFECTS THAT DIFFUSE ONE-DIMENSIONALLY WITH OCCASIONAL TRANSVERSE MIGRATION—H. L. Heinisch (Pacific Northwest National Laboratory),[*] H. Trinkaus (Institute für Festkörperforshung), and B. N. Singh (Risø National Laboratory)

EXTENDED ABSTRACT

This report is based on information presented at ICFRM-12, December 4–9, 2005, and a publication to be published in the Journal of Nuclear Materials.

SUMMARY

The reaction kinetics of the various species of mobile defects in irradiated materials are crucially dependent on the dimensionality of their diffusion processes. Sink strengths for one-dimensionally (1D) gliding interstitial loops undergoing occasional direction changes have been described analytically and confirmed by kinetic Monte Carlo (KMC) simulations. Here we report on KMC simulations investigating the transition from 1D to 3D diffusion for 1D gliding loops whose 1D migration is interrupted by occasional 2D migration due to conservative climb by dislocation core diffusion within a plane transverse to their 1D glide direction. Their transition from 1D to 3D kinetics is significantly different from that due to direction changes. The KMC results are compared to an analytical description of this diffusion mode in the form of a master curve relating the 1D normalized sink strength to the frequency of disturbance of 1D migration.

PROGRESS AND STATUS

Introduction

There are experimental observations of features in irradiated materials that cannot be rationalized in terms of the 3D diffusion kinetics of vacancy and SIA defects assumed in conventional rate theory [1,2]. Moreover, in it has been recognized that some deviation of the reaction kinetics of SIA clusters from that for pure 1D diffusion are necessary for proper representation of phenomena described by the theory of radiation damage [3]. Computer modeling has shown that energetic displacement cascades in metals produce clusters of self-interstitial crowdion defects (actually small glissile dislocation loops) that diffuse by one-dimensional (1D) glide along close packed directions with migration energies less than 0.1 eV [4,5]. Under certain conditions, the 1D migrating loops can individually undergo a thermally-activated change in the direction of their 1D migration (i.e., a change in the direction of the Burgers vector of the dislocation loop) to a different close-packed direction [6,7].

An analytical treatment of defect interactions for defects following the reaction kinetics for 1D to 3D via the changing of Burgers vectors was developed for use in reaction rate theories of microstructure evolution under irradiation [8]. As part of that work, KMC simulations of the 1D to 3D transition for defects interacting with a variety of sizes and densities of sinks were also performed that corroborated the analytical theory. In the present work, we examine a different type of 1D/3D reaction kinetics in which the 1D paths of gliding loops are occasionally interrupted by excursions due to conservative climb by dislocation core diffusion . The 2D climb excursion is in a plane, normal to the direction of glide, after which glide is resumed along the original glide direction. This mode of defect migration was considered some time ago, for example by Gösele and Seeger [9], who referred to this mode as “preferential 1D migration,” especially in the case where the climb excursions are small and infrequent. An analytic theory similar to that for 1D/3D “direction change” reaction kinetics has been developed that describes the effects of the frequency of climb excursions on sink strengths throughout the range from pure 1D to pure 3D. This paper reports on KMC simulations performed in support and corroboration of the analytical theory, the development of which will be described in detail elsewhere.

---

[*]Pacific Northwest National Laboratory (PNNL) is operated for the U.S. Department of Energy by Battelle Memorial Institute under contract DE-AC06-76RLO-1830

Computer Simulations

The KMC model consists of immobile spherical "absorbers" that are unsaturable, maintaining a constant radius R and number density N throughout the simulations. The absorbers are randomly arranged in a large test volume, and migrating "defects" are introduced into the volume one at a time, starting at random positions near the center of the volume and hopping on a face-centered cubic lattice until being absorbed by an absorber. During the migration of each defect, its deviations from pure 1-D hopping occur regularly according to the conditions under investigation. All hops of a defect are chosen randomly from the possible hops permitted by the restrictions on its motion. The "lifetime" of each defect is defined as the total number of hops it makes before being absorbed by one of the absorbers. Each data point in the KMC results reported in Figs. 1 and 2 represents the average behavior of at least 1000 migrating defects.

In Fig. 1, the values of the sink strengths determined from the KMC simulations are plotted as a function of the average distance traveled by the defects in each 1D migration segment, i.e., the distance traveled between the occurrences of the non-1D events. In this paper, the non-1D events studied are either a change in the direction of the 1D migration (1D/3D) or a 2D climb excursion transverse to the 1D migration direction (preferential 1D). In both cases the average length of the 1D segments is proportional to the average of the square root of the number of 1D hops in each 1D segment. For 1D/3D migration, the 1D (glide) migration of each defect is regularly interrupted by a change in direction of the 1D migration. In both cases less frequent interruption of the 1D glide results in greater distance traveled during each individual 1D glide migration path segment. The two sets of data points plotted between the preferential 1D and 1D/3D data sets are results for the preferential 1D mode when the defects make multiple 2D climb hops during each excursion from 1D migration. The addition of larger climb excursions during each interruption of 1D pushes the sink strengths for preferential 1D toward the 1D/3D values.

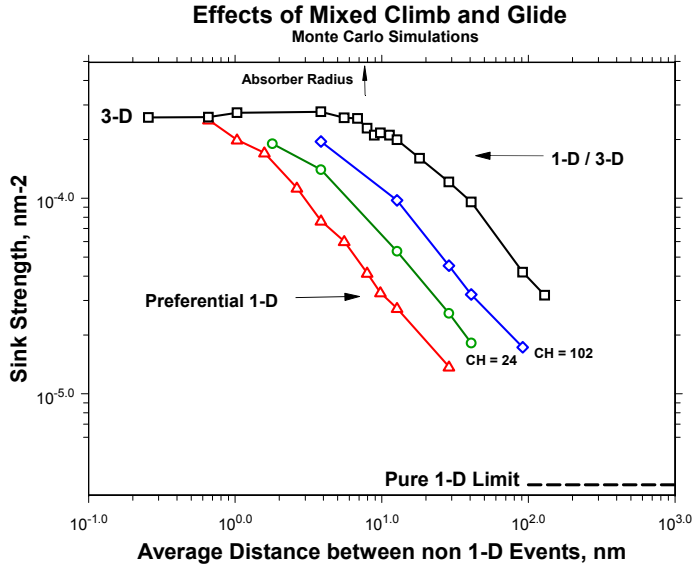

Fig. 1. Sink strength as a function of the average length of 1D migration path between disturbances of the 1D migration by diffusive climb events (Preferential 1D) compared to effects of the disturbance by change of glide direction (1D/3D). Data lying between the "1D/3D" and "Preferential" curves are for cases of Preferential 1D in which more "climb hops" (CH=24,102) are performed during each climb excursion of the preferential 1D migration.

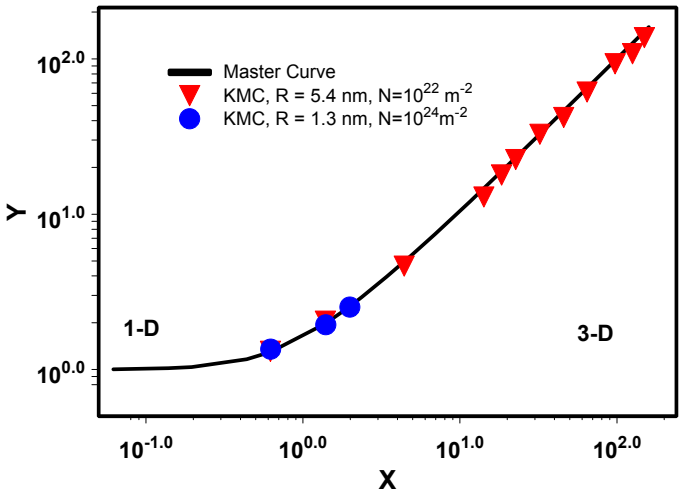

Fig. 2. Comparison of the analytical expression of the "Preferential 1D Master Curve," to the KMC results for two different conditions involving absorbers of different radius R and number density N.

Analytical Master Curve

A master curve relating sink strength to the "disturbance of 1D diffusion" for 1D/3D defect migration was developed earlier by Trinkaus et al. [10], and it was shown to match very well with sink strength data generated in KMC simulations for 1D/3D migration. This master curve concept has subsequently been reconfigured and extended to describe preferential 1D migration as well. The new master curve is presented here for comparison with results of the KMC simulations. Details of the derivation of the new master curve and discussion of its implications will be presented in another publication.

The master curve has the form

$$Y = 0.5\{1 + [1 + 4X^2]^{1/2}\} \quad (1)$$

where Y is the sink strength normalized to its value for pure 1-D

$$Y = k^2/k_1^2 \quad (2)$$

and X is a measure of the "disturbance of 1-D diffusion." The "disturbance of 1-D diffusion" for disturbance by Burgers vector changes (1D/3D) is represented as

$$X = (L^2k_1^2/12+k_1^4/k_3^4)^{-1/2} \quad (3)$$

where L is the 1-D path length between direction changes. For preferential 1D, the disturbance of 1D diffusion by conservative climb is given as

$$X = (\delta^{1/2}\, f(\delta)\, k_3^2/k_1^2) \quad (4)$$

where $\delta = D_{tr}/D_{lo}$, the ratio of the transverse and longitudinal diffusivities, and

$$f(\delta) = 3[1-\delta]^{1/2}/\{(1 + 2\delta) \arccos(\delta^{1/2})\}\,. \quad (5)$$

In Fig. 2, the KMC results for Preferential 1D migration are compared to the analytical master curve, Equation 1. For Fig. 2, simulations were also performed for a system of absorbers having a smaller size, R = 1.8 nm, and a higher number density, $N = 10^{24}$ m^{-3}, especially to achieve results closer to the pure 1D

limit, as well as to test the master curve over a range of conditions. The agreement of the master curve with the KMC results for both sets of absorbers is excellent.

Conclusions

The KMC simulations confirm the 1-D to 3-D behavior predicted by the analytical expressions for both the loop glide direction change mechanism (1D/3D) and the glide-climb (preferential 1-D) mechanism. The master curve relating the normalized sink strength to the disturbance of 1-D diffusion, corroborated by KMC modeling, illustrates the validity of the comprehensive analytical representation of these phenomena. Furthermore, the analytical representation of 1D to 3D diffusion reaction kinetics utilized to form the master curve is well-suited for modeling damage accumulation under the locally anisotropic diffusion conditions of defects in materials where such 1D-migrating defects are formed.

References

[1] H. Trinkaus, B. N. Singh, and A. J. E. Foreman, J. Nucl. Mater. 199 (1992) 1; 206 (1993) 200; 249 (1997) 91; 251 (1997) 172.
[2] H. Trinkaus, B. N. Singh, and S. I. Golubov, J. Nucl. Mater. 283–287 (2000) 89.
[3] S. I. Golubov, B. N. Singh, and H. Trinkaus, J. Nucl. Mater. 276 (2000) 78.
[4] Yu. N. Osetsky, A. Serra, B. N. Singh, and S. I. Golubov, Philos. Mag. A 80 (2000) 2131.
[5] B. D. Wirth, G. R. Odette, D. Maroudas, and G. E. Lucas, J. Nucl. Mater. 276 (2000) 33.
[6] N. Soneda and T. Diaz de la Rubia, Philos. Mag. A 78 (1998) 995.
[7] F. Gao, D. J. Bacon, Yu. N. Osetsky, P. E. J. Flewitt, and T. A. Lewis, J. Nucl. Mater. 276 (2000) 213.
[8] A. V. Barashev, S. I. Golubov, and H. Trinkaus, Philos. Mag. A 81 (2001) 2515.
[9] U. Gösele and A. Seeger, Philos. Mag. 34 (1976) 177.
[10] H. Trinkaus, H. L. Heinisch, A. V. Barashev, S. I. Golubov, and B. N. Singh, Phys. Rev. B 66 (2002) 060105(R).

THERMAL HELIUM DESORPTION SPECTROMETRY OF HELIUM-IMPLANTED IRON–D. Xu, T. Bus, S. C. Glade, and B. D. Wirth (University of California, Berkeley)

OBJECTIVE

The objective of this work is to understand the kinetics and energetics of helium transport and clustering in iron implanted with He ions as a function of He ion energy and dose.

SUMMARY

Elemental iron implanted with He at different energies and doses is studied using thermal helium desorption spectrometry (THDS). Currently examined energies and doses include: 100 keV, and 1 x 10^{11}, 1 x 10^{13}, and 1 x 10^{15} He/cm^2, respectively. While no clear desorption signals have been observed for the two lower dose samples, the present results reveal that for the iron implanted to 1 x 10^{15} He/cm^2 the majority of the implanted He atoms desorb at ~ 1000ºC and at > 1100ºC. Both conventional reaction model and Johnson-Mehl-Avrami (JMA) transformation model kinetics were utilized to fit the lower temperature (~ 1000ºC) desorption event of the 1 x 10^{15} He/cm^2 dosed iron. Surprisingly, single (either 1st or higher) order fits can not adequately describe the event. Excellent fits are obtained when combining a lower (n ~ 1.1) order with a higher (n ~ 5.8) order JMA fit. Additionally, spurious desorption peaks and certain complex desorption features have been observed which may affect future THDS studies.

PROGRESS AND STATUS

Introduction

The development of fusion reactors requires knowledge of material behavior under fusion environments, in particular with regard to high levels of helium produced by (n,α) reactions. It has been established that implanted or internally produced He can cause significant mechanical property degradation [1-5]. A crucial aspect, therefore, is to understand how helium atoms migrate and are trapped by microstructural features in irradiated materials. While a large amount of theory, modeling and experimental research has been performed in the past years, the understanding of this problem is still far from complete. Thermal helium desorption spectrometry (THDS) has been employed to experimentally study irradiation-induced structural defects and their interactions with He atoms in a variety of materials. For example, nucleation and growth of He-vacancy clusters were reported in vanadium and vanadium alloys [6], and the sequential releases of interstitial He and He-Vacancy clusters were reported in SiC [7] based on the THDS spectra.

In iron and ferritic alloys, computer simulations have been performed on defect production in collision cascades caused by helium injection [8], effect of He-vacancy complexes on the mechanical properties [9], thermal stability of He-vacancy clusters in iron [10], and the He-grain boundary interaction [11]. Experimentally, nuclear reaction depth profiling [12], transmission electron microscopy [13], positron annihilation lifetime and coincidence Doppler broadening (CDB) techniques [14,15] have been used in addition to THDS [10,16–17] to study the He migration and He-induced defect clusters in iron.

In this work, we use THDS to study the kinetics and energetics of helium in iron implanted with 100 keV He to three different doses, 1 x 10^{11}, 1 x 10^{13}, and 1 x 10^{15} He/cm^2. Constant rate heating ramps were employed to thermally desorb the implanted He. The resulting desorption signals were fit to both conventional reaction model and Johnson-Mehl-Avrami (JMA) transformation model kinetics. Surprisingly, single (either 1st or higher) order fits can not adequately describe the signals in either model. Excellent fits were obtained when combining a lower (~ 1) order with a higher (~ 6) order in the JMA model. Spurious desorption peaks and complex desorption features observed are also presented.

Experimental Methods

Figure 1 is a sketch of our recently built THDS at UC Berkeley [18]. Both the sample chamber and the measurement (quadrupole mass spectrometer) chamber are maintained at ultra-high vacuum with a pressure of about 10^{-10} Torr (at room temperature). Both the sample holder and the resistive heating filament are made of tungsten. The He, as well as other species (N_2, H_2, etc.), is signaled by the mass spectrometer (maintained at room temperature) while the sample is being heated according to a desired temperature profile. The synchronized sample heating and mass spectrometer measurement are both controlled through a LABVIEW program which simultaneously records all relevant data. During an actual measurement, liquid N_2 is constantly flowing through a channel between the inner and outer walls of the sample chamber to prevent the temperature rise of the walls and subsequent heating of the gas species.

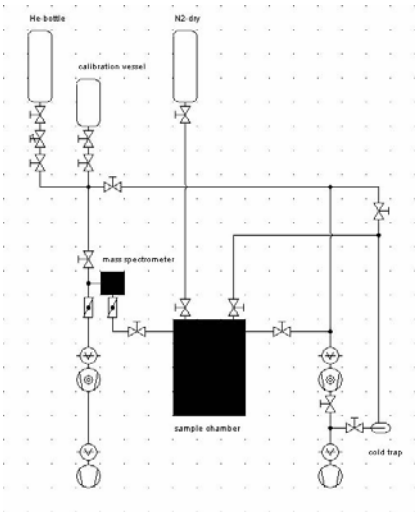

Fig. 1. Structural sketch of the Berkeley THDS instrument.

A THDS system can be operated in either static (no pumping during a measurement) or dynamic mode (gas being constantly pumped out during a measurement). In this study, dynamic mode was employed to prevent accumulation of desorbed He in the measurement chamber. In the dynamic mode with a fixed chamber volume *V*, assuming He at room temperature T_r, the He pressure inside the chamber *P*, as seen by the mass spectrometer, is governed by the differential equation:

$$VdP = K_B T_r d\overline{N} - \frac{PV}{\tau} dt \,, \tag{1}$$

in which τ is a pumping time constant, and $d\overline{N}$ is the number of desorbed He atoms from the sample in the time period of *dt*. The pumping constant τ is determined by the pumping speed and thus is adjustable. If τ is very small such that $dP/dt << P/\tau$ [1], then one obtains $d\overline{N}/dt \propto P$. However, as will be shown and discussed later, even when τ is indeed negligible, some non-negligible spurious signals (even peaks) which apparently do not result from the desorption of implanted He may still contribute to the measured pressure *P*. Therefore, a more careful expression should be: $d\overline{N}/dt \propto (P - P_{base})$ where P_{base} can be regarded as the signal measured from an otherwise-similar but non-implanted control sample. The control measurements were performed using the same settings (including the temperature control parameters,

[1]The accuracy of this assumption can be checked during data analysis by numerically comparing these two terms. τ can be found in calibration procedure. In this work, τ = 0.3s and the assumption is sufficiently satisfied.

the starting system pressure, the liquid N_2 flow rate, etc.) as for the corresponding actual desorption measurements.

A tube of 1 ml volume in connection with a 500 ml reservoir was used for calibration measurements. The calibration factor for the mass spectrometer was determined to be ~ 5.5 x 10^{-22}C/He-atom. Iron plates of 1mm thickness with a purity of 99.5% were purchased from Goodfellow and then commercially implanted with 100 keV helium to three different doses: 1 x 10^{11}, 1 x 10^{13}, and 1 x 10^{15} He/cm^2. Constant rate heating ramps at rates of 0.5 K/s and 1 K/s were used for both the control and the actual desorption measurements.

Results and Discussion

TRIM/SRIM calculations

The damage, He distribution, V/He (Vacancy/He) ratio and other factors related to He implantation in Fe were calculated with TRIM (SRIM 2003) software [19]. For 100 keV He implantation, the vacancy/He ratio is 87 and the peak He concentration at a dose of 1 x 10^{15}/cm^2 is about 700 appm, which appears at a depth of 340 nm.

Spurious peaks

A comparison between two samples: S10 (1 x 10^{15}/cm^2 dosed) and S12 (non-implanted control) is shown in Fig. 2a. The same heating control parameters were used for both samples which produced almost identical actual temperature profiles during the measurements. Fig. 2a shows that both samples exhibit a set of medium temperature He peaks in the range of ~ 600–880ºC, and, more importantly, the positions of these medium temperature peaks are almost identical for the two samples. However, the implanted sample S10 displays much stronger signals than the non-implanted S12 at temperatures higher than ~ 880ºC, including a fully developed peak at 1017ºC and a broad peak with an onset of ~ 1130ºC.

Apparently, the medium temperature peaks in the range of ~ 600–880ºC are not due to the desorption of implanted He, and thus are referred to as spurious peaks (signals) throughout this paper. The real identifiable desorption events start from above 880ºC in the 1 K/s ramping measurement of S10. Since the magnitudes of the spurious peaks are not negligible compared with the real desorption peaks, it is thus crucial to perform a control analysis before making peak assignments, particularly if the He desorption under consideration occurs in a relatively low temperature range (e.g., below 880ºC). Whether such spurious peaks also contributed to the observed signals in previous THDS studies is unclear.

While the exact origin of the spurious peaks is still under investigation, they appear to be related to the mutual desorption of several non-implanted species. As shown in Fig. 2b, other channels of the mass spectrometer, such as N_2, as well as the total system pressure, also exhibit peaks at basically the same temperatures.[2] Moreover, even a copper gasket was found to exhibit similar peaks on all channels of the mass spectrometer (including He) at relatively lower temperatures from 500 to 750ºC. It must also be noted that these spurious peaks do not appear when an empty-chamber (without any sample) is measured, indicating system cleanliness is not the problem. Rather it appears that surface contamination of the sample might be partly responsible for the spurious peaks.

[2]These other channels are distinguished from the He channel at temperatures higher than ~ 880 ºC where the implanted He starts to desorb. Note that a logarithm scale is used in Fig. 2b for comparison of different channels.

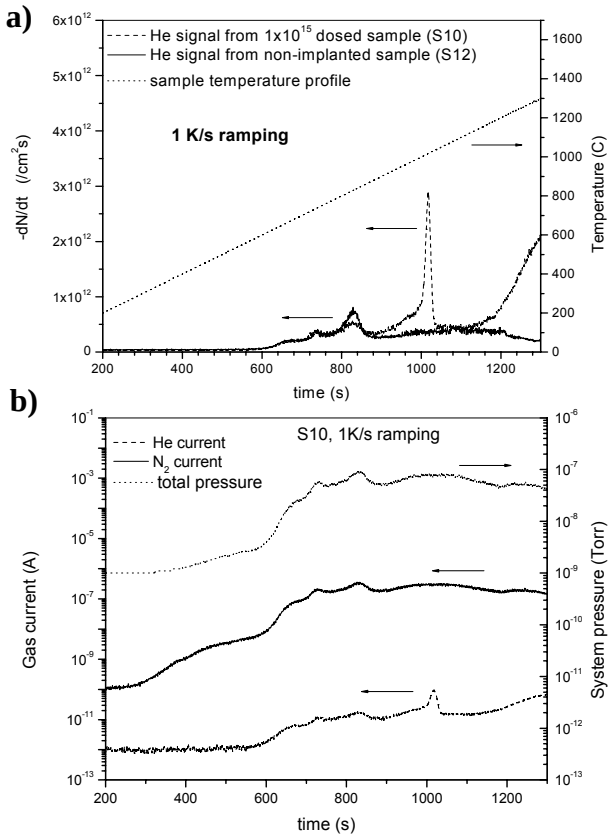

Fig. 2. a) Comparison between He signals measured from two samples, S10 (1 x 10^{15}/cm^2 dosed) and S12 (non-implanted); and b) correlations among He signal, other gas signals (represented by N_2), and total system pressure, measured from sample S10—note that a logarithmic scale is used.

Samples of 1 x 10^{15}/cm^2 dose

- *Reaction model analysis*

From the 1 K/s (β_1) constant rate ramping data presented in Fig. 2a (dashed line), the peak temperature T_p of the first desorption event of the 1 x 10^{15}/cm^2 dosed iron was determined to be 1017ºC. The ramping measurement was also performed at a heating rate of 0.5 K/s (β_2), which shifted the T_p to 993ºC.

A number of previous studies (e.g., [20]) have assumed that He desorption obeys a 1st order chemical reaction model, i.e., $dN/dt = -K_0 \exp(-Q/K_B T) * N$, where N is the number of remaining He atoms in the sample corresponding to a given desorption event, K_0 is a frequency factor, Q is the activation energy of the desorption event, and K_B is the Boltzmann constant. By solving the equation $d^2N/dt^2 = 0$ under the constant rate ramping condition (i.e., $dT/dt = \beta$), it can be found that the peak temperature T_p on the dN/dt signal satisfies the equation $\ln(\beta/T_p^{\,2}) = -Q/K_B T_p + \ln(K_0 K_B/Q)$. Therefore, the use of two

sets of T_p vs. β data can determine both the activation energy Q and the frequency factor K_0. In this case, we obtain $Q = 3.8$ eV and $K_0 = 2.04 \times 10^{13}$ /s. Nevertheless, as shown in Fig. 3, a back-calculation of dN/dt using these parameters and the assumed 1st-order reaction model reveals that the 1st order assumption in fact does not provide satisfactory agreement with the experimental peak, particularly with respect to the peak sharpness (half-maximum width) and steepness. Moreover, even when Q and K_0 are allowed to vary around these values (3.8 eV and 2.04×10^{13} /s), similar fit curves are obtained and the sharpness of the entire event still can not be adequately described.

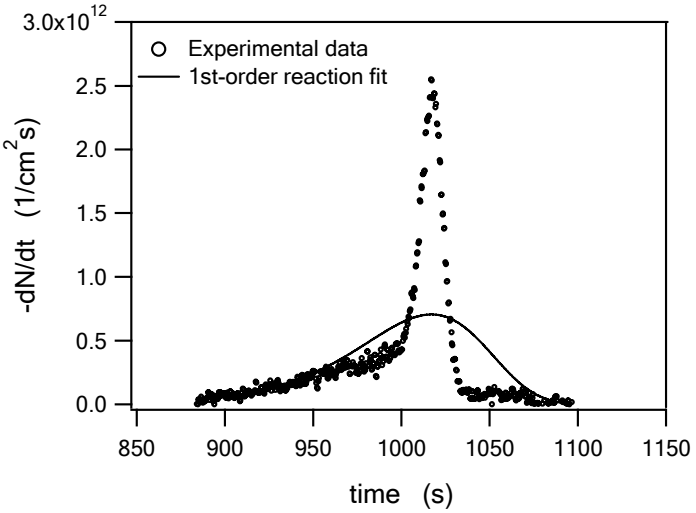

Fig. 3. First-order fit using reaction model for the 1017ºC desorption event of the 1 x 10^{15}/cm^2 dosed sample: $n = 1$, $Q = 3.81$ eV, $K_0 = 2.04 \times 10^{13}$ /s.

- *Johnson-Mehl-Avrami (JMA) model analysis*

A non-1st-order reaction model was then considered in an attempt to obtain better fits. From the general form of the reaction model, i.e., $dN/dt = -K_0 \exp(-Q/K_B T) * N^n$ (where n is the order of reaction), one can obtain: $d^2N/dt^2 = dN/dt * [\beta Q/(K_B T^2) + (n/N) * dN/dt]$. Therefore, at the desorption peak, we have $Q/n = -[K_B T_p^2/(\beta * N_p)] * \left.\frac{dN}{dt}\right|_p$. N_p (as well, it is important to note that N is a function of t) can be numerically determined using the dN/dt data. Hence, Q/n is determined to be 15.8 eV for the 1017ºC desorption event. Thus we obtain $dN/dt = -K_0[N * \exp(-15.8/K_B T)]^n$. Hence, if the general form of the reaction model is a good description of the event, the plot of $\ln(-dN/dt)$ vs. $\ln[N * \exp(-15.8/K_B T)]$ should be close to a straight line with a slope of n and an intercept of $\ln K_0$. However, a plot of the 1017ºC event obeys this linearity only at the early stage (up to 1000 s, i.e., 1000 ºC) of the event, but significantly deviates thereafter, indicating the inadequacy of this general reaction model for the description of this event.

A JMA kinetic model [21,22] was then employed to analyze the desorption event at $T_p = 1017$ºC. The general form of the JMA model can be written as: $x = 1 - \exp(-K^n t^n)$, where $K = K_0 \exp(-Q/K_B T)$, x is the transformed (in this case, desorbed) fraction of He atoms corresponding

to a certain event, i.e., $x \equiv 1 - N(t)/N_0$. Therefore, the desorption rate can be derived as: $dN/dt = -N_0 dx/dt = -N_0 * nK^n t^{n-1} \exp(-K^n t^n) * [1 + \beta t Q/(K_B T^2)]$. According to Henderson's analysis (Appendix A7 in Ref. [23]), the activation energy Q in this model[3] can be approximated using the peak shifting approach, i.e., $Q \approx$ slope of the plot of $\ln(\beta/T_p^{\,2})$ vs. $-1/K_B T_p$ [4]. Analysis of the two sets of T_p vs. β data presented earlier results in $Q \approx 3.8$ eV. Thus, we fixed Q to this value and varied n and K_0 to obtain a series of fits for the desorption signal, four of which are shown in Fig. 4. As was the case with the 1st-order-reaction fit, the 1st-order JMA fit can not describe the sharpness of the desorption peak. However, as the order n increases, the JMA fit gets finer and the fit-peak increases such that it better accounts for the sharpness of the experimental peak. On the other hand, a higher order (e.g., $n = 4$) JMA fit can not adequately describe the early stage ($t < 1000$ s) of the experimental signal.

The fact that neither the 1st order, nor a single higher order fit can satisfactorily account for the entire signal leads to the hypothesis that more than one single-order event is involved. Indeed, as shown in Fig. 5, by combining a low order component with a high order component within the JMA model, the entire signal can be fit very well. The fitting methodology is described in the Appendix. The fit result suggests that ~ 44% of the total He atoms involved in this entire event desorb according to a low order (n ~ 1.1) in the early stage and the remaining 56% desorb with a higher order (n ~ 5.8). However, the microscopic mechanism underlying this order change during a single desorption event requires further investigation.

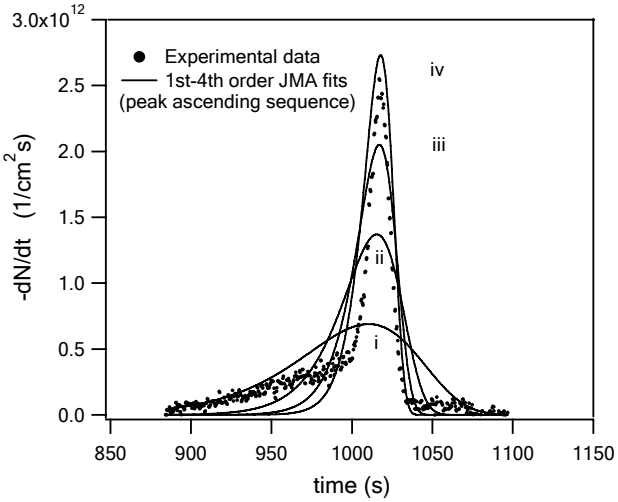

Fig. 4. Single-order JMA fits for the 1017ºC desorption event of the 1 x 10^{15}/cm^2 dosed sample, with fixed activation energy $Q = 3.81$ eV, and varied n and K_0 (in the peak ascending sequence): a) $n = 1$ and $K_0 = 8.6 \times 10^{11}$ /s; b) $n = 2$ and $K_0 = 7.8 \times 10^{11}$ /s; c) $n = 3$ and $K_0 = 7.5 \times 10^{11}$ /s; d) $n = 4$ and $K_0 = 7.4 \times 10^{11}$ /s.

[3]Note that Q here is equivalent to the $\Delta H/n$ in Henderson's analysis, and K_0 here is equivalent to Henderson's $K_0^{1/n}$. The form used here is more reasonable in terms of physical meaning of the JMA model.

[4]This is essentially the same technique used for the determination of the activation energy in the earlier 1st-order reaction analysis. However, the intercepts in the two analyses are different.

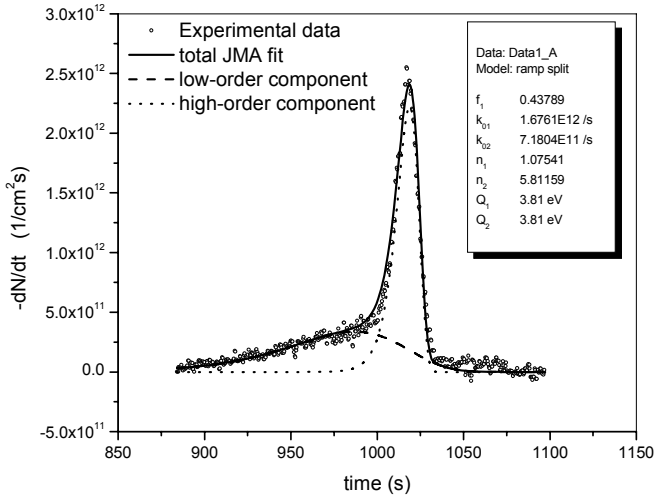

Fig. 5. Combined JMA fit for the 1017ºC desorption event of the 1 x 10^{15}/cm^2 dosed sample, consisting of a low order and a high order component. Note f_1 is the number fraction corresponding to the low order component (refer to the Appendix for fitting methodology).

Complex desorption behavior

The above analyses are based on the desorption signal recorded during the first heating ramp of a sample. However, this event was also observed during immediate cooling after first heating and even during subsequent (without opening chamber) re-heating and re-cooling, as illustrated in Fig. 6 by sample S3. Only after a sample was held isothermally at a very high (1330ºC) temperature for a long time (~ 30 min) did the event disappear completely during subsequent heat-up and cool down. While the existence of multiple de-trapping and migration mechanisms with a range of activation-energies is a tentative explanation for this complex behavior, the exact reason is not yet clear.

Samples of 1 x 10^{13} and 1 x 10^{11}/cm^2 dose

The ~ 1000ºC desorption event observed for the samples implanted to a He dose of 1x10^{15}/cm^2 was not unambiguously observed from the 1 x 10^{11} and 1 x 10^{13} He/cm^2 dosed samples for the same heating ramp conditions. Rather, these lower dosed samples exhibited very similar signals (spurious peaks) as the non-implanted samples. The absence of strong desorption signals from these two samples may not be a surprise since the total number of implanted He atoms in these samples is much lower than the 1 x 10^{15} He/cm^2 dosed sample. It appears necessary to improve the signal to noise ratio of the mass spectrometer in order to successfully detect any desorption events occurring in these lower dosed samples, in addition to performing the implantations at lower He ion energy.

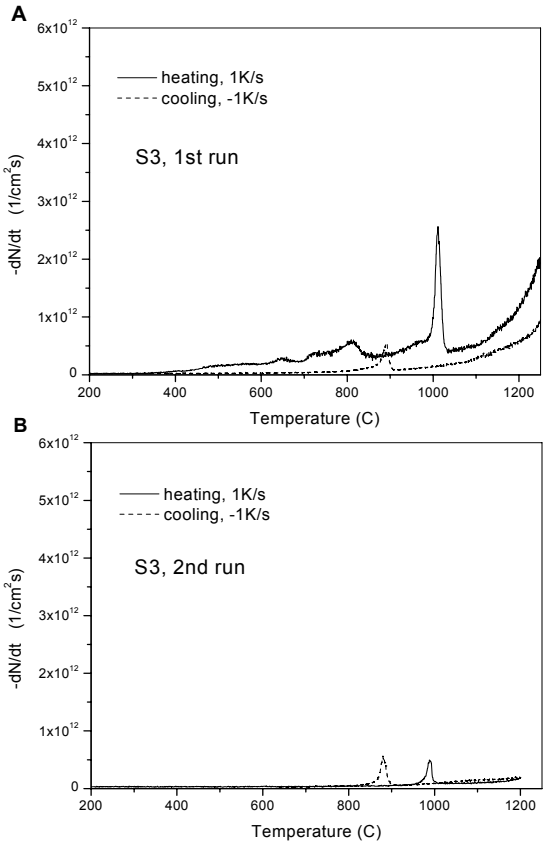

Fig. 6. First and second heating-cooling cycles of sample S3 showing the repetitive appearance of the same desorption event.

Conclusions

He desorption from iron implanted with 100 keV He to a dose of 1 x 10^{15}He/cm^2 occurs mainly at high temperatures (above 880ºC). Two desorption events have been observed for this sample during a constant rate ramping process: one with a fully developed peak at 1017ºC (in a 1 K/s ramp), the other with an onset of ~ 1100ºC, but not fully developed up to 1330ºC. The 1017ºC desorption event has been analyzed using both conventional reaction model and JMA model kinetics. First order equations from either model can only describe the broad early part of the event but not the steep desorption peak. A higher order JMA model can account for the peak steepness, but does not satisfactorily describe the early broad part. The superposition of a low-order (n ~ 1.1) and a high-order (n ~ 5.8) component produces excellent fits to the entire desorption event. The activation energy, Q, for this event was determined to be ~ 3.8 eV based on the peak shift with heating rates, and was confirmed by the data fitting. He desorption signals from the 1 x 10^{11} and 1 x 10^{13}/cm^2 He implanted samples have not been successfully detected at present. Future efforts will focus on a systematic examination of He release as a function of implanted He ion energy and dose, in addition to further analysis to determine the governing He de-trapping and migration mechanisms controlling the release peaks at 1017 and ~ 1100ºC.

Acknowledgements

This work has been supported by the Office of Fusion Energy Sciences, U.S. Department of Energy, under Grant DE-FG02-04ER54750.

Appendix

Methodology for the two-order JMA fit (shown in Fig. 6) for the 1017ºC desorption event of the 1 x 10^{15} /cm^2 dosed sample:

1) $N_{01} = f_1 * N_0$ and $N_{02} = (1 - f_1) * N_0$;
2) $dN / dt = dN_1 / dt + dN_2 / dt$;
3) $dN_i / dt = -N_{0i} * dx_i / dt = -N_{0i} * n_i K_i^{n_i} t^{n_i - 1} \exp(-K_i^{n_i} t^{n_i}) * [1 + \beta * tQ_i / (K_B T^2)]$ $(i = 1,2)$;
4) $K_i = K_{0i} \exp(-Q_i / K_B T)$ $(i = 1,2)$,

where f_1 is the number fraction corresponding to the low order component, and N_0 is the total number of He atoms for the entire desorption event.

References

[1] E. E. Bloom and F. W. Wiffen, J. Nucl. Mater. 58 (1975) 171.
[2] L. K. Mansur and W. A. Coghlan, J. Nucl. Mater. 119 (1983) 1.
[3] H. Ullmaier, Nucl. Fusion 24 (1984) 1039.
[4] L. K. Mansur and M. L. Grossbeck, J. Nucl. Mater. 155 (1988) 130.
[5] H. Trinkaus and B. N. Singh, J. Nucl. Mater. 323 (2003) 229.
[6] A. V. Fedorov, A. van Veen, and A. I. Ryazanov, J. Nucl. Mater. 233 (1996) 385.
[7] E. Oliviero, M. F. Beaufort, J. F. Barbot, A. van Veen, and A. V. Fedorov, J. Appl. Phys. 93 (2003) 231.
[8] I. Mori, T. Morimoto, R. Kawakami, and K. Tominaga, Nucl. Instrum. Methods Phys. Res. B 153 (1999) 126.
[9] A. A. Selezenev, V. G. Golubev, and N. S. Ganchuk, Chem. Phys. Rep. 17 (1998) 295.
[10] K. Morishita, R. Sugano, B. D. Wirth, and T. D. de la Rubia, Nucl. Instrum. Methods Phys. Res. B 202 (2003) 76.
[11] R. J. Kurtz and H. L. Heinisch, J. Nucl. Mater. 329 (2004) 1199.
[12] M. B. Lewis and K. Farrell, Nucl. Instrum. Methods Phys. Res. B 16 (1986) 163.
[13] K. Arakawa, R. Imamura, K. Ohota, and K. Ono, J. Appl. Phys. 89 (2001) 4752.
[14] T. Ishizaki, Q. Xu, T. Yoshiie, and S. Nagata, Mater. Trans. 45 (2004) 9.
[15] T. Iwai, Y. Ito, and M. Koshimizu, J. Nucl. Mater. 329 (2004) 963.
[16] R. Sugano, K. Morishita, A. Kimura, H. Iwakiri, and N. Yoshida, J. Nucl. Mater. 329 (2004) 942.
[17] R. Vassen, H. Trinkaus, and P. Jung, Phys. Rev. B 44 (1991) 4206.
[18] S. C. Glade, B. D. Wirth, and H. Schut, Fusion Materials Semiannual Progress Reports, DOE/ER-0313/37 (2004) 136.
[19] J. F. Ziegler, J. P. Biersack, and U. Littmark, The Stopping and Range of Ions in Matter, Pergamon, New York (1984).
[20] A. van Veen, A. Warnaar, and L. M. Caspers, Vacuum 30 (1980) 109.
[21] W. A. Johnson and R. F. Mehl, Trans. Am. Inst. Min. Metall. Engs. 135 (1939) 416.
[22] M. Avrami, J. Chem. Phys. 7 (1939) 1103.
[23] D. W. Henderson, J. Non-Cryst. Solids 30 (1979) 301.

MOLECULAR DYNAMICS SIMULATIONS OF POINT DEFECT INTERACTIONS IN FE-CR ALLOYS–K. L. Wong, J. H. Shim, and B. D. Wirth (University of California, Berkeley)

OBJECTIVE

The objective of this work is to understand the effect of Cr on the diffusion of single, di-, and tri-interstitials in Fe-1%Cr and Fe-10%Cr alloys using molecular dynamics simulations.

SUMMARY

Two different Finnis-Sinclair-type potentials were used to model Fe-1%Cr and Fe-10%Cr alloys, which alternately describe Cr as under- or over-sized in body-centered cubic Fe. In general, the diffusivity of the single interstitials and di- and tri-interstitial clusters was reduced in the Fe-10%Cr alloys, irrespective of interatomic potential, although the underlying mechanism(s) were different. When Cr is undersized, interstitial diffusion is retarded through a trapping mechanism associated with bound Cr-interstitial (mixed dumbbell) complexes, whereas oversized Cr atoms retard interstitial diffusion by enhancing the rotation frequency away from one-dimensionally mobile <111> interstitial dumbbell configurations.

PROGRESS AND STATUS

Introduction

Fe-Cr alloys are candidate first wall and breeder blanket materials in future fusion reactors. Radiation damage from high-energy fusion neutrons creates large excess point defect and point defect cluster concentrations in displacement cascades, which, in conjunction with transmutant helium and hydrogen, are ultimately responsible for microstructure evolution that can produce deleterious changes to performance-limiting properties. Thus, predicting material performance under irradiation requires an understanding of point defect properties, including their migration and clustering behavior and any modification in this behavior as a result of interaction with solutes, impurities and other defects. In this study, molecular dynamics (MD) simulations employing two different Fe-Cr potentials are used to study the effect of 1-10% Cr on self-interstitial and small interstitial cluster migration.

Studies of the effect of Cr on displacement cascade evolution in Fe-Cr alloys have observed no effect on defect production [1, 2]. Although no differences were observed in the absolute number of defects formed, Cr may have an influence on the migration properties of point defect clusters that can influence eventual defect fate and produce a larger effect on microstructural properties. Recent work by Terenyev [3] has observed changes in the diffusional character of interstitial defects based on EAM Fe-Cr potentials, although the mechanistic cause was not determined.

In this work, we investigate the effect of Cr on point defect properties and microstructural evolution in irradiated Fe-Cr alloys. The initial focus is on single interstitial and small interstitial cluster transport using MD simulations. Two different Fe-Cr interaction potentials [2] were used, which show differing size effects of Cr in the body-centered cubic (BCC) Fe matrix. The next section describes the simulation method and interaction potentials, and section 3 presents a discussion of the results of MD simulations on the effect of Cr on single, di-, and tri- interstitial diffusion in Fe-1% and 10%Cr alloys.

Simulation Methods

Molecular dynamics simulations were performed using the MDCASK code [4] to investigate the effect of 1% and 10% Cr on the diffusivity of single, di-, and tri-interstitials. The simulation cell consisted of a 50x50x50 bcc unit cells (250,000 + N atoms) with periodic boundary conditions and either a single, di-, or tri-interstitial (N = 1, 2, or 3). Pure Fe and randomly distributed ferritic alloys with 1% and 10% Cr were simulated. Single interstitials were initially oriented in the <111> direction; clusters of di- or tri-interstitials were inserted as parallel <111> dumbbells. The MD simulations were performed at temperatures from

400 to 1000K ,with additional low temperature simulations for single interstitials at 50 to 200K. Two different cross-potentials for the Fe-Cr interaction were used, which show contrasting size effects of Cr in the Fe matrix. Simulations were conducted for 500 ps with the defect diffusivity sampled every 10 to 200 ps.

Interatomic Potentials

Finnis-Sinclair-type potentials were used to describe the interatomic interactions. The Ackland potential [5] was used to describe pure Fe, and the Finnis-Sinclair potential [6] was used for Cr atom interactions. The Ackland potential correctly predicts the stability and formation energy of self-interstitial atoms in bcc Fe, although it may predict too small of an energy difference between the <110> and <111> split-dumbbell configurations according to recent ab-initio results [7]. The diffusion and the migration mechanism of single and small self-interstitial atom clusters is well understood with the Ackland potential [8], and the goal of this project is to understand the effect of Cr on the diffusion mechanism(s) as compared to pure Fe.

Two different Fe-Cr interaction potentials were obtained from Shim and co-workers [2], which were fit to the heat of mixing and lattice constant data using the method outlined by Konishi et al. [9]. The two cross-potentials show contrasting size effects of Cr in the Fe matrix. The Fe-Cr I potential predicts Cr to be oversized relative to Fe, creating a compression field around the Cr that is repulsive to neighboring Fe in the matrix. Mixed dumbbells do not form readily in either <110> (E_b = -0.40 eV) or <111> (E_b = -0.26 eV) configurations. A <110>-oriented Fe dumbbell with a Cr atom oriented perpendicularly to the axis of the dumbbell has a very small binding energy of +0.02 eV, while Cr oriented parallel to the dumbbell has a repulsive interaction energy of –0.16 eV. The Fe-Cr II potential predicts undersized Cr in bcc Fe, creating a tension field around the Cr that is attractive to neighboring Fe in the matrix. Mixed dumbbells are stable in both <110> (E_b = +0.10 eV) and <111> (E_b = +0.20 eV) configurations with the Fe-Cr II potential. The orientation of a Cr atom parallel to the axis of a <110> dumbbell has a binding energy of +0.06 eV, while a Cr atom oriented perpendicular to the dumbbell produces a slightly negative interaction energy of –0.01 eV. Recent ab-initio calculations by Domain [10] predict a binding energy of 0.0 and +0.3 eV for <110> and <111> mixed dumbbells, respectively.

Results and Discussion

Figure 1 shows the percentage of Cr observed in mixed dumbbells in single interstitial and in di- and tri-interstitial clusters for Fe-10%Cr alloys as a function of temperature and interatomic potential. The oversized/repulsive Cr using the Fe-Cr I potential prevents the formation of mixed interstitial dumbbells at all temperatures, and the percentage of Cr in single interstitials is significantly lower (10x) than the matrix Cr concentration. Di and tri- interstitial clusters do have increased Cr content relative to single interstitials using the Fe-Cr I potential, but do not reach the matrix concentration. Thus, interstitial diffusion in Fe-Cr alloys as predicted by the Fe-Cr I potential, consists of interstitial defects, which are essentially pure Fe dumbbells, diffusing through a matrix containing oversized/repulsive Cr. With the Fe-Cr II potential, single, di-, and tri- interstitials are significantly enriched in Cr (2x – 8x matrix Cr concentration), as expected from the positive binding energy of mixed dumbbells in both <110> and <111> orientations. Since mixed dumbbells and even a few Cr-Cr dumbbells readily form, the interstitial defect diffusion behavior predicted by the Fe-Cr II potential is more complex.

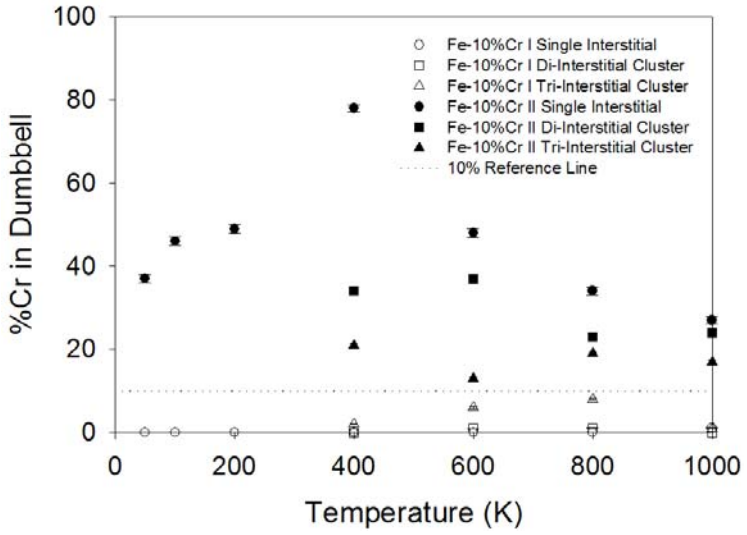

Fig. 1. Percentage of Cr in single interstitial and in di-, tri- interstitial clusters for Fe-10%Cr alloy.

Figure 2a plots the defect diffusivity for the single interstitial in pure Fe and an Fe-10%Cr alloy, using both Fe-Cr potentials. The mean square displacement and diffusivity was calculated by sampling the center of mass of the defect for time intervals between 10 and 200ps. The simulation data was fit to a standard Arrhenius form, and the resulting diffusion pre-factors and migration (activation) energies are presented in Table 1. For single interstitials (Fig. 2a), the effect of 10% Cr on interstitial diffusivity was minimal at the highest simulated temperatures (800 and 1000K), while the Cr atoms decreased interstitial diffusivity at intermediate temperatures (400 and 600K), irrespective of the Fe-Cr potential. At lower temperatures (100 and 200K), significantly more variation in diffusion behavior occurred, although the interstitial was predicted to be most mobile using the Fe-Cr II potential. Little to no interstitial mobility was observed in pure Fe and the Fe-10%Cr alloy using the Fe-Cr I potential at 100 and 200K, corresponding to the single interstitial oriented predominantly as a <110> dumbbell. Thus, the Arrhenius fit to the single interstitial diffusion data was limited to the temperature range from 400 to 1000K. Over this range, both potentials indicate that Cr retards interstitial diffusivity except at the highest temperatures, and increases the temperature sensitivity. The fits indicate an increase in the diffusional pre-factor (~ 12X) and an increase in the activation energy to 0.23±0.01 eV for interstitial migration in Fe-10%Cr compared to an essentially athermal value of 0.04 eV in pure Fe. Despite the similar effect of Cr atoms on the single interstitial diffusivity, the underlying mechanism is different with the two different potentials.

Table 1. Calculated pre-factors and migration energies for single interstitials in pure Fe and 1% and 10% Fe-Cr alloys

		Single Interstitial		Di-Interstitial		Tri-Interstitial	
	Potential	D_0 [cm^2/s]	E_m [eV]	D_0 [cm^2/s]	E_m [eV]	D_0 [cm^2/s]	E_m [eV]
Pure Fe	Ackland Fe	7.7e-4	0.04	8.0e-4	0.03	1.3e-3	0.06
Fe-1%Cr	Fe-Cr I	1.1e-3	0.06	9.6e-4	0.06	2.5e-4	0.05
	Fe-Cr II	2.4e-3	0.11	5.7e-3	0.16	5.6e-3	0.03
Fe-10%Cr	Fe-Cr I	9.4e-3	0.22	6.5e-3	0.11	6.3e-4	0.12
	Fe-Cr II	9.6e-3	0.24	6.0e-4	0.10	7.3e-4	0.10

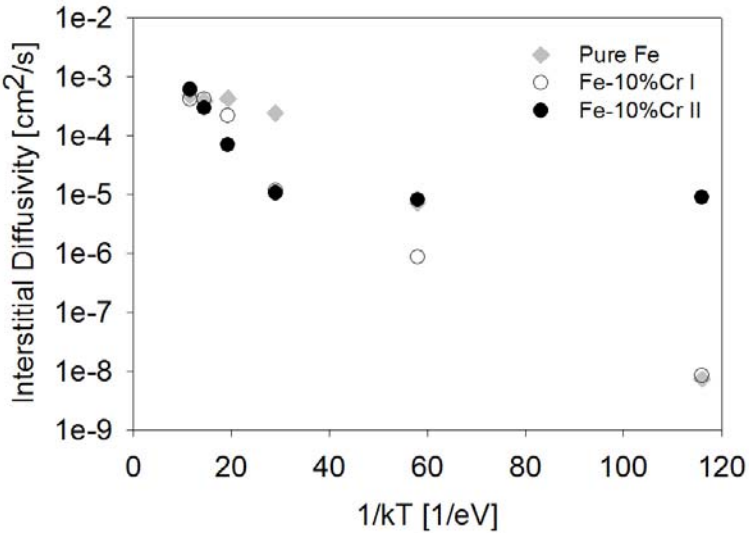

(a)

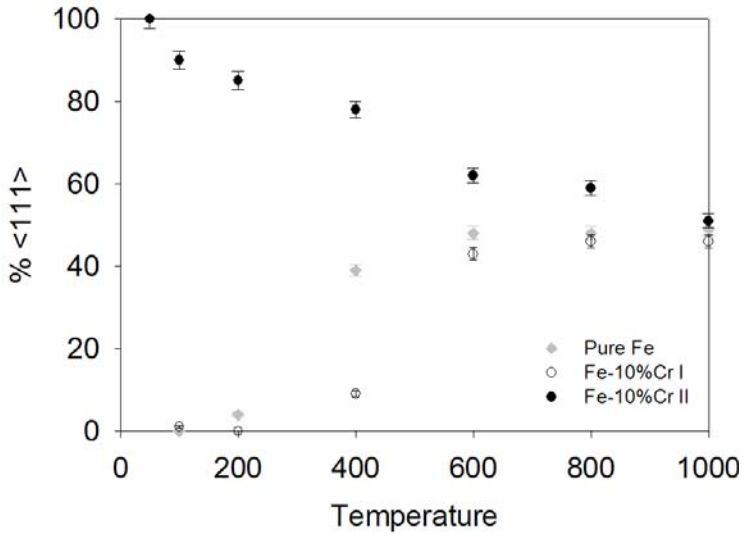

(b)

Fig. 2. Diffusivity of single interstitials for pure Fe and Fe-10%Cr alloys (a). Percentage of time single interstitials are oriented in the <111> direction for Fe-10%Cr alloy (b).

The Ackland Fe potential predicts that single self-interstitials migrate by rotating between <110> and <111> orientations, and undergo subsequent translation along the <111> directions through a crowdion saddle point [10]. Thus, <110> orientations represent intermediate stationary orientations during rotations between <111> translation directions. Hence, the migration mechanism of dumbbells is highly dependent on defect orientation. Figure 2b plots the percentage of time that single interstitials are oriented in the <111> direction for the 10% Cr concentration, as a function of temperature and the Fe-Cr potential. In general, the interstitial spends more time in <111> orientations with the Fe-Cr II (undersized Cr atoms) and less with the Fe-Cr I potential (oversized Cr atoms). At temperatures above 600K, the effect of Cr, regardless of size, on the fraction of <111> dumbbells is negligible and both the Fe-Cr I and Fe-Cr II

simulations results converge towards those of pure Fe, as does the diffusivity (Fig. 2a). At intermediate temperatures, the diffusivity is suppressed, regardless of the size of Cr, as shown in Fig. 2a. The higher concentration of oversized/repulsive Cr atoms using Fe-Cr I decreases the fraction of time spent in <111> dumbbells compared with pure Fe and produces an increase in the migration energy for Fe-Cr I, presumably associated with more frequent rotations. Dumbbells that encounter a Cr along its axis of migration preferentially rotate to align the Cr atom perpendicular to the dumbbell, leading to decreased Cr content in the interstitial with the Fe-Cr I potential, as shown in Fig. 1. The enhanced rotation into different <111> orientation retards 1-D migration along any single <111> direction. The undersized/attractive Cr atoms using the Fe-Cr II potential stabilize the <111> dumbbell orientation relative to the <110> especially at intermediate to low temperatures (below 600K) due to preferential alignment of dumbbells parallel to Cr, including mixed dumbbell formation. The stabilization of the <111> dumbbell leads to a reduction in rotation into <110> orientations and is responsible for trapping the interstitial, presumably responsible for the higher migration energy. Visualization of the MD simulations at low temperatures shows that the <111> dumbbell with the Fe-Cr II potential continues to make lattice jumps due to attraction of neighboring undersized Cr atoms.

Small interstitial clusters consist of parallel <111>-oriented dumbbells, and their migration consists of individual 1-D crowdion jumps along <111> directions, with rotations into different <111> orientations providing a 3-D diffusion character [10, 11, 12]. Figure 3 shows the effect of 10% Cr on the diffusivity of di- (Fig. 3a) and tri-interstitials (Fig. 3b). For both di- and tri-interstitials, diffusivity is decreased by Cr, with a somewhat larger decrease predicted by the Fe-Cr I (oversized Cr atom) potential. As with the single interstitial, the temperature dependence of the di- and tri-interstitial diffusivity is increased by Cr (larger activation energy). However, the effect on the pre-factor is not as pronounced as for the single interstitial.

Figure 4 shows the center of mass trajectory of di-interstitials during 500ps at 600K for pure Fe and Fe-10%Cr alloys using the Fe-Cr I and Fe-Cr II potentials. The di-interstitial in pure Fe has a distinctly 1-D migration behavior with only a single observed rotation between <111> orientations. The addition of oversized/repulsive Cr atoms using the Fe-Cr I potential prevents prolonged one-dimensional translation segments of interstitial migration along the <111> directions and assists cluster rotation to align the Cr perpendicularly with the dumbbells. The net effect is to reduce the interstitial cluster diffusivity, although the 3-D character may increase. In contrast, the di-interstitial in a matrix of undersized/attractive Cr using the Fe-Cr II potential shows similar, primarily 1-D translation character as the di-interstitial in pure Fe. However, the undersized/attractive Cr does tend to suppress the very long 1-D translations by attracting (trapping) the cluster to jump back and forth between neighboring Cr atoms, thereby limiting the range of 1-D translations and the overall interstitial cluster diffusivity.

Conclusions

MD simulations, using two different Fe-Cr potentials, have been performed to determine the effect of Cr on the diffusion of single interstitials and small interstitial clusters in Fe-Cr alloys. One potential (Fe-Cr I) predicts that Cr is an over-sized solute atom, while the other (Fe-Cr II) predicts that Cr is undersized. The MD results reveal that Cr decreases the diffusivity of both single interstitials and di- and tri-interstitial clusters, except at the highest temperatures, irrespective of the atomic size of Cr (interatomic potential). Arrhenius fits to the defect diffusivity reveal that Cr increases the activation energy for interstitial/interstitial cluster migration, while also increasing the diffusion pre-factor. While the effect of Cr on interstitial/interstitial cluster diffusivity was similar for the two Fe-Cr potentials, the underlying mechanisms were different. A significant enrichment (2x – 8x matrix concentration) of Cr is observed in the interstitial defects using the Fe-Cr II potential (under-sized Cr atom), indicating the formation of mixed dumbbells. The formation of mixed dumbbells, which are energetically preferred, suggests a trapping mechanism that retards interstitial diffusion by decreasing the length of <111> translational segments for the under-sized Cr solute atom. The Fe-Cr I potential predicts a repulsive interaction between an oversized Cr atom and interstitial defects, which is observed to increase the rotation frequency of single interstitials between <111> and <110> orientations and of interstitial clusters between different <111> orientations. This increased rotation also reduces the diffusional length of one-dimensional <111> jump segments and

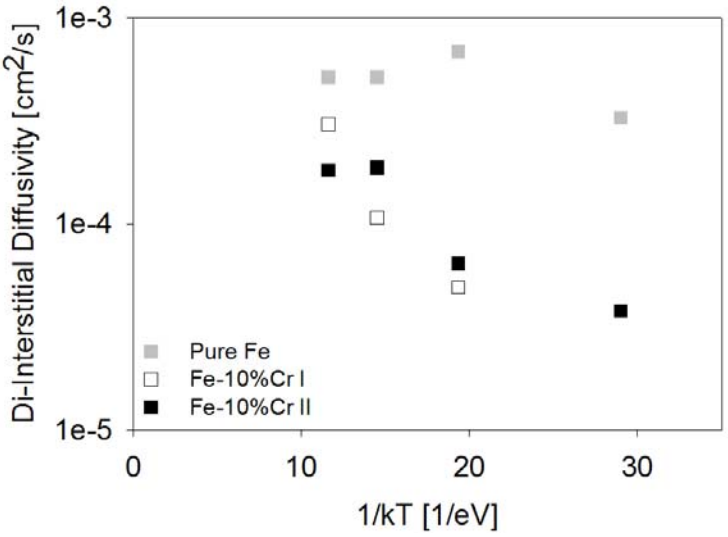

(a)

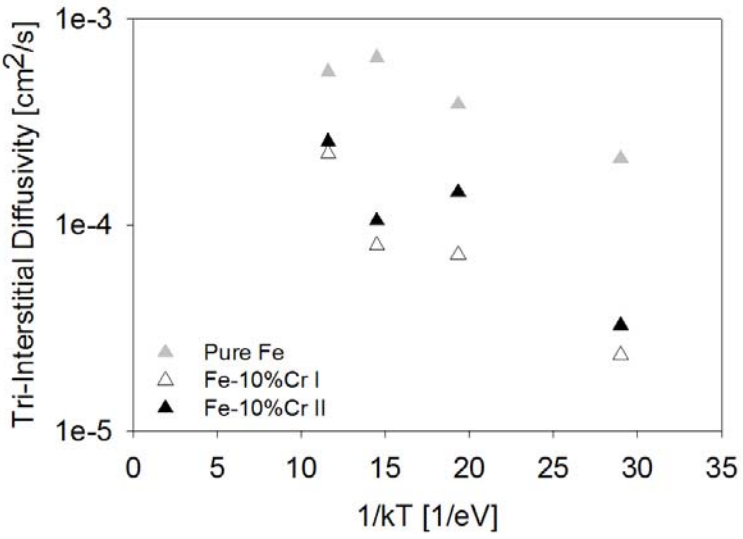

(b)

Fig. 3. Diffusivity of di- (a) and tri- (b) interstitials clusters for pure Fe and Fe-10%Cr alloys.

correspondingly decreases the interstitial/interstitial cluster diffusivity. Future modeling efforts will quantify the amount of Cr diffusion by interstitials, and develop Monte Carlo models of isochronal annealing recovery to compare with experimental observations.

Acknowledgements

This work has been supported by the Office of Fusion Energy Sciences, U.S. Department of Energy, under Grant DE-FG02-04ER54750.

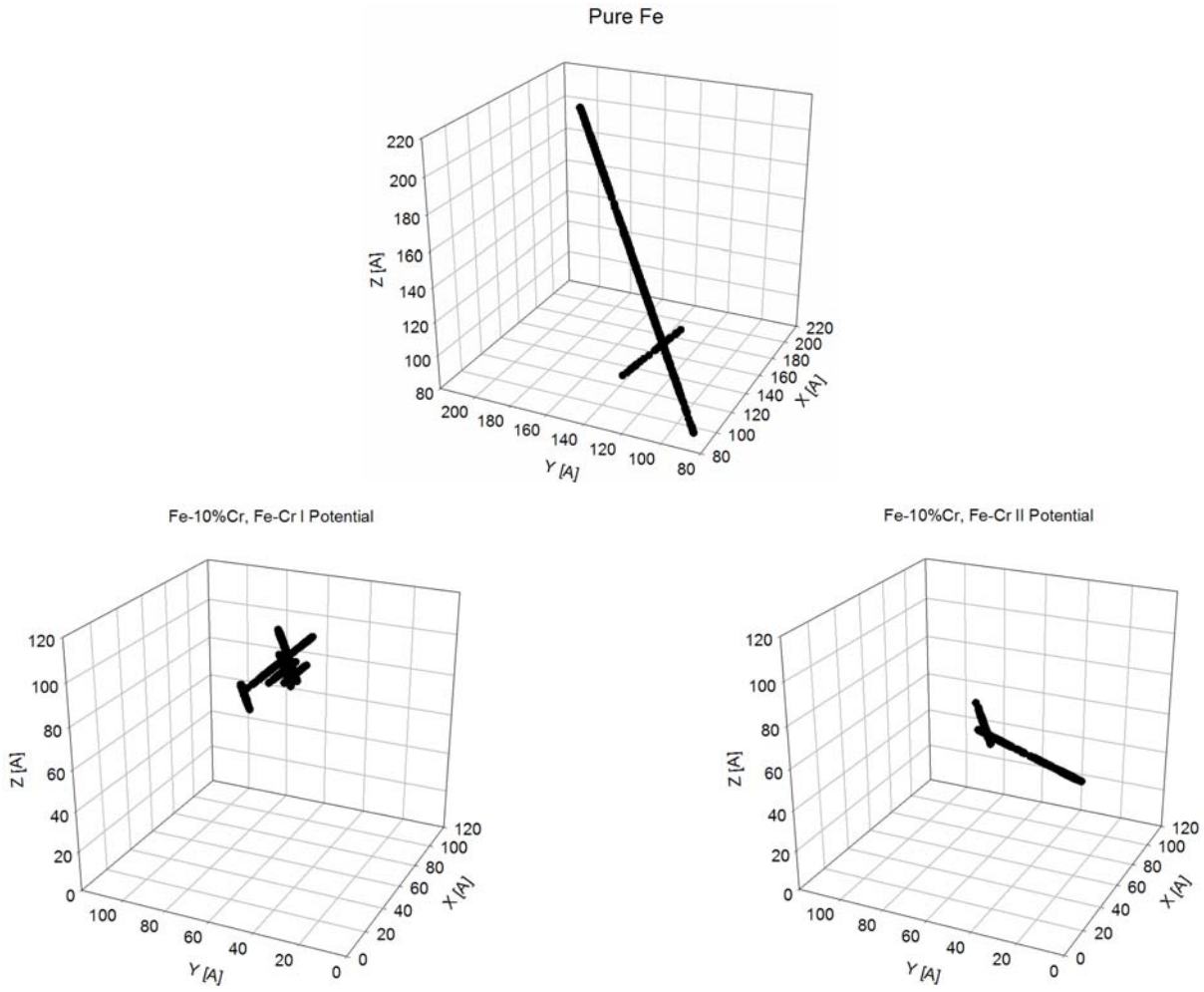

Fig. 4. Center of mass trajectory of di-interstitials at 600K for pure Fe (a) and Fe-10%Cr alloys using Fe-Cr I (b) and Fe-Cr II (c).

References

[1] L. Malerba, D. Terentyev, P. Olsson, R. Chakarova, and J. Wallenius, J. Nucl. Mater. 329 (2004) 1156.
[2] J.-H. Shim, H.-J. Lee, and B. D. Wirth, Journal of Nuclear Materials (in press).
[3] D. Terentyev and L. Malerba, J. Nucl. Mater. 329 (2004) 1161.
[4] T. Diaz de la Rubia and M. W. Guinan, J. Nucl. Mater. 174 (1990) 151.
[5] G. J. Ackland, D. J. Bacon, A. F. Calder, and T. Harry, Philos. Mag. A 75 (1997) 713.
[6] M. W. Finnis and J. E. Sinclair, Philos. Mag. A 50 (1984) 45.
[7] F. Willaime, C. C. Fu, M. C. Marinica, and J. Dalla Torre, Nucl. Instrum. Methods Phys. Res. Sect. B: Beam Interact. Mater. Atoms 228 (2005) 92.
[8] J. Marian, B. D. Wirth, A. Caro, B. Sadigh, G. R. Odette, J. M. Perlado, and T. Diaz de la Rubia, Phys. Rev. B 65 (2002) 144102.
[9] T. Konishi, K. Ohsawa, H. Abe, and E. Kuramoto, Comp. Mater. Sci. 14 (1999) 108.
[10] C. Domain, personal correspondence.
[11] Yu. N. Osetsky and D. J. Bacon, Philos. Mag. Lett. 79 (1999) 273.
[12] B. D. Wirth, G. R. Odette, D. Maroudas, and G. E. Lucas, J. Nucl. Mater. 276 (2000) 33.

ATOMISTIC MODELING OF THE INTERACTION OF HE WITH NANOCLUSTERS IN FE—R. J. Kurtz, F. Gao, and H. L. Heinisch (Pacific Northwest National Laboratory*), B. D. Wirth (University of California, Berkeley), G. R. Odette and T. Yamamoto (University of California, Santa Barbara)

Extended abstract of a paper submitted to the Journal of Nuclear Materials as part of the proceedings of the 12th International Conference on Fusion Reactor Materials, Santa Barbara, California, December 4–9, 2005.

INTRODUCTION

Structural materials of a fusion power system will be exposed to high concentrations of He produced from nuclear transmutation reactions. Helium is essentially insoluble in metals so there is a strong tendency for it to form bubbles that can significantly degrade mechanical properties. A strategy to effectively manage He is to provide a high-density of internal interfaces to serve as He bubble nucleation sites and vacancy-interstitial recombination centers. Nanostructured ferritic alloys are being developed to provide improved creep strength and He management capability compared to conventional steels. A key characteristic of these materials is the high-density (~ 10^{24} m^{-3}) of nanometer-scale (~ 3 nm diameter) Y-Ti-O clusters. We describe molecular dynamics simulations to assess the interaction of He atoms, vacancies and He-vacancy complexes with coherent Cu nanoclusters in Fe. The potentials employed here were adjusted to explore the effect of nanocluster elastic properties on He trapping efficiency.

Computational Procedure

The Fe-Cu-He interatomic potential used here was constructed from various binary potentials obtained from the literature. All of the potentials use the Finnis-Sinclair formalism. Ackland et al. [1] have previously described the development of the Fe-Fe, Cu-Cu, and Fe-Cu potentials in detail. The Fe-He and He-He interactions have also been described previously [2]. For the Cu-He interaction the Wilson-Johnson potential was used in this work [3]. Table 1 lists important physical properties calculated from the Fe-Cu-He potential along with comparisons to experimentally measured values. The calculated properties for the bcc phase of Cu are also presented in Table 1. It should be noted that the lattice parameter of bcc Cu is ~ 3.3% larger than bcc Fe so coherent Cu nanoclusters in a Fe matrix are positive misfit particles. It is also evident from Table 1 that coherent Cu nanoclusters are elastically stiffer than Fe. Such features are considered to be representative of the physical and mechanical characteristics of Y-Ti-O nanoclusters.

To explore the effect of nanocluster elastic properties on He trapping efficiency the Cu-Cu and Fe-Cu potentials were modified so that the lattice parameter and cohesive energy for the modified fcc phase were the same as for real Cu, but the elastic constants were decreased to c_{11} = 100 GPa, c_{12} = 75.4 GPa and c_{44} = 35.3 GPa. Following an approach similar to the derivation of the original Cu potential, cubic splines were used to describe the potential functions. The form of the spline functions for the pair interaction and electron density, respectively, are as follows:

$$V(r) = \sum_{k=1}^{6} a_k (r_k - r)^3 H(r_k - r) \quad (1)$$

$$\phi(\mathrm{r}) = \sum_{\mathrm{k}=1}^{6} \mathrm{A_k} (\mathrm{R_k} - \mathrm{r})^3 \mathrm{H}(\mathrm{R_k} - \mathrm{r}) \quad (2)$$

where H is the Heaviside step function, and r is the distance between atoms. Table 2 gives the lattice parameter and elastic constants for the new fcc and bcc phases of the modified Cu potential. The bcc

*Pacific Northwest National Laboratory (PNNL) is operated for the U.S. Department of Energy by Battelle Memorial Institute under contract DE-AC06-76RLO-1830.

lattice parameter produced by the present potential is slightly larger than that given by the Ackland et al. potential, i.e., 0.304 nm as compared with 0.296 nm. It is evident that the elastic constants for the bcc phase are much smaller than those given by the Ackland potential, which is consistent with the general tendency of fcc Cu, as shown in Table 2.

Table 1. Physical properties of Fe-Cu-He Finnis-Sinclair potential

Property	BCC Fe		FCC Cu		BCC Cu
	Calc.	Expt.	Calc.	Expt.	Calc.
Lattice parameter, nm	0.2867	0.2867 [4]	0.3615	0.3615[5]	0.2961
Atomic volume, nm^3	0.0118	0.0118	0.0118	0.0118	0.0130
c_{11}, GPa	243	230 [6]	169	169 [6]	290
c_{12}, GPa	145	135 [6]	122	122 [6]	192
c_{44}, GPa	116	117 [6]	76	75 [6]	147
Cohesive energy, eV	4.316	4.28 [7]	3.519	3.49 [7]	3.496
Point defect formation energies					
Vacancy, eV	1.70	1.6–2.2 [8–11]	1.19	1.1–1.3 [11–14]	1.32
Di-vacancy (1nn), eV	3.26	-	2.21	-	2.42
Di-vacancy (2nn), eV	3.22	-	2.42	-	2.55
Substitutional He, eV	3.25	-	2.75	-	2.54
He_1V_2 complex (1nn), eV	4.49	-	3.60	-	3.42
He_1V_2 complex (2nn), eV	4.76	-	3.98	-	3.73

Table 2. Physical properties of the modified Cu potential

Property	FCC Phase	BCC Phase
Lattice parameter, nm	0.3615	0.3041
Atomic volume, nm^3	0.0472	0.0281
c_{11}, GPa	100	198
c_{12}, GPa	75.4	103
c_{44}, GPa	35.3	66.1
Cohesive energy, eV	3.519	3.599
Point defect formation energies		
Vacancy, eV	1.00	1.67
Di-vacancy (1nn), eV	1.88	3.13
Di-vacancy (2nn), eV	2.00	3.19
Substitutional He, eV	2.68	2.67
He_1V_2 complex (1nn), eV	3.41	3.97
He_1V_2 complex (2nn), eV	3.69	4.15

For the Fe-Cu interaction, the many-body part of the cross potential is taken as the geometric mean of the elemental values, as described in detail by Ackland and Vitek [15], i.e., $\varphi_{AB}=(\varphi_{AA}\varphi_{BB})^{1/2}$. The pair component was fit to the unrelaxed single substitutional impurity (SSI) energy, and the cohesive energies and lattice parameters of fictitious L_{12} compounds, Fe_3Cu and Cu_3Fe. Based on experimental data, the heat of solution per atom can be easily calculated from the solubility limit [1], which gives the SSI energy of Cu in Fe and Fe in Cu to be 0.317 eV. Ackland et al. [1] generated the properties of the fictitious Fe_3Cu and Cu_3Fe compounds from electronic structure calculations. The cohesive energy for the present fitting is taken to be -3.9917 and -3.616 eV for Fe_3Cu and Cu_3Fe, respectively, while the lattice parameter is taken to be 0.36795 and 0.36493 nm. The cohesive energy and lattice parameter of these two

compounds, along with the experimental SSI energies, provide sufficient data for the fit of the pair component of the new cross potential.

Coherent Cu clusters embedded in a Fe matrix were used to explore how positive misfit nanodispersiods or precipitates may trap He. A 3D periodic computational cell was employed consisting of ~ 250,000 atoms. Cu nanoclusters 1–4 nm in diameter were placed at the origin of the model. Since the lattice parameter of bcc Cu is larger than Fe the Cu cluster seeks to expand, but is constrained by the surrounding Fe matrix. Consequently, models were prestrained close to the expected volume expansion of the system, estimated from $\Delta V/V=N_{Cu}(\Omega_{Cu}-\Omega_{Fe})$ where $\Delta V/V$ is the volume strain, N_{Cu} was the number of Cu atoms in the cluster, and Ω_{Cu}, Ω_{Fe} are the atomic volumes of Cu and Fe, respectively. Various He_mV_n complexes (m = 1, n = 1,2) were inserted at various distances from the Fe/Cu interface to explore the spatial dependence of the He_mV_n complex interaction with the Cu cluster. A conjugate gradient relaxation scheme was used to relax the model. The cell volume was adjusted during the relaxation to achieve zero pressure.

Results

Figure 1 shows the interaction energy between either a single vacancy (V_1) or a substitutional He atom (He_1V_1) as a function of their distance from a 2 nm diameter coherent bcc Cu cluster. The dependence of vacancy and He binding on interface character was explored by placing mono-vacancies or a substitutional He atom at different distances from either the {100} or {101} face of the Cu cluster. In this case the elastic properties of the bcc Cu nanocluster were stiffer than bcc Fe as given in Table 1. The calculated binding energies for mono-vacancies and substitutional He at the interface were nearly the same at ~ 0.58 eV. The distance dependence of the interaction energy for both types of point defects was also nearly the same, and no significant effect of interface character was found. To a first approximation the binding energies are roughly equal to the defect formation energy in bcc Fe minus the defect formation energy in bcc Cu. From Table 1 the predicted binding energies for a mono-vacancy and a substitutional He atom are 0.38 eV and 0.71 eV, respectively. It should be noted the defect formation energies given in Table 1 are computed for the pure metals at zero temperature and pressure, hence, the defect formation energies in the Cu nanocluster and in Fe near the nanocluster will be different due to the compressive stress state that exists in these regions.

Figure 2 presents the defect-nanocluster interaction energy results for both di-vacancies (V_2) and He/di-vacancy complexes (He_1V_2) in the vicinity of a 2 nm coherent Cu nanocluster that was stiffer than Fe. Both first nearest neighbor (1nn) and second nearest neighbor (2nn) di-vacancy configurations were considered. The dependence of binding energy on interface character was also examined and found not to be significant. The binding energies of di-vacancies and He/di-vacancy complexes were nearly the same at ~ 0.85 eV near the interface. Similar to the mono-vacancy and substitutional He, the binding energy for di-vacancies and He/di-vacancy complexes can be predicted from the difference in their defect formation energies in Fe and Cu. For 1nn V_2 and He_1V_2 defects the binding energies predicted from the data in Table 1 are 0.84 and 1.07 eV, respectively. Similarly, for 2nn V_2 and He_1V_2 defects the predicted binding energies are 0.67 and 1.03 eV, respectively. The predicted binding energies are fairly close to the calculated value, which is somewhat unexpected given that these defects simultaneously reside in both the Cu nanocluster and in the Fe matrix.

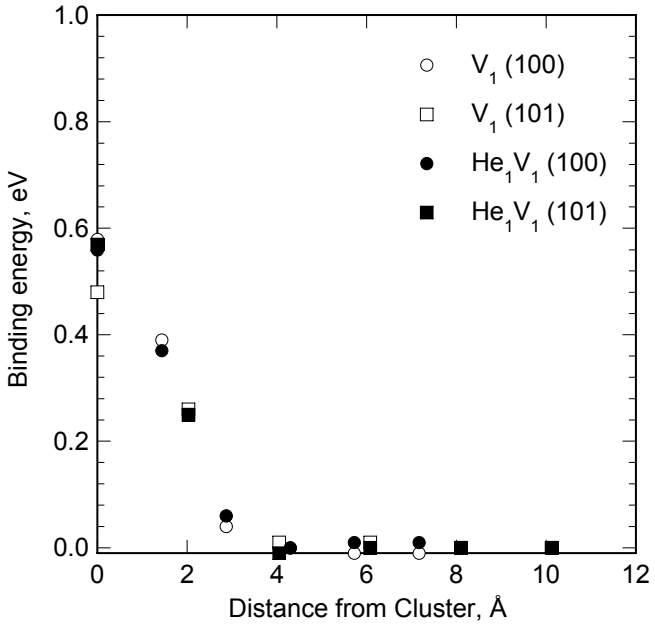

Fig. 1. The interaction energy between a single vacancy (V_1) or a substitutional He atom (He_1V_1) and a 2 nm coherent bcc Cu cluster in Fe as a function of the distance from either the {100} or {101} face of the Cu cluster. The Cu cluster is elastically stiffer than Fe.

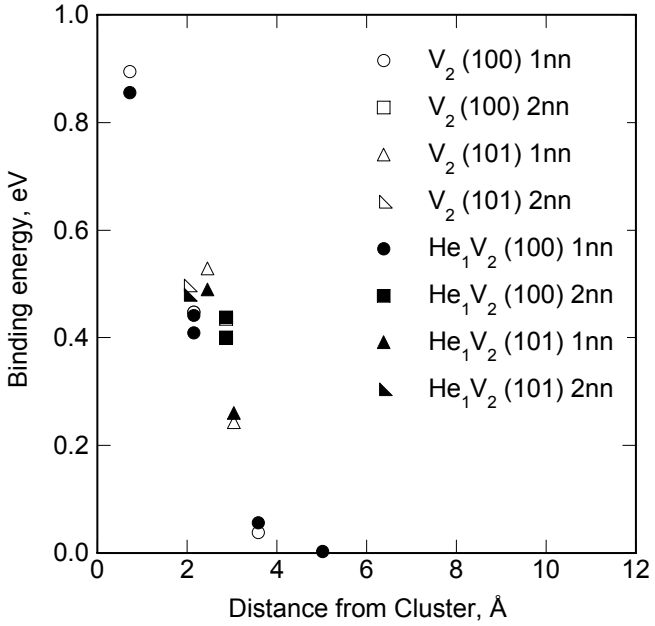

Fig. 2. The interaction energy between a di-vacancy (V_2) or a He/di-vacancy (He_1V_2) complex as a function of distance from a 2 nm coherent bcc Cu cluster in Fe. Di-vacancy configurations are either first nearest neighbor (1nn) or second nearest neighbor (2nn). The Cu cluster is elastically stiffer than Fe.

The dependence of the 1nn He_1V_2 complex binding energy on nanocluster size was examined. The He_1V_2 complex was more weakly bound to a 1 nm diameter nanocluster (~ 0.55 eV) than to clusters ranging from 2–4 nm. The binding energy was approximately the same for 2–4 nm diameter clusters (~ 0.85 eV). It is not surprising that the He_1V_2 complex is more weakly bound to the 1 nm cluster since this nanoparticle consists of only 59 Cu atoms. Most of the Cu atoms in the nanocluster have Fe atoms for neighbors consequently the properties of defects near the nanocluster will be dominated by the defect properties of Fe.

Figures 3 and 4 display results analogous to those shown in Figs. 1 and 2 except that the interatomic potentials were modified to produce a bcc phase that has about the same lattice parameter as bcc Cu but with elastic properties softer than Fe. Note the cohesive energy for the modified fcc phase is the same as fcc Cu, but the cohesive energy of the modified bcc phase is about 0.1 eV greater than the original bcc Cu. The larger cohesive energy may partially account for the 0.35 eV increase in the mono-vacancy formation energy. The results clearly show that vacancies and He-vacancy complexes are more weakly bound to the modified bcc nanoclusters. In addition, mono-vacancy binding energies (0.28–0.35 eV) were lower than substitutional He binding energies (0.39-0.49 eV). The defect formation energy data given in Tables 1 and 2 suggest this trend. The vacancy formation energy in the modified bcc phase is only 0.03 eV smaller than bcc Fe, so weaker binding of mono-vacancies is expected. Similarly, the substitutional He formation energy in the modified bcc phase is 0.13 eV greater than in bcc Cu, so weaker binding would be anticipated. Further, the differences in defect formation energies suggest that substitutional He atoms would be bound more strongly than single vacancies to the modified bcc phase as shown in Fig. 3. Di-vacancies and He_1V_2 complexes were also more weakly bound to the modified bcc phase, which results from the increased defect formation energies in the modified bcc phase relative to bcc Cu (see Tables 1 and 2). Differences in defect formation energy predict that di-vacancies should be more weakly bound to the nanocluster than He_1V_2 complexes, but the results displayed in Fig. 4 indicate the opposite was observed.

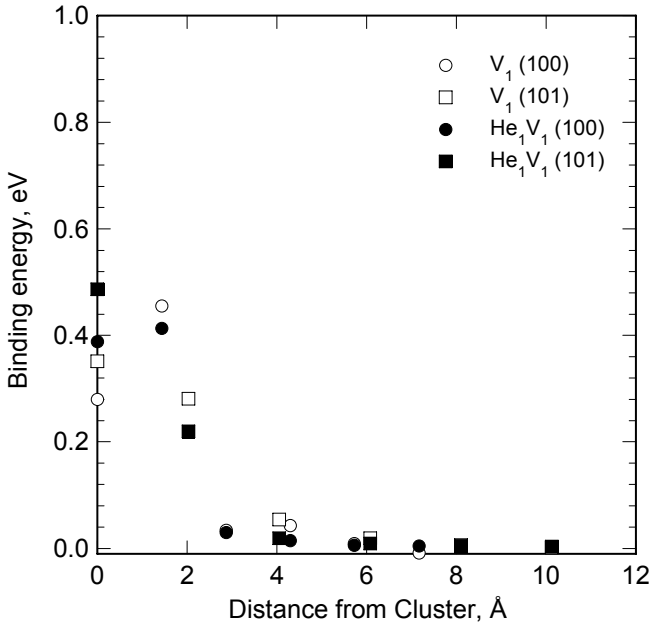

Fig. 3. The interaction energy between a single vacancy (V_1) or a substitutional He atom (He_1V_1) as a function of distance from a 2 nm cluster in Fe. The interatomic potential for Cu was modified to make the nanocluster elastically softer than the Fe matrix.

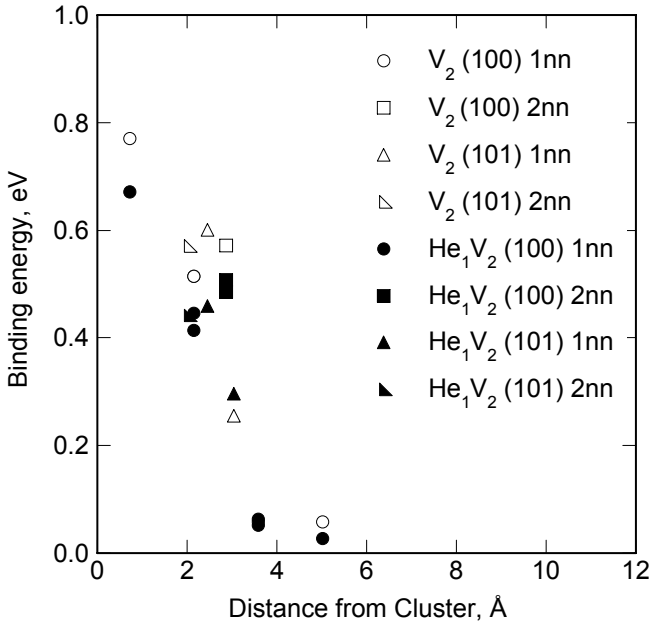

Fig. 4. The interaction energy between a di-vacancy (V_2) or a He/di-vacancy (He_1V_2) complex as a function of distance from a 2 nm Cu cluster in Fe. Di-vacancy configurations are either first nearest neighbor (1nn) or second nearest neighbor (2nn). The interatomic potential for Cu was modified to make the nanocluster elastically softer than the Fe matrix.

Conclusions

Atomistic computer simulations were used to explore the effectiveness of coherent nanoclusters for trapping He in a Fe matrix. All point defect complexes considered in this study were bound to 2 nm Cu clusters with binding energies ranging from 0.50–0.58 eV for single vacancies and substitutional He atoms. Di-vacancies and He/di-vacancy complexes were more strongly bound with binding energies of ~ 0.85 eV. He/di-vacancy complex binding energy increases with cluster size and reaches a maximum of ~ 0.85 eV for clusters ≥ 2 nm in diameter. Point defects were not as strongly bound to nanoclusters elastically softer than Fe when compared to binding energies to nanoclusters elastically stiffer than Fe. Differences in point defect formation energies were likely responsible for the different binding energies observed rather than the specific elastic properties of the nanoclusters. The point defect "capture radius" for 2 nm Cu clusters was about 0.4 nm, independent of defect formation energy differences or nanocluster elastic properties.

References

[1] G. J. Ackland, D. J. Bacon, A. F. Calder, and T. Harry, "Computer Simulation of Point Defect Properties in Dilute Fe-Cu Alloy Using a Many-Body Interatomic Potential," Philos. Mag. A. 75(3) (1997) 713–732.

[2] R. J. Kurtz and H. L. Heinisch, "The Effects of Grain Boundary Structure on Binding of He in Fe," J. Nucl. Mater. 329–333 (2004) 1199–1203.

[3] W. D. Wilson and R. D. Johnson, "Rare Gases in Metals, Interatomic Potentials and Simulation of Lattice Defects," P. C. Gehlen, J. R. Beeler, Jr., and R. I. Jaffee (eds.), Plenum Press, New York (1972) 375–390.

[4] R. Kohlhaas, P. Dunner, and P. N. Schmitz, "The Temperature-dependance of the Lattice Parameters of Iron, Cobalt, and Nickel in the High Temperature Range," Z Angew Physik 23(4) (1967) 245–249.

[5] M. E. Straumanis and L. S. Yu, "Lattice Parameters, Densities, Expansion Coefficients, and Perfection of Structure of Cu and Cu-In Alpha-Phase," Acta Crystallogr. 25A (1969) 676–682.

[6] Landolt-Boernstein, Numerical Data and Functional Relationships in Science and Technology, New Series, Group III, Vol. 2, Springer-Verlag, Berlin (1979).
[7] C. Kittel, Introduction to Solid State Physics, Sixth Edition, John Wiley & Sons, Inc., New York (1986) 55.
[8] K. Fuederer, K.-P. Doering, M. Gladisch, N. Haas, D. Herlach, J. Major, H.-J. Mundinger, J. Rosenkranz, W. Schafer, L. Schimmele, M. Schmolz, W. Schwarz, and A. Seeger, "Vacancy Formation in Thermal Equilibrium in Ferromagnetic Iron and Cobalt Studied by the Spin Rotation of Positive Muons," Mater. Sci. Forum 15–18 (1987) 125.
[9] L. De Schepper, G. Knuyt, L. M. Stals, D. Segers, L. Dorikens-Vanpraet, M. Dorikens, and P. Moser, "Migration and Formation of Vacancies in α-Iron," Mater. Sci. Forum 15–18 (1987) 131.
[10] H.-E. Schaefer, K. Maier, M. Weller, D. Herlach, A. Seeger, and J. Diehl, "Vacancy Formation in Iron Investigated by Positron Annihilation in Thermal Equilibrium," Scr. Metall. 11 (1977) 803.
[11] H.-E. Schaefer, "Investigation of Thermal Equilibrium Vacancies in Metals by Positron Annihilation," Phys. Status Solidi (a) 102 (1987) 47.
[12] S. Nanao, K. Kuribayashi, S. Tanigawa, M. Mori, and M. Doyama, "The Measurement of the Formation Energy of a Vacancy in Cu by Positron Annihilation," J. Phys. F 3(1) (1973) L5–L8.
[13] H. Fukushima and M. Doyama, "The Formation Energies of a Vacancy in Pure Cu, Cu-Si, Cu-Ga, and Cu-Mn Solid Solutions by Positron Annihilation," J. Phys. F 6(5) (1976) 677–685.
[14] O. Le Bacq, F. Willaime, and A. Pasturel, "Unrelaxed Vacancy Formation Energies in Group-IV Elements Calculated by the Full-Potential Linear Muffin-Tin Orbital Method: Invariance with Crystal Structure," Phys. Rev. B 59(13) (1999) 8508.
[15] G. J. Ackland and V. Vitek, "Many-Body Potentials and Atomic-Scale Relaxations in Noble-Metal Alloys," Phys. Rev. B 41 (1990) 10324–10333.

DIFFUSION OF He INTERSTITIAL AND SMALL CLUSTERS AT GRAIN BOUNDARIES IN α-Fe—

F. Gao, R. J. Kurtz, and H. L. Heinisch, Jr. (Pacific Northwest National Laboratory)*

EXTENDED ABSTRACT (submitted to the Journal of Nuclear Materials as part of the proceedings of the 12th International Conference on Fusion Reactor Materials, Santa Barbara, California, December 4–9, 2005)

A systematic molecular dynamics study of the diffusion mechanisms of He interstitial and their small clusters at two representative interfaces, Σ11 and Σ3, has been carried out in α-Fe. The diffusion coefficient of a He interstitial and the effective migration energies were determined, and the diffusion mechanisms of single interstitials and di-He interstitials are discussed in detail. A di-He interstitial cluster can kick out a self interstitial atom (SIA) at high temperatures, forming a He_2V complex. The SIA migrates rapidly near interfaces, whereas the He_2V complex is immobile at the temperatures considered. This small cluster may serve as a smallest nucleation for the formation of helium bubbles at interfaces.

Most of the details pertaining to the methodology used in the calculations of the atomic arrangements of GBs have been described in detail elsewhere [1,2]. Two symmetric tilt GBs, Σ3 {112} Θ = 70.53°, Σ11 {323} Θ = 50.48°, were employed to study diffusion of He interstitials and small clusters in the temperature range from 600 to 1200 K. The interatomic potentials used in this research have been described in detail previously [3]. The migration simulations were followed for 1–14 ns, depending on the temperature. The diffusivity, D, of He atoms can be determined from the sum of the mean square displacements (MSD) of He atoms. To accurately calculate the diffusion coefficient of He atoms, the method used here is based on decomposing the single trajectory into a set of shorter independent segments with equal duration, and then an average MSD, D_i (i indicates the ith time interval for the segment) for each segment is calculated. The time interval of segments varies from 10 ps to 500 ps, and then D_i is averaged over all time intervals. With the diffusion coefficients of He atoms obtained at different temperatures, the activation energy for He migration in GBs, E_m, can be estimated from the Arrhenius Relation where D_0 is the pre-exponential factor and k_β is the Boltzmann constant.

$$D = D_0 \exp\left(-\frac{E_m}{k_\beta T}\right), \qquad (1)$$

The mean square displacements of a He interstitial are determined as a function of time for the Σ3 and Σ11 GB using the method described above. During the simulation, a large number of He jumps are observed, but the dynamic processes occasionally involve the jumps of Fe atoms. However, the contribution of Fe jumps to the total MSD is negligible. The diffusion coefficients estimated for the He interstitial in both GBs are given in Fig. 3 as a function of reciprocal temperature, where circle symbols represent the data calculated for the Σ3 GB and square symbols indicate the data obtained for the Σ11 GB. The data approximately follow an Arrhenius relationship, from which the corresponding activation energies, E_m, and pre-exponential factors, D_0, can be determined. The best fits of these results to Eq (1) give the values of E_m and D_0 to be 0.28 eV and $4.39 \times 10^{-4} cm^2/s$ for the Σ3 GB, and 0.34 eV and $4.3 \times 10^{4} cm^2/s$ for the Σ11 GB, respectively.

The migration mechanisms of He interstitials in GBs have been studied by analysis of the computer-generated trajectories. The result suggests that the He interstitial mainly migrates with one-dimensional behavior at low temperature. However, it has been observed that the migration path of the He interstitial changes from one-dimensional (1D) diffusion to two-dimensional (2D) diffusion in the interface plane at

*Pacific Northwest National Laboratory (PNNL) is operated for the U.S. Department of Energy by Battelle Memorial Institute under contract DE-AC06-76RLO-1830.

800 K and three-dimensional (3D) diffusion at higher temperatures in the Σ3 GB. This behavior is consistent with its small binding energy, which is the lowest He binding energy among all the GBs calculated [4]. In the Σ11 GB the He interstitial is strongly bound to the middle plane on which the initial starting position of the He interstitial is allocated, and it can only move in the spaces between the three planes. These results demonstrate that interstitial He diffusion and the corresponding migration mechanisms depend significantly on the atomic structures of the GBs.

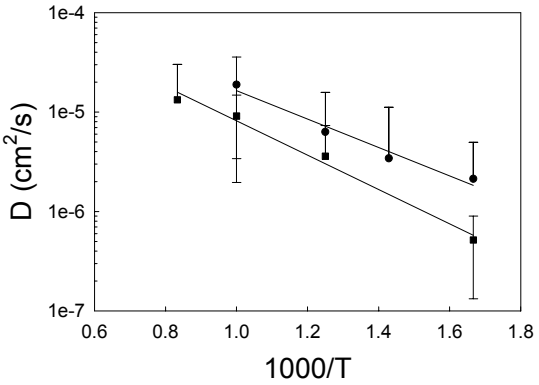

Fig. 1. Diffusion coefficients of He interstitial as a function of reciprocal temperature in the Σ3 and Σ11 GBs in α-Fe, where reciprocal temperature is scaled by 1000.

Figures 2(a) and (b) show the mean square displacements of a di-He interstitial cluster as a function of time for the Σ3 and Σ11 GB, respectively. In general, the migration behavior is more complicated than that of a single He interstitial observed above. In the Σ3 GB the MSDs increase generally with increasing time for the temperatures of 600, 800 and 1000 K, but there exist significant fluctuations. During the simulation, a large number of He jumps are observed, and the di-He interstitial cluster mainly migrates along a <110> direction in the plane containing the interface, which is similar to that observed for a single He interstitial.

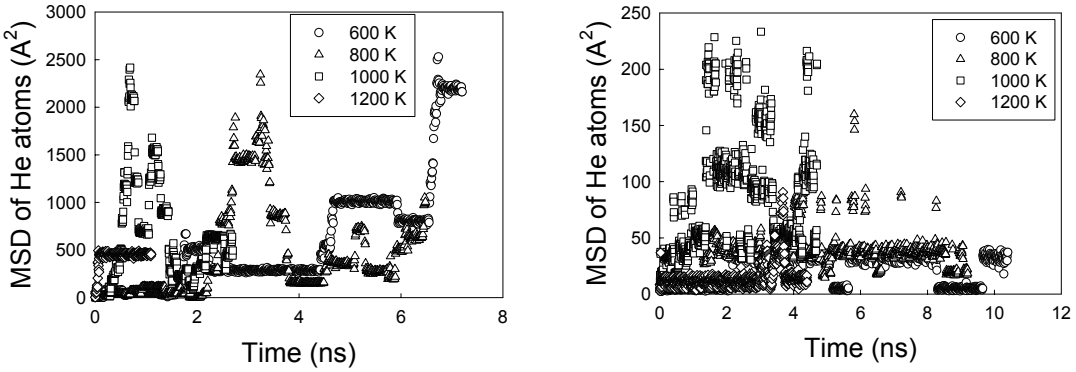

Fig. 2. Mean-square displacements of the di-He interstitial cluster as a function of time for the temperature range between 600 and 1200 K on (a) the Σ3 GB and (b) the Σ11 GB.

The dissociation of the two He atoms is not observed at any of the temperatures considered. One very interesting result observed for the migrating di-He interstitial cluster is that the MSD at 1200 K initially increases as time advances, but it is almost constant during subsequent simulations. A detailed atomic analysis of this situation reveals that the migrating di-He interstitial cluster causes an Fe atom to be "kicked out" from its lattice site, resulting in the creation of a vacancy and a self interstitial atom (SIA). The SIA immediately migrates away from the di-He interstitial cluster, and this leads to the formation of a He_2V complex.

Figure 3 shows the creation of a SIA that has a crowdion configuration along the $[1\bar{1}1]$ direction, and two He atoms, where the vacancy between them is not plotted. The large dark spheres represent Fe atoms, the small gray spheres vacant sites and the large gray spheres He atoms. In the Σ3 GB the SIA migrates

only along the interface axis even at high temperatures, and this may be due to the strong binding of a SIA to the interface. A similar kick-out mechanism is also observed for the simulation temperature of 1000 K at about 1.7 ns. After a SIA is kicked out from its lattice site, the He_2V complex is observed to be very stable, and the subsequent simulations only involve the configuration changes of the complex without significant diffusion. Thus the He_2V complex might serve as a smallest nucleation object for bubble formation at interfaces, but this needs to be confirmed by simulating the diffusion of He atoms with different He concentrations at interfaces. In the present simulations, the diffusion coefficients of a di-He interstitial cluster cannot be estimated from the MSDs because the high temperature simulations result in the generation of a Frenkel pair. Similar to the simulations at 1200 K in the $\Sigma 3$ GB, a SIA is also emitted by the di-He interstitial cluster in the $\Sigma 11$ GB, and the SIA diffuses away from the cluster within a very short simulation time, resulting in the formation of a He_2V complex.

Fig. 3. Atomic plot showing the emission of a self interstitial atom that forms a <111> crowdion.

Conclusions

The diffusion of He interstitials and small He clusters along the $\Sigma 11$<110>{323} and $\Sigma 3$<110>{112} GBs in α-Fe has been studied using molecular dynamics methods The diffusion coefficient of a single He interstitial is calculated using the mean square displacements of He atoms, and the effective migration energies were determined to be 0.28 eV and 0.34 eV for $\Sigma 3$<110>{112} GBs and $\Sigma 11$<110>{323}, respectively. The MSDs of a di-He interstitial cluster in the $\Sigma 3$ GB are much larger than those in the $\Sigma 11$ GB, which is consistent with the fact that the di-He interstitial cluster is mobile in the $\Sigma 3$ GB at low temperatures. At higher temperature in both the $\Sigma 3$ and $\Sigma 11$ GBs the di-He interstitial cluster can kick out a self interstitial atom, and the SIA migrates rapidly along the interfaces, with <111> crowdion and <110> migration mechanisms in the $\Sigma 3$ and $\Sigma 11$ GBs, respectively. The H_2V complex may serve as a smallest nucleation site for the formation of helium bubbles at interfaces.

References

[1] R. J. Kurtz, R. G. Hoagland, and J. P. Hirth, Philos. Mag. A79 (1999) 665.
[2] R. J. Kurtz, R. G. Hoagland, and J. P. Hirth, Philos. Mag. A79 (1999) 683.
[3] K. Morishita, R. Sugano, B. D. Wirth, and T. Diaz de la Rubia, Nucl. Instrum. Methods Phys. Res. B 202 (2003) 76.
[4] R. J. Kurtz and H. L. Heinisch, J. Nucl. Mater. 329–333 (2004) 1199.

MODELLING THERMODYNAMICS OF ALLOYS FOR FUSION APPLICATION—A. Caro, B. Sadigh, M. Caro, J. Marian (Lawrence Livermore National Laboratory), E. Lopasso (Centro Atomico Bariloche, Argentine), and D. Crowson (Virginia Polytechnical Institute)

OBJECTIVE

This research has two main objectives.

- On one side is the development of computational tools to evaluate alloy properties, using the information contained in thermodynamic functions to improve the ability of classic potentials to account for complex alloy behavior.

- On the other hand, to apply the tools so developed to predict properties of alloys under irradiation.

SUMMARY

Atomistic simulations of alloys at the empirical level face the challenge of correctly modeling basic thermodynamic properties. In this work we develop a methodology to generalize many-body classic potentials to incorporate complex formation energy curves. Application to Fe-Cr allows us to predict the implications of the ab initio results of formation energy on the phase diagram of this alloy.

PROGRESS AND STATUS

We address the problem of alloy description with atomistic models from the perspective of thermodynamics. We derive the phase diagram of a model Hamiltonian, namely, the embedded-atom EAM potential for Fe-Cr.

To do so, we follow the procedure described in [1–2] and apply it to Iron alloys with different Chromium concentrations. The same computational thermodynamics tools developed in [3] were applied with success in the case of Fe-Cu alloys to predict the phase diagram of such a system.

Gibbs free energies for the solid and liquid phases are calculated using MD simulations for pure elements and for several Fe-Cr alloys. In this work, we use the Fe potential reported in [4] and the Cr potential reported in [5]. For the cross potential we use the methodology described in [6] that incorporates the complex formation energy curve for Fe-Cr. The cross potential is derived so that it reproduces the calculated *ab initio* formation energy Δh of Olsson et al. [7]. The formation energy of bcc ferromagnetic Fe-Cr alloys given in [7] can be reproduced by a Redlich-Kister expansion to 4th order in (1–2x) as follows:

$$\Delta h = x(1-x)\sum_{0}^{n} L_p (1-2x)^p \tag{1}$$

As we see in Fig. 1, Δh is highly non-symmetric and even changes sign at low Cr composition.

Phase Diagram of the Fe-Cr Empirical Potential

We calculate the free energy per particle at a given temperature T, $f(T)$, through thermodynamic integration between the state of interest and a reference state at temperature T_0 with known free energy $f(T_0)$. The free energy per particle is given by the Gibbs-Duhem integral:

$$f(T) = f(T_0)\frac{T}{T_0} - T\int_{T_0}^{T} \frac{h(\tau)}{\tau^2} d\tau \tag{2}$$

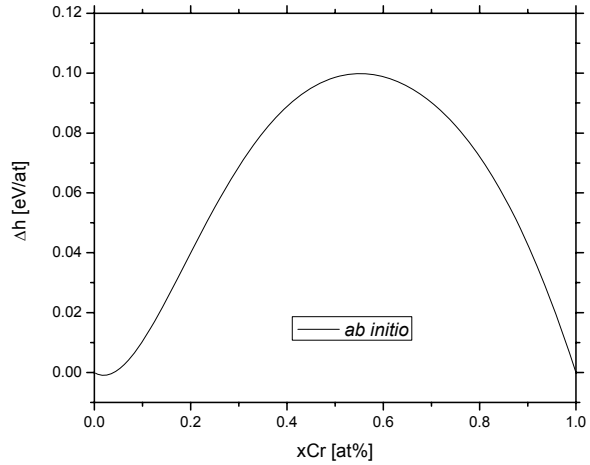

Fig. 1. Calculated mixing enthalpy for ferromagnetic bcc Fe-Cr alloys, corresponding to Fe-Cr in the low temperature range (T < 1000 K).

Second-order polynomials are adjusted to the simulation results of the internal enthalpy for solid and liquid Fe-Cr alloys, and the integral of Eq. (2) is solved analytically.

The resulting Gibbs free energies and entalphy per particle are computed as:

$$g(T) = A + B\,T + C\,T^2 + D\,T\,LN(T) \qquad (3)$$
$$h(T) = \tilde{A} \; \tilde{D}T \; \tilde{C}T^2$$

We can also express the free energy of a random solid solution phase of an alloy with composition x at temperature T as:

$$g(x,T) = g_{ref}(x,T) + g_{mix}(x,T) + \Delta g(x,T) \qquad (4)$$

where g_{ref}, g_{mix} are given by (k is Boltzmann constant equal to 8.617385 x 10^{-5} eV/K):

$$g_{ref}(x,T) = (1-x)\,g_{Cr}(T) + x\,g_{Fe}(T)$$
$$g_{mix}(x,T) = kT\,[(1-x)\,ln(1-x) + x\,ln(x)]$$

The excess Gibbs energy of mixing can also be conveniently expressed by a Redlich-Kister expansion [8] as:

$$\Delta g(x,T) = x(1-x)\sum_{0}^{n} L_p(T)(1-2x)^p \qquad (5)$$

where $L_p(T)$ is the pth-order binary interaction parameter.

Bearing Eqs. (4–5) in mind, we choose to express the functional form of each coefficient A, B, C, and D in Eq. (3) as:

$$Coeff = C_{Fe}\,(1-x) + C_{Cr}\,x + x\,(\tilde{1}-x)\Sigma\, L_p^{Coeff}\,(\tilde{1}-2x)^p$$

With these values we build up a database for Fe-Cr and use the software package Thermo-Calc [8] to calculate the phase diagram shown in Fig. 2.

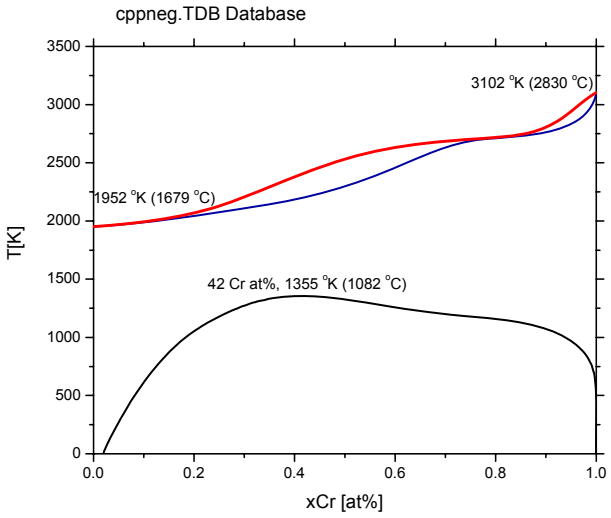

Fig. 2. Predicted phase diagram obtained from the application of the Thermo-Calc software to the database cppneg. TDB generated using the Fe-Cr empirical potential.

The Heat of Formation

Experimental points have been reported at T = 1600 K. The SSOL library in Thermo-Calc (CALPHAD) package reproduces these points accurately as shown in Fig. 3.

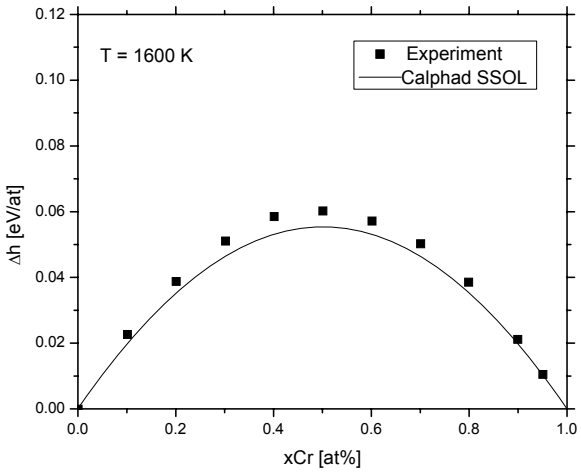

Fig. 3. Heats of formation of Fe-Cr as described in the database of CALPHAD and experimental measurements.

Our database cppneg.TDB based on the Fe-Cr empirical potential reproduces well the calculated *ab initio* formation energy at low temperature as shown in Fig. 4.

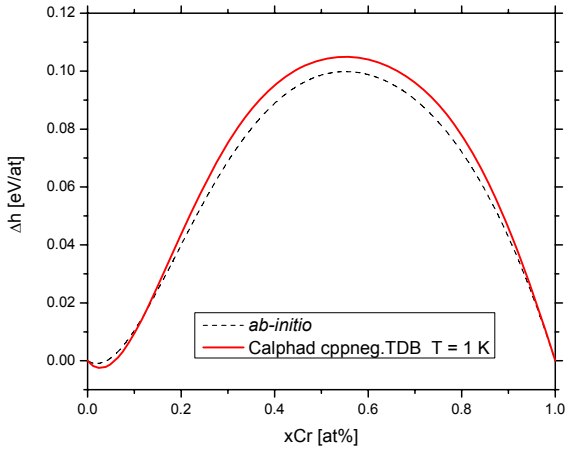

Fig. 4. Heats of formation of Fe-Cr as described in the database built upon our potential and the ab initio results.

The point of controversy is the difference in the formation enthalpy of the ferromagnetic solid solution between *ab initio* calculations and CALPHAD SSOL (see Fig. 5) :

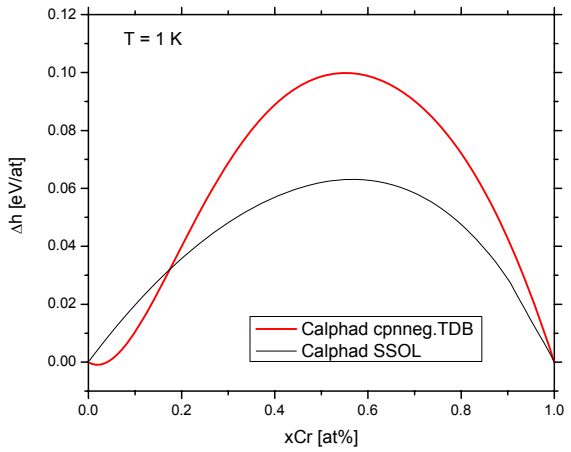

Fig. 5. Heats of formation of Fe-Cr as described in the database of CALPHAD and our own based on the ab inito results.

The Entropy calculated for the classic potential appears to be remarkable close to the CALPHAD values indicating a good over-all reproduction of the dynamics of the system (see Fig. 6).

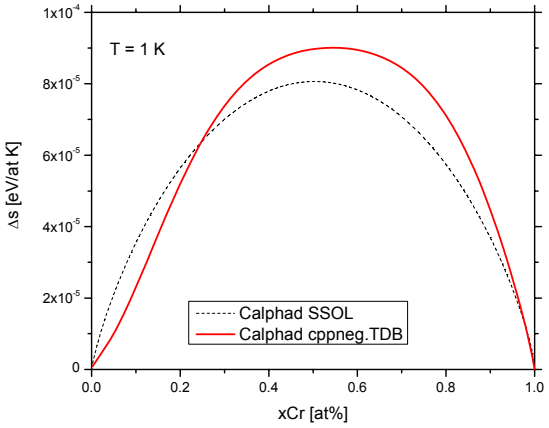

Fig. 6. Entropy of formation of Fe-Cr as described in the database of CALPHAD and our own database based on ab initio results.

Comparison with the Experimental (CALPHAD) Phase Diagram

The experimental phase diagram is obtained using the SSOL library in Thermo-Calc, as reported in Fig. 7. Melting points are shown in the table below:

	Fe	Cr
SSOL	1810 K (1537 C)	2180 K (1907 C)
Cppneg.TDB	1952 K (1679 C)	3102 K (2830 C)

Pure Cr is poorly described, as its melting point is significantly above the experimental value. The phase diagram obtained using Thermo-Calc appears in the graph below. Note that BCC, FCC, Sigma, and Liquid phases of the SSOL database are included.

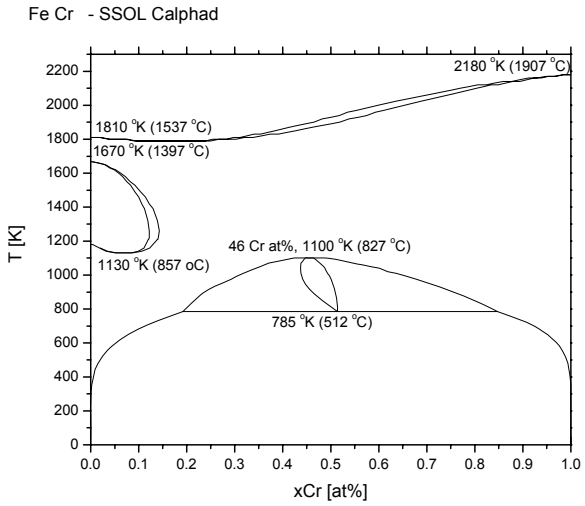

Fig. 7. Experimental phase diagram of the Fe-Cr system.

Neglecting all phases but Liquid and BCC, we obtain the phase diagram shown in Fig. 8.

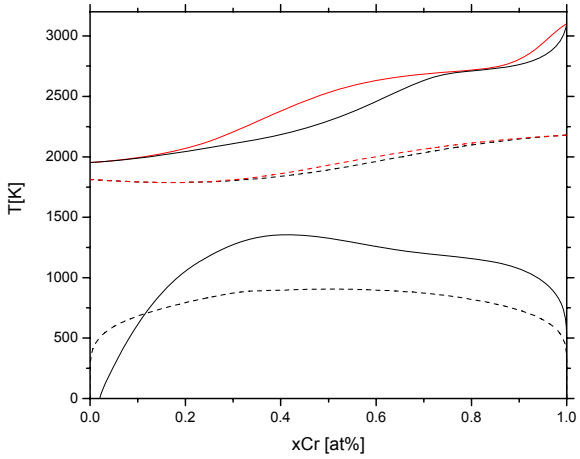

Fig. 8. Phase diagram reporting only liquid and bcc phase of the Fe-Cr system as measured experimentally (dotted lines) and as implied by the ab initio results (solid lines).

Solid lines correspond to the results obtained in this work. Dash lines correspond to SSOL CALPHAD database. The "experimental" (CALPHAD) miscibility gap has a maximum at 904.7 K (x_{Cr} ~ 0.515 at%) and is quite symmetric as compared to the highly nonsymmetrical miscibility gap is found in our work. The miscibility gap has a different shape at low concentration, the solid curve goes to zero at x_{Cr} = 0.0197 at %.

These results prove on one side the ability of our approach to go from ab initio results to classic potentials, and to go form classic potentials to thermodynamics. From here on, we can reliably use the potentials so developed to evaluate non equilibrium processes induced by radiation.

References

[1] E. Ogando Arregui, M. Caro, and A. Caro, "Numerical evaluation of the exact phase diagram of an empirical Hamiltonian: Embedded atom model for the Au-Ni system," Phys. Rev. B 66 (2002) 054201.
[2] E. M. Lopasso, M. Caro, A. Caro, and P. E. A. Turchi," Phase diagram of an empirical potential: The case of Fe-Cu," Phys. Rev. B 68 (2003) 214205.
[3] A. Caro, P. E. A. Turchi, M. Caro, and E. M. Lopasso, "Thermodynamics of an empirical potential description of Fe-Cu alloys," J. Nucl. Mater. 336 (2005) 233–242.
[4] M. I. Mendelev, S. Han, D. J. Srolovitz, G. J. Ackland, D. Y. Sun, and M. Asta, Philos. Mag. 83 (2003) 3977.
[5] J. Wallenius, P. Olsson, C. Lagerstedt, N. Sandberg, R. Chakarova, and V. Pontikis, Phys. Rev. B 69 (2004) 094103.
[6] A. Caro, D. A. Crowson, and M. Caro, "Classical many-body potential for concentrated alloys and the inversion of order in iron-chromium alloys," Phys. Rev. Lett. 95 (2005) 075702.
[7] P. Olsson, I. A. Abrikosov, L. Vitos, and J. Wallenius, "Ab initio formation energies of Fe-Cr alloys," J. Nucl. Mater. 321 (2003) 84–90.
[8] N. Saunders and A. P. Miodownki, *CALPHAD: A comprehensive guide*, R. W. Cahn (ed.), Pergamon Materials Series, Oxford, New York, 1998.

10. DOSIMETRY, DAMAGE PARAMETERS, AND ACTIVATION CALCULATIONS

ERRATUM to "NEUTRON DOSIMETRY AND DAMAGE CALCULATIONS FOR THE HFIR-MFE-200J-1 IRRADIATION," in Fusion Materials Semiannual Progress Report for Period Ending December 31, 1997, DOE/ER-0313/23, pp. 329–332.

Table 2 of this report contains an error. The thermal neutron fluence should be 0.35×10^{22} n/cm^2. The error has been corrected, and a revised version of the report is available on-line in DOE/ER-0313/23. Anyone who downloaded and/or referred the original report is encouraged to obtain the corrected copy.

11. MATERIALS ENGINEERING AND DESIGN REQUIREMENTS

No contributions.

12. IRRADIATION FACILITIES AND TEST MATRICES

No contributions.